Gravitational wave astronomy with current and future generation detectors

Please check the document version of this publication:

• A submitted manuscript is the version of the article upon submission and before peer-review. There can be important differences between the submitted version and the official published version of record. People interested in the research are advised to contact the author for the final version of the publication, or visit the DOI to the publisher's website.
• The final author version and the galley proof are versions of the publication after peer review.
• The final published version features the final layout of the paper including the volume, issue and page numbers.

Link to publication

Download date: 11 May. 2024

Gravitational Wave Astronomy With Current And Future Generation Detectors

Ayatri Singha

Doctoral dissertation

GRAVITATIONAL WAVE ASTRONOMY WITH CURRENT AND FUTURE GENERATION DETECTORS

Ayatri Singha

2024

Gravitational Wave Astronomy With Current And Future Generation Detectors
 Dissertation, Maastricht University, Maastricht
Cover design by ©picsartgeeks.com
Cover picture adapted from
[1] Artist's impression of the underground Einstein Telescope, a planned third-generation gravitational-wave detector. © NIKHEF
[2] Premium Photo: Gravity planet earth gravitational waves concept physical and technology background design with gravity grid and spheres line warp curved spacetime in the general theory of relativity (freepik.com)
[3] https://www.flickr.com/photos/jurvetson/898622334

GRAVITATIONAL WAVE ASTRONOMY WITH CURRENT AND FUTURE GENERATION DETECTORS

DISSERTATION

to obtain the degree of Doctor at Maastricht University,

on the authority of the Rector Magnificus, Prof. dr. Pamela Habibović

in accordance with the decision of the Board of Deans,

to be defended in public

on Thursday 4th April 2024, at 10:00 hours

by

Ayatri Singha

Supervisor:

Prof. Stefan Hild

Co-supervisor:

Dr. Stefan Danilishin

Assessment Committee

Prof. Marcel Merk, Full Professor at GWFP, Maastricht University (chair)

Prof. Chris van den Broeck, Utrecht University

Prof. Andreas Freise, Vrije Universiteit Amsterdam

Dr. Gideon Koekoek

Dr. Jessica Steinlechner

Contents

List of Figures

Chapter 1

Introduction to gravitational waves

1.1 Gravitational waves - A new window on the universe

In 1915, the discovery of the gravitational field equations of general relativity by Albert Einstein marked the beginning of a new theory of gravity [73, 164]. According to Newton's law of gravity, the gravitational force between objects is proportional to the mass of the two bodies and becomes smaller as the distance between two objects increases. The law does not discuss the speed at which information travels in the gravitational field. In 1905, Einstein prescribed no interaction and information can travel faster than the speed of light, and Newton's law of Gravity violated this principle. Based on this controversy, Einstein developed the theory of gravity, in which gravity is not a force like Newton's law, but rather the manifestation of the curvature of space-time. According to Einstein's theory of general relativity [97], one can find the wave-like solution to Einstein's equation for the curvature of space-time, and the waves are the ripples in the fabric of space-time. The space gets deformed by the mass, and the space's deformation manifests how the mass moves. Einstein pointed out that there could be gravitational waves just like electromagnetic waves. Electromagnetic waves are produced by dipolar radiation from an oscillating dipole (positive and negative charges separated by some distance). However, a similar analogy was not possible for gravitational waves, because there is no charge concept for mass [58]. Gravitational waves transport energy as gravitational radiation, a

form of radiative energy [133]. Heavy and compact objects, such as a binary neutron star and binary black holes moving in orbit, lose energy in the form of gravitational waves. This energy is significant when the objects come close together and merge. During the merger, a significant amount of mass is converted into gravitational energy, so the amplitude of the gravitational waves is at its maximum. In 1974, Russell Hulse and Joseph Taylor first detected indirect evidence for gravitational wave emission from the orbital motion of two neutron stars in the system PSR 1913+16 [139, 138, 137]. They observed the electromagnetic radiation emitted by the pulsar, which showed a decrease in the frequency of the pulses over time. The stars were gradually inspiraling towards each other, and the decay in their energy was roughly consistent with the predicted energy carried by the gravitational waves.

Gravitational wave detectors are specifically designed instruments used to detect and measure the extremely tiny disturbances in space-time caused by passing gravitational waves. These detectors, such as the Laser Interferometer Gravitational-Wave Observatory (LIGO) and the Virgo detector, employ advanced techniques to measure minuscule changes in the distances between mirrors caused by passing gravitational waves. In September 2015, the first direct detection of gravitational waves came from the coalescence of binary black holes [4] 1.3 billion light-years away. This was detected by both LIGO at Hanford and Livingstone. To date, the Advanced LIGO and Virgo observatories have made nearly ninety confident detections, from which we have measured the intrinsic and extrinsic parameters of the GW source, as well as the astronomical parameters of the universe [17, 22, 21]. The discovery of gravitational waves has provided a new and unique tool to peer into the Universe, allowing us to do multi-messenger astronomy. Another breakthrough discovery made by GW detectors is the detection of the GW signal emitted by the binary neutron star system (BNS), GW170817 [212]. This type of system is of paramount importance for multi-messenger astronomy. Multi-messenger astronomy is astronomy that uses multiple messengers such as the electromagnetic spectrum, gravitational waves, neutrinos, cosmic rays, etc., from violent astronomical events. Binary neutron star systems are particularly interesting because they are accompanied by strong and continuous gravitational wave emission, and emit electromagnetic radiation over a wide range of wavelengths during the late inspiral [177, 201]. The merger of BNS systems may lead to a short gamma-ray burst or even a kilonova transient

due to r-process nucleosynthesis of heavy elements [206]. In addition to information about the abundance of heavy elements in the Universe, observations of BNS systems can reveal the state of ultrahigh-density matter, the formation mechanism of magnetars, etc. We can also indirectly observe the early universe by looking at how gravitational waves from that time have affected the matter and radiation we observe today.

To make the breakthrough discovery, we need to improve the sensitivity of the detectors and increase their duty cycle to maximize the coincidence time of multiple detectors. More separate detectors will help to detect the gravitational wave signal with more confidence (less chance of coincidence with an instrumental glitch), precise sky localization, and accurate source parameter estimation due to improved signal-to-noise ratio (SNR)[44, 215]. Currently, operational detectors such as Advanced LIGO and Advanced Virgo are upgraded before each science run to increase sensitivity, allowing us to detect more events with higher precision. In addition to LIGO and Virgo, there is the Kamioka Gravitational Wave Detector (KAGRA), a large underground interferometer with 3km arm length and the first detector to use cryogenic mirrors[2, 39]. GEO600 [223, 108], another ground-based interferometric gravitational wave detector near Hannover in Germany, with an arm length of 600m. KAGRA joined LIGO, Virgo, and GEO600 in the search for gravitational waves towards the end of the third observing run O3 (in February 2021). LIGO, Virgo, KAGRA, and GEO600 are currently being upgraded for their fourth joint observing run, O4 (late 2022). There is also a planned advanced detector, LIGO-India [209, 191], which is expected to join the global network by 2030. Although second-generation detectors have achieved significant milestones in gravitational wave astronomy, their sensitivity is limited by various sources of noise. To further reduce the noise and improve sensitivity by at least a factor of 10, new technologies will have to be chosen that are difficult to implement in current detectors. Scientists have therefore proposed plans for next-generation gravitational wave detectors, such as the Einstein telescope and the Cosmic Explorer, which will have ten times the sensitivity of the advanced LIGO and will also observe at a much lower frequency, about 3 Hz, and in the range up to several kilohertz. The plan for the Einstein telescope is to be built underground to reduce seismic noise at low frequencies, as discussed in 1.4.1. The Einstein telescope (possibly also the Cosmic Explorer [113]) is planned to operate at a cryogenic temperature, which will help reduce the thermal noise, discussed in 1.4.3.

1.2 Sources of gravitational waves

Any non-spherical or non-cylindrical symmetric accelerating object can produce gravitational waves. Unlike an electromagnetic wave, the second-order time derivatives of the dipole moment cannot contribute to gravitational waves due to the conservation of energy and momentum. Therefore, the leading order of GWs comes from the variation of the quadruple moment. The brightest source of gravitational waves must be compact and massive. Neutron stars and black holes are the most compact objects in the Universe and therefore the brightest sources of gravitational waves. We can classify gravitational wave sources into four categories, which are discussed below.

1.2.1 Compact binaries coalescence

Compact binaries, consisting of a pair of neutron stars, a pair of black holes, or a neutron star and a black hole, are powerful sources of gravitational radiation [157]. Like the Hulse-Taylor binary [138], these systems spend millions of years at very low luminosity. But as the two compact objects come closer together, they brighten to the point where they can be detected at cosmological distances, just seconds to minutes before they merge. They are thought to be pristine systems, with no accretion disks or other contaminants, so their dynamics are governed entirely by the back-reaction of gravitational radiation [103, 84]. Using the post-Newtonian approximation to general relativity [57, 85], we can find the orbital period and thus the frequency of the emitted gravitational waves. We observe that the amplitude and frequency of the signal increase monotonically as a function of time, producing a characteristic chirp. A circular binary will merge by radiation reaction from gravitational wave emission on a timescale of T_{merge} [157, 171]

$$T_{\mathrm{merge}} \approx 6 \times 10^8 \frac{M_\odot^3}{m_1 m_2 (m_1 + m_2)} \left(\frac{a}{10^{11} \ \mathrm{cm}} \right)^4 \ \mathrm{years} \ , \qquad (1.1)$$

where m_1 and m_2 are the component masses and a is the orbital radius. The radius of the Sun is approximately 10^{11} cm, which means that two Suns revolving around each other and separated by a distance of 10 solar radii will take around 3×10^{12} years to merge. Stellar masses BBH and BNS, with total masses ranging from one to a few hundred solar masses, are the main GW sources for the currently operating ground-based interferometric GW detectors Advanced LIGO and Advanced Virgo. These

1

detectors are sensitive to GWs at frequencies between about 20 Hz and a few kHz and over ranges of up to few hundred megaparsecs for binary neutron star mergers and a few thousand megaparsecs for binary black hole mergers [92]. To detect GWs from the collisions of supermassive black holes [94, 111], the frequency band needs to be pushed down a few Hz to mHz. The third generation of detectors, such as the Einstein telescope, is proposed to reach down to 1 Hz, rather than the 10-20 Hz limit of advanced detectors. There is also proposed space-based gravitational wave detector, the Laser Interferometer Space Antenna (LISA), which will have a strain sensitivity of better than 1 part in 10^{20} in the low-frequency band around 0.1 mHz and 1 Hz [35, 70, 217]. LISA will consist of three spacecraft separated by 2.5 million km in a triangular formation following the Earth in its orbit around the Sun. Observing the GWs from the BBH inspirals can provide us with an important tool to test the general theory of relativity in the strong gravity [227, 55], the astrophysical origin of the population of black holes [161, 142, 112], information on their possible formation history, and constraints on the rate of such mergers in the Universe [52]. The LIGO/Virgo network has detected nearly ninety compact binary sources such as binary black holes, binary neutron stars, and even a high mass ratio event from which we found evidence for higher order modes [160, 67]. The masses of the detected events during three observing runs, O1, O2, and both O3a and O3b, are shown in figure 1.1.

1.2.2 Continuous gravitational waves

Neutron stars with a time-varying quadrupole, generated by non-axisymmetric rotation, accretion of matter, or energy transfer from a differentially rotating core to the crust, can serve as a continuous source of gravitational waves [185, 173]. Any bumps or imperfections in the spherical shape of the neutron star will generate gravitational waves as it spins. If the spin rates remain constant over time, the frequency and amplitude of the emitted gravitational waves remain constant, which is why they are known as continuous gravitational waves [11, 6, 185]. Over time, the frequency of these signals changes slowly as the neutron star emits energy in the form of electromagnetic and gravitational waves during its orbital motion. Due to the limited sensitivity of the current detector, we couldn't detect the signal from continuous gravitational wave sources. The detection of continuous GWs from spinning neutron stars will shed light on the true nature of GWs. If we can detect just one
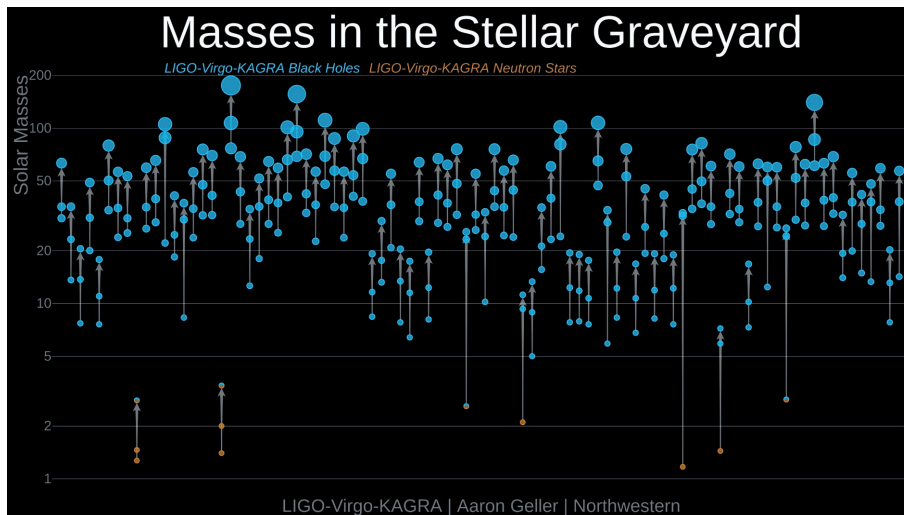
Figure 1.1: List of compact binary sources detected by LIGO and Virgo and KAGRA during the O1, O2, O3a, and O3b science runs (figure taken from [100]). The compact objects are ordered by date of discovery along the x-axis. Solid blue circles indicate the black holes, and orange represents neutron stars. There are three masses in each system, the bottom two being the source masses and the third being the final mass of the system after the merger. Credits: LIGO-Virgo-KAGRA Collaborations/Frank Elavsky, Aaron Geller/Northwestern.

such continuous wave source with moderately stable timing, we can place very strong constraints (due to the large effect of Doppler corrections from detector motion) on the speed of GWs. Therefore, the detection of continuous GWs is the goal for the advanced GW detectors and the third generation of gravitational wave detectors. Detecting continuous GWs would also make it possible to reveal stars that would otherwise remain invisible to us, and to probe them with a messenger that would carry important information about their internal structure and composition [109].

1.2.3 Core collapse supernovae

Core-collapse supernovae and related phenomena are cosmic laboratories for high energy density gravitational, plasma, nuclear, and particle physics. In particular, it may be possible to extract information about the

nuclear EOS directly from GW observations. By detecting the gravitational waves emitted during a core-collapse supernova [167, 148], scientists can learn more about the structure and dynamics of the collapsing star, the formation of neutron stars and black holes, and the nature of the particles and forces involved in the explosion [205]. This information can help us better understand the evolution of stars, the origin of heavy elements in the Universe, and the fundamental laws of physics that govern the cosmos.

All stars similarly go through their first stage, converting hydrogen into helium. As the hydrogen is used up, the fusion reaction slows down and less energy is released. Gravity, therefore, causes the core to contract, depending on the internal structure of the star [141, 65]. When a star runs out of fuel and there is no force to support it against gravity, the star begins to collapse in on itself, causing the core temperature to become extremely high and releasing high-energy gamma-ray bursts [61, 163].

In scenarios where the theoretical gravitational wave signal is well established, such as binary coalescences, the detection process involves the generation of triggers using a matched filtering technique. In a multi-detector array, such as the current Advanced LIGO and Advanced Virgo networks, a transient GW signal is expected to produce nearly simultaneous triggers in all three detectors. The time delay is determined by the direction of the gravitational wave and the associated light travel time. However, when dealing with unmodelled signals, such as those emitted by core-collapse supernovae, the matched-filter technique becomes impractical because modeling such systems involves extremely complicated physics of mass-energy conversion fractions, asymmetry due to convective radiation, and so on [168]. Although there have been advances in numerical simulations, our understanding of the dynamics of supernova explosions remains incomplete. The intricacies of stellar collapse involve extremely complex physics, and the computational resources required for accurate simulations pose a significant challenge in the treatment of core-collapse supernovae. GW signals from core-collapse supernovae are typically much fainter than those from binary mergers. Due to this lower signal strength and the stochastic nature of the signal, the background of GW searches for core-collapse supernovae is expected to be significantly contaminated by short-lived noise transients that may mimic true signals. The challenge is compounded when data from multiple detectors are not available simultaneously. Even with improvements in detector

reliability and a 70% duty cycle, it is expected that about one-fifth of the data in upcoming observing periods for the LIGO-Virgo network will consist of single-interferometer data. Given the rarity of such events, it is important to extend the detector coverage and refine the search background to increase the probability of detecting gravitational wave signals.

The analysis of unmodeled gravitational wave signals requires alternative methods. Time-frequency transformations, such as the Continuous Wavelet Transform or the Short-Time Fourier Transform with time-frequency excess power statistics, can be used to identify significant features or events [75, 154]. The coherent WaveBurst (cWB) algorithm specializes in short-duration transient signals and uses a time-frequency representation to identify and characterize GW bursts. Bayesian methods, exemplified by the BayesWave algorithm, provide a template-free approach that reconstructs GW signals without assuming a specific waveform morphology [143, 205]. Machine learning approaches, including deep learning, explore data-driven pattern recognition for hard-to-characterize signals. Advanced techniques are constantly being developed to reduce noise, but this remains a challenge. Despite the current lack of detection of such signals, continued advances in detector technology, data analysis techniques, and theoretical models will improve the chances of detecting gravitational waves from core-collapse supernovae in the future. The next generation of detectors with improved sensitivity would expand the observable volume of the Universe, increasing the chances of detecting supernova events.

1.2.4   Stochastic gravitational-wave background

The stochastic gravitational wave background refers to a diffuse and random gravitational wave signal that arises from the collective contribution of many unresolved and independent sources distributed throughout the universe [78, 1]. Unlike discrete and individually detectable gravitational wave events, such as those produced by binary mergers or supernovae, the stochastic background represents a statistical ensemble of gravitational waves from a large number of sources. The signals from these sources combine to form a continuous and isotropic background that is present at all frequencies.

The stochastic background can arise from a variety of cosmological and astrophysical processes [180, 93], including:

Inflationary cosmology: The rapid expansion of the universe during

the inflationary epoch in the early universe is thought to have generated gravitational waves [38, 31]. These primordial gravitational waves would have imprinted their signatures on the fabric of spacetime, resulting in a stochastic background that persists to this day.

Cosmic phase transitions: Phase transitions [150, 187] that occurred in the early universe, such as the transition between different states of matter, could have produced gravitational waves. These phase transitions can generate a stochastic background that carries information about the fundamental physics of the early universe.

Compact binary mergers: Although individual binary mergers can be detected as separate gravitational wave events, the collective contribution of many unresolved binaries, such as merging black holes or neutron stars throughout the Universe, can contribute to the stochastic background [181, 10, 189].

Primordial black hole collisions: If primordial black holes exist, their collisions could generate gravitational waves that contribute to the stochas -tic background [47].

Moreover, various astrophysical phenomena, such as rotating neutron stars, supernovae, or cosmic strings, can also contribute to the stochastic background.

The detection and characterization of the stochastic gravitational wave background pose unique challenges compared to the identification of individual gravitational wave sources. It requires statistical analysis techniques to distinguish the faint background signal from instrumental noise and astrophysical foregrounds. Correlations between multiple detectors are used to extract the background signal, as it appears as a random pattern in the detectors' output.

Current and future gravitational wave observatories, including LIGO, Virgo, and future missions such as the space-based Laser Interferometer Space Antenna (LISA), aim to detect and study the stochastic gravitational wave background. Detecting this background provides valuable insights into the early universe, cosmological processes, and the population properties of unresolved gravitational wave sources.

1.3 Observation of gravitational waves

In figure 1.1, we have seen a list of compact binary sources, detected by two LIGO and Virgo detectors during three observing runs. During the first observing run, O1, from 12 September 2015 to 19 January 2016, a

total of 51 days of data were collected by two LIGO detectors. In the second observing run, O2, from 30 November 2016 to 25 August 2017, a total of 118 days of data were collected. In the third run, the two LIGO instruments, the Virgo detector, and the GEO600 began their third observing run, O3, which lasted one year, from 4 April 2019 to 27 March 2020.

During O1, we made our first gravitational wave detection of GW15O914 [4], from colliding black holes with initial masses of 36^{+5}_{-4} $M_\odot$ and 29^{+4}_{-4} $M_\odot$ at a luminosity distance of 410^{+160}_{-180}Mpc. The final black hole mass was 62^{+4}_{-4} $M_\odot$ and $3.0^{+0.5}_{-0.5}$ $M_\odot c^2$ energy was emitted as gravitational waves. The GW150914 event was observed with a matched filter SNR of 24 and a false alarm rate of 1 event per 203000 years. Three binary black holes were detected in the first run.

In O2 we have detected seven binary black hole mergers and one binary neutron star (GW17O817). On 14 August 2017, Virgo joined the network, and the first triple detection of a binary black hole merger was named GW17O814 [7]. This event has a false alarm rate of less than 1 in 27000 years and a matched filter signal-to-noise ratio of 18 for the three-detector network. The initial masses were two black holes with masses $30.5^{+5.7}_{-3.0}$ $M_\odot$ and $25.3^{+2.8}_{-4.2}$ $M_\odot$, which then merged into one black hole with a remnant mass of $53.2^{+3.2}_{-2.5}$ $M_\odot$. The signal was first observed by the LIGO Livingston detector and then by the LIGO Hanford and Virgo detectors with a delay of 8 ms and 14 ms respectively. Three days later, on 17 August 2017, LIGO and Virgo made a remarkable discovery by observing the first binary neutron star merger. What made GW170817 particularly remarkable was the simultaneous detection of electromagnetic radiation at multiple wavelengths, from gamma rays to radio waves. Shortly after the gravitational wave detection, an intense burst of gamma rays, known as a short gamma-ray burst (GRB 170817A), was observed by the Fermi and INTEGRAL satellites [5]. Follow-up observations by various ground- and space-based telescopes detected the event in optical, infrared, and radio wavelengths. These observations revealed the presence of a kilonova, an explosion resulting from the merger of neutron stars [36, 210, 208]. The GW170817 event had a combined network signal-to-noise ratio of 32.4 and a false alarm rate of less than one per 80000 years. The source was localized with 90% probability within a sky region of 28 deg^2 and had a luminosity distance of 40^{+8}_{-14} Mpc, the closest and most precisely localized gravitational wave signal to date [91]. The event GW17O814 was the second best-localized

source (39 deg^2) after the binary neutron star merger GW17O817.

In the third observing run, O3, 76 compact binary mergers were detected with a false alarm rate of less than 1 per year. Among these, two events, GW200105 and GW200115, detected on 5 and 15 January 2020 respectively, were produced by the merger of a binary black hole and a neutron star [20]. The coincident detection of GW200115 by both LIGO and Virgo makes it a strong signal with a false alarm rate of 1 in 100 years. The initial objects were a $5.7^{+1.8}_{-2.1}$ $M_\odot$ black hole and a $1.5^{+0.7}_{-0.3}$ $M_\odot$ neutron star at a luminosity distance of 300^{+150}_{-100} Mpc. They evolved into a remnant black hole. During the other event, GW200105, the LIGO Hanford director was not operational and due to the lower signal-to-noise ratio of Virgo, this event was effectively detected by LIGO Livingston. The false alarm rate for this event was 1 in 2.8 years. The initial compact binary object of this system was an $8.9^{+1.2}_{-1.5}$ $M_\odot$ back hole and $1.9^{+0.3}_{-0.2}$ $M_\odot$. The primary masses of both GW200105 and GW200115 are well above the maximum mass of a neutron star [184, 10, 77]. The probability that the mass of the second compact object is within the mass range of known neutron stars [37, 13, 18], is 89%-96% and 87%-98% [20], for GW200105 and GW200115 respectively. Another very interesting event is GW190814, which is the most asymmetric binary system ever detected by the LIGO and Virgo detectors, with a signal-to-noise ratio of 25 and a false alarm rate of 1 in 1000 years. The primary components of this event were a black hole in the mass range 22.2-24 $M_\odot$ and an extremely heavy neutron star (which theoretically does not exist) or a light black hole with a mass of 2.50-2.67 $M_\odot$. The mass of the lighter component places this object in the mass gap between a neutron star and a black hole. This inferred secondary mass exceeds the most massive known pulsar in the Galaxy [14], which is $2.14^{+0.10}_{-0.09}$ $M_\odot$ with a 68.3% credible interval and comparable to the BH remnant mass of GW170817 [16]. The most massive system observed so far is GW190521, a GW signal consistent with a binary BH merger with a total mass of about 150 $M_\odot$ (component masses 85^{+21}_{-14} $M_\odot$ and 66^{+17}_{-18} $M_\odot$), leaving a remnant of about 140 $M_\odot$ [24, 190]. GW190521 is a significant discovery because the primary black hole mass falls in the black hole mass gap, where no astrophysical black hole can be formed by the pair-instability supernova. The star cannot collapse in on itself and form a black hole with mass greater than 65 solar masses [45, 129, 226], and thus a remnant with mass 142 $M_\odot$, providing the first clear evidence for the existence of an intermediate-mass black hole [202, 51]. The confidence level for this

event was also very high, with an SNR of 14.5 and a false alarm rate of less than 1 in 5000 years.

1.4 Ground-based gravitational wave detectors

Detections of gravitational waves by ground-based gravitational wave detectors, such as the advanced LIGO, Virgo and KAGRA, have opened up a new perspective on the universe and turned them into powerful telescopes. These unprecedented achievements have paved the way for further advances and exciting discoveries in the near future. By continuously improving the sensitivity of gravitational wave detectors, we can expect more frequent detections and improved precision in source parameter estimation. A series of upgrades have already extended the reach of these detectors, with LIGO now able to reach up to 140 Mpc, Virgo up to 60 Mpc, and KAGRA up to 0.7 Mpc [176]. These advances in sensitivity promise to unlock the secrets of the cosmos and shed light on previously unexplored phenomena. For the O4 and O5 runs, the target reach of LIGO, Virgo and KAGRA is shown in figure 1.2. In addition, future second-generation detectors, such as LIGO-India, are expected to join the global network by 2030, bringing a tremendous improvement in parameter estimation from gravitational wave signals [209].
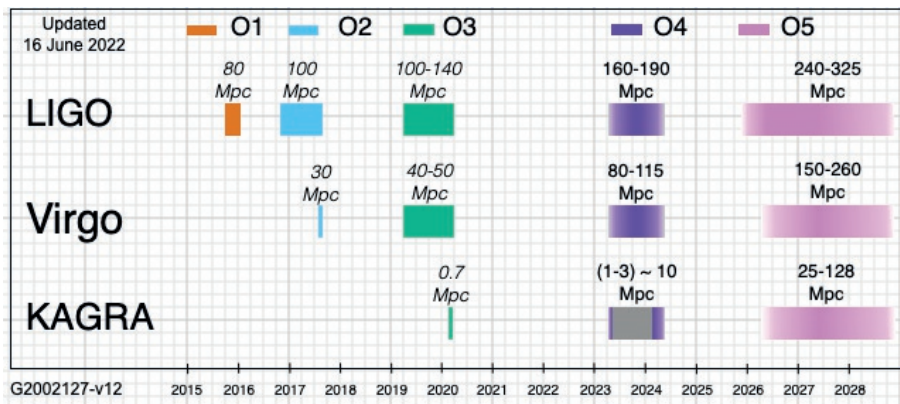
Figure 1.2: Reach of the detectors during three science runs and the target for future runs. Figure taken from [87].

The amplitude of gravitational waves is inversely proportional to the luminosity distance of the source [53, 159], causing stretching and squeezing as the wave passes through space. For the Fabry-Perot-

1

Michelson interferometer with 4 km arm lengths, as in the case of LIGO, the effective change in the differential length of the two arms is incredibly small, on the order of 4×10^{-18} m. This value is twelve orders of magnitude smaller than the wavelength of the light used for the measurement, which is about 1 micron. As a result, measuring such minute variations with the relatively coarse ruler of light wavelength proves to be an arduous task. The main challenge stems from the fact that gravitational wave signals are incredibly weak and can easily be masked by environmental disturbances from sources on Earth. The effective isolation of the detector's test masses from these environmental disturbances is therefore an extremely complex experimental endeavour. As a result, the development of the experimental techniques needed to detect gravitational waves has taken nearly half a century. Identifying and minimising sources of noise has played a crucial role in the successful detection of gravitational wave signals. In addition to environmental noise, there is coating Brownian thermal noise, which can be reduced by using low-loss materials such as silicon and lowering the temperature. Quantum radiation pressure noise arises from uncertainty in the position of the suspended mirror due to fluctuations in the recoil force of reflected photons. Quantum shot noise arises from statistical fluctuations in the number of photons detected by the photodiode. Other fundamental noise sources such as Newtonian noise (discussed in section 1.4.5) and excess gas noise (section 1.4.4) also contribute to the overall noise profile. Figure 1.3 shows the different limiting noise curves for Advanced LIGO. In this section, we will mainly discuss the different noise sources and the techniques used in the interferometer to suppress the effect of noise.

1.4.1 Seismic Noise

Seismic noise results from ground vibrations caused by various factors such as earthquakes, wind, microcosmic sources (e.g. ocean waves), and anthropogenic activities. The presence of seismic noise limits the sensitivity of the detector, typically below 50 Hz. The amplitude spectrum of seismic waves also exhibits characteristics above the 10 Hz scale, which can be described by the equation [74]:

$$x(f) = 10^{-9} \, (10 \, \text{Hz}/f)^2 \, \frac{\text{m}}{\sqrt{\text{Hz}}}. \tag{1.2}$$

aLIGO new design curve: NSNS (1.4/1.4 $M_\odot$) 173 Mpc and BHBH (30/30 $M_\odot$) 1606 Mpc
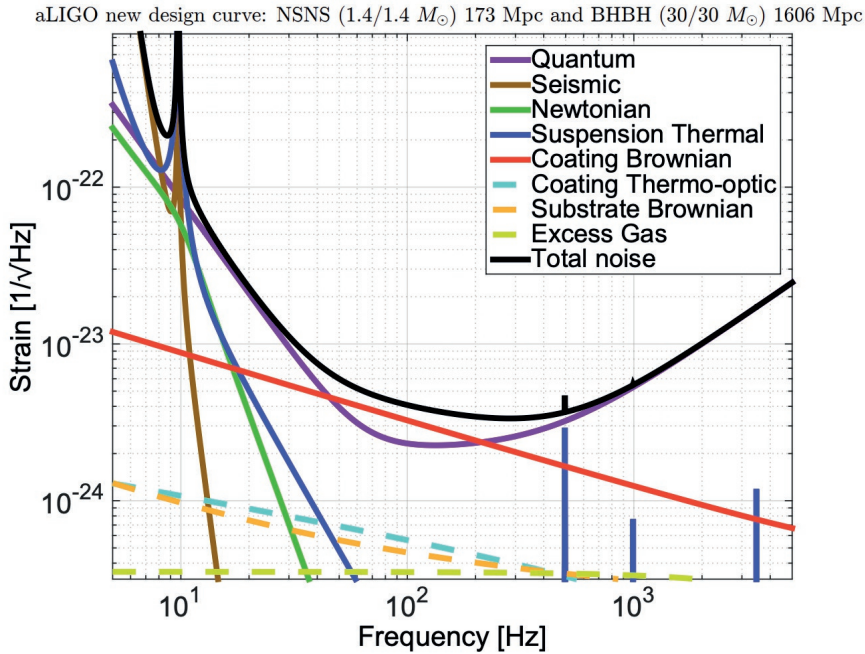
Figure 1.3: Advanced LIGO sensitivity curve, plotted using the square root of the power spectral density of the noise[105] Different colored curves indicate different noise budgets due to a particular type of noise. The black curve indicates the total noise (amplitude spectral density) of the detector. Figure taken from [46].

For example, assuming a reference frequency of $100\,\mathrm{Hz}$, the value of $x(f)$ is $10^{-11}\,\mathrm{m}/\sqrt{\mathrm{Hz}}$, which is about 9 orders of magnitude higher than the required sensitivity level of $10^{-20}\,\mathrm{m}/\sqrt{\mathrm{Hz}}$. To mitigate this problem, mechanical oscillators can be used as filters, providing passive isolation against seismic noise above the resonance frequency. By combining multiple mechanical isolators into a multi-stage system, seismic noise can be effectively suppressed to achieve the desired sensitivity level. A notable example is the use of cascaded pendulums in the suspension of the Virgo test masses, comprising seven stages that attenuate seismic noise by approximately 15 orders of magnitude [26]. However, passive isolation systems face challenges related to thermal stability. Changes in temperature lead to changes in the length of the pendulum, making precise alignment a difficult task [134, 214]. One challenge with low

1

frequency passive isolation systems is the stiffness of the springs, which is proportional to ω^2. As a result, these systems tend to be very soft at low frequencies. Supporting the isolated payload, which can weigh several hundred kilograms, places significant stress on the springs. This high stress level makes alignment between different systems difficult. To improve isolation, a combination of active noise cancellation and passive isolation can be used [88, 19]. Active isolation systems consist of inertial sensors, actuators and a controller. The inertial sensors measure the position of the isolated test mass, while the actuators, under the control of the controller, apply an equal and opposite force to compensate for ground vibration and maintain the mirror in the desired position [155]. However, a disadvantage of the active isolation system is its dependence on the performance of the inertial sensors. The sensors must be more sensitive than the motion of the passively isolated mass to effectively reduce its motion further.

1.4.2 Quantum Noise

In advanced gravitational wave (GW) detectors, sensitivity across the detection band is expected to be limited by quantum noise [86], which arises from the quantum fluctuations of the electromagnetic vacuum.

Quantum noise in GW detectors consists of shot noise, which dominates at high frequencies, and radiation pressure noise, which dominates at low frequencies. Shot noise is caused by the dual quantum nature of light, which has both wave-like and particle-like properties. The number of photons arriving at the detector follows a statistical distribution known as the Poisson distribution. This distribution arises from the probabilistic nature of quantum mechanics, where the detection of each individual photon is random and uncertain, with a standard deviation equal to

$$\Delta N_\gamma = \sqrt{N_\gamma}. \tag{1.3}$$

The shot noise is defined by the variation of the phase $\Delta\phi$, which is inversely proportional to the square root of the number of photons:

$$\Delta\phi \propto \frac{1}{\Delta N_\gamma} \propto \frac{1}{\sqrt{N_\gamma}}. \tag{1.4}$$

The fluctuation in the number of photons leads to a fluctuation in the power, given by:

$$\Delta P = \frac{1}{T}\sqrt{N_\gamma}\hbar\omega_0 \propto \sqrt{P}, \tag{1.5}$$

where ω_0 is the laser frequency and P is the power. The strain sensitivity due to shot noise can be expressed as:

$$S_n^{1/2}(f)|_{\text{shot}} \propto \frac{1}{L}\sqrt{\frac{1}{P}}. \tag{1.6}$$

To reduce the shot noise, it is necessary to increase the power at the beam splitter, which can be achieved by increasing the laser power or improving the recycling factor of the power recycling cavity.

On the other hand, the photon flux exerts a pressure when it interacts with the mirror surface. This radiation pressure varies with the variation in the number of photons, resulting in a stochastic force on the mirror. The spectral density of the displacement of the mirror due to the radiation pressure is given by:

$$S_n^{1/2}(f)|_{\text{rad pres}} \propto \frac{1}{L f^2}\sqrt{\frac{P}{m}}, \tag{1.7}$$

where m is the mass of the mirror and f is the frequency. The shot noise is proportional to $P^{-1/2}$, while the radiation pressure noise varies as $P^{1/2}$. This is a direct consequence of Heisenberg's Uncertainty Principle, where the photons exert an impulsive force on the mirror in the form of radiation pressure, disturbing the measurement of the mirror's position and creating a quantum back-action.

The combined effect of shot noise and radiation pressure noise can be written as:

$$S_n^{1/2}(f)|^{tot} = \sqrt{S_n(f)|_{\text{shot}} + S_n(f)|_{\text{rad pres}}} \tag{1.8}$$

which yields:

$$S_n^{1/2}(f)|^{tot} = \sqrt{\frac{4\hbar}{m\omega^2 L^2}}\sqrt{\frac{1}{2}(K + \frac{1}{K})}, \tag{1.9}$$

where, $K = \frac{4P\omega_0}{c^2 m \omega^2}$ and $\omega = 2\pi f$. The optimum value of parameter K is the one at which the contributions from shot noise and radiation pressure noise are equal. This balance between the two noise sources gives rise to the standard quantum limit (SQL) in gravitational wave detectors. The SQL imposes a fundamental limit on the precision with

which certain conjugate variables, such as position and momentum, can be simultaneously measured. The SQL ($S_{SQL}^{1/2}(f)$) can be expressed as:

$$S_{SQL}^{1/2}(f) = \sqrt{\frac{4\hbar}{m\omega^2 L^2}} \tag{1.10}$$

The existence of SQL is a consequence of the Heisenberg uncertainty principle, which states that there is an inherent limit to the precision with which certain pairs of physical quantities can be known simultaneously. However, it's important to note that the uncertainty principle does not impose a limit on how well one can measure the position of an object.

To overcome the SQL and improve the sensitivity of gravitational wave detectors, researchers have explored the use of non-classical states of light. One such state is a squeezed state, which exhibits correlations between radiation pressure noise and shot noise. By creating these correlations, the measurement and back-action can partially cancel each other, resulting in an effective reduction of the combined noise below the SQL. In order to achieve this cancellation over a broad range of frequencies, a frequency-dependent correlation is necessary. This can be achieved by injecting squeezed light with a squeezing angle that is continuously adjusted as a function of the observation frequency. In addition to utilizing squeezed states, another approach to surpassing the SQL is through the use of quantum non-demolition (QND) devices, such as speed meters.

1.4.3 Thermal Noise

Thermal noise arises from thermodynamic temperature fluctuations in the test mass and introduces vibrations in both the mirrors and the suspensions [153]. Suspension thermal noise is caused by thermal fluctuations in the suspension fibres, which induce oscillations in the test mirror suspension and result in horizontal displacement of the mirrors. The displacement power spectral density due to thermal noise can be derived from the fluctuation-dissipation theorem, which is inversely proportional to the real part of the mechanical impedance of the system. This implies the presence of internal damping or internal friction caused by the inelasticity of the system. The mechanical loss angle (ϕ) represents the phase lag between stress and strain in the system when stress is applied. To minimize the thermal noise of the suspension, mirrors are

suspended using monolithic fused silica fibre suspensions, which have a lower loss angle.

Thermal fluctuation of the test masses occurs due to the Brownian motion of the atoms within the mirror at temperature T. The mechanical thermal noise of the test mass and coatings [132] arises from the mechanical loss caused by internal friction in multi-layer coatings, following the fluctuation-dissipation theorem [28]. This type of noise is a significant limitation to the detector sensitivity over a wide frequency range, typically from 50 to 250 Hz. The general expression for the power spectral density of the displacement from the thermal noise of the mirrors and coating for the GW detector, can be written as:

$$S^{TN}(f) = \frac{2k_B\,T}{\sqrt{\pi^3}\,f}\frac{1-\sigma^2}{wY_{\text{subs}}}(\phi_{\text{subs}} + \frac{2}{\sqrt{\pi}}\frac{1-2\sigma}{1-\sigma}\frac{d}{w}\phi_{\text{coat}}), \qquad (1.11)$$

where k_B is the Boltzmann constant, T is the absolute temperature, w is the radius of the laser beam at the mirror surface, Y_{subs} and σ are the material Young's modulus and Poisson's ratio, respectively. d is the thickness of the coating, and ϕ_{coat} and ϕ_{subs} are the mechanical loss angles associated with the coating and mirror substrate, respectively. The dominant contribution to thermal noise comes from the highly reflective coating, which can be reduced by using thinner coatings and selecting materials with lower mechanical loss for the coating.

Temperature variations can cause displacement noise due to the expansion of materials, known as thermo-elastic noise, which occur in both the bulk of the mirror and its coatings. In addition, changes in the refractive index of coatings with temperature can cause thermo-refractive fluctuations. Thermo-elastic noise can also cause fluctuations in the refractive index of the mirrors themselves. An effective approach to reducing thermal noise is to lower the temperature, which reduces the thermal energy responsible for Brownian motion [99] and helps to minimize dissipation losses. In the KAGRA gravitational wave detector, for example, the mirrors are cooled to 23 K, creating a cryogenic environment that reduces thermal noise. In addition, the use of materials such as sapphire for the mirrors can provide excellent properties at low temperatures. In future third-generation gravitational wave detectors, such as the Einstein telescope, there are plans to operate at cryogenic temperatures (23 K) using silicon as the mirror substrate. This choice aims to minimize expansion due to small temperature changes and further reduce thermal noise.

1

1.4.4 Residual Gas Noise

Residual gas noise is a form of noise caused by statistical fluctuations in the residual gas present in the vacuum tubes of a gravitational wave interferometer. As gas molecules pass through the beam, they can impart phase perturbations in the laser field. This impulsive disturbance from the gas molecules can contribute to the residual gas noise in the interferometer.

To model the residual gas noise, the effect of these impulsive disturbances is integrated over all possible velocity ranges of the gas molecules, resulting in the statistical fluctuations of the gas molecules and their overall effect on the phase of the laser field. The power spectral density of the residual gas noise can be expressed as:

$$S_L(f) = \frac{4\rho(2\pi\alpha)^2}{v_0} \int_0^{L_0} \frac{\exp\left[-2\pi f w(z)/v_0\right]}{w(z)} dz, \tag{1.12}$$

where L_0 is the beam path length, $w(z)$ is the Gaussian radius of the beam profile, v_0 is the most likely velocity given by $(2\pi k_B T/m)^{1/2}$, where m is the mass of the gas molecules and k_B is the Boltzmann constant. T is the absolute temperature and α is the molecular polarisability. The presence of residual gas noise is an important consideration in gravitational wave interferometers, as it can affect the overall sensitivity and performance of the detector.

In addition, interactions between the gas molecules and the test mirror at the end of the arm can lead to small changes in momentum. These interactions contribute to the overall residual gas noise in the gravitational wave detector. The 1996 study by Zucker et al. [231] investigates the measurement and characterisation of these momentum changes caused by gas molecules. Understanding and mitigating the effects of these interactions is crucial for accurately assessing and reducing the effects of residual gas noise in gravitational wave detectors.

1.4.5 Gravity Gradient Noise

Gravity gradient noise, also known as Newtonian noise, is caused by perturbations in gravity acting on the test mirror. As seismic waves propagate through the surrounding medium, they induce variations in its density, resulting in fluctuating gravitational forces acting on the mirror. A more detailed analysis of this noise will be discussed in chapter 2 of this dissertation.

1.4.6   Other noise

In addition to the sources of noise discussed above, there are other sources of noise that can affect the performance of a gravitational wave detector. These include:

1. The technical noise associated with the feedback system or servo-loop used to control the interferometer's degrees of freedom. Fluctuations in laser power can introduce displacement noise. This affects the accuracy of the measurements. 2. Seismic noise or movement in the walls of the detector housing. This motion can couple to the mirror magnets through phenomena such as diamagnetism and eddy currents, leading to noise. 3. The presence of scattered light in the detector can lead to noise. As this light interacts with the walls of the detector tube, it can couple with seismic noise before potentially reflecting back into the beam. Special measures are taken to mitigate this, such as the use of circular rings mounted in the arms of the detector to capture and absorb unwanted scattered light.

These various sources of noise highlight the challenges of designing and operating gravitational wave detectors, and efforts are being made to minimise their impact on the sensitivity of the detector.

1.5   Michelson interferometer as a gravitational wave detector

The simplest Michelson interferometer consists of a light source, a 50-50 beam splitter, and two mirrors, as shown in figure 1.4. Let's consider the spatial component of the incident electric field:

$$E = E_0 \, \exp(i(-\omega_L t + k_L x)), \tag{1.13}$$

where ω_L is the frequency of the laser, $k_L = \frac{\omega_L}{c}$ is the wavevector of the laser light and c is the speed of light. The incident beam is split into two parts at the beam splitter: one is transmitted along the X axis and the other along the Y axis. Let L_X and L_Y be the lengths of the two perpendicular arms of the interferometer.

The part of the incident electric field transmitted through the beam splitter travels along the X axis and returns to the beam splitter at time $t_0 + \frac{2 L_X}{c}$. The beam reflected from the beam splitter travels along the Y axis and returns to the beam splitter at time $t_0 + \frac{2 L_Y}{c}$. Finally, the
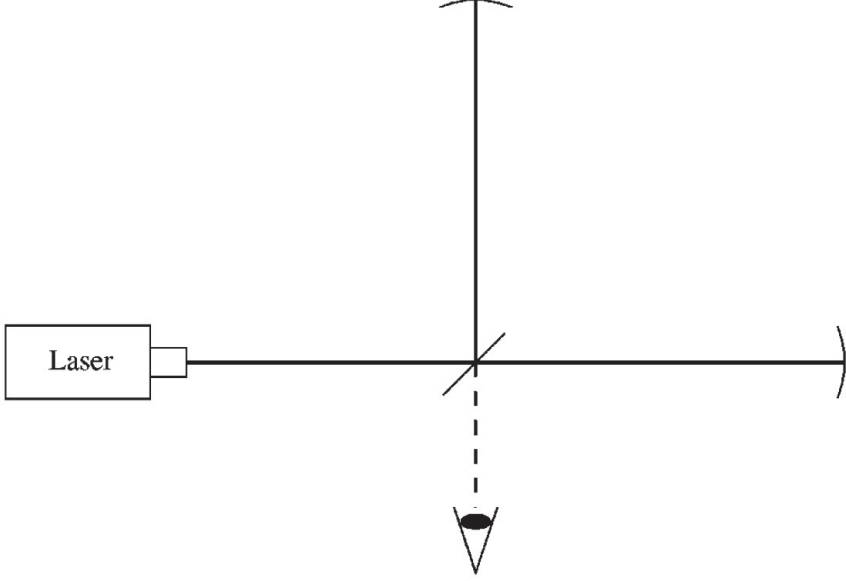
Figure 1.4: A basic Michelson interferometer consists of a beam splitter and two end mirrors. Laser light hits the beam splitter, which splits the beam into transmitted and reflected beams, and both beams are reflected by the end mirrors and return to the beam splitters, interfering. The interference pattern depends on the phase shift due to the change in the differential arm length of the two perpendicular arms. Figure taken from [56] (figure 2 in [56]).

two beams recombine at the beam splitter. The two electric fields at the beam splitter can be expressed as:

$$E_1 = -\frac{1}{2} E_0 \, e^{i(-\omega_L t + 2 \, k_L L_X)}, \tag{1.14}$$

$$E_2 = +\frac{1}{2} E_0 \, e^{i(-\omega_L t + 2 \, k_L L_Y)}. \tag{1.15}$$

Therefore, the total electric field at the output can be expressed as:

$$E_{\text{out}} = E_1 + E_2 = -iE_0 e^{-i\omega_L t} e^{i \, k_L (L_X + L_Y)} \sin[k_L(L_Y - L_X)] \tag{1.16}$$

The output power measured by the photodetector can be given as:

$$P_{\text{out}} = |E_{\text{out}}|^2 \propto E_0^2 \sin^2[k_L(L_Y - L_X)]. \tag{1.17}$$

The output power at the photodetector is therefore proportional to the sine squared ($\sin^2$) of the change in the length of the arms of the interferometer. However, the differential change in arm length due to gravitational waves is extremely small, because gravitational waves only stretch space by a tiny amount. To measure these tiny fluctuations in space-time, additional optical and mechanical components must be added, as discussed below.

1.6 Optical layout of the gravitational wave interferometer

The measurable length change induced by a gravitational wave depends on the total length of each arm of the interferometer. If the wavelength of the gravitational wave is much larger than the size of the detector, then the strain induced by gravitational waves can be expressed as:

$$h = \frac{\Delta L}{L} \tag{1.18}$$

The change in length due to gravitational waves is challenging to measure because of the extremely small amplitude of the strain. For example, the first detected gravitational wave from GW150914 by the LIGO detectors was a strong event that had reached a strain amplitude of 10^{-21}. We could not measure this signal with a simple Michelson interferometer because its performance is limited by various internal and external noise sources discussed in section 1.4. The optimal arm length of the interferometer is given by:

$$L = \frac{\lambda_{gw}}{4} = 750 \, \text{km} \frac{100 \, \text{Hz}}{f_{gw}}. \tag{1.19}$$

For $L = \frac{\lambda_{\text{gw}}}{4}$, the time shift of the photon entering into the arm is properly synchronized with the phase of the gravitational wave. For longer arm lengths, there can be partial cancellation of the phase shift. Hence, the optimal arm length of the interferometer is several hundred kilometers in order to detect a gravitational wave. However, building a interferometer with such a large arm length on Earth is practically impossible due to technological and financial limitations. Therefore, the idea is to effectively increase the arm length by several hundred kilometers using Fabry-Perot cavities (discussed in section 1.6.1) which is effectively folding the optical path of the light.

To decrease shot noise, the power of the laser needs to be increased. Although the maximum power of currently available lasers typically falls within the range of several hundred watts. To achieve this, the light that is coming back to the laser is recycled by placing a mirror called the power recycling mirror. To reduce external noise, the interferometer is enclosed in a vacuum and mounted on a seismic isolation system.

The basic optical layout of the gravitational wave interferometer is shown in figure 1.5.
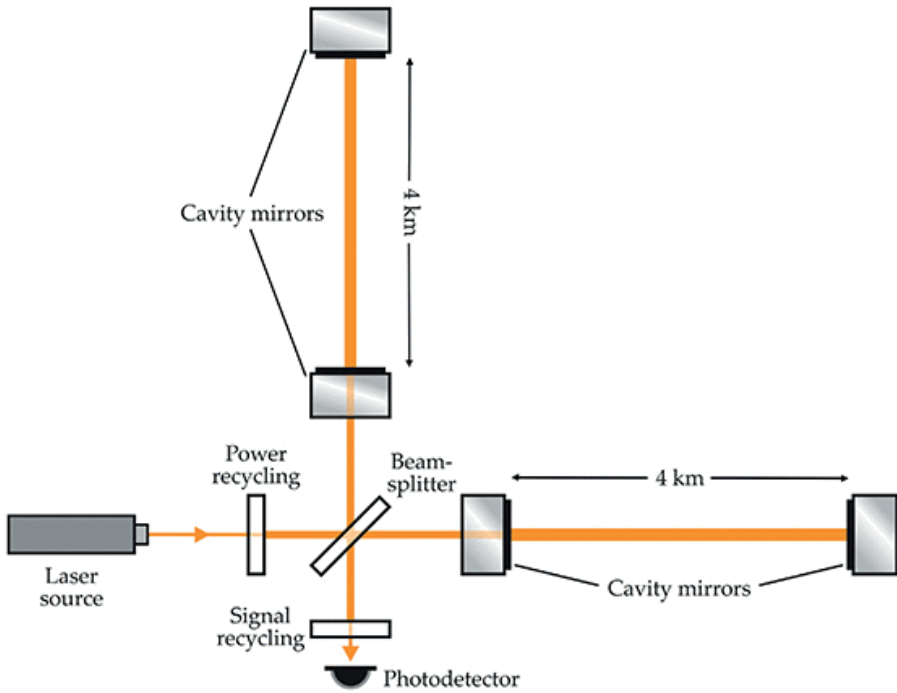
Figure 1.5: Optical layout of gravitational wave interferometer. Figure taken from [147].

1.6.1 Fabry-Perot cavities

A Fabry-Perot cavity consists of two mirrors, where most of the incident light is reflected off the mirrors, but a small portion of the light is transmitted and circulates between the mirrors [224, 158]. The phase of the leakage beam is highly sensitive to the distance between the mirrors when the cavity is near resonance. Therefore, a Fabry-Perot cavity can

be used as a high-precision measuring device [178].

The resonance condition of the cavity occurs when $2L = n\lambda$, where L is the distance between the mirrors, n is an integer, and λ is the wavelength of the light. At resonance, the constructive interference of the reflected waves enhances the transmitted intensity, resulting in a sharp peak in the transmission spectrum. The distance between two adjacent maxima in the transmission spectrum is called the free spectral range of the cavity, denoted by $\Delta\omega_L$, which can be calculated as:

$$\Delta\omega_L = \frac{\pi c}{L}. \tag{1.20}$$

The finesse of the Fabry-Perot cavity characterizes the spectral selectivity and quality factor of the resonator. It is defined as the ratio of the free spectral range (the distance between successive resonances) to the full width at half maximum of a resonance peak and can be expressed as:

$$\mathcal{F} = \frac{\pi\sqrt{r_i\,r_o}}{1 - r_i\,r_o}, \tag{1.21}$$

where r_i and r_o are the amplitude reflectivities of the two mirrors. Higher finesse corresponds to a narrower resonance peak and a more selective cavity. Higher finesse is desirable in applications as it indicates the ability of the cavity to store and amplify light at specific wavelengths.

The storage time of a Fabry-Perot cavity is the average time that photons spend in the cavity before being lost. The storage time τ_s of photons inside the Fabry-Perot cavity is fine-tuned and can be approximated as:

$$\tau_s \approx \frac{L}{c}\frac{\mathcal{F}}{\pi}. \tag{1.22}$$

When the finesse is high, the storage time becomes comparable to the period of a gravitational wave. In this case, the sensitivity of the detector decreases because the positive and negative sides of the gravitational wave signal are summed, leading to a reduced signal-to-noise ratio. Therefore, in gravitational wave interferometers, it is important to carefully design the cavity fineness and storage time to optimize the detection sensitivity for gravitational waves while minimising any adverse effects.

1

1.6.2   Signal and Power Recycling Mirrors

As mentioned earlier, the quantum shot noise is reduced as the laser power increases. To meet this challenge, scientists have ingeniously introduced the power recycling mirror (PRM). In the absence of a GW signal, no light comes out at the photodetector and the light circulating in the arms goes back to the laser and is therefore wasted. The addition of a PRM captures the returning light that has passed through the interferometer arms and redirects it back to the beam splitter. The PRM is placed between the laser and the beam splitter, creating another Fabry-Perot cavity. By resonating the cavity for the input laser light, the Power Recycling Mirror (PRM) enables the power incident on the beam-splitter to be about a few kilowatts.

For a similar reason, signal recycling has been added to the interferometer by a signal recycling mirror (SRM)[122]. The SRM is placed at the anti-symmetric port of the Michelson interferometer. It helps in decreasing the fineness of the signal sidebands, although it does not affect the carrier light. In doing so, it effectively widens the frequency bandwidth of the detector's operation. This broadening of the bandwidth allows the detector to capture a wider range of gravitational wave frequencies, increasing its ability to detect and analyze different signals. However, this broadening of the frequency bandwidth comes at the cost of reduced sensitivity. The integration of the signal recycling mirror with power recycling and Fabry-Perot arm cavities forms a dual-recycled Fabry-Perot Michelson interferometer, further enhancing the capabilities of gravitational wave detectors [211, 107].

1.7   Future gravitational wave detectors

To continuously enhance the sensitivity of gravitational wave detectors, commissioning is performed before each science run. Looking ahead to future gravitational wave detectors, the goal is to achieve a minimum factor of 10 improvements in sensitivity compared to the best currently operating detector, along with an expansion of the frequency bandwidth for detection.

The low-frequency band is particularly interesting because of its potential for observing various astrophysical phenomena, including white dwarf stars (in the millihertz frequency range), supermassive black holes, and continuous sources such as pulsars. Therefore, it is essential that future generations of detectors incorporate new technologies that effect-

ively reduce the noise level to enable the detection of these low-frequency signals.

Several proposed future gravitational wave detectors include the Einstein Telescope (ET) [174], the Cosmic Explorer [183], the space-based detector LISA (Laser Interferometer Space Antenna) [196, 40], and the Lunar Gravitational Wave Detector (LWGA) [126, 140]. These detectors are expected to be operational within the next few decades and have different characteristics and objectives.

Laser Interferometer Space Antenna is designed to operate in the frequency range from 0.1 mHz to 1 Hz. With its unique frequency range, LISA will complement ground-based detectors such as the Einstein Telescope by observing gravitational wave signals that cannot be detected from Earth. Another exciting project, the Lunar Gravitational Wave Antenna, aims to place a gravitational wave detector on the surface of the Moon. This project fills the frequency gap between LISA and the Einstein telescope, providing complementary capabilities for gravitational wave observations. The LWGA concept involves deploying a network of inertial sensors on the Moon that would act as gravitational wave detectors. The stable, low-noise lunar environment provides isolation from terrestrial disturbances such as seismic and atmospheric noise. The development and operation of these future gravitational wave detectors hold great promise for advancing our understanding of the Universe and will enable the detection of gravitational wave signals over a wider frequency range, making a significant contribution to the field of gravitational wave astronomy.

1.8   Overview of the dissertation chapters

This dissertation is structured into several chapters, each addressing specific aspects of the research on gravitational wave detectors and their noise sources.

Chapter 2 provides a comprehensive overview of Newtonian and gravitational gradient noise and their impact on the sensitivity of current and future gravitational wave detectors at low frequencies. The chapter discusses the different types of seismic waves and their specific impact on Newtonian noise. By exploring the intricate relationship between seismic waves and Newtonian noise, the chapter sheds light on the underlying mechanisms and provides a comprehensive understanding of Newtonian noise and its implications for current and future detectors, offering valu-
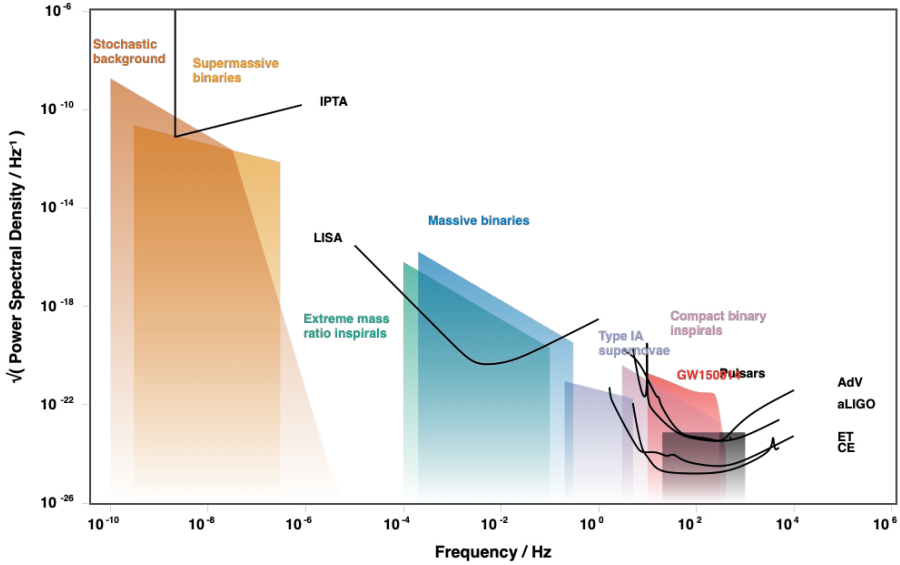
Figure 1.6: Sensitivities of current and future generation ground and space-based GW detectors. Figure produced with http://gwplotter.com.

able insights into noise mitigation and optimization strategies. It also presents key findings from previously published research, focusing in particular on the Newtonian noise budget for the underground gravitational wave detector known as the Einstein Telescope.

In chapter 3, a comprehensive and detailed numerical evaluation is performed to analyze the Newtonian noise curve specifically for Virgo. The study takes into account the unique features of Virgo's building infrastructure, such as the presence of clean rooms or recess-like structures positioned under each test mirror (input and end test mirrors forming the two main Fabry-Perot arm cavities of the detector). By considering the displacements generated by an isotropic Rayleigh field, the chapter demonstrates a significant reduction in strain noise. In particular, an overall reduction factor of 2 is observed in the frequency range from 12 to about 15 Hz, which is not included in previous models. The reduction factor is frequency-dependent and also varies between individual test masses. This in-depth analysis provides valuable insights into the characterization of Newtonian noise within the Virgo detector setup, providing crucial information for optimizing noise reduction strategies and improving overall detector performance.

Seismic Newtonian Noise (NN) occurs when seismic waves pass in close proximity to the suspended test masses of a gravitational wave detector. This type of noise is predicted to be the largest contributor to the total Newtonian noise for ground-based detectors. Accurately modelling this contribution is a significant challenge. To gain a better understanding of the seismic field around the four test masses at the Virgo site, arrays of seismometers have been deployed. In chapter 4, I present the results of a spectral analysis performed on the array data collected from one of the buildings at the north end of Virgo to identify the dominant modes of the seismic field. Several modes can be associated with known seismic sources. By analysing these modes over a range of frequencies, I construct a dispersion curve specifically for Rayleigh waves. In particular, we found that the Rayleigh speed within the frequency range relevant to Newtonian noise (10-20 Hz) is remarkably low (less than or equal to 100 m/s), which has significant implications for Virgo's seismic Newtonian noise. Using the new velocity estimates, I found that the recess formed under the suspended test masses, facilitated by a basement in the end buildings, results in a tenfold reduction in Newtonian seismic noise.

In the following three chapters, I focus on exploring different scientific cases in the field of gravitational wave astronomy, taking advantage of the capabilities of future gravitational wave detectors. The third generation of detectors, such as the Einstein Telescope and the Cosmic Explorer, will have significantly improved sensitivity compared to the current generation of detectors. The network of these advanced detectors will have at least a tenfold increase in detection range and improved accuracy in estimating the parameters of gravitational wave sources.

Chapter 5 discusses the basic configuration of the Einstein telescope. This configuration consists of two different instruments optimized for different frequency ranges: one for low frequencies (LF) and the other for high frequencies (HF). I have developed an optimal filter to effectively combine data from both instruments within the xylophone structure of the Einstein telescope. I have performed a comprehensive evaluation of the figures of merit for both the Einstein telescope and the Cosmic Explorer. These figures of merit include crucial aspects such as signal-to-noise ratio, antenna patterns, horizon redshift, etc. By investigating these scientific cases and assessing the potential of advanced detectors, we contribute to the broader understanding of gravitational wave astronomy.

1

Accurate determination of the source position of a gravitational wave source is a crucial goal for studying the potential of the network of gravitational wave detectors. Chapter 6 of this dissertation addresses this goal by using the Fisher information matrix approximation to compute the angular resolutions of two advanced detectors: the Einstein Telescope and the Cosmic Explorer (CE). In our analysis, we consider the possibility of configuring the Einstein Telescope as a triangular detector with an arm length of 10 km, as well as an L-shaped detector with arm lengths of 10 km, 15 km, and 20 km, respectively. Using the Fisher information matrix approach, we are able to estimate the sky localization uncertainty for both modelled and unmodelled gravitational wave sources within the detector array. Based on our assessment of sky localization accuracy, we have observed improved network efficiency for the Einstein Telescope when employing the proposed triangular configuration.

Chapter 7 represents our research focusing on the potential of the intrinsic null stream of the Einstein Telescope. We have shown ET's null stream can be used to optimize the operator for estimating sky localization, in the network comprising third-generation detectors such as the Cosmic Explorer and the Einstein Telescope. However, it's important to note that this optimization doesn't lead to an improvement in sky localization accuracy. Instead, its primary advantage lies in reducing an additional null stream associated with the ET. This reduction can offer computational advantages because we have one less null stream to analyze in our residual data. Subsequently, I have utilized this null stream to improve the calibration model of the ET through a method known as self-calibration. The self-calibration method relies on detected gravitational wave events and the residual signals left in the null stream due to the calibration error. I've applied this method to assess how one can enhance the calibration model of the ET based on the number of events detected by the detector.

Chapter 2

Introduction to Newtonian noise

2.1 Introduction

Newtonian noise (NN), also known as gravity gradient noise, emerges from the fluctuations in local gravitational fields. It poses a challenge to interferometric gravitational wave detectors because the test mirrors within the interferometer are subject to perturbations caused by gravity variations due to seismic waves, atmospheric changes, and other factors. This non-stationary noise source is particularly dependent on seismic ground vibrations, and is therefore highly variable over time. Historically, the observation of Newtonian noise has been limited by the sensitivity of detectors, which is insufficient below 20 Hz, where Newtonian noise becomes one of the dominant noise sources. However, future runs of advanced detectors have the potential to observe and study Newtonian noise, providing an opportunity to validate theoretical models and predictions [125].

Atmospheric Newtonian noise, caused by fluctuations in local gravitational fields, has only been observed by gravimeters at millihertz frequencies. However, in the context of current advanced detectors such as LIGO or Virgo, atmospheric Newtonian noise is not a major problem. This is because advanced detectors like LIGO and Virgo face several other dominant noise sources, such as seismic noise, thermal noise and radiation pressure noise, which limit their sensitivity below 20 Hz. To mitigate the effects of Newtonian noise, future detectors, such as the Einstein Telescope, which will improve low-frequency sensitivity by a factor

of almost 10000, are planned to go underground, taking advantage of the reduced seismic noise levels found in such environments [162, 175]. Hence, it may be important to carefully consider atmospheric Newtonian noise for third generation detectors [64].

To model the influence of NN on the sensitivity of a GW detector, we first need to monitor the local seismic field nearby the input and output test mirrors [170]. This can be accomplished by deploying seismometers and tiltmeters in proximity to the test masses to measure relevant ground displacements. Seismic Newtonian noise is a primary source of gravity fluctuation, arising from density changes caused by ground vibrations near the test masses. These density changes are a consequence of compressional seismic waves or surface/interface displacements within the surrounding medium. As a result, surface displacements near the test masses occur, leading to associated gravity fluctuations that constitute the dominant component of Newtonian noise.

Seismic waves can be broadly classified into two main categories: surface waves and body waves [30, 54]. It is important to understand the characteristics of these waves in the context of Newtonian noise, have been discussed in section 2.2. Surface waves, such as Rayleigh waves and Love waves, propagate along the surface of the medium. Rayleigh waves are primarily associated with vertical motion, causing the ground to move in an elliptical or rolling motion. Love waves, on the other hand, are characterized by horizontal motion and shear deformation in near-surface layered media. While both Rayleigh waves and Love waves can induce surface displacements, it is important to note that Love waves do not contribute to Newtonian noise as they do not result in density changes within the medium [118]. The magnitude of Rayleigh waves decays exponentially with depth, making their impact more pronounced near the surface. Body waves, including compressional (P) waves and shear (S) waves, can propagate through media in all directions. Rayleigh waves are often more dominant compared to body waves when it comes to surface detectors. For underground detectors like the proposed Einstein Telescope, the main contribution to Newtonian noise comes from body waves rather than Rayleigh waves. Since underground detectors are shielded from surface disturbances, the seismic sources that affect them are primarily associated with body waves that propagate through the Earth's interior. For the LIGO and Virgo detectors, the dominant seismic sources are part of the detector infrastructure (pumps, ventilation,...) and produce predominantly surface seismic waves, which

means that our subsequent analysis can focus on NN from Rayleigh waves [135, 81, 83].

Seismic NN is estimated to be the main contribution to the overall NN compared to other contributions like acoustic NN or NN from infrastructure [90]. Although the effect of NN cannot be screened out directly from the detector, there are still some conventional ways to reduce this noise. Firstly, one can select a seismically quiet region to build up the detector [115, 50, 80, 82]. By choosing a location with low levels of natural and anthropogenic seismic activity, the detector can achieve higher sensitivity to gravitational waves. In this context, one can consider going underground like Einstein Telescope due to reduced seismic noise. Studies have shown that at depths of about 1 km, underground seismic noise can be approximately an order of magnitude weaker than surface noise above 1 Hz [95, 41, 60, 72].

Another method to reduce NN that is relevant for the current detectors is known as Newtonian noise subtraction [120]. This technique involves deploying seismic sensors around the test mass to measure the environmental vibrations and obtain information about the density perturbation of the ground. By analyzing the data from these sensors, it is possible to estimate the associated gravity perturbation on the test mass and the resulting Newtonian noise. The estimation of Newtonian noise and its subsequent subtraction from the gravitational wave (GW) channel data is typically done using Wiener filters since they are designed to minimize the influence of Newtonian noise on the GW measurements. To optimize the effectiveness of Newtonian noise cancellation, it is advantageous to deploy the seismometers on the surface near the test mass. This is because the surface seismic field generally contributes the most significant portion of Newtonian noise, as observed by detectors like LIGO and Virgo. However, the cancellation of Newtonian noise is a challenging task. The real seismic field observed at detectors like Virgo is complex due to the presence of infrastructure, which can interact with the seismic waves from local dominant seismic sources. This interaction may not align well with the analytical models used to characterize the seismic field and can introduce additional complexities. Furthermore, the cancellation process is affected by the surface conditions. A flat surface is preferred over a rough one, since rough surfaces can cause seismic scattering, making the cancellation problem more complicated. Additionally, the limited number of sensors can lead to incomplete information about the seismic field. Optimal placement of seismometers

becomes crucial to capture the relevant characteristics of the field and improve the accuracy of Newtonian noise cancellation.

Another exotic way to reduce the NN is by modifying the infrastructure, e.g., by building the recess or moats surrounding the test mass, which can act as a shield against Newtonian noise. Hughes and Throne proposed the idea of digging moats deep enough so that surface waves would be reflected from them, leading to a significant reduction in seismic NN, provided that the moat depth exceeds the wavelength of the Rayleigh wave [136]. However, this approach is more effective when the seismic noise sources are located at a considerable distance from the test masses. In the case of currently operating detectors like Advanced LIGO and Virgo, the seismic sources are more local, i.e., closer to the test masses. Harms and Hild demonstrated that modifying the local topography, such as creating a recess around the test mass, can also contribute to NN reduction in surface detectors [119].

The linear (root power) NN spectral density of each test-mass displacement, assuming a flat surface, can be expressed as:

$$X_{\mathrm{NN}}(f) = \frac{1}{\sqrt{2}} 2\pi\gamma G\rho_0 \frac{\xi(f)}{(2\pi f)^2} \exp(-2\pi h/\lambda), \qquad (2.1)$$

where $\xi(f)$ is the linear spectral density of vertical ground vibration, primarily dominated by an isotropic Rayleigh-wave field. G represents the gravitational constant, ρ_0 is the density of the ground, h is the height of the test mass above the ground, and λ denotes the Rayleigh wavelength at frequency f. A recess structure can effectively lower the density close to the test mass, or in other words, increase the effective height h of the center of test mass above the ground. The existence of a recess, in turn, reduces the NN spectra in a specific frequency band. The extent of this reduction depends on the size of the recess structure and, to some degree, its precise shape. Harms and Hild conducted calculations to determine how the NN reduction factor varies with different recess parameters, finding that feasible constructions could achieve significant NN reduction factors ranging from 2 to 4. However, modifying the experimental setup of currently operating detectors to remove ground beneath the mirrors and establish supporting pillars for the vacuum chambers is not a practical solution. Nonetheless, the Virgo detector was constructed with recess structures and cleanrooms beneath the test masses, which were used during the test-mass installation process from below the vacuum chambers. This raises the question of the extent to which NN is reduced in Virgo due to these recess structures. In the

subsequent chapters, an evaluation of Virgo's expected NN reduction resulting from these recess structures is carried out numerically.

2.2 Seismic waves

Seismic waves can be categorized into four main types: P-wave, S-wave, Rayleigh wave, and Love wave. Figure 2.1 illustrates these different types of seismic waves propagating through a medium.

The P-wave and S-wave are collectively referred to as body waves because they can propagate through the volume of the medium. The P-wave, also known as the primary wave or compressional wave, causes the medium to move back and forth in the same direction as the wave travels. It results in the compression and expansion of the rock or material it passes through. P-waves are the fastest seismic waves and typically travel through solid rocky mediums at speeds ranging from 6 to 8 km/s. On the other hand, S-waves, also known as secondary waves, shear and twist the material, causing it to move perpendicular to the direction of propagation. S-waves propagate slower than P-waves, with speeds around 3.5 km/s in hard materials.

Rayleigh waves and Love waves are classified as surface waves, which means they propagate primarily along the Earth's surface. Surface waves have larger amplitudes compared to body waves. Rayleigh waves, often called "ground rolls", are a combination of longitudinal waves (P-waves) and vertically polarized transverse waves (SV-waves or S-waves with vertical displacement). They result in particle motion in an elliptical path, causing both vertical and horizontal ground movement.

The Love wave, named after A.E.H. Love, is formed by the interference of horizontally oscillating transverse waves. The particles in Love waves move in a transverse shear motion along the direction of propagation. Love waves propagate within a specific layer of the Earth, which is separated by another layer with a higher propagation velocity. Unlike Rayleigh waves, Love waves do not change the density of the medium and do not contribute to Newtonian noise since they do not induce gravity gradients. However, Love waves can cause surface displacements.

Both Rayleigh waves and Love waves exhibit a decrease in amplitude with depth.
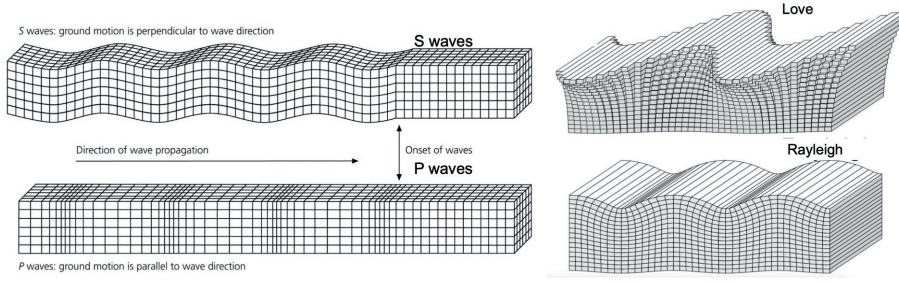
Figure 2.1: Different types of Seismic waves propagating horizontally and the corresponding ground displacements. Figure taken from [66].

2.3 Analytical expression of seismic fields

In this section, we discuss the properties of seismic waves and derive the expression for the seismic field relevant to the calculation of gravity perturbation (which will be discussed in section 2.4). We adopt the mathematical approach and formulas presented in [117] and [30] as the basis for our analysis. The particle displacement field arising from compressional P-waves can be written as:

$$\vec{\xi}^P(\vec{r}, t) = \xi_0^P(\vec{K}_P, \omega)\, e^{i(\vec{K}_P \cdot \vec{r} - \omega t)}\, \hat{e}_k^P, \tag{2.2}$$

where ω is the frequency, $\vec{K}_P$ is the wave vector given by $\vec{K}_P = \frac{\omega}{\alpha}$, ξ_0^P is the amplitude of the P-wave, and $\hat{e}_k^P$ represents the direction of wave propagation through the media. The speed of P-wave, α, depends on the material's properties and can be expressed in terms of Lamé's constants, λ and shear modulus, μ. Specifically,

$$\alpha = \sqrt{\frac{\lambda + 2\mu}{\rho}}, \tag{2.3}$$

where ρ is the density of the material.

The particle displacement field arising from shear S-waves can be written as:

$$\vec{\xi}^S(\vec{r}, t) = \xi_0^S(\vec{K}_S, \omega)\, e^{i(\vec{K}_S \cdot \vec{r} - \omega t)}\, \hat{e}_k^S, \tag{2.4}$$

where $\vec{K}_S$ is the wave vector given by $\vec{K}_S = \frac{\omega}{\beta}$, and ξ_0^S is the amplitude of the S-wave. The S-wave speed, β, depends on the shear modulus (μ) and the density of the material, and can be calculated as:

$$\beta = \sqrt{\frac{\mu}{\rho}}. \tag{2.5}$$

Lamé's constants can be derived from the P-wave and S-wave velocities and can be expressed as:

$$\lambda = \rho(\alpha^2 - \beta^2). \tag{2.6}$$
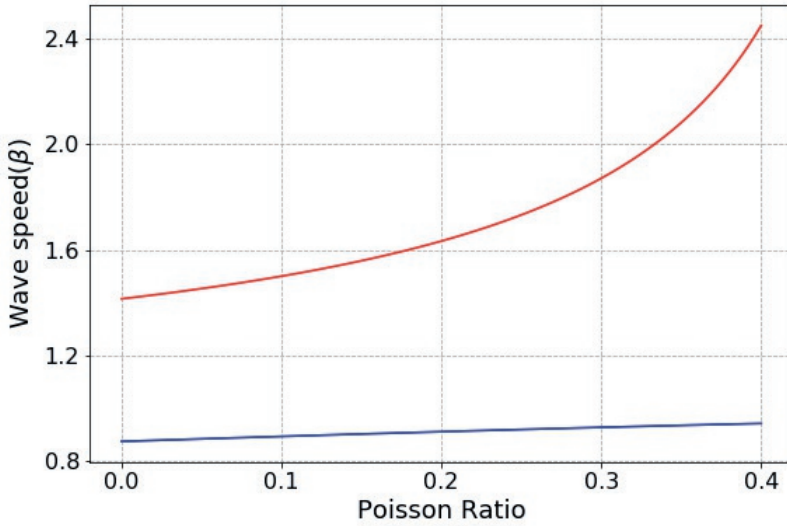
Figure 2.2: Dependence of Rayleigh wave speed (C_R) and P-wave speed (α) w.r.t. Poisson's ratio. Blue and red curves show Rayleigh wave speed and P-wave speed, respectively, in the unit of S-wave speed (β).

This relationship leads to another useful expression relating the two seismic speeds as a function of the Poisson ratio σ:

$$\beta = \alpha\sqrt{\frac{1 - 2\sigma}{2 - 2\sigma}}. \tag{2.7}$$

Now, let's turn our attention to Rayleigh waves. Rayleigh waves can propagate through the surface layer of a material and can also be reflected and scattered at the interface between two media. However, for simplicity, we will ignore these effects in the numerical simulation of the Rayleigh wave field. The Rayleigh wave speed, denoted as C_R, is related to the S-wave speed, β, by the Poisson's ratio of the material. In most materials with a Poisson ratio of 0.25, the Rayleigh wave speed is typically 0.9 times the S-wave speed (β). Due to their slower spread and confinement to the Earth's surface, surface waves carry more energy in a smaller volume and therefore have larger wave amplitudes compared to body waves.

Let's consider a Rayleigh wave propagating along the surface of an isotropic elastic half-space, with a wave vector $(\vec{k})$ aligned with the direction of $\hat{e}_k$. Here, $\hat{z}$ denotes the vertical direction. The wavevector $\vec{k}$ can be decomposed into horizontal and vertical components as K_ρ and K_z. The vertical wavenumbers can be expressed as:

$$
\begin{aligned}
K_z^P &= \sqrt{K_P^2 - K_\rho^2} \\
K_z^S &= \sqrt{K_S^2 - K_\rho^2}.
\end{aligned}
\tag{2.8}
$$

In general, body waves propagate through the medium and reflect from the surface, which can result in K_ρ being larger than K_P and K_S. Hence, it is more convenient to use the q-parameter, which can be written as:

$$
\begin{aligned}
q_z^P &= \sqrt{K_\rho^2 - K_P^2} \\
q_z^S &= \sqrt{K_\rho^2 - K_S^2}.
\end{aligned}
\tag{2.9}
$$

One standard way to express a particle displacement field is in terms of its scalar and vector potential, given by:

$$
\vec{\xi}^R(\vec{r}, t) = \nabla \phi(\vec{r}, t) + \nabla \times \vec{u}(\vec{r}, t).
\tag{2.10}
$$

In the case of an infinite half-space, the scalar and vector potentials allow the wave equations to be separated into uncoupled ones, although they are coupled by the stress-free boundary condition at the free surface. Hence, we can write:

$$
\phi = A \, e^{-q_z^P Z} e^{i(\vec{K}_\rho \cdot \vec{\rho} - \omega t)}
\tag{2.11}
$$

and

$$u = -i\zeta \, A \, e^{-q_z^S \, Z} \, e^{i(\vec{K}_\rho \cdot \vec{\rho} - \omega t)}, \tag{2.12}$$

where $\zeta = \sqrt{\frac{q_z^P}{q_z^S}}$, representing the ratio of the scalar and vector potential amplitudes, and Z is the z-coordinate of the half-space, with the surface at $Z = 0$. The solid half space occupies the region $Z \geq 0$. The horizontal and vertical components of the Rayleigh wave field can be expressed as:

$$\xi_{\text{hor}}^R(\vec{r}, t) = \frac{\partial \phi}{\partial Z} + \frac{\partial u}{\partial \rho} = A(k_\rho \, e^{-q_z^P \, Z} - \zeta q_z^S \, e^{-q_z^S \, Z}) \sin(\vec{K}_\rho \cdot \vec{\rho} - \omega t)$$

$$\xi_{\text{vert}}^R(\vec{r}, t) = \frac{\partial \phi}{\partial \rho} - \frac{\partial u}{\partial Z} = -A(q_z^P \, e^{-q_z^P \, Z} - \zeta k_\rho \, e^{-q_z^S \, Z}) \cos(\vec{K}_\rho \cdot \vec{\rho} - \omega t). \tag{2.13}$$

The detailed mathematical calculations can be found in [128]. The velocity of the Rayleigh wave ($|C_R|$) is related to the speed of the S-wave (β) through the equation:

$$R\left(\left(\frac{C_R}{\beta}\right)^2\right) = 0, \tag{2.14}$$

where $R(x) = x^3 - 8x^2 + 8x\frac{(2-\sigma)}{(1-\sigma)} - \frac{8}{1-\sigma}$, and σ represents the Poisson's ratio. The Rayleigh wave speed can be determined by solving the above equation for different Poisson ratios (σ). The dependence of the Rayleigh wave speed and P-wave speed on the Poisson's ratio is shown in figure 2.2. Hence, we can write the total displacement field due to the Rayleigh wave as:

$$\vec{\xi}_{\text{tot}}^R(\vec{r}, t) = \xi_{\text{hor}}^R(\vec{r}, t) \, \hat{e}_k + \xi_{\text{vert}}^R(\vec{r}, t) \, \hat{e}_z. \tag{2.15}$$

2.4 Gravity perturbation from seismic waves

So far, we have discussed different types of seismic waves and formulated the seismic field for Rayleigh waves, as they are the main contributors to Newtonian noise in current surface detectors. In the absence of seismic waves, the gravitational field on the test mass remains constant. However, when a seismic wave arrives, the particles become displaced

from their equilibrium position, inducing density perturbations that result in fluctuations in the gravitational field near the test mass. These fluctuations in the gravity field affect the motion of the test mass itself. Gravity fluctuations can also arise from density perturbations in the atmosphere or from any moving object near the test mass [64]. While we typically focus on seismically driven Newtonian noise due to its least understood nature, accurately modeling the gravity perturbations arising from complex seismic fields remains a challenge. The optimal approach is to understand the seismic sources and then design the seismometer array to provide the necessary information for modeling gravity perturbations. Factors to consider include whether the seismic sources are transient or stationary, distant or local, and whether they are located on the surface or underground.

In this section, we will derive the expression for the gravity perturbation on a test mass in terms of the seismic fields. We can start with the equation of continuity, which formulates the density perturbation in the medium caused by the seismic field as:

$$\delta\rho = \nabla \cdot (\rho(\vec{r})\,\vec{\xi}(\vec{r},t)). \tag{2.16}$$

Here, $\vec{\xi}(\vec{r},t)$ denotes the seismic or particle displacement field. $\rho(\vec{r},t)$ is the density of the surrounding medium. Therefore, the fluctuation of the gravity potential at the location of the test mass can be written as:

$$
\begin{aligned}
\delta\phi(\vec{r_0},t) &= -\int \frac{G\,\delta\rho(\vec{r},t)}{|\vec{r}-\vec{r_0}|}dV \\
&= -G\int \frac{\nabla\cdot(\rho(\vec{r})\,\vec{\xi}(\vec{r},t))}{|\vec{r}-\vec{r_0}|}dV \\
&= -G\int (\rho(\vec{r})\vec{\xi}(\vec{r},t))\cdot\nabla\frac{1}{|\vec{r}-\vec{r_0}|}dV \\
&= G\int (\rho(\vec{r})\vec{\xi}(\vec{r},t))\cdot\frac{\vec{r}-\vec{r_0}}{|\vec{r}-\vec{r_0}|^3}dV.
\end{aligned}
\tag{2.17}
$$

Hence, the acceleration onto the test mass due to the fluctuation of potential can be expressed as:

$$
\begin{aligned}
\delta\vec{a}(\vec{r_0},t) &= G\int \rho(\vec{r})(\vec{\xi}(\vec{r},t)\cdot\nabla_0)\frac{\vec{r}-\vec{r_0}}{|\vec{r}-\vec{r_0}|^3}dV \\
&= G\int \rho(\vec{r})\frac{1}{|\vec{r}-\vec{r_0}|^3}(\vec{\xi}(\vec{r},t)-3\,(\hat{e}_{rr_0}\cdot\vec{\xi}(\vec{r},t))\hat{e}_{rr_0})dV
\end{aligned}
\tag{2.18}
$$

where $\hat{e}_{rr_0}$ is the unit vector pointing from r to r_0, and ∇_0 represents the gradient with respect to the position of the test mass ($\vec{r}_0$). Therefore, it is possible to compute the integral numerically by assuming a grid configuration that represents the surrounding medium around the test mass. We can express a discrete version of the integral in Equation 2.18 for particle displacement that gives rise to gravity perturbations at the position of the test mirror (r_0) as follows:

$$\delta\vec{a}(r_0, t) = G\rho_0 \sum_i V_i \frac{1}{|\vec{r}_i - \vec{r_0}|^3} \left(\vec{\xi}(\vec{r}_i, t) - 3(\hat{e}_i \cdot \vec{\xi}(\vec{r}_i, t))\hat{e}_i \right), \quad (2.19)$$

where, $\vec{r}_i$ denotes the position of the i-th grid point, $\vec{\xi}(\vec{r}_i, t)$ is the corresponding Rayleigh displacement, and $\hat{e}_i$ is the unit vector pointing from $\vec{r}_0$ to $\vec{r}_i$ ($\hat{e}_i = \frac{\vec{r}_i - \vec{r}_0}{|\vec{r}_i - \vec{r}_0|}$). By summing over the grid points, assuming a finite-element model, one can estimate the gravity perturbations resulting from vertical surface displacement and the (de)compression of rock beneath the surface.

2.5 Analytical model of Newtonian noise for surface detectors

In 1984, Saulson presented an analytical model for Newtonian noise and estimated the magnitude of the forces caused by density fluctuations. His model assumed a detector located on the surface with a half-space geology characterized by a density ρ [193]. The ground's density fluctuation was assumed to be coherent over a characteristic scale of $\lambda/2$ meters, where λ represents the wavelength of the seismic wave. These fluctuations were considered uncorrelated in different regions. By assuming that random forces from different regions add in quadrature, Saulson derived an expression for the X-component of Newtonian acceleration (parallel to the detector arm):

$$|\delta a(f)|^2 = \sum_i |\frac{F_i}{M}| = G\sum_i \frac{|\delta m_i|^2 \cos^2 \theta_i}{|r_i|^2}. \quad (2.20)$$

Here, F_i represents the force acting on mass M. Saulson introduced a lower cutoff value of $\lambda/4$ for the integration to avoid singularities as $|r_i|$ approaches zero. It was also assumed that the change in mass density δm_i is proportional to the displacement δx_i of the coherent region, which
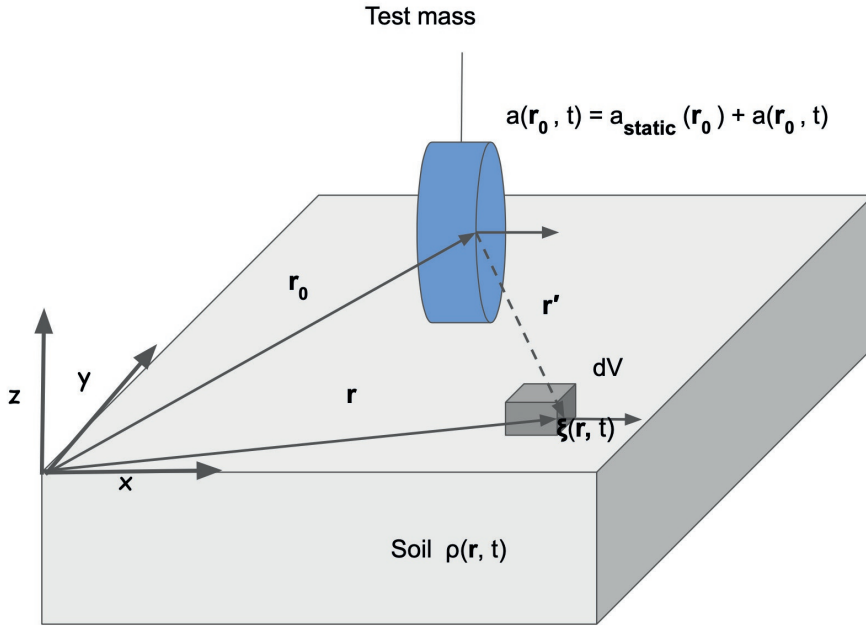
Figure 2.3: Schematic diagram of the effect of Newtonian noise on a test mass suspended at $\vec{r}$ in the reference coordinate system XYZ. Due to the local seismic field $\vec{\xi}(\vec{r}, t)$, the volume element dV undergoes displacement, which results in a change in density $\rho(\vec{r}, t) = \rho_0(\vec{r}) + \delta\rho(\vec{r}, t)$. This causes the change in test mass acceleration $\vec{a}(\vec{r}_0, t)$, which is the sum of the static contribution $\vec{a}_{static}(\vec{r}_0)$ and contribution due to Newtonian noise $\delta\vec{a}_{NN}(\vec{r}_0, t)$ arising from the density fluctuation.

can be estimated using a seismometer. Saulson's results for horizontal displacement Newtonian noise for four test masses can be expressed as:

$$|\delta x_1(f)|^2 = \frac{|\delta a_1(f)|}{(2\pi f)^4} = \frac{16\pi^2}{3} \frac{G^2\rho^2}{(2\pi f)^4} |\delta x(f)|^2 \ (\text{m}^2\,\text{Hz}^{-1}). \qquad (2.21)$$

The factor $16\pi^2/3$ arises due to the lower cutoff $\lambda/4$. It is important to note that this model was derived for a surface detector where the test mass is surrounded by a half-spherical cavern with a frequency-dependent radius of $\lambda/4$. Therefore, this result is not applicable to underground detectors. To make the analytical model more realistic, one needs to consider a plane Rayleigh wave-field, contributions from

the bulk and surface of the half-space, dispersive properties of the soil, and other factors [48, 136].

The expression for Newtonian noise by Saulson [193] can be modified for a surface detector as follows [119]:

$$|\delta x_1(f)|^2 = 4\pi^2\beta^2 \frac{G^2\rho^2}{(2\pi f)^4} |\delta x(f)|^2 e^{\frac{-2\pi h}{\lambda}} \ (\text{m}^2\,\text{Hz}^{-1}). \tag{2.22}$$

Here, h is the height of the test mass with respect to the ground, and $\beta < 1$ is associated with the dispersive properties of the site's geology [136].

2.6 Newtonian noise cancellation

Seismic noise sources, both local (such as vibrational modes of buildings, machine vibrations, traffic noise) and distant, contribute to the overall seismic level at any detector site. Since it is not possible to directly reduce the gravitational coupling between the test mass and the seismic field, it becomes important to perform ambient Newtonian noise (NN) subtraction in order to reduce its overall impact. The process of Newtonian noise cancellation involves monitoring the seismic field with high accuracy and resolution, based on which the displacement of the test mass due to gravity fluctuations can be predicted and subtracted then from the output signal of the interferometer.

To achieve this, a network of seismic sensors is deployed to accurately monitor the ground's seismic motion. The data from these sensors are used to estimate the expected displacement of the test mass due to gravity fluctuations. This estimation is done using techniques such as the Wiener filter, which minimizes the variance of the error function between the measured signal and the predicted signal. Let us consider a given time series $x(t) = h(t) + n(t)$, where h represents the underlying gravitational wave signal and n is the noise. Using the Wiener filter, we can construct the expected signal $\hat{x}(t)$ using data from the sensors to minimize the variance of the error function. The mathematical approach is adopted from [49].

In the frequency domain, the error function can be expressed as:

$$\begin{aligned} E(f) &= x(f) - \hat{x}(f) \\ &= x(f) - \sum_i \alpha_i(f)\chi_i(f), \end{aligned} \tag{2.23}$$

where α_i represents the coefficients for the Wiener filter and $\chi_i(f)$ is the Fourier series of the signal from the i-th sensor. We assume a non-stationary case for simplicity. Therefore, the variance of E becomes:

$$\langle E^*(f)E(f)\rangle = \langle x^*(f)x(f)\rangle - \sum_i \alpha_i \langle x^*(f)\chi_i(f)\rangle - \sum_j \alpha_j^* \langle \chi_j^*(f)x(f)\rangle$$
$$+ \sum_{i,j} \alpha_j^* \alpha_i \langle \chi_j^*(f)\chi_i(f)\rangle.$$

(2.24)

The coefficients can be chosen in a way that minimizes the variance:

$$\alpha_j = \langle \chi_i^*(f)\chi_j(f)\rangle^{-1} \langle \chi_i^*(f)x(f)\rangle \tag{2.25}$$

In our case, for the network of seismometers, we can express,

$$\langle \chi_i^*(f)\, x(f)\rangle = \frac{1}{2}C_{SN_i}(f)$$
$$\langle x^*(f)x(f)\rangle = \frac{1}{2}(C_{NN}(f) + C_{HH}(f)) \tag{2.26}$$
$$\langle \chi_i^*(f)\chi_j(f)\rangle = \frac{1}{2}(C_{SS}(f) + C_{\varepsilon\varepsilon}(f)).$$

Here, $\langle \chi_i^*(f)\, x(f)\rangle$ represents the cross-spectral covariance between the i'th seismometer response $\chi_i(f)$ and the observed data from the interferometer, denoted as $x(f)$. $C_{SN_i}(f)$ is the spectral covariance vector, which characterizes the correlation between the i'th seismometer and the Newtonian noise. $\langle x^*(f)x(f)\rangle$ represents the power spectrum of the observed data $x(t)$. $C_{NN}(f)$ is the power spectrum of the Newtonian noise in the output of the interferometer. $C_{HH}(f)$ represents the power spectral density due to the gravitational wave background. It assumes that all other noise sources, apart from the gravitational waves, are uncorrelated and contribute to the power spectrum in a separate term. $\langle \chi_i^*(f)\chi_j(f)\rangle$ is the cross-correlation matrix between the seismometers. It characterizes the correlations between different seismometer responses and provides information about the spatial coherence of the seismic field. $C_{SS}(f)$ represents the cross-spectral density between the seismometers and it describes the correlation between the measurements of different seismometers at different positions in the network. $C_{\varepsilon\varepsilon}(f)$ is the cross-spectral density between the sensor noise, which is assumed

to be uncorrelated with other noise sources. In this analysis, we assume $C_{NN} \gg C_{HH}$ and ignore $C_{\varepsilon\varepsilon}(f)$.

The Newtonian noise subtraction can be characterized by the relative residual or the fractional error function, which is defined as the ratio of the suppressed amplitude to the unsuppressed amplitude of the interferometer signal:

$$R = \frac{\langle E^*(f)E(f) \rangle}{Y^*(f)Y(f)} = 1 - \frac{C_{SN}^* \, (C_{SS})^{-1} \, C_{SN}}{C_{NN}}, \qquad (2.27)$$

where $Y^*(f)Y(f)$ is the power spectrum of the detector output $Y(f)$ without noise subtraction. The value of R ranges between 0 and 1, where $R = 1$ indicates that the sensor array is ineffective in performing Newtonian noise cancellation, while $R = 0$ represents 100% subtraction of Newtonian noise.

Badaracco et al. [42], have presented results for optimal sensor placement by modeling the complex seismic field using Gaussian process regression (GPR). They applied their method to the Virgo west end building using 37 seismometers and utilized the Wiener filter for optimization, as discussed earlier. To determine C_{SS}, GPR was employed to increase the sample density since only 37^2 data points cover the 4D hypervolume. The 4D nature arises because C_{SS} is a function of the x and y positions of an arbitrary pair of seismometers. The optimal placement of the seismic array was determined, and a relative residual of $R = 0.1$ (corresponding to more than a factor of 3 in Newtonian noise cancellation) was achieved with at least 20 seismometers. The results are depicted in figure 2.4.

Although this analysis did not consider the contribution of body waves, the technique is valuable for designing a seismic array network that can effectively cancel Newtonian noise in current and future surface detectors, even in complex geological conditions.

2.7 Newtonian noise for underground detector

The Einstein Telescope is planned to be an underground gravitational wave detector with 10 km long arms, aiming for a sensitivity improvement of approximately 10,000 times in the frequency range of 5 to 15 Hz, compared to currently operating detectors. The underground location offers quieter seismic noise compared to surface measurements due to the exponential decay of seismic Rayleigh waves with depth. However, underground anthropogenic noise, such as Newtonian noise (NN), can
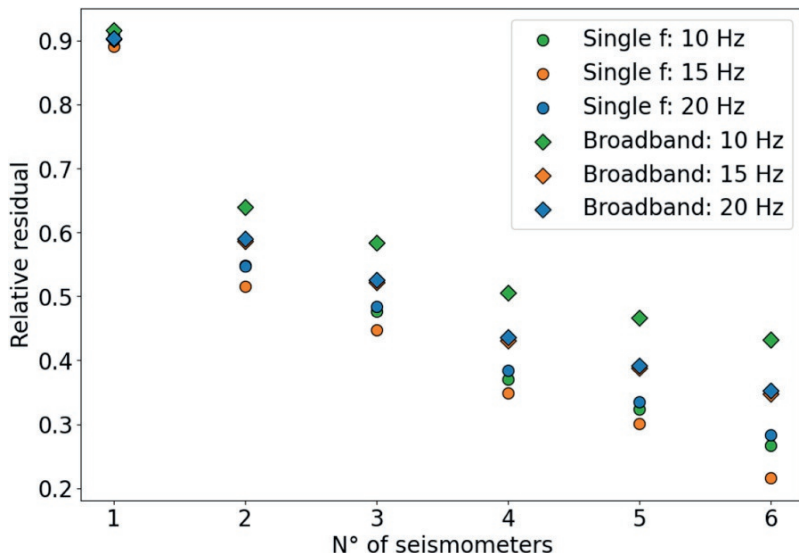
Figure 2.4: The residual R versus the number of optimally placed seismometers. The diamond dots represent the results obtained via broadband optimization for frequencies 10, 15, and 20 Hz, while the circular dots represent the same for single-frequency optimization. Figure taken from [42].

still be a concern, making it important to understand and model the local seismic field and geology.

Two candidate sites have been considered for the possible location of the Einstein Telescope: the EMR site (located at the border region between the Netherlands, Belgium, and Germany) and the Sardinia site. Underground displacement measurements have been performed at both sites. Figure 2.5 and 2.6 show the spectral histograms of horizontal and vertical ground displacements obtained from Terziet (EMR site) and P2 borehole (Sardinia site), respectively.

Harms et al. in [127] derived a lower limit on the seismic NN spectra and estimated NN for the Sardinia and EMR sites, as shown in figure 2.7. They used a simple analytical approach, assuming a homogeneous medium and negligible size of the cavern compared to the seismic wavelength ($\lambda/2\pi$). The gravitational acceleration produced by compressional and shear waves can be expressed as:

$$\delta\vec{a}(r_0, t) = \frac{4\pi G\rho}{3}(2\,\vec{\xi}^P(\vec{r}_0, t) - \vec{\xi}^S(\vec{r}_0, t)). \tag{2.28}$$
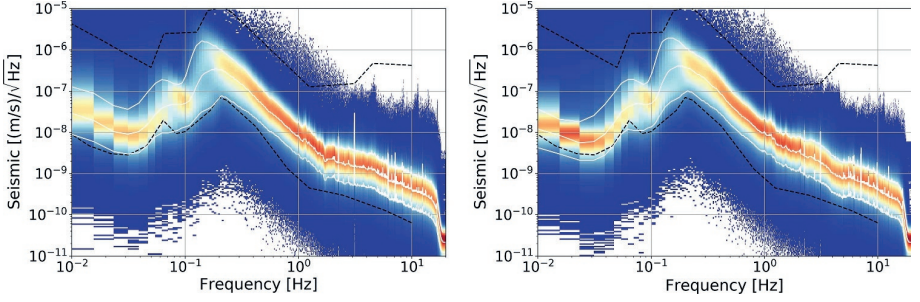
Figure 2.5: Spectral histogram of horizontal(left) and vertical(right) ground displacements obtained from Terziet, EMR at a depth of 250 m. Data have been collected from September 30, 2019, to September 14, 2020. The white curves represent the distribution's 10th, 50th, and 90th percentile. The black dashed lines represent Peterson's high and low noise model. Plot taken from [127]
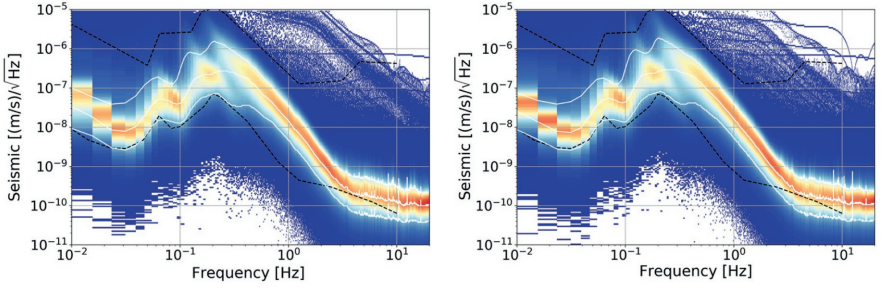
Figure 2.6: Spectral histogram of horizontal(left) and vertical(right) ground displacements obtained from P2 borehole, Sardinia site at a depth of 264 m. Data have been collected from October 1, 2021, to April 30, 2022. The white curves represent the distribution's 10th, 50th, and 90th percentile. The black dashed lines represent Peterson's high and low noise model. Plot taken from [127]

where ρ is the density of the homogeneous medium, $\vec{\xi}^P$ and $\vec{\xi}^S$ are the compressional and shear wave contents, respectively. It should be noted that the negative sign in equation 2.28 does not imply a reduction in NN. Both components of shear waves contribute uncorrelated noise. This equation, derived for the gravity perturbation of a test mass within a small spherical cavity ($r_1 \rightarrow 0$, or $k\,r_1 \ll 1$, where k is the P-wave wave number and r_1 is the radius of the cavity), can be obtained straightfor-
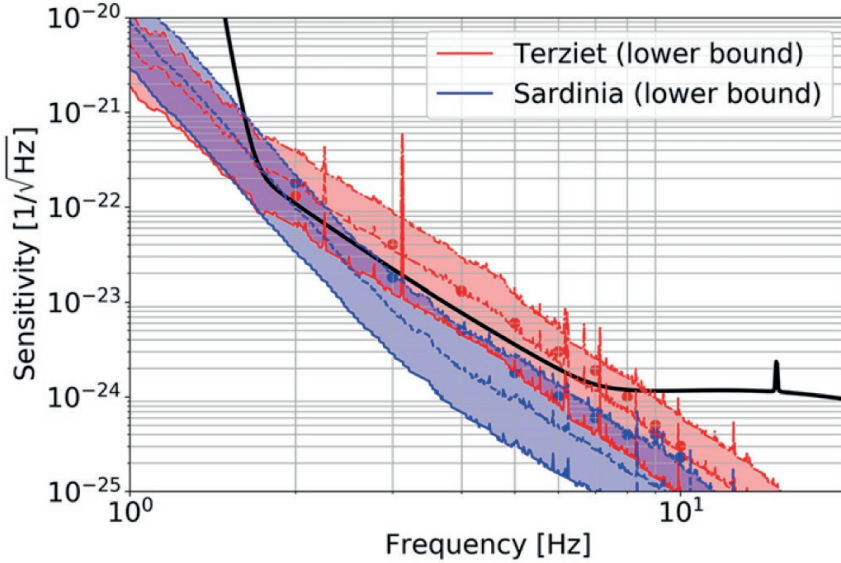
Figure 2.7: Lower bound on seismic Newtonian noise for the candidate sites of ET, assuming a rock density of $\rho = 2800, \mathrm{kg/m^3}$. Taken from [127]. The blue and red markers represent NN estimates at Terziet and Sardinia, respectively, as published in [43] and [32]. The black curve represents the modeled sensitivity curve of the ET.

wardly as shown in [124]. The model includes a bulk contribution and a contribution from the cavern wall. To estimate the lower limit of NN, Harms et al. ignored the bulk contribution as it is dependent on the specific geology. They focused solely on the cavern wall displacement to provide a conservative estimate of the lower limit of NN, which can be expressed as:

$$\delta\vec{a}(r_0, t) = G\rho \int dS(\vec{n}(\vec{r}) \cdot \vec{\xi}(\vec{r}, t))\frac{\vec{r} - \vec{r_0}}{|r - r_0|^3} = -\frac{4\pi G\rho}{3}\vec{\xi}(\vec{r_0}, t)). \quad (2.29)$$

M. Bader et al. [43] provided an estimation of the Newtonian noise at the Terziet site in Limburg by solving elastodynamic wave equations with site-specific parameters, as shown in figure 2.8. They considered five layered geologies based on passive and active array analyses. For layered geology, NN acceleration can be expressed as the sum of a volume
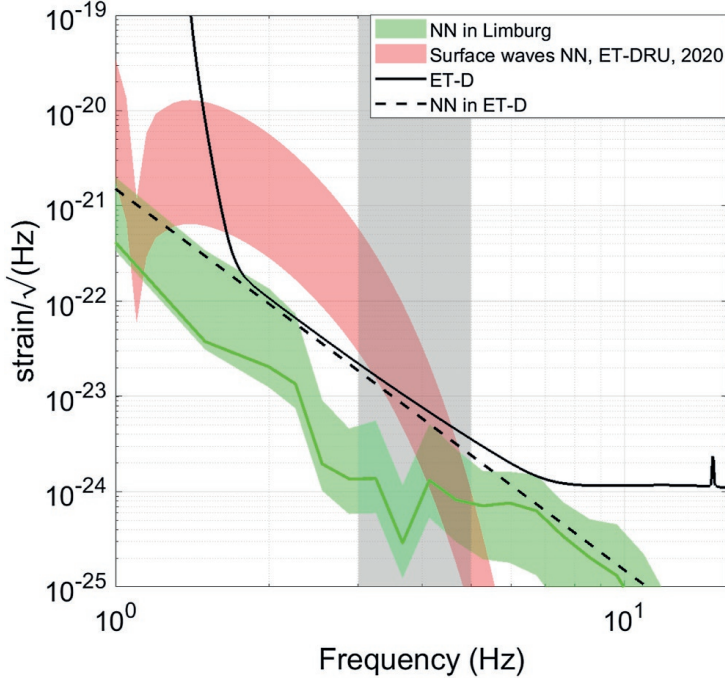
Figure 2.8: Estimation of Newtonian noise at the EMR site from surface sources for a test mass located at a depth of 250 m and enclosed inside a cavern with a radius of 10 m. The red band denotes NN at the surface, and the green band shows NN at an underground location compatible with the design sensitivity curve of ET-D and its NN contribution (black trace). The grey band indicates the region of significant uncertainty in geological modeling due to the underestimation of underground displacement seismic field. Taken from [43].

integral and a surface integral:

$$\vec{a}(f) = \sum_{m=1}^{N} G \int_{v} \rho_m (\vec{u} \cdot \nabla)\vec{k} \, dV_m + (\rho_{m-1} - \rho_m) \int_{s} (\vec{u} \cdot \hat{n}_m)\vec{K} \, dS_m, \quad (2.30)$$

where $\hat{n}_m$ is the vector normal to the horizontal layer, $\vec{k} = \frac{\vec{x}}{|\vec{x}|}$, ρ_m is the density of the m'th layer, and the 3D displacement seismic wave field is given by $\vec{u}(\vec{x}, f) = (u_1(\vec{x}, f), u_2(\vec{x}, f), u_3(\vec{x}, f))$. Figure 2.8 represents the NN in Limburg due to seismic displacement of the entire subsurface and the free surface arising from surface excitation. The dip below 3 Hz is an artifact resulting from the underestimation of horizontal displacement in
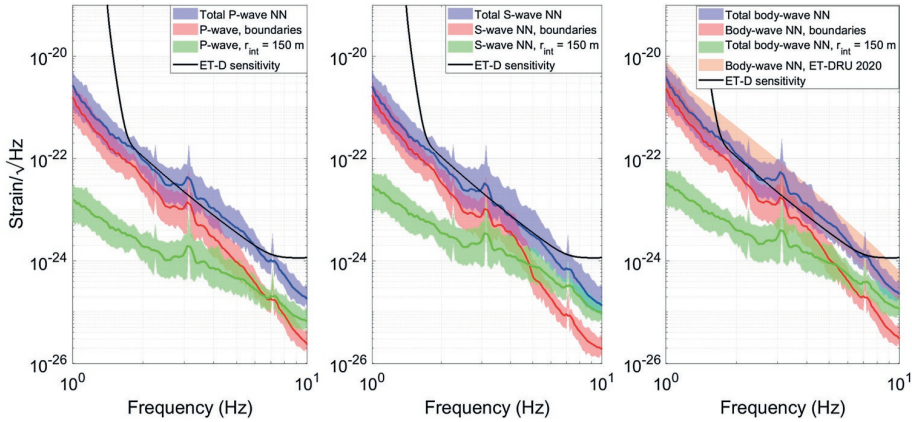
Figure 2.9: Estimation of NN for random body wave background at the EMR site of the Einstein Telescope, considering an underground test mass at a depth of 250 m enclosed by a cavern with a radius of 10 m. The black curve denotes the ET-D sensitivity, and the blue curve represents the total NN contribution from p-waves (left), s-waves (middle), and the total body wave NN (right) obtained by summing up the contributions of p-waves and s-waves. The red and green bands represent the individual contributions from mass movements across the boundary and displacements of the volume up to a radius of 150 m around the test mass, respectively. The width of the shaded region indicates the distribution between the 10th and 90th percentiles. The orange band (right) represents the body wave background from the Einstein Telescope design report 2020. Figure taken from [43].

the model seismic field. It is important to consider not only the seismic displacements of different sites but also their underground geology and seismic characteristics. Figure 2.9 shows the estimation of NN due to body waves for the EMR site of the Einstein Telescope. The body wave field can be modeled as:

$$\vec{u}(\vec{x}) = (\vec{A} \cdot \hat{\xi}) \, \hat{\xi} \, e^{-i\left(\frac{\hat{\xi} \cdot \vec{x}}{V_p} - \omega t\right)} + (\vec{A} - (\vec{A} \cdot \hat{\xi}) \, \hat{\xi}) \, e^{-i\left(\frac{\hat{\xi} \cdot \vec{x}}{V_s} - \omega t\right)}, \qquad (2.31)$$

where $\vec{A}$ is the amplitude in the direction of the displacement, $\hat{\xi}$ is the direction of wave propagation, $\vec{x}$ represents the coordinates, and V_p, V_s are the p-wave and s-wave speeds. For numerical calculations, constant P and S-wave velocities are assumed at all frequencies, and the fields are generated from the superposition of plane waves with random phases. Finally, the figure 2.10 shows the overall prediction of NN, which includes

contributions from body wave backgrounds and surface excitations. The estimated NN is approximately a factor of 2 higher than the model sensitivity of ET-D due to the more significant contribution of the body wave background. However, the soft soil surface profile in the Limburg region acts as a shield against surface excitation. An NN cancellation scheme is required to reduce NN from body waves.
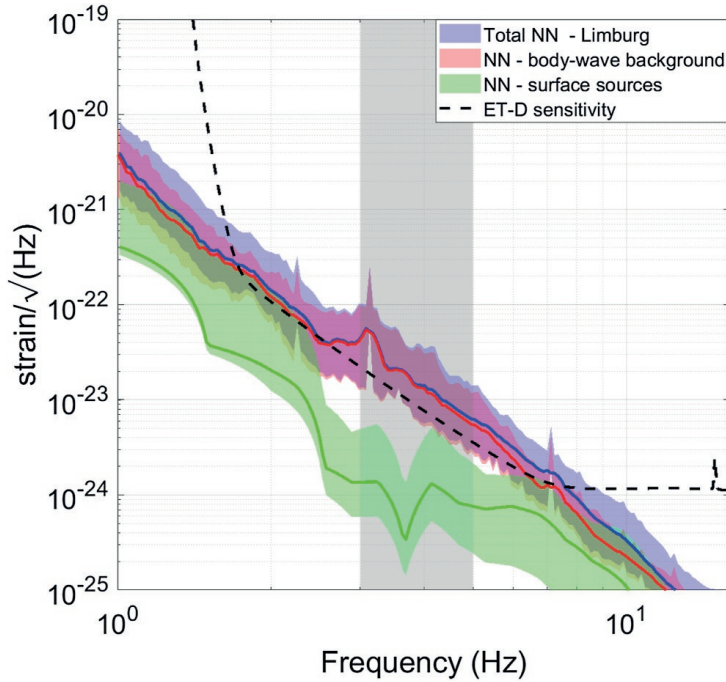
Figure 2.10: Prediction of Newtonian noise for the EMR site. The blue band denotes the total NN, which closely matches the body wave NN. The black dotted curve represents the ET-D sensitivity. The width of the color band indicates the distribution between the 10th and 90th percentiles. Figure taken from [43].

These studies provide estimates and predictions of Newtonian noise for the Sardinia and EMR sites, taking into account various geological factors and seismic characteristics. They highlight the importance of considering underground geology and seismic wave properties in the evaluation of NN for future gravitational wave detectors like the Einstein Telescope.

Chapter 3

Newtonian-noise reassessment for the Virgo gravitational wave observatory including local recess structures

3.1   Introduction

Newtonian noise (NN) limits the low-frequency sensitivity of gravitational wave detectors and cannot be reduced directly. In previous chapters we have discussed indirect methods of reducing NN, such as coherent Newtonian noise cancellation, selecting seismically quiet sites, going underground, or constructing recess-like structures under the test mirrors to suppress density fluctuations in the surroundings. In this chapter we focus on NN reduction by recesses. The Virgo gravitational wave observatory already has open spaces or recesses (part of clean rooms) beneath the test masses. However, previous calculations of Virgo's NN spectra have relied on analytical equations that assume a flat surface, leaving room for improvement in accurately modelling the effects of recesses. Therefore, the primary objective of this chapter is to perform a comprehensive numerical evaluation of the NN spectra, taking into account the intricate dimensions of the clean rooms located in Virgo's central, northern and western buildings. My aim is to quantitatively assess the reduction factor in the overall NN strain spectra, paying particular attention to the influence of isotropic Rayleigh wave fields and analysing how this reduction factor varies with the direction

of wave propagation.

Section 3.2 discusses the numerical modeling approach for simulating the Rayleigh-wave field, which is crucial for evaluating NN reduction. Section 3.3 outlines the proper dimensions of recesses under the input and end test mirrors in Virgo's central and end buildings. Section 3.4 describes simulation of the isotropic Rayleigh-wave field near the test mirrors and estimates the resulting gravity perturbation using a finite-element model. I demonstrate the reduction in gravity perturbation achieved by the recesses. In section 3.5, I discuss the choice of the grid size and density required for finite element analysis. Section 3.6 represents the computation of the NN decrease for each main test mass in Virgo and combines the results to obtain the overall NN reduction factors. In addition, section 3.6 considers directional seismic fields and analyses how the NN reduction factors for the Virgo end test masses vary with the direction of wave propagation. This chapter relies on the work presented in [199].

3.2 Numerical models of seismic fields

I focus here on the kinematic simulation of the seismic field because it can be done with less computational effort than a fully dynamic solution. Many other aspects, such as the reflection of seismic waves from infrastructure [156, 102] and mode conversions [228], can be taken into account to build more realistic seismic fields, which I haven't considered in this model. The complexity of the seismic field can vary depending on various factors such as geographical location, local geological conditions and the presence of infrastructure. It is difficult to incorporate all these complexities into a single model that covers all possible scenarios. Therefore, a simplified model provides a reasonable approximation that helps us to capture the essential behaviour of the seismic field and serves as a basis for further analysis. This model assumes an isotropic seismic field where the 2D direction is randomly chosen from a uniform distribution. I consider the propagation of a plane wave field from a random direction, repeating this process 20 times to account for variability. The particle displacement contributions from each plane wave are then combined to generate an isotropic seismic field. In the figure 3.1 I show the isotropic seismic field illustrating the displacements caused by the Rayleigh wave field for several surface layers. The amplitude of the Rayleigh wave decreases exponentially with depth. The colour bar in
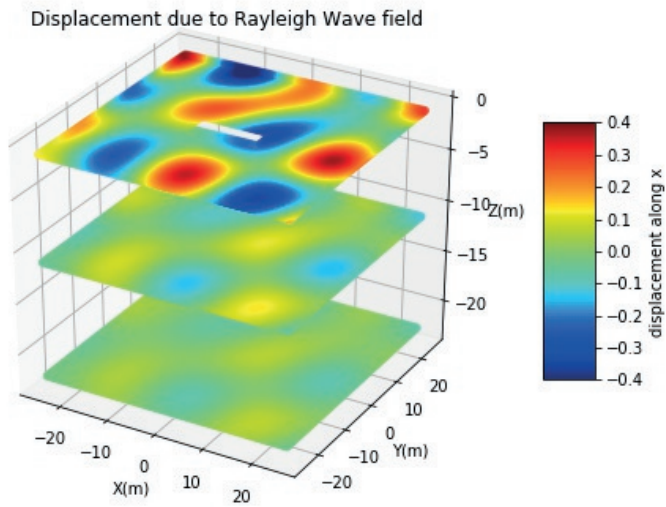
Figure 3.1: Displacements due to the Rayleigh wave field for some surface layers. The amplitude of the field decreases with depth.

the figure 3.1, indicates the magnitude of the Rayleigh field at each grid point, providing insight into the distribution of seismic activity. The recess shape, represented by the white rectangle in the figure 3.1, is significantly smaller than the Rayleigh wavelength. This indicates that the influence of seismic scattering due to the recess can be neglected since the recess does not introduce significant irregularities or heterogeneities that would cause substantial scattering of the seismic waves.

3.3 Recess parameters around Virgo test mirrors
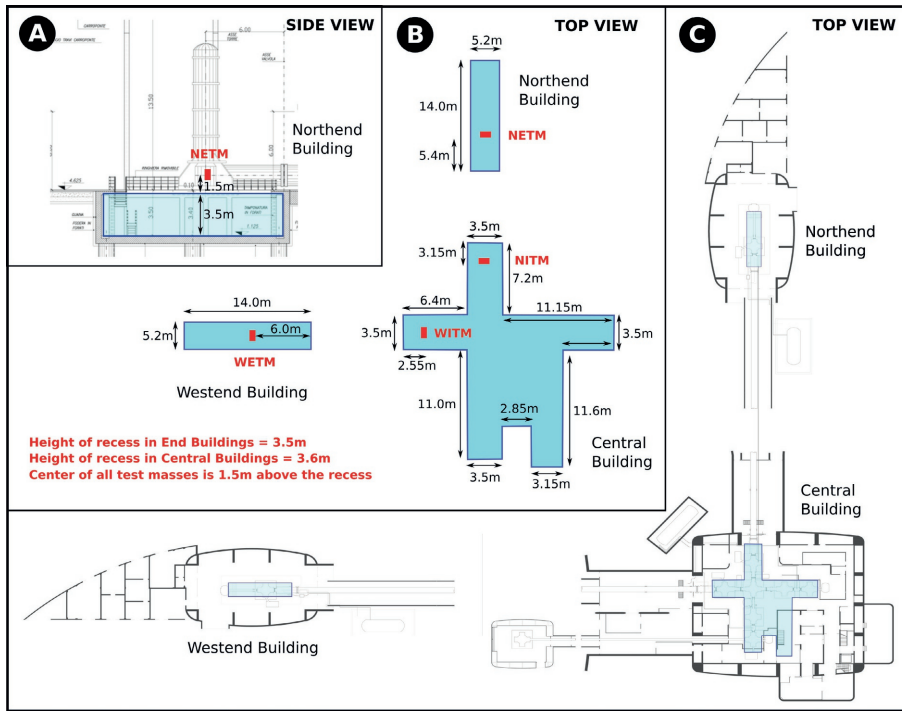
Figure 3.2: Overview of the Virgo configuration (with recess parameters below test mirrors). The sky-blue shaded areas in this figure represent the positions of the recesses under the test mirrors. Part (B): TOP VIEW with red dots representing the test mirrors. Part (A): SIDE VIEW, where we can see the locations of the recesses. The depth of the recesses in the end buildings is 3.5 m, and for the central building, it is about 3.6 m. For each case, the mirror is hanging 1.5 m above surface level.

In this section, we provide details about the recess parameters around the test mirrors in the Virgo Observatory buildings. The purpose of this study is to adjust the Newtonian noise spectrum by considering the presence of cleanrooms beneath the test mirrors, which can act as recesses. It's important to note that these modifications are specific to Virgo, as they take into account the unique dimensions of the space surrounding the test mirrors.

Figure 3.2 presents schematic geometries of the recesses in the Central Building (CEB), North End Building (NEB), and West End Building (WEB) of the Virgo observatory. The recesses are represented by the sky-blue shaded areas in the figure. Part (B) of the figure shows a top view of the recesses, with the red dots indicating the positions of the test mirrors. Part (A) provides a side view, illustrating the location of the recess in the ground label. The depth of the recesses is 3.5 m for the end buildings and approximately 3.6 m for the central building. The test mirrors are positioned 1.5 m above the surface level.

For the end test mirrors (ETMs), the recess shape is a simple rectangle, although it is not symmetric along each arm. On the other hand, for the input test mirrors (ITMs), the entire cleanroom space in the central building is considered, which is larger, more extensive, and less symmetrical compared to the recesses in the end buildings. By incorporating these specific recess dimensions into the modelling and analysis, a more accurate assessment of the reduction of Newtonian noise in the Virgo detector can be made, showing the effectiveness of the recesses in mitigating unwanted noise sources.

3.4 Suppression factors of gravity perturbation on test mirrors due to presence of recesses

In this section, I focus on evaluating the suppression factors of gravity perturbation on the test mirrors in the Virgo observatory due to the presence of recesses. The goal is to refine the Newtonian noise (NN) curve for Virgo by incorporating a more accurate geometric structure of the cleanrooms beneath each test mass. In order to avoid complexity in the model, I consider the isotropic Rayleigh-wave field for various frequencies from 5 to 25 Hz. The isotropic field is generated in this simulation by summing the contributions of plane Rayleigh waves propagating in random directions. The mathematical formulation and intrinsic parameters of the Rayleigh waves can be obtained from the reference [123]. I
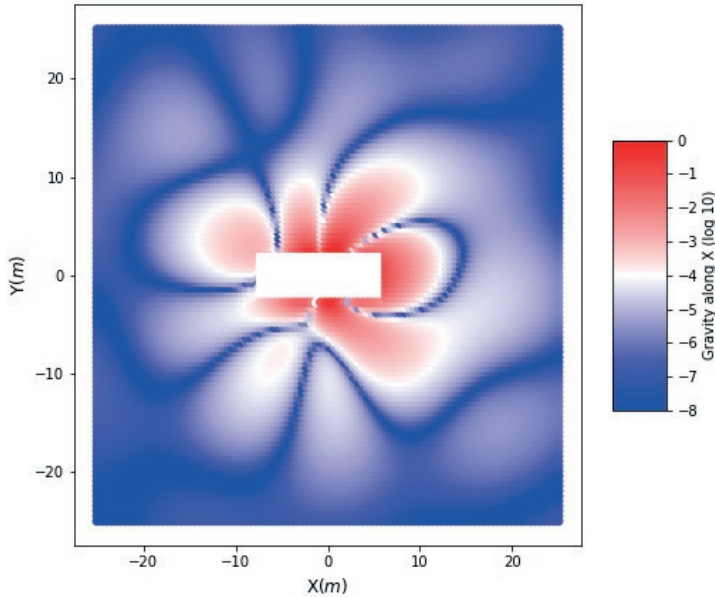
Figure 3.3: Contribution to the Rayleigh gravity perturbation from different parts of the surface displacement field. The layers have been shown including the recess.

estimate the gravity perturbation caused by density fluctuations resulting from the propagation of seismic waves. The discrete version of the integral over particle displacement, which gives rise to gravity perturbations at the position of the test mirror (r_0), can be expressed as follows:

$$\delta\vec{a}(r_0, t) = G\rho_0 \sum_i V_i \frac{1}{|\vec{r}_i - \vec{r}_0|^3} \left(\vec{\xi}(\vec{r}_i, t) - 3(\hat{e}_i \cdot \vec{\xi}(\vec{r}_i, t)) \cdot \hat{e}_i \right). \quad (3.1)$$

In this equation, $\vec{r}_i$ represents the position of the i-th grid point, $\vec{\xi}(\vec{r}_i, t)$ is the corresponding Rayleigh displacement, and $\hat{e}_i$ is the unit vector pointing to $\vec{r}_i$ from $\vec{r}_0$ ($\hat{e}_i = \frac{\vec{r}_i - \vec{r}_0}{|\vec{r}_i - \vec{r}_0|}$). By summing over the finite-element model, one can account for gravity perturbations from vertical surface displacement as well as the (de)compression of the rock beneath the surface. This equation allows us to evaluate the gravity perturbation based

58
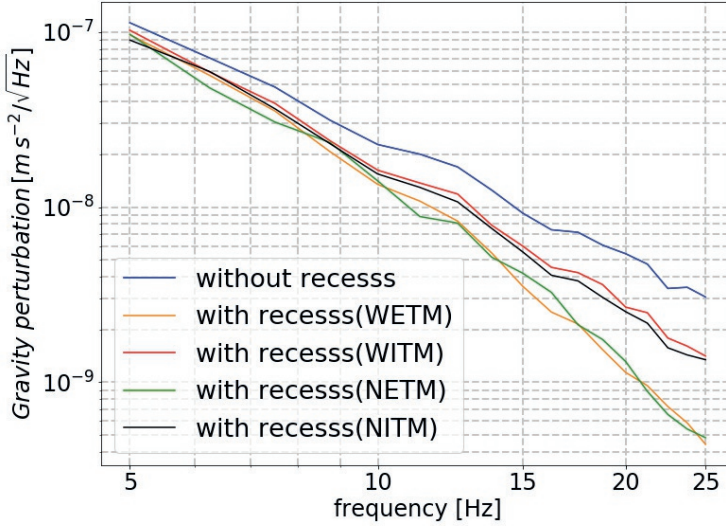
Figure 3.4: Gravity perturbation due to the propagation of Rayleigh waves on input and end test mirrors (ITM and ETM) of the west (W) and north (N) arm.

on a finite-element model of the ground. The displacement of points from their equilibrium position generates a fluctuating gravitational field on the test mirror, resulting in Newtonian noise. Figure 3.3 illustrates the component of the gravity perturbation (along the direction of the arm) on the test mirror due to an isotropic Rayleigh field.

I generate the Rayleigh field with uniform random propagation directions for each reference frequency between 5 and 25 Hz and then compute the gravity perturbation on the test mirror. I perform this calculation for two cases. In the first case, I consider a symmetric grid structure surrounding the test mirror without any recess. Therefore, the gravity perturbation without a recess should be the same for each individual test mirror. In the second case, I evaluate the gravity perturbation by incorporating the recess dimensions into the finite-element model. I repeat this calculation for each test mirror, considering their different recess dimensions (length and width).

Figure 3.4 displays the gravity perturbation on the test masses due to the isotropic seismic field, with and without a recess. As expected,
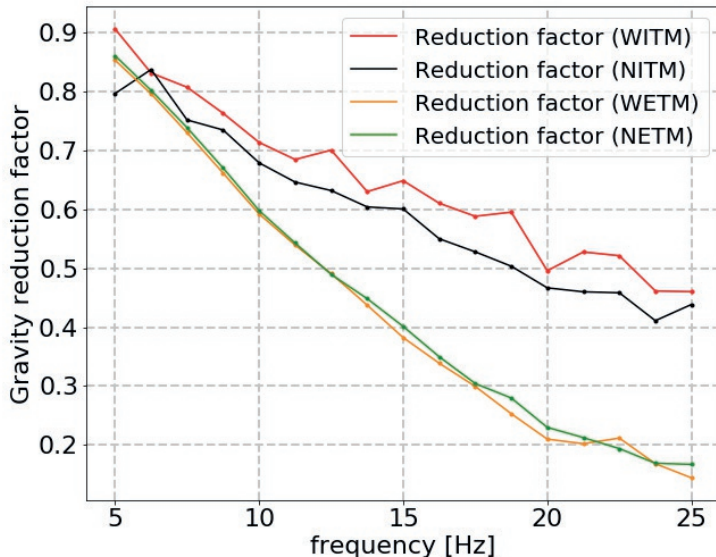
Figure 3.5: Reduction ratio with recess vs without a recess for both input and end mass.

the magnitude of the gravity perturbation is reduced when the recess structure is taken into account, and this effect is more pronounced for the end test mirrors compared to the input test mirrors. Figure 3.5 shows the reduction ratio of the gravity perturbation, which is simply the ratio of the perturbation with a recess to the perturbation without a recess. For the ETMs, a significant reduction (by a factor of 2) is observed in the frequency range between 10 and 15 Hz.

The observed increase in the significance of Newtonian noise reduction at higher frequencies can be attributed to the comparison between the dimensions of the recess and the length of Rayleigh waves. At frequencies where Rayleigh waves have much larger wavelengths compared to the recess dimensions, the recess only excludes a minor part of all the relevant density fluctuations in the ground produced by these waves. The situation improves with shorter wavelength with the caveat that when Rayleigh waves become very short (in Virgo, at frequencies >15 Hz [207]), scattering from the recess becomes important, possibly leading to modifications of the NN reduction not described by our model. There-

fore, while the model provides valuable insights into the reduction of Newtonian noise with a recess, it should be noted that its predictions may deviate from reality at higher frequencies where scattering effects become significant.

3.5 Reduction factor dependence on finite element model (FEM)

In the previous section, I have shown the suppression factors of the gravity perturbation on the test mirrors, which were obtained using a finite element simulation model. In this model, the grid points represent the discretized representation of the surrounding medium around the test mass. By summing the contributions of the grid points to the test mass acceleration using equation 3.1, I calculated the gravity reduction factors.
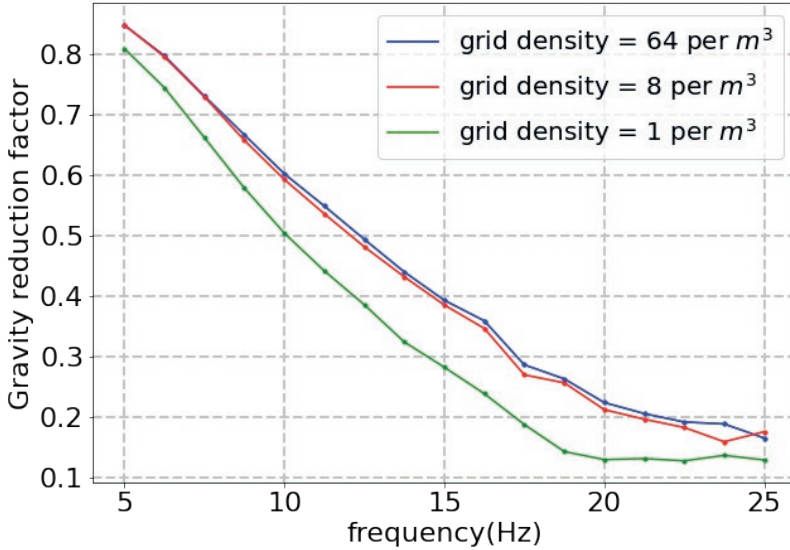
Figure 3.6: Reduction factors of NN for WETM assuming different grid densities of finite element simulation model.

To validate the accuracy and reliability of the results with respect to the finite element model used in this analysis, I have conducted ad-

61

ditional investigations. Specifically, I examined the dependence of the gravity reduction factor on the grid density and grid boundaries of the surrounding medium.

By assuming different grid densities in the finite element model, I estimated the gravity reduction factor due to the recess at various frequencies. Figure 3.6 illustrates the results (for WETM), showing that a grid density of at least 8 points per cubic meter is required to obtain accurate values. If the grid density is lower than this threshold, the estimated reduction factors may not reflect the true behavior accurately. At frequencies above 20 Hz, there is a slight discrepancy between the blue and red curves, suggesting that increasing the grid density at higher frequencies can improve the accuracy of the results. This adjustment ensures that the discrete grid points adequately capture the fine details of the displacement field caused by the Rayleigh waves. Alternatively, rather than increasing the grid density, one could opt for a different approach by maintaining the same number of grid points and reducing the boundary of the finite element model. This strategy takes advantage of the fact that at lower wavelengths, the contribution from regions further away from the test mass becomes negligible in comparison to the immediate vicinity of the test mass. By restricting the model to a smaller boundary, computational resources can be optimized without significantly compromising the accuracy of the reduction factor estimation.

Furthermore, I have investigated the influence of the grid boundaries on the gravity reduction factors by considering different integration regions in the finite element model. Figure 3.7 shows the gravity reduction factors for various choices of the boundary volume. While maintaining a grid density of 8 points per cubic meter, I varied the volume of the boundary region. The results highlight that the model yields reliable outcomes when the X, Y, and Z coordinates of the surrounding medium span from -25 to 25, -25 to 25, and -25 to 0, respectively, with the surface situated at Z = 0. By selecting this appropriate integration region, one can ensure that it captures the essential density fluctuations and their effects on the test mass accurately. Restricting the integration region to this volume allows us to neglect contributions from more distant regions that have a negligible impact on the local effects near the test mass.

In the estimation of the Newtonian noise reduction factors, I employed a consistent grid density of 8 points per cubic meter throughout the finite element model. The overall volume of the finite element model
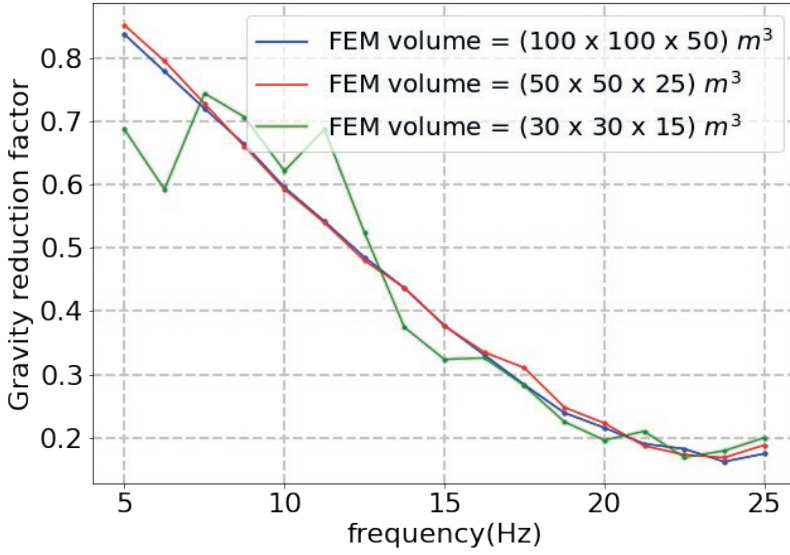
Figure 3.7: Reduction factors of NN for WETM assuming for different boundary of the surrounding medium of finite element simulation model.

was set to be $50 \times 50 \times 25 \, \mathrm{m}^3$. These choices allowed us to accurately assess the gravity reduction factors and their dependence on the recess structure, ensuring reliable results for this analysis.

3.6 Results of Newtonian Noise Suppression in Virgo
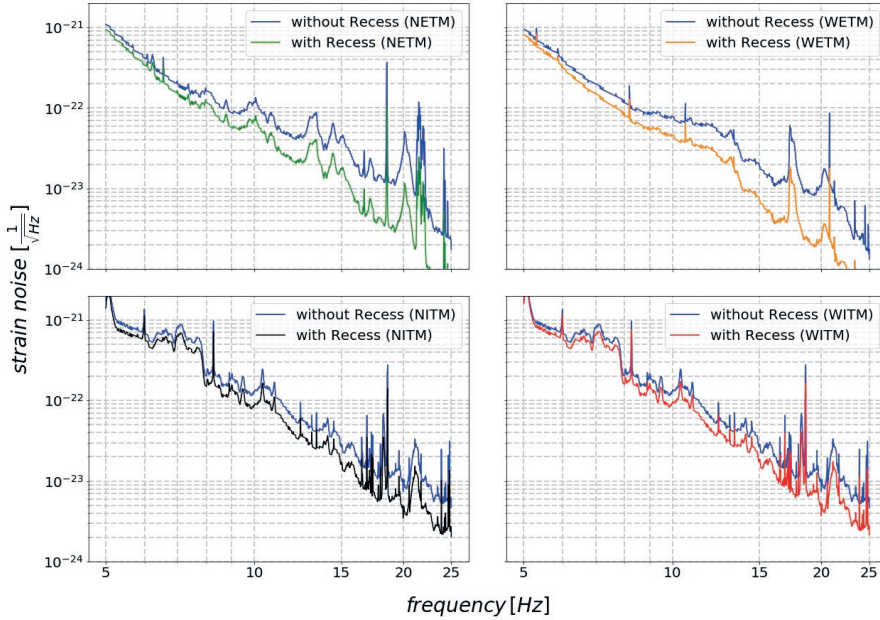
Figure 3.8: (upper left) Newtonian noise spectra for North end test mirror (horizontal displacement along north). (upper right) Newtonian noise spectra for West end test mirror(horizontal displacement along west). (lower left) Newtonian noise spectra for North input test mass (horizontal displacement of NITM along north). (lower right) Newtonian noise spectra for West input test mass (horizontal displacement of WITM along west). For each sub-plots, the blue trace curve is being used to specify the spectra without recess and the other spectra are associated with the corresponding mirror for the particular shape of the recess.

In this section, I present the results of my estimation of the reduction in the absolute level of Newtonian noise due to the presence of the recess underneath the test mirrors in the Virgo gravitational wave detector. Figure 3.8 illustrates the NN spectra for the different test mirrors in Virgo. I consider the seismic spectra recorded from seismometers deployed at various locations within the Virgo site, including the central building, north-end building, and west-end building. I have used the 90th percentiles of vertical seismic spectra to normalize the
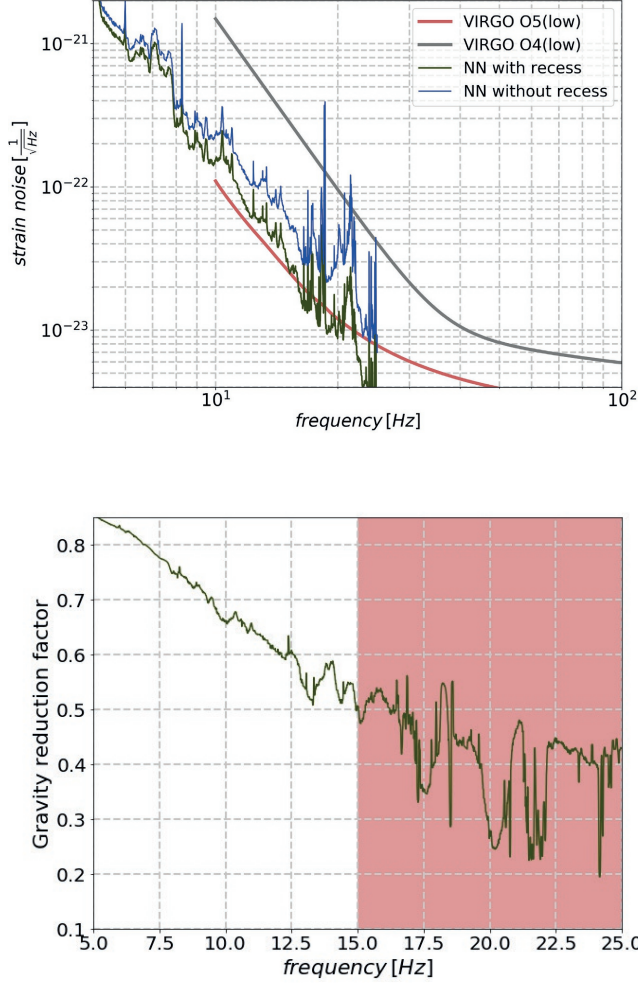
Figure 3.9: (top) Total NN spectrum and its reduction when considering the recesses under test masses. For reference, we have also included the sensitivity of Virgo O4 and O5 for their lower limit. (bottom) Newtonian noise reduction ratio. Newtonian noise suppression at frequencies above 15 Hz (shaded region) in these plots may be significantly affected by seismic scattering (as one can estimate from analytical expressions, which are consistent with observations at the Virgo site [207]), which is not considered in the numerical simulation used for this analysis.

vertical surface displacement in the finite-element model. The model itself then produces vertical and horizontal displacements at the surface and underground consistently according to an analytical equation of the Rayleigh-wave field. We have already found the reduction factors numerically for each test mirror. Just by multiplying those reduction factors for each test mirror with a no-recess NN estimate, I obtain the NN spectra with recess of figure 3.8. The NN spectra without a recess (blue curves) are added for comparison.

Finally, I estimate the overall NN curve shown in figure 3.9 (top). Assuming that NN is uncorrelated between test masses (certainly valid for correlations involving ETMs due to their large distance to other test masses, but also valid for the ITM pair when assuming an isotropic seismic field), NN power spectral densities from individual mirrors can simply be added, and I then plot the square root of the total power spectral density. In figure 3.9 (bottom), I show the reduction ratio for the overall NN spectra. We find the reduction in NN nearly a factor of 2 within 12 to 15 Hz. It is not a smooth curve anymore (compare with figure 3.4) since reduction factors for each test mass are different, which means that the ratio of total NN with and without a recess now depends on the shape of the individual spectra.

3.7 Newtonian-noise reduction due to recess in a directional seismic field

Our analysis of NN suppression was based on the assumption of an isotropic seismic field, where Rayleigh waves were considered to be incident from all directions with equal probability. In reality, seismic sources often exhibit significant anisotropy, leading to variations in wave propagation characteristics based on the direction of propagation. Consequently, it is crucial to comprehensively understand the impact of recesses in relation to the direction of wave propagation, in order to accurately estimate corrections to the results obtained under isotropic assumptions. By considering the presence of recesses, our previous research demonstrated promising results in mitigating NN. However, to translate these findings into practical applications, it is imperative to account for the directional nature of the seismic field. Anisotropic seismic sources, such as local geological features or anthropogenic activities, can introduce spatial variations in wave propagation, influencing the effectiveness of recesses in NN reduction. Understanding these effects is vital for accurately predicting the performance of recess-based NN mitigation strategies. To achieve this objectives, I have conducted an in-depth investigation of the impact of recesses in a directional seismic field. By systematically varying the direction of wave propagation and analyzing the corresponding changes in NN reduction, I have developed a comprehensive understanding of how recesses interact with directional seismic forces. This analysis will enable us to quantify the corrections required to adapt the isotropic results obtained in the previous section to the directional seismic scenario.

The shape of the recess beneath the end test mirrors (ETMs) is not spherically symmetric; rather, it resembles a rectangle. This implies that the reduction factor for Newtonian noise should exhibit a dependence on the propagation angle, denoted as θ, of the seismic wave. To investigate this, I computed the NN reduction factor for individual Rayleigh waves as a function of propagation direction. In figure 3.10 (top), I present the variation of the reduction factor for the West ETM's NN as the seismic field approaches from different angles ($0° \leq \theta \leq 360°$) relative to the arm direction. To illustrate this variation, I have selected three reference frequencies: 5 Hz, 10 Hz, and 15 Hz. By examining the plot, we observe how the reduction factor varies with the angle of propagation θ. The findings demonstrate the importance of considering the directional characteristics of the seismic waves when evaluating the efficacy of the

recess-based approach.

Figure 3.10 (bottom) presents the absolute gravity perturbation, measured in arbitrary units, both with and without a recess, specifically for the reference frequency of 15 Hz. Notably, when the seismic wave arrives from directions perpendicular to the arm ($\theta = 90°, 270°$), the density fluctuation along the arm direction is null without any recess. As the recess surrounding the mirrors is not symmetric, we see some unbalanced gravity field when considering recess, which means that NN never fully vanishes. Hence, when we are taking the ratio of the gravity perturbation with and without a recess, we are finding diverging factors for $\theta = 90°, 270°$. This should not be the case if the recess would be symmetric about the test mirror. The results in figure 3.10 can provide a more accurate estimate of the NN reduction when information about the observed anisotropies of the seismic field is included. While it is desirable to account for anisotropy to achieve a more accurate estimation of Newtonian noise reduction, it is essential to acknowledge and address the complexities and limitations associated with capturing and incorporating anisotropic effects in the analysis. Firstly, anisotropic structures, arising from various factors, such as subsurface geological structures, heterogeneity in the Earth's layers, and localized sources of seismic activity, can be highly complex and challenging to model. Secondly, the anisotropy of the seismic field can exhibit temporal and spatial variations, with seismic sources and subsurface properties changing over time and space. If there are multiple seismic sources present, it introduces additional complexities related to the spatial and temporal distribution of seismic activity. Despite the challenges associated with considering anisotropy, the conclusion holds true. The recesses, even with their non-spherical symmetry, contribute to a substantial reduction in VIRGO NN and provides evidence of the effectiveness of the recess-based approach in mitigating NN. Assuming isotropy simplifies the analysis by considering an average seismic field without detailed knowledge of directional dependencies. This simplification allows for a more straightforward evaluation of NN reduction and facilitates initial assessments of mitigation strategies.

3.8 Summary and outlook

I have re-estimated the Newtonian noise considering the existence of clean rooms or recess-like structures underneath the test mirrors of the

Virgo detector. Accountability of these recesses in numerical simulation leads to suppression of Newtonian noise relative to expectations, mostly due to the fact that a recess increases the distance between test mass and ground. I have obtained a significant suppression factor (by 2 at 15 Hz) in the overall Newtonian-noise spectrum, which is important to include in future Newtonian-noise models for Virgo.

I also investigated the impact of field anisotropy on the reduction factor. Especially at the Virgo end buildings, knowledge of source locations (ventilation, pumps, ...) and seismic-array analyses already indicate an anisotropy of the field [207]. We found that the direction of propagation of the seismic field is important, but the reduction of Newtonian noise is achieved for almost all propagation directions except for those where Newtonian noise without a recess would vanish, i.e., the practically irrelevant case where all Rayleigh waves propagate perpendicular to the detector arm.

The presence of recesses is effective, especially for surface GW detectors where the dominant seismic Newtonian noise comes from comparatively slow Rayleigh waves ($\lesssim 300$ m/s). In this case, the required horizontal extent of the recess below test masses is of order 10 m, which is a feasible modification of a detector infrastructure (as demonstrated at the Virgo site). Reduction of Rayleigh-wave Newtonian noise by a factor of 2 and more is not minor given that a similar reduction by Newtonian-noise cancellation requires large arrays. Better suppression can be achieved by choosing optimized recess geometries as shown in past work [119]. However, given the high seismic speeds in underground environments, it seems unlikely that a similar mechanism can be exploited in the Einstein Telescope [95], which would essentially ask for cavern sizes of around 100 m to be effective.
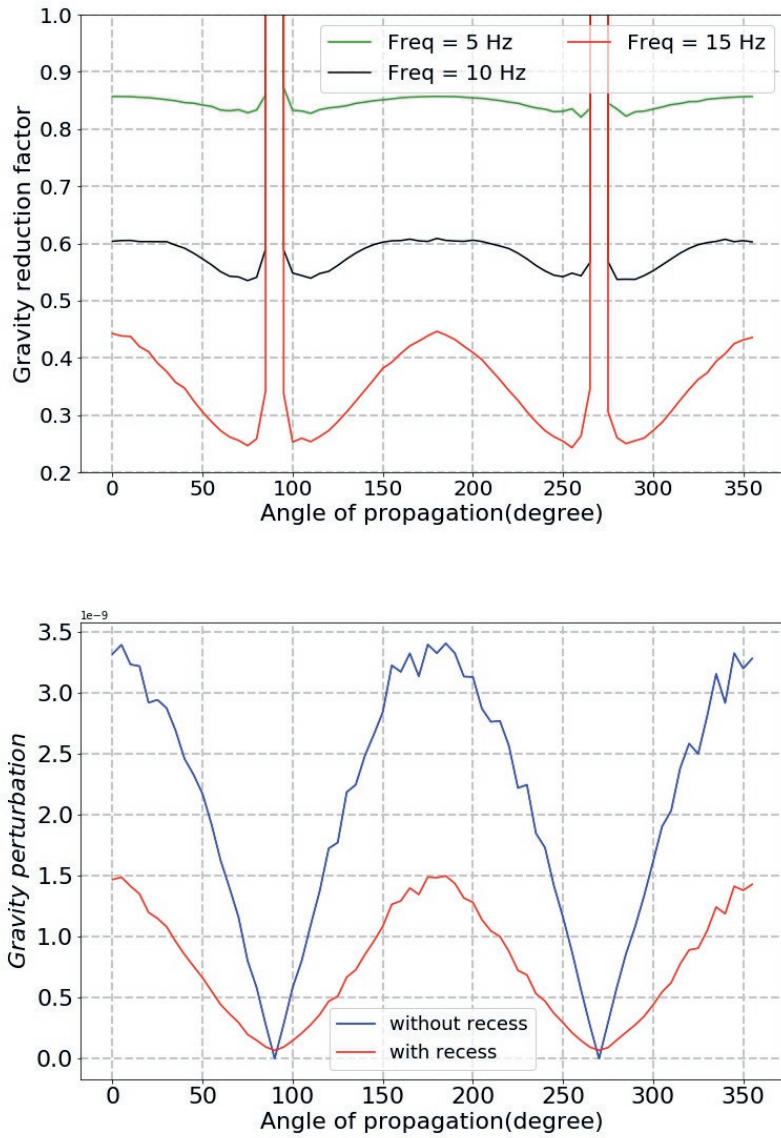
Figure 3.10: (top) Reduction factor vs the direction of propagation of Rayleigh waves for reference frequencies 5, 10, and 15 Hz. (bottom) Gravity perturbation with respect to the angle of propagation for reference frequency 15 Hz.

Chapter 4

Characterization of the seismic field at Virgo and improved estimates of Newtonian-noise suppression by recesses

4

4.1   Introduction

In this chapter, my focus is on conducting a spectral analysis, both spatially and temporally, of the seismic field at the North End Building (NEB) of the Virgo detector. I utilize data obtained from an array consisting of 38 indoor and 11 outdoor sensors, as depicted in figure 4.1. These sensors are $5\,\mathrm{Hz}$ geophones oriented in the vertical direction and are coupled with Innoseis Tremornet readout nodes. My analysis specifically focuses on the data collected from the indoor sensors over a two-week period starting from December 1st, 2019. This chapter relies on the work presented in [200].

The spectral analysis allows us to examine the frequency content of the seismic waves and their propagation characteristics. Specifically, I aimed to determine the direction and speed of seismic wave propagation across different frequencies. This information is crucial for identifying the dominant sources contributing to the seismic field and understanding the behavior of seismic waves in the vicinity of the NEB. We obtain evidence for the scattering of seismic waves and measure the dispersion curve of Rayleigh waves. The latter can be compared with previous results of array measurements carried out outside the buildings between

the two interferometer arms [145].

As we have seen in the previous chapter the presence of the recess in the Virgo detector should result in a significant reduction of Newtonian noise by a factor of at least 2 within the frequency range of 10 Hz to 20 Hz. However, these findings were based on certain assumptions and parameters, including the seismic speed. The seismic speed is a critical parameter for the effect of a recess, which was assumed to be 250 m/s adopting the speed observed at the LIGO sites. In my new analysis presented in this chapter, I revisit the estimation of NN reduction due to the recesses in Virgo. I take into account the observed Rayleigh-wave dispersion, which provides more accurate information about the seismic speed in the specific location of the detector. By incorporating this refined seismic speed value, I have recalculated the recess NN reduction with improved accuracy.
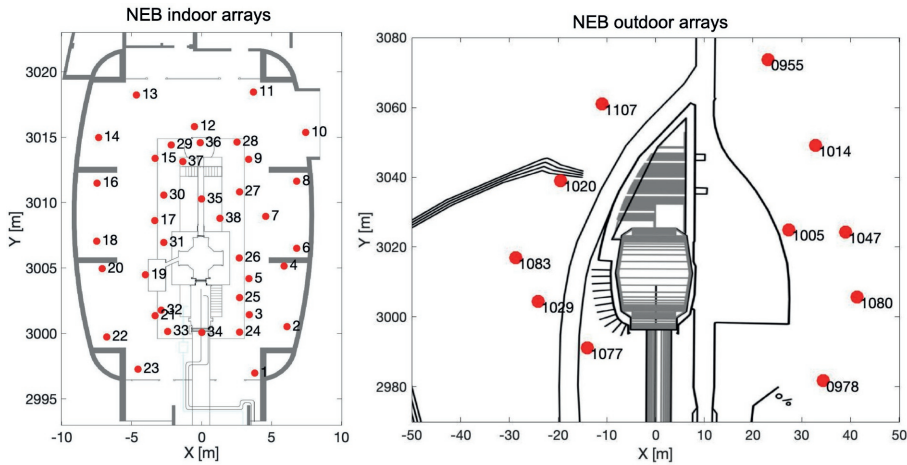
Figure 4.1: Positions of seismometers at the North End building. Left: indoor array. Right: outdoor array.

This chapter is structured as follows. In Section 4.2, I focus on the characterization of the seismic field through spatial spectra, also known as kf-maps. These kf-maps are generated by performing spectral correlations of the data obtained from the seismometer array in the NEB building. I specifically examine kf-maps for three distinct frequencies: 10 Hz, 15 Hz, and 20 Hz. By analyzing these kf-maps, we gain insights into the spatial distribution and characteristics of the seismic field at different frequencies. In Section 4.3, I focus into the reassessment of the

Newtonian noise estimate for the Virgo detector. Firstly, I present the velocity dispersion curve, which is derived from the dominant noise components observed in the kf-maps obtained at various frequencies. This dispersion curve provides valuable information about the propagation characteristics of seismic waves in the vicinity of the NEB. By incorporating the refined seismic speed information, I aim to obtain a more accurate assessment of the NN reduction achieved by the recesses in Virgo. Finally, in section 4.4, I summarize and discuss our findings.

4.2   Characterisation of the seismic field

In this section, I focus on the characterization of the seismic field at the Virgo NEB (North End Building) through an array analysis in wave-vector space ($\vec{k} = (k_x, k_y)$) at different temporal frequencies. The analysis allows us to examine the spatial distribution of seismic signals and identify potential local seismic sources. We consider the data from the Virgo NEB seismometers.

4

To begin, we estimate the cross-spectral density $C(\vec{r}_i, \vec{r}_j, \omega)$ between pairs of seismometers. Here, $\vec{r}_i$ represents the position of seismometer i. This estimation results in an $N \times N$ matrix, where N is the number of seismometers, containing cross-correlations between the seismometer pairs at a specific frequency ω. Based on the cross-spectral density matrix, we calculate a spatial spectrum, denoted as $p(\omega, \vec{k})$, can be written as [149, 116]:

$$p(\omega, \vec{k}) = \sum_{i,j=1}^{N} C(\omega; \vec{r}_i, \vec{r}_j) \, e^{-\vec{k} \cdot (\vec{r}_i - \vec{r}_j)} \tag{4.1}$$

The matrix C is Hermitian, and hence p is real-valued. A Hermitian matrix is equal to its conjugate transpose, indicating that all the elements of the matrix have real values. For our analysis, we calculate such a spectrum for each hour. By performing the analysis on an hourly basis, we can capture the temporal variations and dynamics of the seismic field. The spatial spectrum p is the result of an average over many short-term cross-spectral densities C. By averaging over multiple instances of C, we can obtain a more robust and reliable representation of the seismic field's spatial characteristics. The spatial spectrum $p(\vec{k})$ can be calculated for any frequency, but there is a useful range of spatial frequencies connected to the density of the array and its diameter. The

density of the array refers to the spacing between individual seismometers. With seismometers placed as close as 1 meter to each other and an array diameter of approximately 20 meters along the X direction, our analysis enables the examination of wavenumbers up to 3 rad/m with a resolution of about 0.15 rad/m. This range of spatial frequencies provides valuable information regarding the dominant modes and their directional characteristics within the spectra.
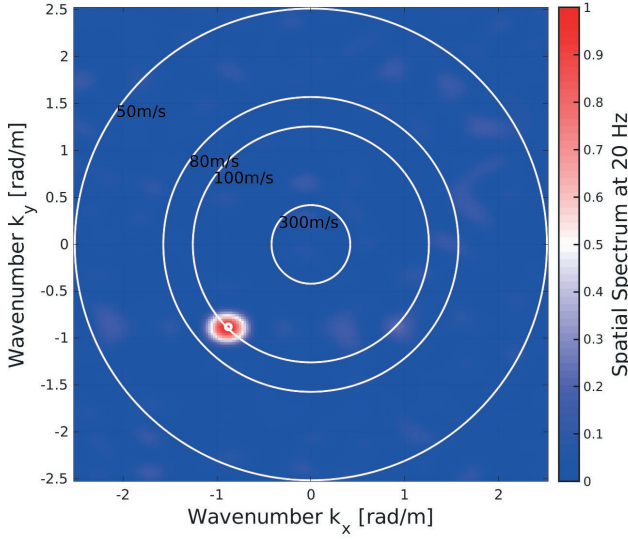
Figure 4.2: Spatial spectrum at 20 Hz obtained from mock data, which contains a sinusoidal wave with the direction and velocity coinciding with the red blob in the plot.

To illustrate the analysis process, we can create mock data consisting of a sinusoidal wavefield with a known velocity and direction. By computing the spectral map, denoted as $p(\omega, \vec{k})$, we can distinguish the injected mode and analyze its properties. Figure 4.2 presents a spectral map generated from mock data, where the sinusoidal wavefield propagates from the direction indicated by the prominent red blob. The velocity of the injected signal is 100 m/s. This example serves as a demonstration of the methodology and its application in distinguishing and characterizing specific modes within the seismic field.

In the first example of a spatial spectrum obtained from NEB seismic arrays, as depicted in figure 4.3 for a frequency of 10 Hz, we observe mul-

tiple modes simultaneously present within the spectrum. These modes are visualized as red blobs, each representing a distinct pattern or behavior in the seismic field. The range of the spectrum is normalized by its maximum value. Normalization allows us to identify the relative strengths or amplitudes of each mode in relation to the maximum amplitude within the spectrum. In addition to the red blobs representing the modes, the plot also includes circles that correspond to a set of phase speeds associated with these modes. The circles serve as a tool for estimating the speeds of the modes through visual inspection. The spatial spectrum depicted in figure 4.3 exhibits significant features at a frequency of 10 Hz. Notably, we observe the presence of two distinct modes, highlighted by the boxed regions, propagating in the same direction. The first mode, characterized by a phase speed of approximately 100 m/s, corresponds to a Rayleigh wave. Rayleigh waves are surface waves that propagate along the boundary between the Earth's crust and the atmosphere. The identification of a mode with a speed of around 100 m/s allows us to classify it as a Rayleigh wave. The second mode in the spectrum displays a phase speed on the order of a few km/s. Body waves are known to exhibit higher velocities compared to surface waves such as Rayleigh waves. Hence, the mode with a phase speed in the km/s range is indicative of a body wave. However, it is important to note that the body wave mode falls near the centre of the spectrum, indicating a range of possible propagation directions. Therefore, based solely on its position of the blobs, we cannot conclude that the body wave mode originates from the same direction as the Rayleigh wave mode.

To determine if the body wave and Rayleigh wave modes originate from the same seismic source, further investigations and analyses are required. These may involve examining their temporal coherence, waveform characteristics, considering geological structures, and studying source mechanisms. To gain a deeper understanding of the temporal behavior and characteristics of the Rayleigh and body wave modes, I have conducted a study on their amplitude variation over time. To accomplish this, I performed calculations of the spatial spectrum $p(\vec{k})$ at a frequency of 10 Hz by averaging data over one-hour intervals, and repeat this for a total of 15 days. I found that the two waves are present continuously, and thus collected the maximum amplitude of the Rayleigh and body waves (associated with the specific direction in the map) for each hour. I show the amplitude variation of the Rayleigh and body waves in figure 4.4. We can observe a similarity in the amplitude variation

4

75
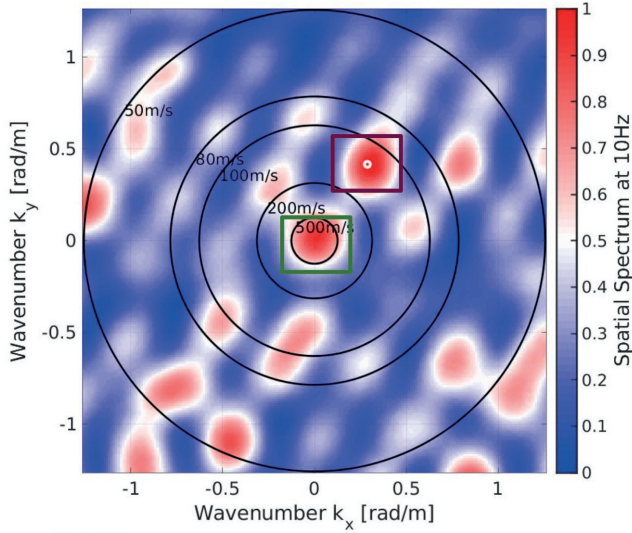
Figure 4.3: Spatial spectrum at 10 Hz obtained from cross-correlations between the seismometers and normalized by the maximum value. The spatial spectrum at 10 Hz captures the presence of multiple modes, with the boxed regions highlighting distinct Rayleigh and body wave modes based on their phase velocity.

patterns of the Rayleigh and body waves. However, it is important to note that a perfect correlation between the amplitudes of Rayleigh and body waves should not be expected, even if they originate from the same source. This is due to the different propagation characteristics of these waves. Furthermore, it is important to consider that other sources in the vicinity may occasionally generate stronger Rayleigh and body waves at 10 Hz, contributing to some differences in their amplitude variation. The magnitude of the body wave is always lower than the Rayleigh wave, which is expected for surface sources. In figure 4.4, the dotted lines represent midnight in local time, providing a reference for the time variations. It is evident that strong disturbances primarily occur during the day, while quieter periods are observed during the night. The location of a highway bridge with respect to the Virgo NEB matches with the direction of observed Rayleigh and body waves. Previous studies investigating the bridge noise have focused on lower frequencies (below 5 Hz) and have identified these waves as frequent transients in spectrograms [98, 146]. Considering the potential origin of these waves from
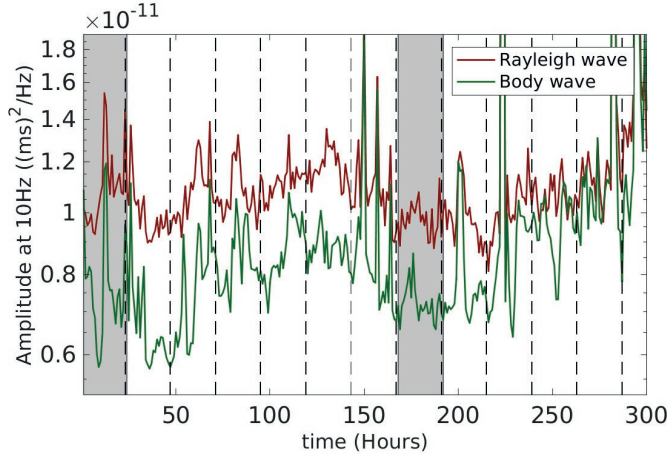
Figure 4.4: Amplitude variation of dominant 10 Hz Rayleigh-wave and body-wave modes w.r.t. time (in hours). Black dotted lines represent midnight in local time. The amplitude of the Rayleigh waves (maroon curve) and the body waves (green curve) are correlated and follow a day-night cycle. The waves tend to arrive with lower amplitude on weekends, here around hours 50 and 200 (grey shaded patch), leading to lower amplitudes in the 10 Hz spectra.

the highway bridge, it is reasonable to expect higher noise levels during the day, coinciding with heavier traffic on the highway.

The positioning of the indoor and outdoor arrays is depicted in figure 4.1. Additionally, figure 4.5 showcases the 3 Hz spatial spectrum of the outdoor array. In this spectrum, we can observe a Rayleigh wave originating from the same direction as the highway bridge. The noise source associated with the bridge is considered local, meaning it originates from or is closely related to the bridge itself. The bridge noise appear as transient signals that are captured in the spectrogram as brief bursts of energy at specific frequencies or frequency ranges. To further analyze the transient trends, we can examine the spectrogram at two distinct time periods: busy time and quiet time. "Busy time" typically refers to a period when there is a high level of activity or noise in the environment which can be associated with peak traffic hours. On the other hand, "quiet time" refers to a period when there is relatively less activity or noise in the environment. This could be during late at night, early morning, or any time when the ambient noise levels are generally lower and there are fewer sources of disturbance. Figure 4.6 displays the
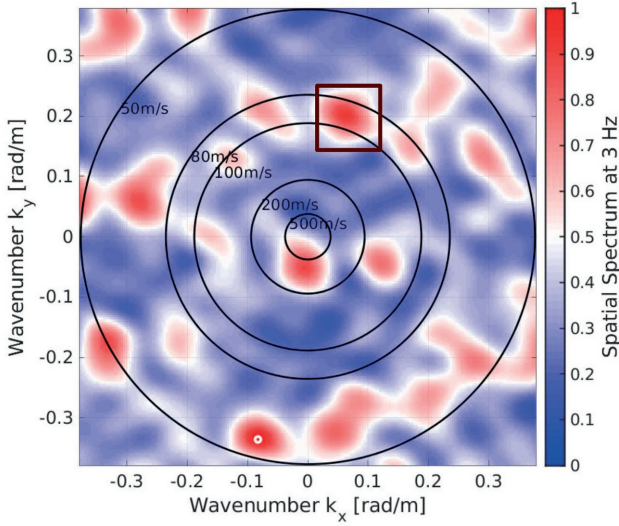
Figure 4.5: Spatial spectrum at 3 Hz drawn from cross-correlations between the 11 outdoor seismometers normalized by the maximum value. The boxed region represents the Rayleigh-wave mode which we have observed already at 10 Hz using the indoor sensors. The white dot in the spectrum corresponds to the maximum amplitude and may arise from aliasing.

spectrogram captured at two distinct time periods: busy time and quiet time. The purpose of this representation is to observe and analyze the transient trends that emerge in the spectrogram during these specific time intervals.

In figure 4.7, the spectral map at 3 Hz is presented for both busy and quiet times. The highlighted box represents a strong Rayleigh wave mode which is absent during the quiet time. The absence of the Rayleigh wave mode during the quiet time suggests that it is likely associated with the source of the noise transients. This observation provides a valuable clue in identifying the source of the noise transients. Consequently, it strengthens the previous findings of past studies that highlight the highway bridge as a significant noise source in the Virgo environment.

In figure 4.8, I present similar plots for frequencies of 15 Hz and 20 Hz. At these frequencies, the spectra become more complex due to the occurrence of aliasing of modes. Aliasing is a phenomenon that arises when fake modes appear in the spectrum as a result of the finite spatial
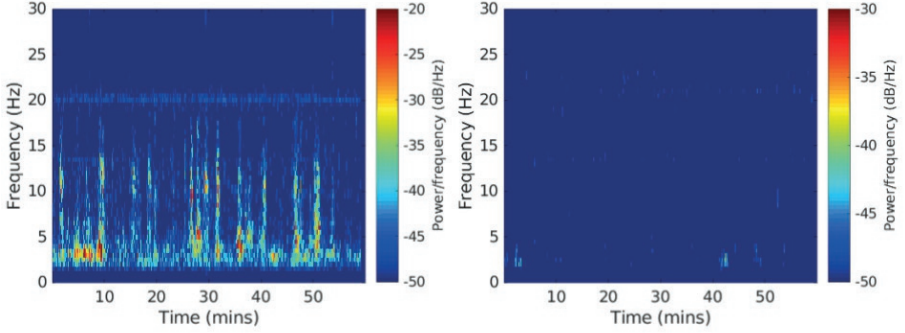
Figure 4.6: Comparison of spectrograms, derived from data collected by a single seismometer, during busy time (left) and quiet time (right). The spectrogram denotes the distribution of energy across frequencies over time. During the night, the presence of transient noise is noticeably diminished or almost absent.
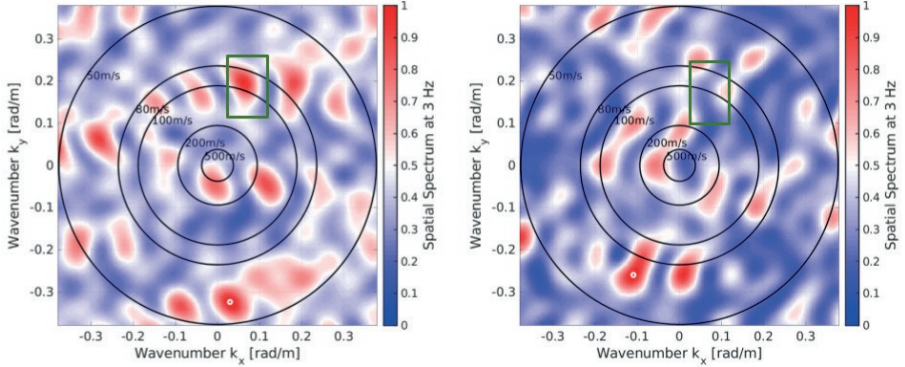
Figure 4.7: Spectral map at 3 Hz obtained from cross-correlations between the 11 outdoor seismometers, normalized by the maximum value. (Left) Busy time or daytime spectral map. (Right) Quiet time or midnight spectral map. The highlighted box indicates the presence of a strong Rayleigh wave mode, observed during the busy time and absent during the quiet time, providing valuable insights into the source of these noise transients shown in figure 4.6.

resolution and bandwidth limitations of the array. The limited spatial resolution of the array and its restricted ability to capture a wide range

of frequencies result in overlapping or distorted modes being erroneously incorporated into the spectrum.
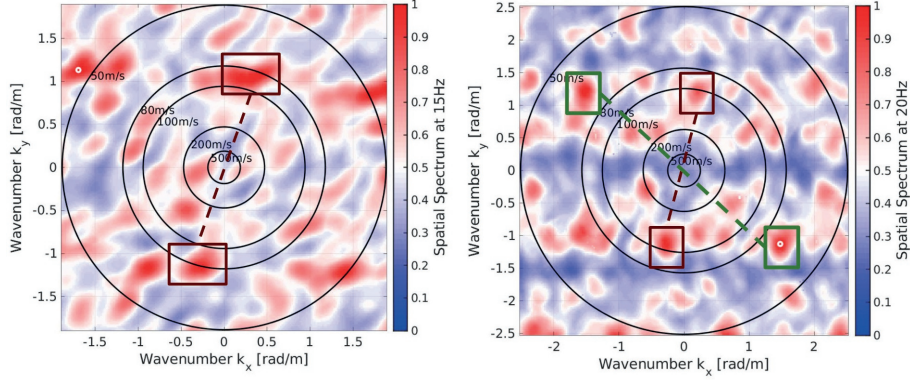
Figure 4.8: Spatial spectra at 15 Hz (left) and 20 Hz (right) normalized by their maximum values. The boxes mark counter-propagating twins, where one is an artifact produced by aliasing.

At 15 Hz, a pair of counter-propagating waves, commonly referred to as a twin, is observed (boxed modes in the left plot). Initially, one might assume that these waves indicate a reflection or the simultaneous presence of seismic sources in opposite directions. However, the properties of the twin are actually consistent with an aliasing effect. As previously mentioned, the largest analyzable wavenumber, limited by the array's spatial resolution, is approximately 3 rad/m. Interestingly, this value aligns closely with the distance between the twin modes observed at 15 Hz. The proximity between the twin modes and the analyzable wavenumber further supports the notion that their appearance is a consequence of the aliasing effect caused by the array's limitations. At 20 Hz shown in the right plot, the aliasing pattern is clearly visible, i.e., identifiable as an artificial pattern in the spatial spectrum. Two twin modes are marked in boxes, and again, the distance between them corresponds roughly to the spectral bandwidth of the array analysis (given by the sensor density).

So, it turns out that Rayleigh waves are so slow at the Virgo site that it is not possible to carry out a good spatial-spectral analysis well above 10 Hz with the NEB array. In order to improve the analysis, one potential solution would be to relocate the sensors closer together. But if sensors would have to be moved closer together, then it would be more
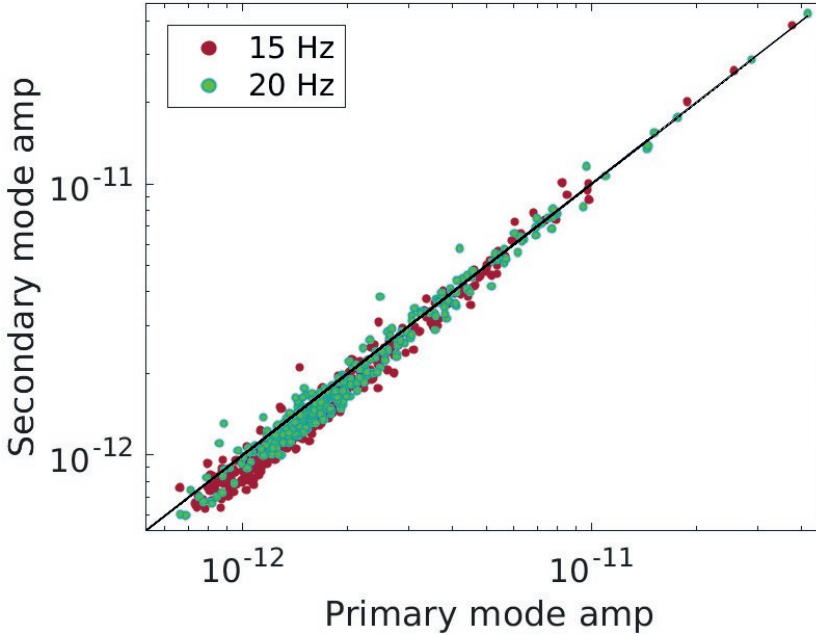
Figure 4.9: Amplitudes of primary and secondary modes shown in figure 4.8. Maroon dotted points represent the amplitude of counter-propagating twins observed at 15 Hz and green dotted points represent the amplitudes of the counter-propagating twins boxed in figure 4.8 at 20 Hz. The solid black line is the straight line of equality (y = x).

difficult to analyze the fast body waves. The larger sensor spacing allows for capturing the broader wavelength range of body waves, ensuring that the signals are not spatially undersampled. The best option would be to add more sensors to increase the sensor density while maintaining the array diameter (and therefore the spatial resolution). For some analyses, though, e.g., to measure the phase speed of a mode, it is possible to simply select one of the two modes of a twin for the analyses since the real wave and its twin alias in the Virgo spatial spectra have the same speeds. However, since the array configuration is irregular, the amplitudes of the aliases are only similar but not the same as of the real waves. Since the dominant modes at 15 Hz and 20 Hz are persistent, one can analyze them over a longer period of time. This longer analysis duration helps compensate for any irregularities in the array configur-

ation and provides more reliable results. Figure 4.9, which shows the comparison of amplitudes for the twin modes, provides valuable insights. The plot demonstrates that the amplitudes of these twin modes are of the same order and exhibit a strong correlation, as indicated by their distribution around the line of equality. It is important to note that the relative amplitudes of the twin modes can be smaller than 1 if the modes selected for analysis do not represent the dominant contribution to the respective spatial spectra. The strong correlation and similarity in amplitudes observed between the twin modes in the plot can be attributed to the phenomenon of aliasing.

A tiltmeter, along with the seismometer array, was deployed at the NEB, providing an additional analysis capability crucial to Newtonian Noise Cancellation (NNC) [69]. The tiltmeter holds a special significance in mitigating NN originating from Rayleigh waves [121]. Rayleigh waves induce tilting of the ground surface as they propagate, leading to variations in the gravitational field that result in NN. By monitoring the ground tilt using a tiltmeter, it becomes possible to quantify and characterize the tilting caused by Rayleigh waves. If a field is composed entirely of plane Rayleigh waves, then the associated NN can be canceled by a single tiltmeter instead of using an array of seismometers. An initial assessment to determine if a field can be roughly characterized as composed of plane Rayleigh waves involves comparing the array-inferred ground tilt with the ground tilt directly measured by a tiltmeter. Limitations of array analyses (aliasing and resolution limits) make the comparison difficult, but a good match between the two was observed at the LIGO Hanford site [116], which is a strong indication that a tiltmeter would be very effective for NNC at Hanford.

To estimate the ground tilt from array data, different approaches and levels of approximation can be employed. I perform this analysis by considering the dominant modes in the spatial spectrum, estimating their wavenumber k and propagation direction ϕ, and then averaging over many estimates. By examining the spatial spectrum of the seismometer array data, I identify the modes that contribute significantly to the overall signal. These dominant modes provide valuable information about the characteristics of the seismic field, including the wavenumber and propagation direction associated with the ground tilt. The power spectral density of the array-inferred ground tilt, denoted as $S_{\tau_x}(\omega)$, can be expressed using the wavenumber k and propagation direction ϕ estimations. It is related to the power spectral density of the seismic field,

denoted as $S_\xi(\omega)$, through the following equation:

$$S_{\tau_x}(\omega) = \langle k^2 \cos^2(\phi) \rangle \, S_\xi(\omega), \tag{4.2}$$

where $S_\xi(\omega)$ is the spectral density of vertical ground displacement $\xi(t)$. The averaging of $k^2 \cos^2(\phi)$ over multiple estimations plays a crucial role in capturing the average behavior of the ground tilt and establishing its relationship with the spectral characteristics of the seismic field.

To determine the value of k for each frequency, I have observed the spectra generated at different frequencies and identified the dominant mode present in each spectral map. Once we have determined the dominant mode in the spectral map for a specific frequency, we can obtain the corresponding coordinates (k_x, k_y) associated with that mode. These coordinates represent the spatial components of the wave vector and provide information about the direction of propagation. As mentioned previously, this analysis involved using a dataset spanning a duration of two weeks. I performed a spectral analysis on each hour of data to generate averaged spectra. I then identified the dominant mode present in the spectra which represent the most significant and prominent feature of the seismic field during that particular one-hour period. Therefore, at the end of the two-week observing time, I compiled a sample of points that corresponds to the dominant modes observed in the spectra. Thereby, I calculate the most probable value of the velocity corresponding to each frequency in the spectra by analyzing the collected data points and determine the velocity value that occurs with the highest frequency or likelihood. The velocity dispersion plot, shown in figure 4.10, serves as a visual representation of the relationship between frequency and velocity. The plot includes blue dots, which represent the data points obtained from the analysis, and a black curve, which represents a fitted curve that captures the overall trend of the data. The red-shaded region on the plot indicates frequencies that lie outside the array bandwidth. These frequencies correspond to seismic waves with wavelengths that are too long to be effectively analyzed by the array. The array's spatial resolution and limitations in capturing long-wavelength waves may restrict accurate estimation of Rayleigh wave properties at such frequencies.

To estimate the propagation direction of Rayleigh waves from the wavenumbers k_x and k_y, we can use the following relationship:

$$\phi = \arctan\left(\frac{k_y}{k_x}\right) \tag{4.3}$$
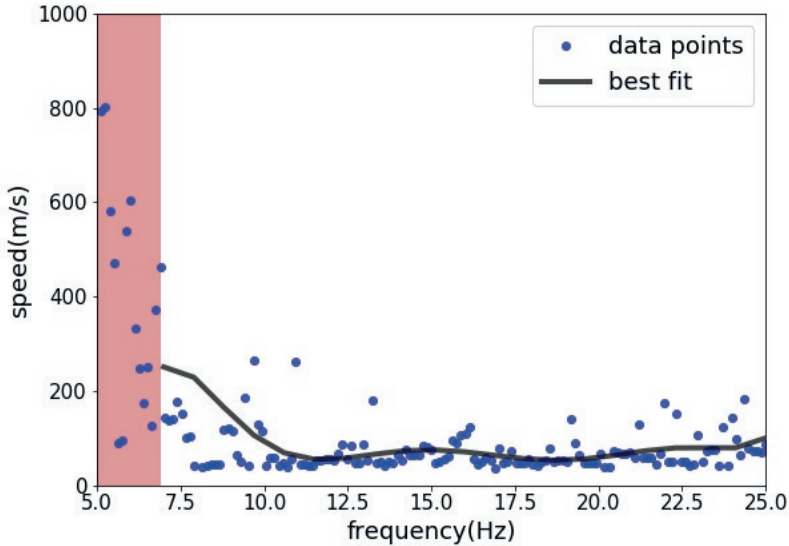
Figure 4.10: Rayleigh dispersion plot showing an average speed versus frequency. Blue dots represent the data points; the black curve is a fit to the data. The red-shaded region marks frequencies outside the array bandwidth (seismic waves are too long to be analyzed).

By analyzing the dominant mode in the spectra obtained from each hour of data, I was able to estimate the corresponding propagation direction. The results of these estimations have been presented in figure 4.11. The figure shows a propagation azimuth histogram, representing the distribution of propagation azimuths for the dominant modes. The radial axis in the histogram represents the range of frequencies or spectral components of the seismic waves. By observing this histogram, we can identify directional characteristics of the seismic wave propagation for each frequency component. The reddish color in the histogram indicates the directions with a high probability of occurrence. The observed scattering of the dominant mode's propagation direction at Virgo indicates a high level of variability in the seismic field, highlighting the complexity of the site compared to LIGO Hanford [125].

By utilizing the estimated values of k and ϕ, I performed calculations to obtain the tilt spectra, as depicted in figure 4.12. The plot shows the spectrum of estimated ground tilt (represented by the blue dotted
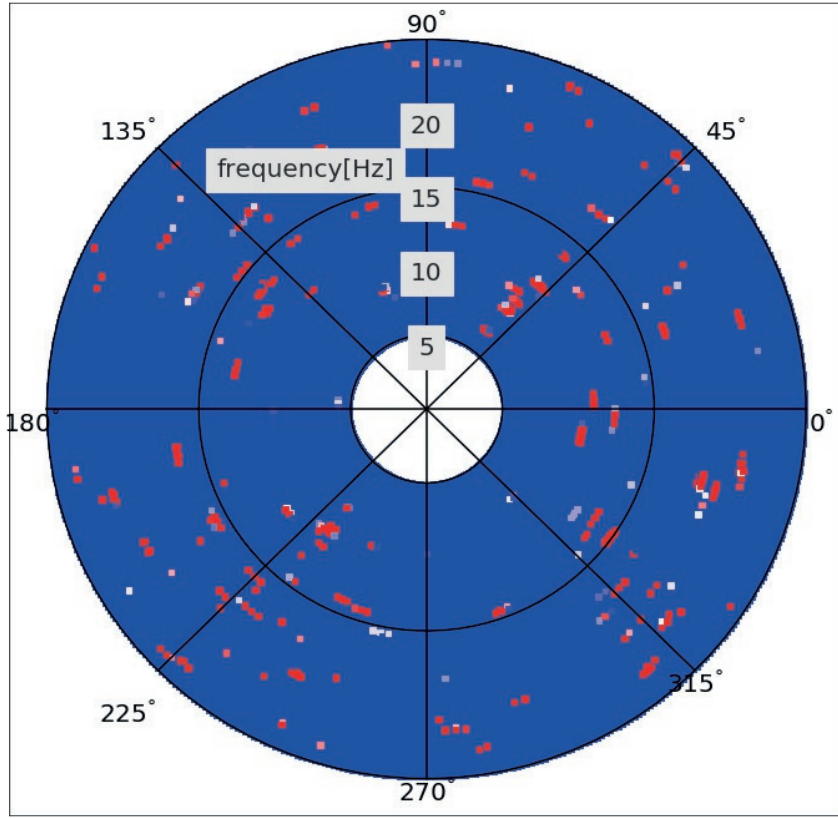
Figure 4.11: The direction of sources, estimated from the k-map special analysis assuming dominating mode (having maximum amplitude) for each frequencies (radial axis) between 5 to 25 Hz).

trace) and the spectrum obtained directly from the ground tiltmeter data (depicted by the orange solid trace). The blue-shaded region in the plot represents the uncertainty or error range associated with the velocity estimation.

The overall level is similar, and one might conclude the match around 15 Hz is good, indicating the presence of plane Rayleigh waves in this frequency band. However, at frequencies of 20 Hz and higher, there is a noticeable mismatch between the array-inferred ground tilt and the measured ground tilt from the tiltmeter. There could be several explanations for the discrepancy observed at higher frequencies. One possibility is that the reflection of waves from the recesses in the surrounding envir-
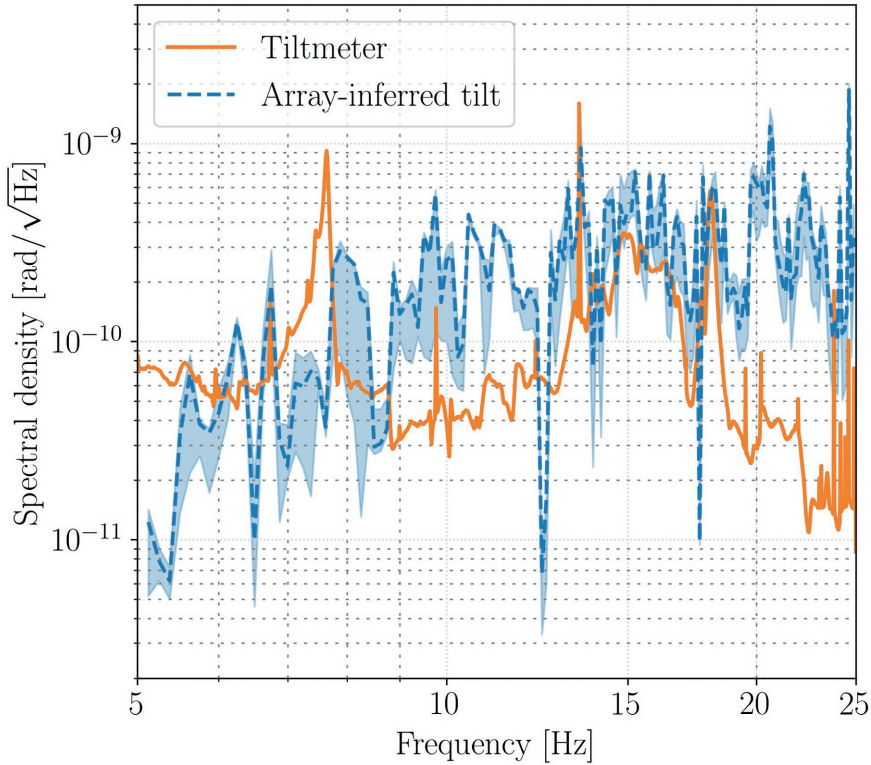
Figure 4.12: The plot shows the estimated ground tilt spectra (blue dotted trace) and the spectra directly estimated from ground tiltmeter data (orange solid trace). The blue-shaded region occurs due to an error limit in the estimation of velocity.

onment could introduce biases in the array analysis. When seismic waves encounter irregularities or features such as recesses, reflections can occur, leading to complicated wave behavior and potential inaccuracies in the analysis. Another possible reason could be the presence of excess seismic noise from nearby sources that may not be captured by the tiltmeter but affect some of the seismometers contributing to the array analysis. Indeed, there could be various other explanations. Furthermore, at low frequencies, it is expected to have a mismatch because the accurate estimation of ground tilt using the array method relies on an estimation of seismic speeds, which, as indicated by the dispersion results, are already known to be inaccurate. The inaccuracies in estimating seismic speeds

can be attributed to various factors, including the complex nature of the seismic field, limitations in the array configuration (such as irregular sensor spacing), the presence of aliasing effects, the internal noise of the sensor, etc. Additionally, it should be noted that our analysis focused solely on the dominant mode in the spectra, neglecting the contribution of sub-dominant modes that may also be present. This might lead to underestimation or overestimation of the true velocities, affecting the overall accuracy of the dispersion result. However, the inclusion of sub-dominant modes in the analysis introduces additional complexities and uncertainties, such as mode coupling or interference, which can make the estimation more challenging.

4.3 Virgo Newtonian noise reassessment

In the context of Virgo Newtonian noise reassessment, the array analysis I have discussed so far provides valuable insights into the seismic field, including its sources, anisotropy, types of waves, and their velocities. Typically, these properties lead to mild corrections (by factors < 2) of NN estimates, but at Virgo, the situation is different. At Virgo, the presence of clean rooms under the test masses introduces a significant dependence of NN on the propagation directions of seismic waves, as seen in the previous chapter. Additionally, the seismic wave speed plays a crucial role in determining the level of NN suppression, as it affects the ratio of recess dimensions to seismic wavelengths. For this reason, recesses are ineffective in environments where seismic waves are fast (e.g., underground), and generally, they are more effective at higher frequencies. With clean rooms under test masses at the Virgo site, we should expect the gravitational coupling between seismic fields and test masses to be lower than, for example, at the LIGO sites. I previously estimated the suppression of Newtonian noise at Virgo by assuming a frequency-independent speed of Rayleigh waves at 250 m/s, which was a reasonable choice based on observations at the LIGO sites. However, the array analysis presented in this chapter, provides new insights into the actual speed of Rayleigh waves at the Virgo site. We have found that the speed of Rayleigh waves at Virgo is significantly lower than our previous assumption of 250 m/s. By incorporating the updated seismic speed information into our assessment of NN suppression, we can refine our calculations and improve the accuracy of our predictions. The lower speed of Rayleigh waves at Virgo, as revealed by the array analysis,
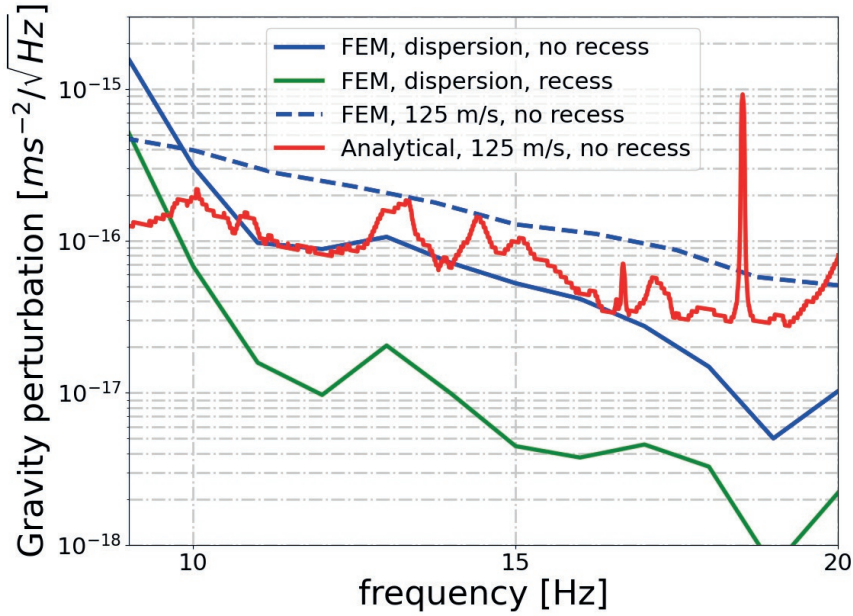
Figure 4.13: Comparison of NN predictions. The solid blue and green spectra are based on the finite-element simulation without and with recess, respectively, and using the observed Rayleigh-wave dispersion. The dashed spectrum is the result of a finite-element simulation without recess and constant speed. Finally, the red spectrum is an analytical estimate without recess for comparison.

suggests that the NN suppression may be more pronounced than initially estimated. This is due to the fact that the ratio of recess dimensions to seismic wavelengths determines the effectiveness of NN suppression, and with lower seismic speeds, the wavelengths become shorter, increasing the potential for suppression. In this section, I focus on the analysis of the Newtonian noise reduction achieved through the recess structure at the Virgo site, taking into account the estimated seismic speed obtained previously. The seismic speed information is depicted in figure 4.10, which presents the dispersion curve indicating the variation of seismic speed with frequency.

For the first set of results, the assumption is that the seismic field is isotropic. Simulations are carried out with and without recess, and either using the observed wave dispersion or assuming a frequency-independent speed of 125 m/s. The finite-element simulation is done by propagating

plane Rayleigh waves through the model, which means, as explained in detail in our previous chapter that a possible effect of waves being reflected from the clean room is neglected. This might lead to significant errors in our NN estimates close to and above 20 Hz. The results of the simulations are summarized in figure 4.13. We see that the green curve, which is the more realistic prediction using the finite-element simulation with recess and the observed wave dispersion, lies up to a factor 10 below the blue curve, which is the result of an analogous simulation without recess. I also point out that the analytical estimate for a flat surface deviates significantly from the dashed curve at lower frequencies, which is explained by the finite size of the model. This effect is worse when waves are longer. The NN estimate based on the slow observed Rayleigh-wave speed is accurate down to 10 Hz.

The analysis of different test masses' Newtonian noise levels is presented in figure 4.14. The blue color indicates the strain noise for each test mass under the assumption of a flat surface. The colored spectra represent the NN estimates considering the dimensions of the cleanrooms and incorporating the estimated velocity dispersion curve.

To assess the noise reduction achieved, figure 4.15 displays the reduction factors for both the input and end test masses. The measurement of seismic speed was performed only at the NEB (North End Building) of the Virgo site. This means that we have direct information about the seismic speed in that specific location. However, in order to estimate the noise reduction at the other two buildings (West End Building and Central Building), where the seismic speed was not directly measured, we make the assumption that the dispersion curve, which describes how the seismic speed varies with frequency, is the same across the entire Virgo site. A comparison is made with the previous chapter 3, where a frequency-independent speed of 250 m/s was chosen (represented by the olive green curve). The results highlight the significant changes observed between the two studies. It makes it clear how much results have changed between the two studies. Reduction factors are different for input test masses, and end test masses since the recess has a different geometry at Virgo's central building. A larger reduction is observed in the end buildings.

The incorporation of seismic dispersion in the estimation of Newtonian noise reduction has indeed led to a greater reduction compared to the previous estimation. The NN spectra, shown in figure 4.16, provide a comprehensive view of the predicted noise levels. The blue spectrum,
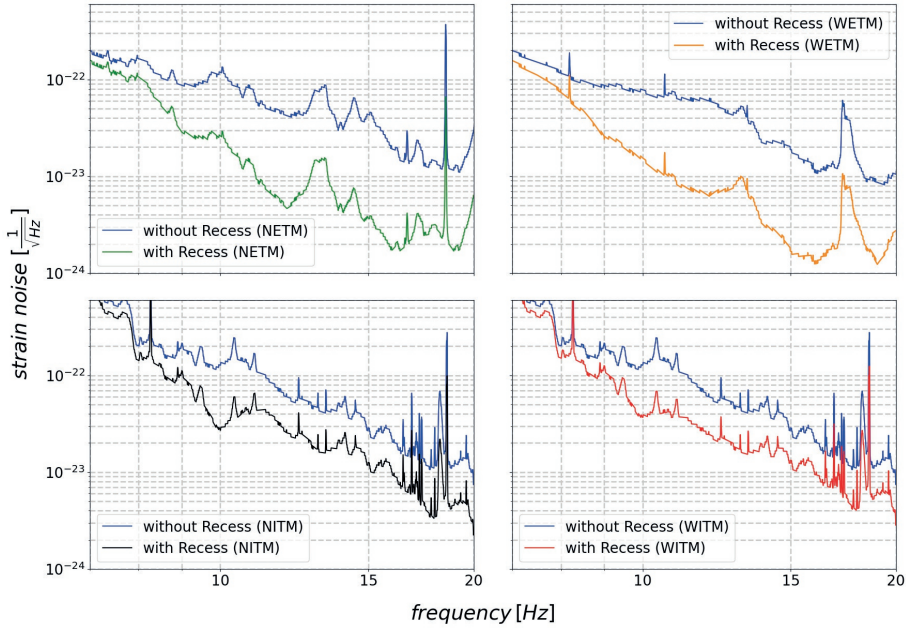
Figure 4.14: (upper left) NN spectra for North end test mirror (Vertical displacement along North). (upper right) NN spectra for West end test mirror (Vertical displacement along West). (lower left) NN spectra for North input test mass (Vertical displacement of NITM along north). (lower right) NN spectra for West input test mass (Vertical displacement of WITM along West). For each sub-plots, the blue trace represents the spectra without recess and other traces represents the spectra for the existence of recess under the corresponding test mirror. Here we have considered the velocity of Rayleigh waves from the estimated dispersion.

computed for a flat surface, serves as a reference to highlight the impact of the recesses inside Virgo buildings. Based on the spectra, it is predicted that the seismic NN will generally lie below the sensitivity targets of the next two observation runs, O4 and O5, with the exception of a few peaks in the spectrum. However, during O5, the predicted reduction factor may be modest, indicating that further optimization may be required to achieve the desired noise reduction levels. These results have important consequences for the Newtonian Noise Cancellation system. According to the findings, the NNC system might only need to provide a minor additional noise reduction, as the seismic NN is already expected to be below the sensitivity targets for most frequencies. To validate and
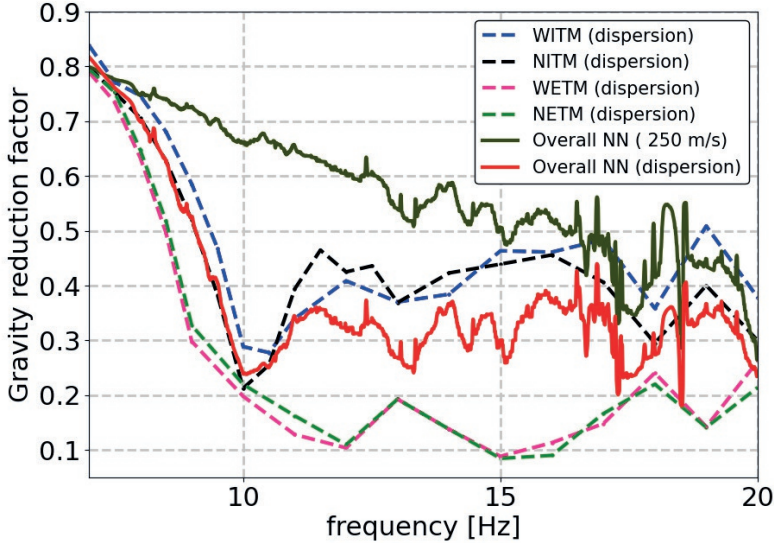
Figure 4.15: Newtonian-noise reduction from a previous study with a seismic speed of 250 m/s (olive green) compared to the new results using the measured dispersion curve (red). Reduction factors for each test mass are shown as dashed curves. Here, ITM, ETM mean input and end test mass. The letters W, N stand for West and North arm.

verify these findings, it will be necessary to conduct speed measurements at Virgo's West End Building and Central Building. These measurements will provide important information to corroborate the estimated seismic dispersion and further refine the predictions of NN reduction. The verification of these findings will contribute to the optimization and fine-tuning of the Virgo detector's performance in preparation for the upcoming observation runs.

4.4 Summary and outlook

In summary, my analysis of seismic array data at Virgo's North End Building has provided valuable insights into the Newtonian noise characteristics and the effectiveness of recess structures in reducing NN. Based on spatial spectra of the field, I measured the dispersion of Rayleigh waves, which I used to update previous Newtonian-noise predictions
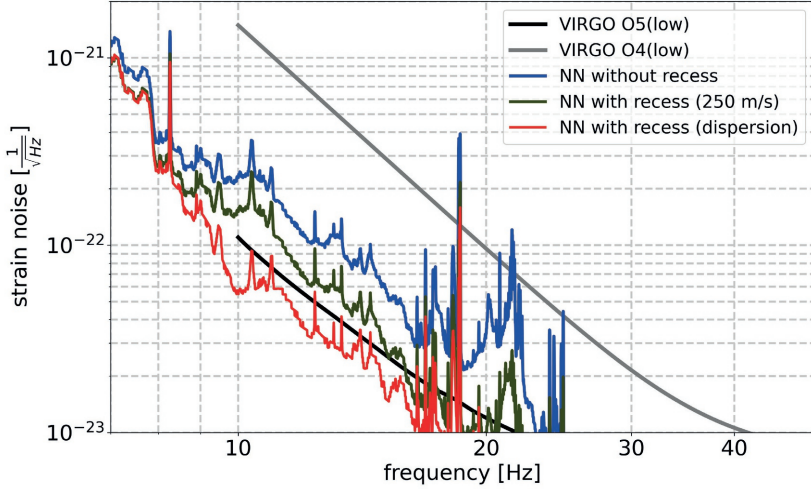
Figure 4.16: Comparing of Virgo NN estimates summing contributions from all four test masses. For reference, we have also included the Virgo sensitivity models for the two upcoming observation runs, O4 and O5 [12]. The blue curve represents the NN for a flat surface. Estimates including the recess are shown for a constant velocity of $250\,\mathrm{m/s}$ (green) and including the estimated Rayleigh-wave dispersion (red).

for Virgo. The updated NN predictions incorporating the observed Rayleigh-wave dispersion suggest that the seismic NN will generally lie below the sensitivity targets of the next two observation runs (O4 and O5) at Virgo. However, there may be a few peaks in the NN spectra that exceed the target levels, indicating the need for further optimization and mitigation strategies. This suggests that the clean rooms located beneath the Virgo test masses play a crucial role in reducing NN, offering a significant advantage in terms of overall detector performance. Specifically, I observed a reduction in NN by a factor of up to 10, highlighting the effectiveness of the Virgo architecture in suppressing this noise source.

In addition to my analysis of seismic array data and NN predictions, I also conducted an estimation of ground tilt using the array data. To validate my estimates, I compared them with the measurements obtained from a tiltmeter positioned at the NEB. We observed a notable mismatch between the estimated ground tilt from the array data and the

measurements recorded by the tiltmeter. This mismatch suggests that the seismic field at the Virgo site is not well characterized by a simple plane Rayleigh-wave model, which is a crucial assumption for tiltmeters to effectively cancel out NN. The presence of clean rooms beneath the Virgo test masses may play a significant role in this mismatch. Roughly above 15 Hz, we speculate that the clean rooms could induce substantial scattering of seismic waves, which would further complicate the representation of the seismic field. Consequently, the scattering effect potentially reduces the effectiveness of tiltmeters in canceling out NN. These findings highlight the importance of considering the complex behavior of the seismic field and its interactions with the detector infrastructure when evaluating the effectiveness of NN cancellation techniques. Further investigations are necessary to better understand the scattering phenomena induced by the clean rooms and to develop appropriate strategies for mitigating their impact on tilt measurements and NN reduction efforts.

This study suggests that the construction of recesses beneath and around the test masses can be an effective method for reducing NN. However, implementing recesses as an upgrade to existing detectors poses significant challenges due to the invasive nature of the operation and the need to modify the mounting of vacuum chambers and pipes to the ground. On the other hand, recesses can be a promising technique to consider at new detector sites. However, it is crucial to evaluate the seismic speeds in advance to accurately predict the effectiveness of recesses for NN suppression. The efficiency of recesses decreases at lower frequencies and higher seismic speeds, which limits their effectiveness in certain scenarios. In particular, for the proposed underground infrastructure of the Einstein Telescope, recesses will not be as effective in mitigating NN due to the combination of lower frequencies and potentially higher seismic speeds at that site. Therefore, alternative approaches and strategies would need to be explored to achieve the desired level of NN reduction at such locations. Overall, the construction of recesses as a means of NN suppression requires careful consideration of the specific site characteristics, seismic speeds, and frequency ranges involved to determine its feasibility and effectiveness.

Chapter 5

Scientific significance and figures of merit for third-generation gravitational wave detectors

The currently operational advanced detectors, Advanced LIGO and Advanced Virgo, have successfully detected a large number of compact binaries, including their mergers with black holes and neutron stars [17, 22, 21], in three observing runs [23, 172]. The landmark first detection of gravitational waves by both LIGO detectors (LIGO Hanford and Livingston) in 2015, together with the groundbreaking multi-messenger detection of electromagnetic and gravitational waves from colliding neutron stars in the GW170817 event, have led to discoveries in astrophysics and cosmology [79, 201, 212]. However, despite these remarkable achievements, the signal strengths of most detections are not sufficient to compensate for various limiting noises to extract more information from the data. As a result, only a few events with sufficiently high signal-to-noise ratios contribute to the precise evaluation of gravitational wave parameters. These parameters include the masses of the binary components (e.g. black holes or neutron stars), their spins, the distance to the source, the sky localisation, the orbital parameters (e.g. eccentricity and inclination), the redshift of the sources, and so on.

Indeed, the current generation of gravitational wave detectors has demonstrated the ability to reach distances of up to about 150 megaparsecs (Mpc) for a standard binary neutron star system with component

masses of 1.4 solar masses ($M_{\odot}$) in the frequency range from 10 Hz to several kilohertz. Third-generation gravitational wave detectors such as the Einstein Telescope and the Cosmic Explorer aim to achieve sensitivities at least ten times better than the current generation of detectors [8, 114, 49]. In addition, the Einstein telescope is designed to observe sources down to frequencies of 3 Hz. The increased sensitivity and broader frequency range of the third-generation detectors will have a profound impact on several scientific observations, including:

1. The detection of intermediate-mass binary black hole systems: These systems, with masses between stellar-mass black holes and super-massive black holes, are of great importance for our understanding of black hole formation, galaxy evolution, gravitational wave astronomy, cosmology and fundamental physics [33, 15].

2. Determining the equation of state (EOS) of dense matter, particularly in neutron stars, is a complex and important area of research in astrophysics [71, 89]. The EOS describes the relationship between the pressure, density and composition of matter under extreme conditions, such as those found in the core of neutron stars.

3. Continuous sources of gravitational waves, such as radio pulsars, provide an excellent opportunity to probe the EOS. The study of the early universe and its evolution involves investigating the conditions and processes that occurred shortly after the Big Bang, and tracing the subsequent evolution of the universe over billions of years [152].

4. It will allow us to measure two independent polarisation states of gravitational waves and test Einstein's theory of general relativity [197, 213, 151].

With the anticipated high detection rate of binary systems by the Einstein Telescope and Cosmic Explorer, we will have a great opportunity to accurately measure the absolute and apparent luminosity distance of these systems. This will provide valuable information about the object's distance and the rate of cosmic expansion at the time the light was emitted. The higher range of the detectors will allow us to investigate the equation of state of dark matter at different redshifts.

Additionally, ET and CE may be able to probe the stochastic background of cosmological origin, including phenomena such as inflation, phase transitions, and cosmic strings. In their work [188], Sachdev et al. conducted a study on the capabilities of the network of third-generation detectors in resolving primordial gravitational wave backgrounds originating from binary neutron star or binary black hole systems. Their

findings indicate that the population of binary black holes can be fully resolved by these detectors. However, the residual background from this population has a negligible effect on the raw sensitivity to stochastic backgrounds. On the other hand, the residual background from BNS sources can dominate over the BBH background and impose limitations on the sensitivity in the search for primordial backgrounds. The Einstein Telescope and the Cosmic Explorer has the potential to unveil the characteristics of compact binary systems and assess their properties by observing a vast number of coalescing binaries and accurately estimating their parameters. By studying millions of coalescing binaries, ET and CE can gather statistical information about their properties, such as their masses, spins, and orbital characteristics. This extensive dataset allows for a comprehensive understanding of the population's distribution and behavior. By comparing the observed population with theoretical models, ET and CE can further refine our understanding of the processes involved in the formation and evolution of compact binary systems.

5.1 Einstein Telescope

The Einstein Telescope is planned to be constructed at a significant depth of approximately 200 to 300 meters underground. This underground location offers isolation from surface seismic activity, ensuring a stable environment for precise gravitational wave measurements. The ET design incorporates three nested detectors, with their arms aligned in the shape of an equilateral triangle. Figure 5.1 provides a visual representation of this configuration. Each side of the triangle will be shared by two detectors, and the length of each arm will span 10 kilometers. Each detector within the Einstein Telescope will adopt a dual recycled Fabry-Perot Xylophone Michelson configuration. This configuration consists of two types of interferometers: low-frequency interferometers and high-frequency interferometers. The Xylophone structure refers to the combination of these two types of interferometers within each detector [131].

The low-frequency interferometer of the Einstein Telescope is designed to operate at a cryogenic temperature of approximately $10\,\mathrm{K}$. This cryogenic temperature helps minimize thermal noise and improve the sensitivity of the detector. The target frequency range for the low-frequency interferometer starts from $3\,\mathrm{Hz}$ and extends up to ap-

proximately 30 Hz. To reduce quantum radiation pressure noise, the low-frequency interferometer will utilize a low power of approximately 18 kW in its arms, which is lower than the initial LIGO setup. The low-frequency interferometer of the Einstein Telescope will incorporate a range of advanced features to enhance its performance and sensitivity. These include 10 dB frequency-dependent squeezing, four 211 kg mirrors, advanced seismic isolation systems, gravity gradient noise subtraction techniques, and cryogenically cooled silicon test masses to reduce thermal noise [25, 34].

On the other hand, the high-frequency interferometer of the Einstein Telescope will be specifically designed to operate within the frequency range of 30 Hz to 10 kHz. It will operate at room temperature and utilize similar technology as the Advanced LIGO and Advanced Virgo detectors. It will have fused silica mirrors of 60 cm in diameter, weighing 200 kg. It will employ the standard dual-recycled Fabry-Perot Michelson configuration. The system will incorporate tuned signal recycling, featuring 3 MW of arm circulating power and 10 dB frequency-dependent squeezing injection to mitigate quantum shot noise. The combination of high power and wide beam size effectively reduces both photon counting (shot) noise and mirror thermal noise, thereby enhancing the interferometer's overall sensitivity to gravitational wave signals. The Xylophone design of each detector in the Einstein Telescope offers an elegant solution for effectively reducing both radiation pressure noise and shot noise. This is achieved by utilizing two separate interferometers operating at distinct arm circulating power settings, which would not be feasible in a single interferometer configuration. Figure 5.2 illustrates the sensitivity of the low-frequency and high-frequency interferometers of the Einstein Telescope, as well as the overall combined sensitivity achieved by the Xylophone design. Furthermore, the triangular arrangement of the Einstein Telescope provides the added advantage of equal sensitivity to both polarizations of the gravitational wave signal. This is in contrast to the currently operating L-shaped detectors, which are more sensitive to one polarization than the other.
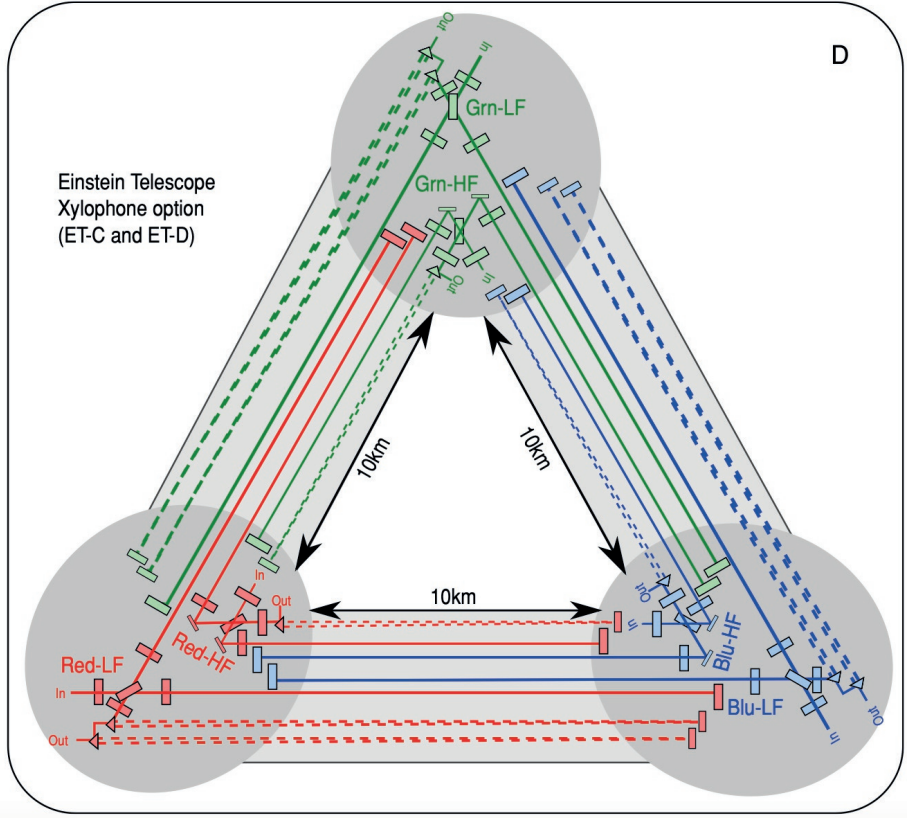
Figure 5.1: Simplified schematic of the ET design [130]

5.2 On combining the data-streams of the low-frequency and high-frequency interferometers in the ET xylophone configuration

Building upon the previous discussion, let's explore the combination of data from the low-frequency and high-frequency interferometers of the Einstein Telescope in order to optimize the overall sensitivity across all frequencies. Let's assume that the data from the low-frequency inter-ferometer is denoted as $d^{LF}(t)$, which consists of the gravitational wave signal $h(t)$ and the corresponding noise $n^{LF}(t)$. Similarly, the data from
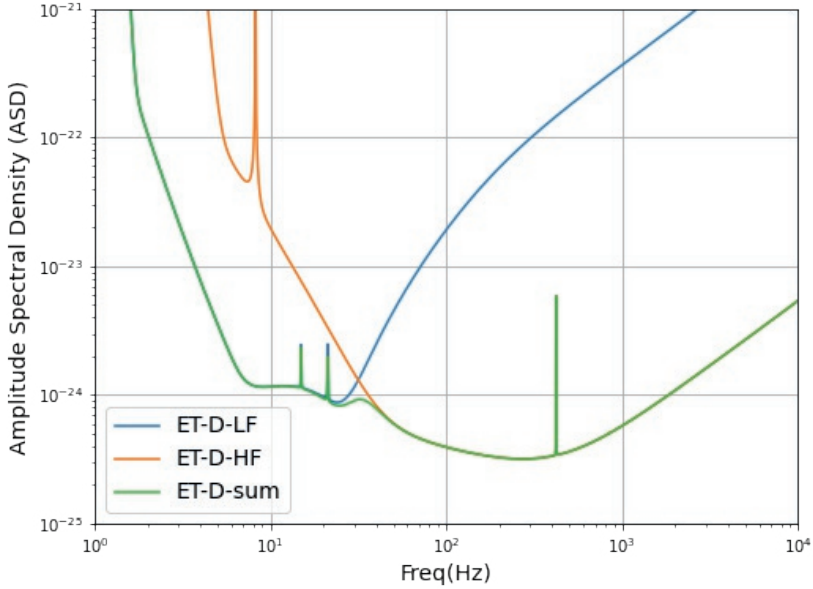
Figure 5.2: The modeled sensitivity of the low-frequency (ET-LF) and the high-frequency (ET-HF) interferometers as well as the combined sensitivity of the xylophone detector, obtained by the optimal combination of the ET-LF and ET-HF sensitivities. Further information about the ET-D sensitivity curve can be found in [130].

the high-frequency interferometer is represented as $d^{HF}(t)$. Hence,

$$
\begin{aligned}
d^{LF}(t) &= h(t) + n^{LF}(t) \\
d^{HF}(t) &= h(t) + n^{HF}(t).
\end{aligned}
\tag{5.1}
$$

In the Fourier domain, we have the expressions for the low-frequency (LF) and high-frequency (HF) data as:

$$
\begin{aligned}
d^{LF}(f) &= h(f) + n^{LF}(f) \\
d^{HF}(f) &= h(f) + n^{HF}(f).
\end{aligned}
\tag{5.2}
$$

To combine the data from the LF and HF interferometers, we introduce a filter function $\alpha(f)$, which determines the weighting of the LF

and HF data in the combined data. The combined data $d^{com}(f)$ can be expressed as:

$$
\begin{aligned}
d^{com}(f) &= \alpha(f)\, d^{LF}(f) + (1 - \alpha(f))d^{HF}(f) \\
&= h(f) + \alpha(f)\, n^{LF}(f) + (1 - \alpha(f))n^{HF}(f),
\end{aligned}
\tag{5.3}
$$

where $\alpha(f)$ represents the coefficient that determines the contribution of the LF and HF data at each frequency. The goal is to find the optimal value of $\alpha(f)$ that minimizes the variance of the combined data. By minimizing the variance, we can determine the optimal coefficient $\alpha(f)$ that minimizes the noise in the combined data. The specific value of $\alpha(f)$ depends on the power spectral densities of the LF and HF noise. The optimal $\alpha(f)$ is chosen to balance the contributions from the LF and HF data in a way that minimizes the overall noise.

$$
\begin{aligned}
\mathrm{Var}[d^{com}] &= \langle (d - \langle d \rangle) | (d - \langle d \rangle) \rangle \\
&= \alpha(\langle h|n^{LF}\rangle + \langle n^{LF}|h\rangle) + (1 - \alpha)(\langle h|n^{HF}\rangle + \langle n^{HF}|h\rangle) \\
&\quad + \alpha(1 - \alpha)(\langle n^{LF}|n^{HF}\rangle + \langle n^{HF}|n^{LF}\rangle) + \alpha^2\langle n^{LF}|n^{LF}\rangle + \\
&\quad (1 - \alpha)^2\langle n^{HF}|n^{HF}\rangle.
\end{aligned}
\tag{5.4}
$$

Here we define the inner product as $\langle A|B \rangle = \int df\, A^*(f)\, B(f)$. We assume that the noise from the high-frequency and low-frequency interferometers is uncorrelated and follows a zero-mean Gaussian distribution. Consequently, we can ignore all the cross terms in the equation 5.4, leading to the simplified expression:

$$
\begin{aligned}
\mathrm{Var}[d^{com}] &= \alpha^2\langle n^{LF}|n^{LF}\rangle + (1 - \alpha)^2\langle n^{HF}|n^{HF}\rangle \\
&= \int [\alpha(f)^2\, S_n^{LF}(f) + (1 - \alpha(f))^2 S_n^{HF}(f)]df
\end{aligned}
\tag{5.5}
$$

In the context of the expression, $S_n^{LF}(f)$ and $S_n^{HF}(f)$ represent the power spectral densities of the low and high-frequency interferometer noise, respectively. By Fourier transforming the autocorrelation function, we obtain the power spectral density, which provides information about the power distribution of the noise in the frequency domain. In the frequency domain, we have the relationship:

$$
\frac{1}{2} S_n(f) = \int_{-\infty}^{+\infty} \langle n(t + \tau)\, n(t) \rangle\, e^{i\pi f \tau}\, d\tau,
\tag{5.6}
$$

where $\frac{1}{2}S_n(f)$ represents the one-sided power spectral density of the noise. This equation relates the power spectral density to the autocorrelation of the noise signal. Here angle brackets $\langle ... \rangle$ denote an ensemble average over many noise realisations

Additionally, in the frequency domain, we can express the relationship between the power spectral density and the inner product of the noise signals as:

$$\frac{1}{2}\delta(f - f')\,S_n(f) = \langle \tilde{n}(f)\,\tilde{n}^*(f')\rangle, \tag{5.7}$$

where $\delta(f - f')$ represents the Dirac delta function. This equation shows that the inner product of the complex conjugate of the noise signal at frequency f with the noise signal at frequency f' is proportional to the one-sided power spectral density.

To determine the optimal coefficient α and minimize the variance of the noise time series, we can set the derivative of the variance $\mathrm{Var}[d^{com}]$ with respect to α to zero:

$$\frac{d\,\mathrm{Var}[d^{com}]}{d\,\alpha} = 0. \tag{5.8}$$

Using the equations for $\alpha(f)$ and the power spectral densities, we can substitute them into the derivative expression and solve for $\alpha(f)$. The equation for $\alpha(f)$ is:

$$\alpha(f)\,S_n^{LF}(f) - (1 - \alpha(f))\,S_n^{HF}(f) = 0 \tag{5.9}$$

$$\alpha(f) = \frac{S_n^{HF}(f)}{S_n^{LF}(f) + S_n^{HF}(f)} \tag{5.10}$$

Hence, we can write the combined data from the low and high-frequency interferometers as:

$$d^{com}(f) = \frac{S_n^{HF}(f)}{S_n^{LF}(f) + S_n^{HF}(f)}d^{LF}(f) + \frac{S_n^{LF}(f)}{S_n^{LF}(f) + S_n^{HF}(f)}d^{HF}(f) \tag{5.11}$$

And the noise power spectral density of the combined data can be expressed as (traced by the green curve in figure 5.2):

$$S_n(f) = \frac{S_n^{LF}(f)\,S_n^{HF}(f)}{S_n^{LF}(f) + S_n^{HF}(f)} \tag{5.12}$$
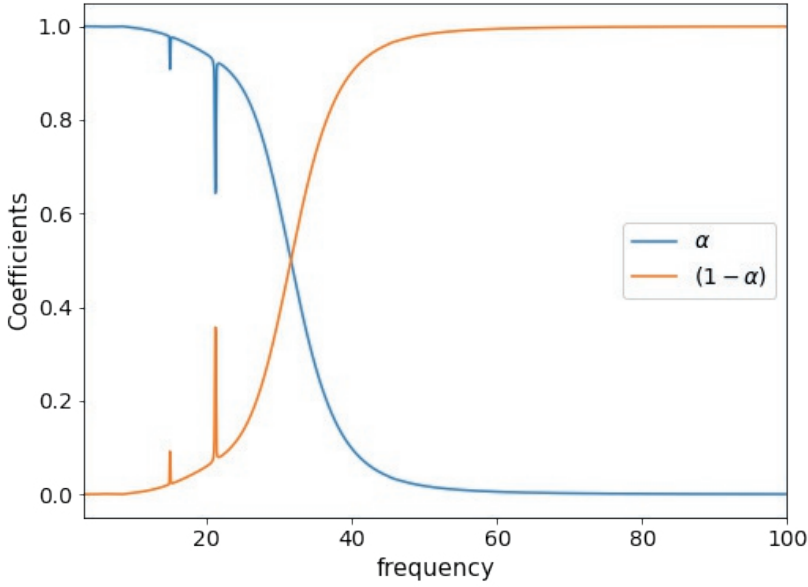
Figure 5.3: Variation of coefficients with frequency for optimal combination of data from the low and high-frequency arm.

5

In figure 5.3, I present the optimal coefficients for combining data from the low and high-frequency arms considering the sensitivity of the ET detector. To combine the data, each coefficient is multiplied by the Fourier transform of the detector strain corresponding to a specific frequency. The combined data is then obtained by summing these weighted contributions from the low and high-frequency arms. The choice of coefficients is crucial because it determines the overall noise power spectral density of the combined data. It is worth noting that the sum of the coefficients is constrained to be equal to unity. This constraint ensures that the combined gravitational wave signal, which is present in both the low and high-frequency arms, remains constant throughout the data combination process. This helps to maintain the integrity of the gravitational wave signal while effectively suppressing the noise.

5.3 Exploring the limits: Sensitivity analysis of third generation gravitational wave detectors

The detection sensitivity of gravitational wave detector networks relies on a multitude of factors, including the precise placements, orientations, and geometries of individual detectors within the network. These characteristics play a crucial role in determining the network's ability to detect and accurately measure gravitational wave signals. By carefully optimizing these parameters, we can enhance the overall sensitivity and performance of the detector network. One important aspect of detector performance is the antenna response function, which represents the directional sensitivity of a detector with respect to the incoming gravitational wave signals. It describes how the detector's orientation and geometry affect its ability to detect waves from different directions with different polarizations. By analyzing the antenna response function, we can assess the detector's sensitivity to gravitational waves arriving from specific angles and optimize its orientation for maximum sensitivity. In addition to the antenna response function, another crucial metric for evaluating the performance of gravitational wave detectors is the signal-to-noise ratio. The SNR quantifies the strength of the detected signal compared to the background noise. A higher SNR indicates a more confident detection and improves the accuracy of parameter estimation for the gravitational wave source. Maximizing the SNR is of utmost importance as it enables scientists to extract valuable scientific information and insights from gravitational wave events. Furthermore, the horizon distance or range of a detector is an important figure of merit that indicates the maximum distance at which the detector can detect a gravitational wave signal with a specific SNR threshold. A larger horizon distance implies a broader reach for the detector network, enabling the detection of more distant and potentially more significant gravitational wave events. Alternatively, we can characterize the maximum redshift (equivalent to the horizon distance) achievable by a detector network. The redshift, arising from the expansion of the universe, leads to a stretching of the observed wavelength of light or gravitational waves. Evaluating the maximum redshift capability of a network of detectors can also enable us to determine its potential for detecting gravitational waves originating from extremely distant cosmic sources. By expanding our ability to detect redshifted sources, we have the opportunity to make groundbreaking discoveries about how the universe has evolved

over time. In this section, we will explore the key factors that determine the overall performance of a detector or network of detectors in gravitational wave studies. These factors include the antenna response function, signal-to-noise ratio (SNR), horizon distance or range, and maximum redshifted sources.

5.3.1 Antenna response function

The antenna response function determines the response of the GW detector to a signal. For far-away sources, it is convenient to express the GW signal in a specific coordinate system where the tensor h^{ij} exhibits certain properties. In this coordinate system, the GW signal is transverse and trace-free. The transverse property means that the GW signal oscillates perpendicular to the direction of propagation. The trace-free property indicates that the sum of the diagonal elements of the tensor h^{ij} is zero. This means that the GW does not cause any net expansion or contraction of space in the transverse direction. The tensor representation of the GW, denoted as h^{ij}, exhibits two distinct components: h_+ and $h_\times$. The tensor h^{ij} takes the following form:

$$
\begin{aligned}
h^{11} = -h^{22} = h_+ \\
h^{12} = h^{21} = h_\times
\end{aligned}
\tag{5.13}
$$

We can define basis polarization tensors $\mathbf{e}_+$ and $\mathbf{e}_\times$ that correspond to the two polarizations of the GW, can be written as:

$$
\begin{aligned}
\mathbf{e}_+ = \hat{e}_x^R \otimes \hat{e}_x^R - \hat{e}_y^R \otimes \hat{e}_y^R \\
\mathbf{e}_\times = \hat{e}_x^R \otimes \hat{e}_y^R + \hat{e}_y^R \otimes \hat{e}_x^R.
\end{aligned}
\tag{5.14}
$$

Here, $\hat{e}_x^R$ and $\hat{e}_y^R$ are the radiation basis vectors. $\hat{e}_x^R$ lies in the plane formed by the wave direction $(\hat{N})$ and the detector axis $(\hat{e}_x)$, as shown in figure 5.4. Also more general scenario is depicted in figure 5.4, where the radiation basis vectors $\hat{\alpha}$ and $\hat{\beta}$ are rotated by an angle ψ with respect to the $\hat{e}_x^R$ and $\hat{e}_y^R$ directions. Figure 5.4 and the following mathematical expressions are adapted from [192]. In this configuration, the new basis polarization tensors can be expressed as follows:

$$
\begin{aligned}
\boldsymbol{\epsilon}_+ = \hat{\alpha} \otimes \hat{\alpha} - \hat{\beta} \otimes \hat{\beta} \\
\boldsymbol{\epsilon}_\times = \hat{\alpha} \otimes \hat{\beta} + \hat{\beta} \otimes \hat{\alpha}.
\end{aligned}
\tag{5.15}
$$
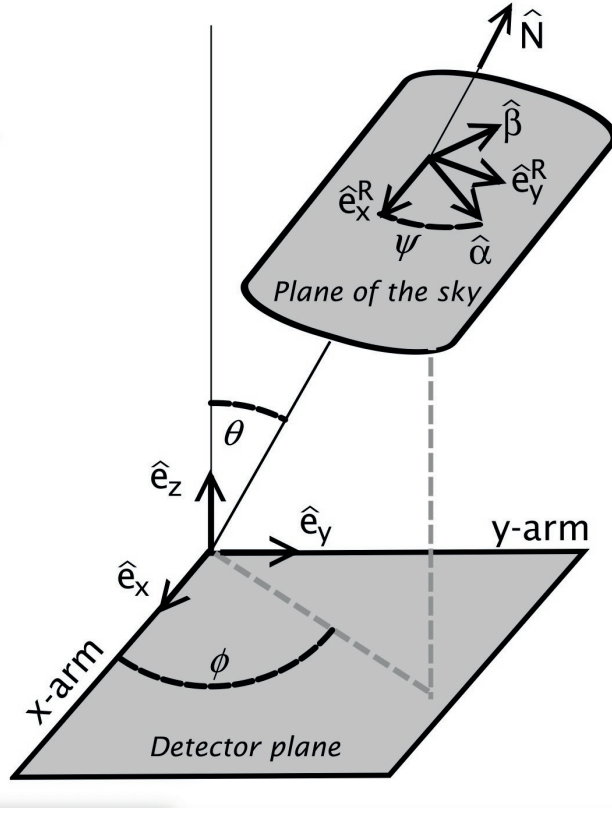
Figure 5.4: Schematic representation of the detector frame and the GW signal polarizations (h_+ and $h_\times$) coming from a direction specified by spherical coordinates (θ, ϕ) relative to the detector axis. The basis vectors of the source frame, $\hat{\alpha}$ and $\hat{\beta}$ are rotated by an angle ψ with respect to the reference basis $\hat{e}_x^R$ and $\hat{e}_y^R$. This rotation is introduced to accommodate a broader range of source orientations. Figure taken from [192].

The relationship between the new polarization basis tensors and the old basis can be expressed as follows:

$$\begin{pmatrix} \boldsymbol{\epsilon}_+ \\ \boldsymbol{\epsilon}_\times \end{pmatrix} = \begin{pmatrix} \cos 2\psi & \sin 2\psi \\ -\sin 2\psi & \cos 2\psi \end{pmatrix} \begin{pmatrix} \mathbf{e}_+ \\ \mathbf{e}_\times \end{pmatrix} \tag{5.16}$$

The metric perturbation h^{ij} can be expressed as a linear combination of the basis polarizations:

$$h^A = d_{ij}^A \, h^{ij} = F_+^A h_+ + F_\times^A h_\times, \tag{5.17}$$

where A stands for the index of the detector. Here, F_+^A and $F_\times^A$ are coefficients that depend on the detector response and the basis polarizations. They can be expressed as inner products between the detector tensor $\mathbf{d}$ and the basis tensors $\mathbf{e}_+$ and $\mathbf{e}_\times$:

$$\begin{aligned}
F_+^A &= d_{ij}^A\, e_+^{ij} = \mathbf{d} : \mathbf{e}_+ \\
F_\times^A &= d_{ij}^A\, e^{ij}\times = \mathbf{d} : \mathbf{e}_\times
\end{aligned} \tag{5.18}$$

The notation ':' represents the Euclidean scalar product (also known as the inner product or dot product) between the tensors. The detector tensor $\mathbf{d}$ represents the orientation and geometry of the detector in a coordinate system fixed to its frame. For example, in the case of an L-shaped detector with arms along the coordinate axes, the detector tensor can be expressed as:

$$\mathbf{d} = \frac{\hat{e}_x \otimes \hat{e}_x - \hat{e}_y \otimes \hat{e}_y}{2} \tag{5.19}$$

The antenna pattern factors F_+ and $F_\times$ describe the sensitivity of the interferometer to different polarizations of the gravitational wave signal, as a function of the source location (θ, ϕ). Using the geometry, we can evaluate these factors as follows:

$$\begin{aligned}
F_+ &= \frac{1}{2}(1 + \cos^2\theta)\cos2\phi\cos2\psi - \cos\theta\sin2\phi\sin2\psi \\
F_\times &= \frac{1}{2}(1 + \cos^2\theta)\cos2\phi\sin2\psi + \cos\theta\sin2\phi\cos2\psi
\end{aligned} \tag{5.20}$$

In these expressions, θ represents the inclination angle of the source relative to the detector's normal vector, ϕ represents the azimuthal angle of the source, and ψ represents the polarization angle of the gravitational wave.

In the case of the Einstein Telescope with three nested detectors, the detector tensors $\mathbf{d}_1$, $\mathbf{d}_2$, and $\mathbf{d}_3$ can be expressed as follows:

$$\begin{aligned}
\mathbf{d}_1 &= \frac{1}{2}(\hat{e}_1 \otimes \hat{e}_1 - \hat{e}_2 \otimes \hat{e}_2) \\
\mathbf{d}_2 &= \frac{1}{2}(\hat{e}_2 \otimes \hat{e}_2 - \hat{e}_3 \otimes \hat{e}_3) \\
\mathbf{d}_3 &= \frac{1}{2}(\hat{e}_3 \otimes \hat{e}_3 - \hat{e}_1 \otimes \hat{e}_1).
\end{aligned} \tag{5.21}$$

Here, $\hat{e}_1$, $\hat{e}_2$, and $\hat{e}_3$ are the unit vectors along the arms of the ET interferometers with $60°$ opening angle. Assuming the detector is in the

XY-plane and one of the vertices lying on the Y-axis, we can express these unit vectors as:

$$\hat{e}_1 = \frac{1}{2}(\sqrt{3}, -1, 0)$$
$$\hat{e}_2 = \frac{1}{2}(\sqrt{3}, 1, 0) \tag{5.22}$$
$$\hat{e}_3 = (0, 1, 0)$$

The unit vectors of the source frame can be written as:

$$\hat{e}_x = \begin{pmatrix} -\sin\phi\,\sin\psi + \cos\theta\,\cos\phi\,\sin\psi \\ \cos\phi\,\cos\psi + \cos\theta\,\sin\phi\,\cos\psi \\ -\sin\theta\,\cos\psi \end{pmatrix},$$
$$\hat{e}_y = \begin{pmatrix} -\sin\phi\,\cos\psi - \cos\theta\,\cos\phi\,\sin\psi \\ \cos\phi\,\cos\psi - \cos\theta\,\sin\phi\,\sin\psi \\ -\sin\theta\,\sin\psi \end{pmatrix} \quad \text{and} \tag{5.23}$$
$$\hat{e}_z = \begin{pmatrix} \sin\theta\,\cos\phi \\ \sin\theta\,\sin\phi \\ \cos\theta \end{pmatrix}$$

For the detector within the triangular ET observatory, featuring arms aligned along $\vec{e}_1$ and $\vec{e}_2$ with a 60°opening angle, the corresponding antenna response functions can be expressed as follows:

$$F_+^1 = -\frac{\sqrt{3}}{4}\left[(1 + \cos^2\theta)\sin 2\phi\cos 2\psi + 2\cos\theta\cos 2\phi\sin 2\psi\right]$$
$$F_\times^1 = +\frac{\sqrt{3}}{4}\left[(1 + \cos^2\theta)\sin 2\phi\sin 2\psi - 2\cos\theta\cos 2\phi\cos 2\psi\right] \tag{5.24}$$

To obtain the antenna response functions $F_{+,\times}^2$ and $F_{+,\times}^3$ for the other two detectors in the Einstein Telescope interferometer, we can take a rotation of the angle ϕ by $\frac{2\pi}{3}$ from the antenna response function $F_{+,\times}^1$:

$$F_{+,\times}^2(\theta, \phi, \psi) = F_{+,\times}^1\left(\theta, \phi + \frac{2\pi}{3}, \psi\right)$$
$$F_{+,\times}^3(\theta, \phi, \psi) = F_{+,\times}^1\left(\theta, \phi - \frac{2\pi}{3}, \psi\right). \tag{5.25}$$

For an L-shaped detector, the maximum values of the antenna pattern factor F_+ and $F_\times$ are both 1. However, for an interferometer with a

60° opening angle, such as the Einstein Telescope, the maximum values of F_+ and $F_\times$ are $\frac{\sqrt{3}}{2}$. The factor of $\sqrt{3}/2$ indicates that ET's response is reduced by approximately 30% compared to an L-shaped interferometer due to its triangular geometry. However, ET has three detectors, which enhance its response by a factor of $\sqrt{3}$. This means that the presence of multiple detectors in ET compensates for its reduced response due to the triangular shape. The overall enhancement factor becomes $3/2$, indicating that ET's response is 50% higher compared to what it would be with a single detector.

In the case of an L-shaped detector, when the gravitational wave source is in an overhead position $(\theta, \phi) = (0, 0)$ with respect to the detector, the coefficients F_+ and $F_\times$ take specific values depending on the angle ψ. When $\psi = 0$: $F_+ = 1$ and $F_\times = 0$. When $\psi = \frac{\pi}{4}$: $F_+ = 0$ and $F_\times = 1$. For an L-shaped detector, these coefficients indicate the sensitivity of the detector to the two polarizations of the gravitational wave. When the source is directly overhead, the detector is maximally sensitive to one polarization and completely insensitive to the other. When $\psi = 0$, the detector is only sensitive to the "+" polarization, and when $\psi = \frac{\pi}{4}$, it is only sensitive to the "×" polarization. On the other hand, for a triangular detector configuration, with its 60° opening angle and three detectors, it can probe both polarizations of gravitational waves effectively. The arrangement of three detectors with different orientations allows for the simultaneous detection and characterization of both the "+" polarization and the "×" polarization of the gravitational wave signals.

Thus antenna pattern factors provide information about how the sensitivity of the interferometer varies with different source directions and polarizations. The antenna power pattern provides information about the shape of the detection volume or the maximum reach of the detector in different directions. By evaluating F_+ and $F_\times$ for various (θ, ϕ) values, we can determine the preferred and null directions of the detector's response, as well as its sensitivity to different polarization states of the gravitational wave signal. The antenna power pattern, denoted as $P(\theta, \phi)$, is a measure of the response of a GW detector to different polarization states and wave propagation angles. For a L-shaped detector, the antenna power pattern can be written as [194]:

$$P(\theta, \phi) = [F_+^2(\theta, \phi, \psi) + F_\times^2(\theta, \phi, \psi)] \qquad (5.26)$$

$$= \frac{1}{4}(1 + \cos^2 \theta)^2 \cos^2 2\phi + \cos^2 \theta \, \sin^2 2\phi \qquad (5.27)$$

The joint response of all three detectors in the ET network can be obtained by considering the sum of the antenna power pattern of each individual detector. The antenna power pattern for ET triangle can be expressed as:

$$P^{ET}(\theta, \phi) = \sum_{A=1}^{3} (F_+^A)^2 + (F_\times^A)^2 = \frac{9}{32}(1 + 6\cos^2 \theta + \cos^4 \theta) \quad (5.28)$$

The joint antenna power pattern, depending only on the colatitude θ of the source, implies that the sensitivity of the ET network to gravitational waves is isotropic in azimuthal directions, i.e., it is independent of the angle ϕ. Specifically, the maximum response occurs when $\theta = 0$, indicating that the source is positioned perpendicular to the plane of the detector. In this configuration, the antenna pattern reaches its maximum value, denoted as $P^{ET}(\theta = 0)$, which is equal to $\frac{9}{4}$. Conversely, the response function of the detector becomes minimum when the source is located at $\theta = \frac{\pi}{2}$, corresponding to a source direction that is parallel to the plane of the detector. In this orientation, the response function, denoted as $P^{ET}(\frac{\pi}{2})$, is equal to $\frac{1}{8}P^{ET}(\theta = 0)$. This characteristic of the triangular topology of the detector allows for virtually all-sky coverage with no null direction. The detector's antenna pattern provides sensitivity to gravitational waves arriving from various directions, ensuring that there are no specific directions in the sky where the response function becomes zero.

Figure 5.5 depicts the square root of antenna power pattern of the incoming GW signals from the direction(θ, ϕ), for a gravitational wave detector, oriented with their axes in the x-y plane. This shows the quadruple nature of an L-shape and the triangular configuration of the detector. The left panel shows the antenna pattern for a detector with a triangular topology, while the right panel displays the antenna pattern factor for an L-shaped detector. The color map represents the amplitude of the antenna response function, which indicates the sensitivity of the detector and its maximum reach in different directions. For an L-shaped detector, the antenna pattern of the detector reveals that the maximum
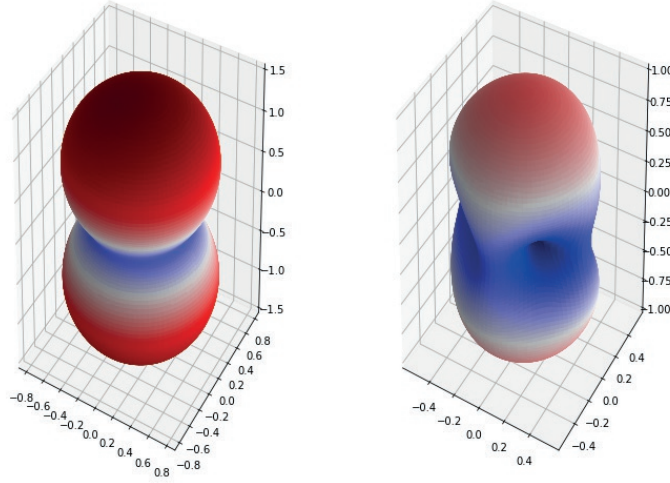
Figure 5.5: Antenna pattern for the gravitational wave detector. Left: Antenna pattern for triangular topology. Right: Antenna pattern factor for L-shaped detector. The interferometer is oriented with axes in the x-y plane, averaged over the polarization angle of the incoming GW signal. The amplitude pattern represents the shape of the detection volume or its maximum reach in different directions.

5

response of the interferometer occurs when the gravitational wave signal propagates from a direction orthogonal to the plane containing the detector. This alignment allows for the optimal detection of the gravitational wave signal. Conversely, the response of the L-shaped detector becomes zero when the gravitational wave signal arrives from a direction coinciding with the bisector of the two arms of the detector. In this particular orientation, the detector is not sensitive to the gravitational wave signal, resulting in a null response. The absence of null directions for the ET triangle is a result of its specific triangular topology and the configuration of the three detectors. Figure 5.6 is the 2D representation of figure 5.5.

The polarization amplitudes of a gravitational wave signal can be ex-
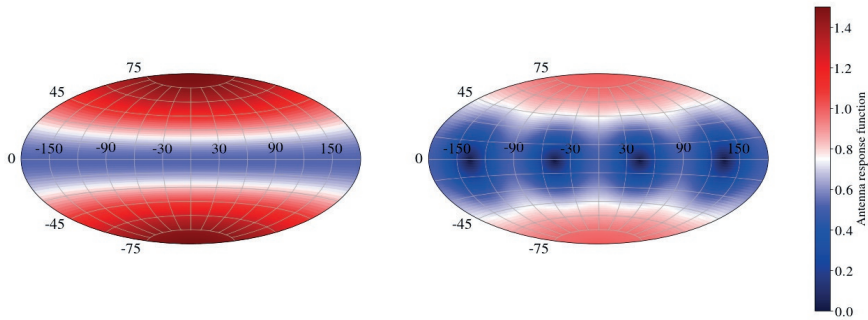
Figure 5.6: Antenna pattern for the gravitational wave detector: 2D projection of figure 5.5. The color bar represents the amplitude of the antenna pattern, which becomes zero for the L-shaped detector. The triangular topology of the detector ensures that there are no null directions, as it consists of three interferometers.

pressed in terms of the inclination angle (i), characteristic strain amplitude (h_0), and the instantaneous phase ($\Phi(t)$). The amplitudes are given by the equations:

$$
\begin{aligned}
h_+ &= \frac{h_0}{2}(1 + \cos^2 i)\cos(\Phi(t)) \\
h_\times &= h_0\cos(i)\sin(\Phi(t)).
\end{aligned}
\tag{5.29}
$$

These equations describe how the gravitational wave signal is polarized along different directions.

The detector's response to the gravitational wave can be represented by the equation

$$
h(t) = F_+ h_+ + F_\times h_\times,
\tag{5.30}
$$

where F_+ and $F_\times$ are the response coefficients. By combining the polarization amplitudes with the response coefficients, we obtain an expression that describes the overall response of the detector to the gravitational wave signal. The response function A, which represents the average response over all possible polarization and inclination angles, is defined as

$$
A = \sqrt{A_+^2 + A_\times^2},
\tag{5.31}
$$

where $A_+ = F_+\left(\frac{1}{2}\right)(1 + \cos^2\theta)$ and $A_\times = F_\times\cos(i)$.
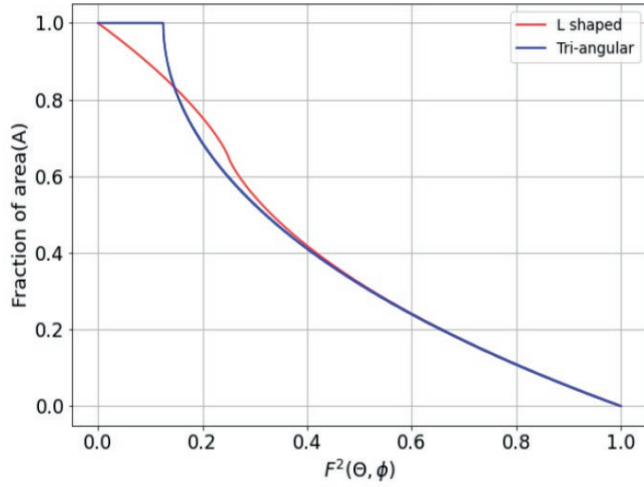
Figure 5.7: The fractional area in the sky over which the response of the detector or the antenna pattern exceeds a fraction of its maximum value. The red and blue curve is for L'shaped and triangular geometry, respectively.

In figure 5.7, the sky coverage of the detector's antenna pattern is illustrated. The fractional area of the sky shown in the plot indicates the portion of the celestial sphere for which the detector's response exceeds a specific threshold (values along x-axis), given as a fraction of its maximum value. The red and blue curves correspond to L-shaped and triangular detector geometries, respectively. For the triangular-shaped detector, the antenna response function has been normalized after dividing by $\frac{3}{2}$ (maximum value). Notably, the blue curve exhibits a flat region, indicating the absence of a null direction for the triangular-shaped detector.

Together, these equations and figures provide insights into the polarization amplitudes of gravitational wave signals, the detector's response, and the sky coverage of different detector geometries.

5.3.2 Signal-to-noise ratio

The Signal-to-noise ratio can be calculated using the matched filtering technique. Matched filtering involves correlating the detector's output with a theoretical waveform template that represents the expected GW

signal. The SNR is then obtained by integrating the correlation output over a suitable frequency range. The optimal signal-to-noise ratio of a detector, obtained through matched filtering with a template waveform, can be expressed as:

$$\rho^2 = 4 \int_0^\infty \frac{|\delta L(f)/L|^2}{S_n(f)} df \qquad (5.32)$$

$S_n(f)$ represents the one-sided noise power spectral density, L is the characteristic length of the arms of the gravitational wave detector, and $\delta L(f)$ corresponds to the differential arm length of the detector. In the case of short-duration gravitational waves, when the effect of Earth's rotation is insignificant over the observation time of the signal, it is reasonable to assume that the antenna pattern of the detector remains constant and does not vary with time. This simplifying assumption allows for a time-independent characterization of the detector's antenna pattern during the detection of such GWs. Additionally, GW sources can have random polarization, allowing for an ensemble of GW sources with various polarization angles (ψ) at any specific direction (θ, ϕ). When calculating the average power signal-to-noise ratio, it is necessary to consider an ensemble average over all possible source polarizations. Consequently, the power SNR can be expressed as:

$$<\rho^2> = 2(F_+^2(\theta,\phi,\psi) + F_\times^2(\theta,\phi,\psi)) \int_0^\infty \frac{|H(f)|^2}{S_n(f)} df, \qquad (5.33)$$

where $|H(f)|^2 = |h_+(f)|^2 + |h_\times(f)|^2$. By evaluating this equation, we obtain the average power SNR, which quantifies the strength of the gravitational wave signal relative to the noise in the detector, taking into account the antenna pattern, polarization, and noise characteristics of the detector. We have expressed the antenna pattern power pattern as:

$$P(\theta,\phi) = F_+(\theta,\phi,\psi)^2 + F_\times(\theta,\phi,\psi)^2 \qquad (5.34)$$

This implies that:

$$<\rho^2> = 2 P(\theta,\phi) \int_0^\infty \frac{|H(f)|^2}{S_n(f)} df \qquad (5.35)$$

By considering the detector's antenna pattern ($P(\theta,\phi)$) and the noise power spectral density ($S_n(f)$), the equation provides insights into how the detector responds to gravitational wave signals with different directions and polarizations.

5.4 Horizon distance

We have seen the antenna response function for the network of detectors, which manifests the ability to detect signals from an arbitrary direction. The horizon distance refers to the maximum distance from which a gravitational wave source can be detected by a detector. It represents the extent to which the detector can probe the universe for gravitational wave signals. To determine whether a GW source is detectable, we consider the signal-to-noise ratio, which compares the strength of the signal to the level of background noise. The SNR must be higher than a certain threshold value (ρ_{th}) for the detection to be successful. Mathematically, we express this as:

$$\rho^2 \geq \rho_{th}^2, \tag{5.36}$$

where ρ is the SNR. The SNR can be computed using the antenna power pattern $P(\theta, \phi)$, which describes the directional sensitivity of the detector, and the integral of the signal power spectrum $|H(f)|^2$ divided by the noise power spectrum $S_n(f)$ over all frequencies:

$$2\, P(\theta, \phi) \int_0^\infty \frac{|H(f)|^2}{S_n(f)}\, df \geq \rho_{th}^2. \tag{5.37}$$

The antenna power pattern, denoted by $P(\theta, \phi)$, describes the directional sensitivity of the detector. In this context, we consider the amplitude of the gravitational wave signal, denoted as $H(f)$, which is inversely proportional to the distance of the source, d. To establish a reference point, let's assume the magnitude of the signal at a distance $d = r$ is denoted as $H_r(f)$.

Given this assumption, we can express $H(f)$ as $H(f) = \frac{r\, H_r(f)}{d}$. With this relation, we can derive the expression for the signal-to-noise ratio, denoted as ρ, which plays a crucial role in determining the detectability of a gravitational wave signal. The expression for ρ^2 is given by:

$$\rho^2 = \frac{2}{d^2}\, P(\theta, \phi) \int_0^\infty \frac{|rH_r(f)|^2}{S_n(f)} df. \tag{5.38}$$

The expression inside the integral in the previous equation is independent of the direction of the gravitational wave source, and the product $|rH_r(f)|^2$ remains constant. Consequently, the signal-to-noise ratio primarily relies on two factors: the luminosity distance, denoted as d, and the antenna power pattern $P(\theta, \phi)$.

The horizon distance of a gravitational wave detector refers to the maximum distance at which a gravitational wave source, observed from an overhead position with optimal polarization, can be detected at the detection threshold. When a source is observed from an overhead position with optimal polarization, it means that the gravitational wave signals align in the most favorable way with the detector's sensitivity pattern, maximizing the chances of detection. The horizon redshift can be considered as the critical redshift value beyond which the observed or detected objects are effectively beyond our observational capabilities. As the universe expands, the light from objects located beyond the horizon distance becomes increasingly redshifted and eventually redshifted to a point where it is undetectable or beyond the reach of the detector.
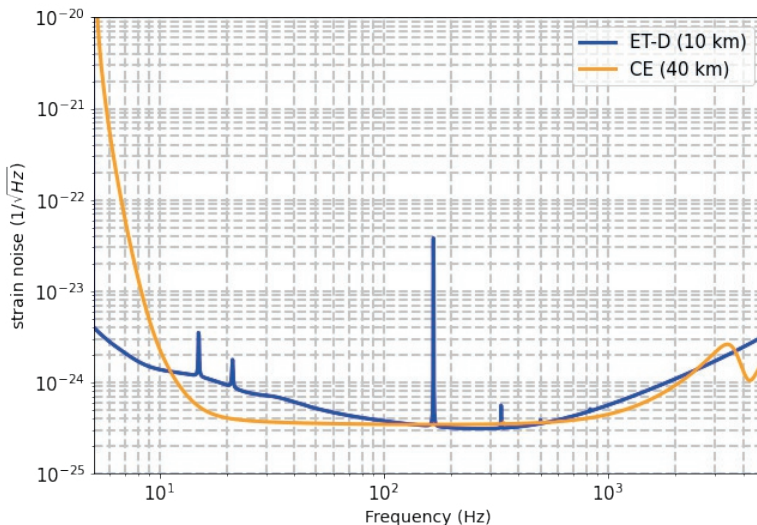
Figure 5.8: The sensitivity of the proposed Einstein Telescope (blue curve) and compared to the target sensitivity of Cosmic Explorer 1 (orange curve). The sensitivity curve of Cosmic Explorer has been generated using gwinc (Updated numbers March 2018). The data file for the sensitivity curves has been uploaded in 1*

In the figure 5.8, the sensitivity curves of the Einstein Telescope and the Cosmic Explorer are displayed (data files in [1]). In this case, the

---

[1]https://surfdrive.surf.nl/files/index.php/s/Td1HcK8CGrpF5QX
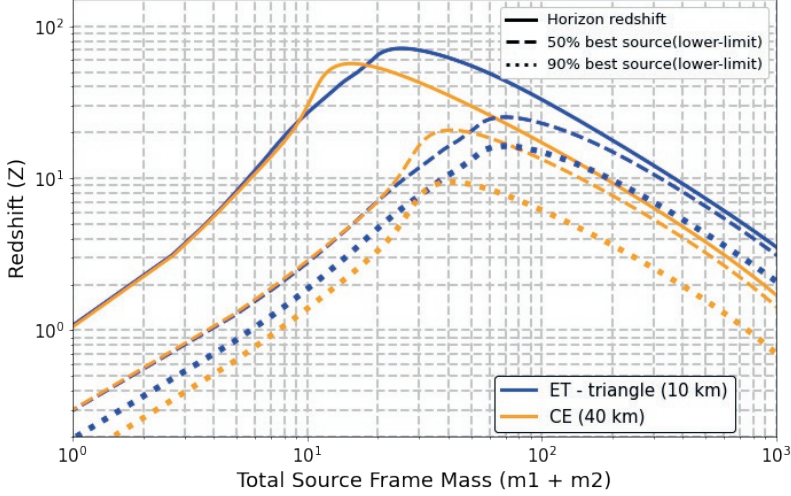
Figure 5.9: The maximum redshift for the ET and CE, assuming equal-mass, non-spinning binaries systems, is shown as a function of total source-frame mass. The binaries are distributed isotropically in sky location and inclination angle. The solid lines denote the horizon-redshift, i.e., none of the sources can be detected further. The dashed and dotted curves denote the redshift (lower limit) for 50% and 90% sources, respectively.

term "sensitivity" refers to $\sqrt{S_n(f)}$, which represents the square root of the amplitude spectral density of noise. The sensitivity curves provide information about the detector's noise characteristics as a function of frequency, taking into account the overall noise budget of the detector. In the figure 5.9, the horizon redshifts for the Einstein Telescope and the Cosmic Explorer are shown. The horizon redshift represents the redshift value beyond which none of the sources placed overhead can be detected by the respective detectors (as indicated by the solid curves).

As we have seen before, the performance of the detector depends on the direction of the source. To account for this, the sources are assumed to be uniformly distributed over all sky locations, with random polarization and inclination angles. The dashed curve in the figure represents the lower limit of the redshift for the 50% best sources from all over the sky. This means that the redshift of each of the 50% best sources

falls between the solid and dotted curves. Similarly, the dotted curve represents the lower limit of the redshift for the 90% best sources. The comparison between the Einstein Telescope and the Cosmic Explorer reveals some differences in their horizon redshifts and sensitivity. For lower source masses, CE shows a slightly higher horizon redshift compared to ET. This is due to CE's lower limiting noise in the frequency range of 10 to several kHz, which improves its sensitivity for such masses. On the other hand, for higher source masses, the horizon redshift is higher for ET. This is because ET has better sensitivity below 10 Hz compared to CE, which allows it to detect higher-mass sources at greater distances. It is worth noting that ET's triangular shape provides it with a better detector response in general, leading to higher redshifts for the 90% best sources. This is an expected outcome, as the enhanced sensitivity and design of ET enable it to detect a broader range of sources.

From the figure 5.8, it is evident that there are significant differences in the sensitivity curves of ET and CE. The noise amplitude is lower for CE in the frequency range of 10 Hz to several kilo-Hz, which can be attributed to its longer arm length of 40 km compared to the 10 km arm length of ET. This lower noise amplitude indicates that CE should be more sensitive and capable of detecting weaker signals in this frequency range. However, for a more realistic evaluation of the detector performance, we should consider the plot in figure 5.9, which describes the maximum redshift attainable by each detector. This provides a clearer picture of their capabilities. There is a range of source masses for which ET outperforms CE in terms of reach. Gravitational waves can originate from a wide variety of astrophysical events and sources distributed in all directions in the sky. Therefore, it is essential to consider the full-sky coverage of detectors when assessing their capabilities and performance. By accounting for the isotropic nature of gravitational wave sources and considering their random arrival directions, we have obtained a more comprehensive and unbiased evaluation of the detectors' figure of merit. This analysis helps us understand how well the detectors can assist us in detecting and studying gravitational wave events from various sources across the entire celestial sphere.

Chapter 6

Sky resolution of the network of 3G GW detectors for different topologies of the Einstein Telescope observatory.

6.1   Introduction

The reconstruction of the sky position for compact binary coalescence sources emitting gravitational waves, as detected by current detectors, has been a central challenge in the field [198, 144]. When a potential event is identified by the search pipeline [3, 96, 27], which involves sophisticated algorithms and data analysis techniques, further analysis is conducted to determine the precise location of the source in the sky. To reconstruct the sky position, several factors are taken into account. First, the time of arrival of the gravitational wave signal in different detectors plays a key role. By comparing the arrival times at different detector locations, scientists can triangulate the source position in the sky. Moreover, the distinctive strength of the gravitational wave signal perceived by each detector contributes valuable insights to the reconstruction process. This sensitivity variation across the sky can be described by the antenna pattern factor (discussed in previous chapter), related to the geometric arrangement of the detectors.

The unique advantage of gravitational wave detectors, in comparison to electromagnetic telescopes, is their ability to detect GW signals from all directions in the sky. Unlike electromagnetic radiation, which can be

obstructed by various astrophysical objects such as dust, gas, or other barriers, gravitational waves can freely travel through these obstacles. By analyzing the relative amplitudes observed by different detectors, one can generate a posterior probability distribution that captures the likelihood of the GW source being located in various regions of the sky. The precise sky position of the GW source is of utmost importance for conducting electromagnetic follow-up observations. When a GW event is detected, astronomers aim to identify potential electromagnetic counterparts associated with the event. However, since the electromagnetic signatures of compact binary coalescence events are expected to be transient, it is crucial to have rapid access to accurate sky position information from the network of GW detectors. Successful electromagnetic follow-up can aid in identifying the host galaxy, investigating the local environment of the progenitor, and estimating the Hubble constant through measurements of luminosity distance [9, 62, 165]. Therefore the reconstruction of the sky position using the global network of GW detectors is an active area of research, with a focus on achieving rapid and highly accurate localization by improving the likelihood function [101].

The upcoming fourth observing run of LIGO, VIRGO, and KAGRA, set to begin in mid-2023, is expected to bring significant advancements in sensitivity. LIGO aims to achieve a sensitivity of 160-190 Mpc for detecting binary neutron stars, while Virgo is targeting a sensitivity of 80-115 Mpc. These sensitivities represent improvements of a factor of two for Virgo compared to the previous observation cycle (O3). KAGRA, on the other hand, plans to start with a sensitivity greater than 1 Mpc during the fourth run, gradually improving to reach its target sensitivity of 10 Mpc. The enhancement in the sensitivity of LIGO involves the injection of frequency-dependent squeezed vacuum states will play a role in reducing the impact of broadband quantum noise [166]. Doubling the sensitivity of the detectors can lead to an eight-fold increase in the detection rate. It will greatly enhance parameter estimation accuracy, as improved sensitivity empowers detectors to capture gravitational wave signals with stronger SNR due to reduced background noise. This increased sensitivity enables improved fitting of observed waveforms to theoretical templates, leading to enhanced accuracy in parameter estimation. In [229], Zhang et al. have shown the potential of gravitational-wave detections from binary compact object mergers, combined with electromagnetic observations, to serve as "standard sirens" for studying the universe's expansion history. Through simulations based on

the Einstein Telescope's observations, the study illustrates how these gravitational-wave data can break parameter degeneracies and significantly strengthen cosmological constraints, including those pertaining to matter density, the Hubble constant, and the equation-of-state parameter of dark energy.

The advancements in gravitational wave detector technology continue with the development of third-generation detectors such as the Einstein Telescope and Cosmic Explorer. These future detectors are expected to achieve a remarkable ten-fold improvement in sensitivity compared to current detectors in the frequency range of 20 to 10 kHz. This substantial enhancement in sensitivity allows for the detection of weaker gravitational wave signals and the exploration of a broader range of astrophysical phenomena. Moreover, one notable advantage of future detectors is their increased detection bandwidth. Unlike the current generation of detectors that primarily focus on the late inspiral and merger stages of the gravitational wave signal, future detectors will have the capability to observe the entire gravitational wave signal from the early inspiral stage to the final ringdown phase. This expanded detection range provides valuable information about the complete evolution of the merging systems, enabling more detailed studies of the astrophysical processes involved. The improved sensitivity, particularly at lower frequencies, offers significant benefits for early warning systems in gravitational wave astronomy. Early warning systems rely on detecting the early inspiral phase of compact binary systems, which can provide crucial information about the upcoming merger event. The field of multimessenger astronomy will greatly benefit from the improved sensitivity and early warning capabilities of future detectors [59]. By precisely determining the sky position of a gravitational wave source, astronomers can promptly direct their instruments towards the same location and search for electromagnetic counterparts associated with the gravitational wave event [169].

The accuracy of determining the sky position for gravitational wave sources in a network of detectors is influenced by various factors. These factors include the number of detectors in the network, their sensitivity, the geometry of the detectors, and their relative positions on Earth. The directional sensitivity of the detectors depends on antenna pattern factors, which are influenced by the interferometers' geometry and the orientation of their arms. As a result, the detectors do not have equal sensitivity to all directions in the sky or to both polarizations

6

of gravitational waves. Due to the variations in sensitivity and directional response, the accuracy of sky localization can be affected. The uncertainty in determining the source's sky position is influenced by the specific plane of detectors in the network. If the direction of propagation of emitted gravitational waves coincides with the plane of the detectors, the angular resolution of source localization may be poor. Therefore, for future generations of gravitational wave detectors, it is important to investigate the optimal geometry and orientation of the detectors in the network.

Currently, the operational gravitational wave detectors, including LIGO, VIRGO, and KAGRA, adopt an 'L'-shaped topology where the interferometer arms are perpendicular to each other. The 'L' topology has proven to be successful in the detection of gravitational waves and has contributed significantly to the field of gravitational wave astronomy. For the third-generation instruments, the question of optimal topology is yet to be decided. Although the Cosmic Explorer almost certainly will follow the 'L'-topology, the conceptual design study of the Einstein Telescope assumes the shape of an equilateral triangle for the network of its three xylophone detectors, comprising two interferometers each. Although the question of whether the Einstein Telescope should follow the triangular or L-shaped topology arises from time to time [63].

In this chapter, I will investigate which of the following combinations will work best based on sky localization accuracy. First, I consider the CE + ET network with a triangular topology for ET, and second, I consider the same network with ET as a single 'L' shaped detector. To assess the performance of these configurations, I calculate the signal-to-noise ratio and reach for a wide range of source masses in the 3G network. To evaluate the angular resolution, I have used the Fisher information matrix approach, which provides an estimation of the uncertainty in the source's sky position. Wen et al. [221] have derived explicit analytical expressions for the angular resolution in networks with arbitrary numbers of detectors, and I utilize these expressions in this analysis. By considering both the triangular and 'L' shaped configurations of the Einstein Telescope and incorporating Cosmic Explorer in each case, I calculate the angular resolution for each configuration and make a comparative analysis. This analysis allows us to assess the benefits and drawbacks of the two configurations and gain insights into their respective capabilities in accurately localizing gravitational wave sources in the sky. The estimation of the angular resolution is part of a broader

series of analyses aimed at comprehensively evaluating the performance and characteristics of the Einstein Telescope's triangular and 'L' shaped configurations.

This chapter is organized as follows. In section 6.2, I initiate by calculating the signal-to-noise ratio for the detection of gravitational wave events by the GW detectors, while considering the potential source locations across the entire sky. This SNR computation offers insight into the detectability and magnitude of the GW signals, as captured by a specific detector or a network of detectors. Next, in section 6.3, I compute the redshift distribution of astronomical sources observed by the 3G detectors. In section 6.4, I show the network of detectors that I have considered for the study on sky localization capabilities. This includes the selection of specific detectors, their characteristics, and their geographical distribution. To establish the mathematical foundation for my analysis, I discuss some mathematical expressions in section 6.5. This section covers essential concepts and tools necessary for understanding the subsequent calculations and estimations. In section 6.6, I discuss the Fisher matrix approach, a powerful tool for estimating the lower error bound of an estimator in a method-independent manner. Moving on to the results, in section 6.8, I present and discuss the outcomes of the analysis regarding the directional precision of sky localization. These results shed light on the achievable accuracy in determining the sky positions of GW sources based on the network of detectors under investigation. Finally, I summarise the results and discuss them in section 6.9.

6.2   Signal to noise ratio

The signal-to-noise ratio (ρ) is a measure of the strength of a signal relative to the background noise. It is calculated by comparing the amplitude of the signal to the standard deviation of the noise. In this section, we show the signal-to-noise ratio results for the Cosmic Explorer and the Einstein Telescope taking as a source the equal mass compact binaries ($10\ M_{\odot}$) that are uniformly seeded on the sky at a fixed luminosity distance, with both polarisation angle and inclination angle of the source set to zero with respect to the detectors. Figure 6.2 illustrates the distribution of signal-to-noise ratios for different configurations. The top plot compares the SNR for the Einstein Telescope with a triangular configuration to an 'L' shape with equal arm lengths ($10\,\mathrm{km}$). The bottom plot shows the SNR for the Einstein Telescope with an 'L' shape and
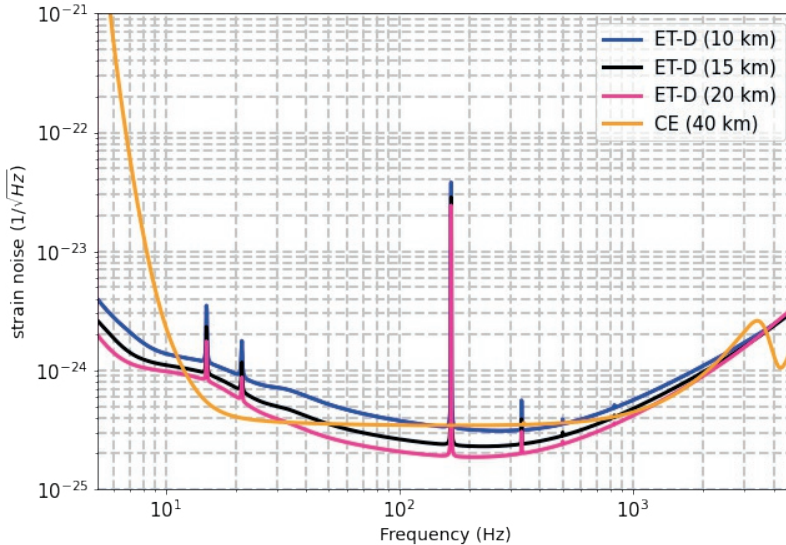
Figure 6.1: Sensitivity curves of Einstein Telescope (ET-D) and Cosmic Explorer (CE1). The sensitivity curves of the Einstein Telescope utilized in this analysis, corresponding to detector arm lengths of 10, 15, and 20 km, were generated using the pyGwinc software [186]. PyGWinc (Python Gravitational-Wave Interferometer Noise Calculator) is an open-source software tool employed for modeling the amplitude spectral curve of noise in gravitational wave interferometers.

different arm lengths (15 km and 20 km). As expected, increasing the arm length of the Einstein Telescope enhances the SNR. However, the 'L' shaped configuration exhibits some blind spots, resulting in null SNR values when the signal lies in the plane formed by the detector and the source location. In contrast, the triangular configuration of the Einstein Telescope, which consists of three detectors, does not have these blind spots. To quantitatively compare the configurations, we plot the cumulative distribution of sources based on their SNR in figure 6.3.
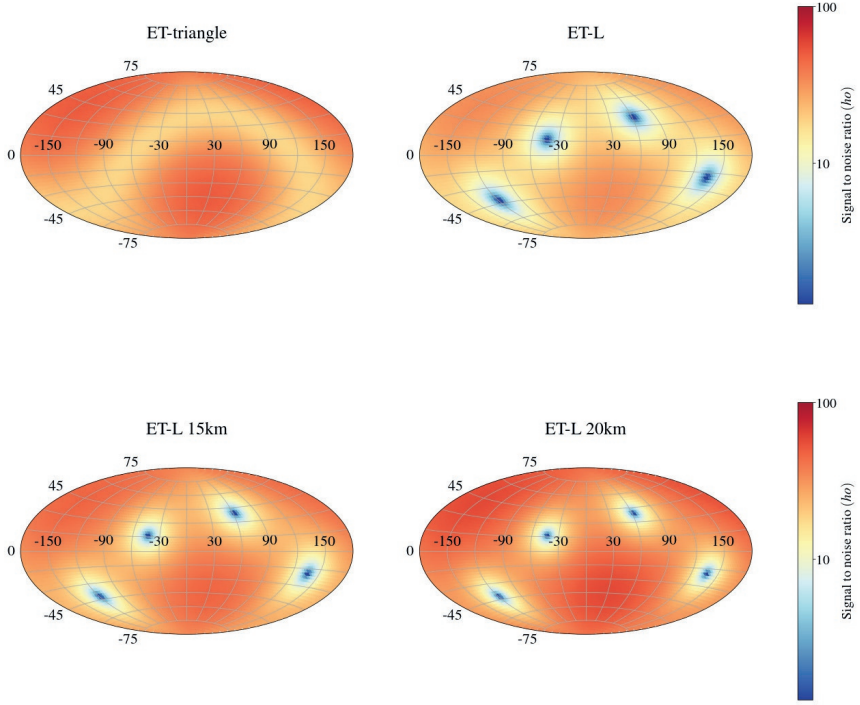
Figure 6.2: Signal-to-noise ratio (SNR) for sources distributed uniformly over the sky. Top left: ET-triangle with a 10 km arm length. Top right: ET-'L' shaped with a 10 km arm length. Bottom left and right: ET-'L' shape with 15 km and 20 km arm lengths, respectively. The color bar illustrates the magnitude of optimal signal-to-noise ratio for a compact binary source situated at the same luminosity distance and positioned at the corresponding point.

6

The x-axis represents the magnitude of the SNR, while the y-axis displays the fraction of uniformly distributed sources across the sky with an SNR greater than or equal to the corresponding value on the x-axis. It's important to note that the chosen luminosity distance of the source influences the SNR values. In the case of an 'L' shaped Einstein Telescope with a 10 km arm length, the SNR starts from zero and gradually rises to a maximum value of approximately 32, depending on the luminosity distance of the source. A higher maximum SNR indicates a greater sensitivity of the detector. This is reflected in the curve shifting
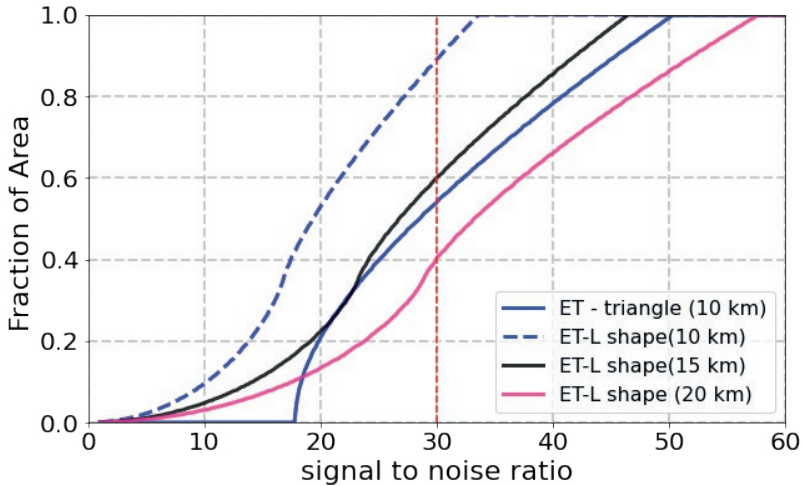
Figure 6.3: Cumulative distribution plot illustrating the distribution of sources based on their signal-to-noise ratio (SNR), derived from the SNR distribution shown in figure 6.2. The plot represents the cumulative fraction of sources distributed uniformly across the sky, with the x-axis indicating the magnitude of the SNR and the y-axis representing the fraction of sources with an SNR greater than or equal to the corresponding value on the x-axis.

towards the right, indicating a higher SNR can be achieved. For the 'L' shaped Einstein Telescope with arm lengths of 10 km, 15 km, and 20 km, the maximum signal-to-noise ratio values are approximately 35, 45, and 55 respectively. This indicates an improvement in sensitivity and the ability to detect weaker signals with higher precision as the arm length increases. Comparatively, the triangular configuration of the Einstein Telescope with a 10 km arm length yields a maximum SNR close to 50. Notably, there are no sources with a zero SNR for the triangular configuration, as the minimum SNR starts above 15 for this particular source, indicating a favorable baseline sensitivity. The reference line at an SNR value of 30 provides valuable information about the detectability of gravitational wave sources. In the case of ET-L shaped with a 10 km arm length, it indicates that 95% of sources distributed uniformly across the sky will have an SNR less than 30. This implies that only 5% of the sky area will allow for the detection of sources with an SNR greater than 30.

When considering ET-'L' with 15 km and 20 km arm lengths, we find that approximately 40% and 60% of the uniformly distributed sources, respectively, will be detectable with an optimal SNR greater than 30. In other words, for ET-'L' with a 15 km arm length, 40% of the sky area will contain sources that can be detected with an SNR above 30. Similarly, for ET-'L' with a 20 km arm length, the coverage increases to 60% of the sky area. Comparatively, the ET triangle configuration performs slightly better than ET-'L' with a 15 km arm length in terms of the percentage of sources detectable with an SNR above 30. However, it is not as effective as ET-'L' with a 20 km arm length, which provides a higher percentage of detectable sources.

6.3 Maximum detectable redshift for compact binary sources

In this section, we explore the the maximum attainable redshift by the 3G detectors for compact binary sources, versus the total mass for various detectors [114]. The horizon distance of a detector is defined as the distance at which a source is just at the detection threshold, represented by a signal-to-noise ratio (ρ_{th}) of 8 when optimally overhead. In this analysis, we consider binary systems with equal masses and assume that they are non-spinning. The mass range of the binary systems spans from 1 solar mass ($M_\odot$) to 1000 $M_\odot$.

Figure 6.4 showcases the maximum redshift achievable by various detectors. The yellow curve represents the Cosmic Explorer, while the solid blue curve corresponds to the Einstein Telescope with a triangular topology. Additionally, the blue dashed curve represents the Einstein Telescope with an 'L' shape, assuming a fixed arm length of 10 km. Furthermore, we depict the horizon redshift for the 'L'-shaped Einstein Telescope with arm lengths of 15 km (black curve) and 20 km (red curve). Analyzing the plot, we observe interesting trends. The horizon distance of the Cosmic Explorer is generally lower than that of the Einstein Telescope for higher mass binaries, primarily due to the superior low-frequency sensitivity of the latter. Additionally, the Einstein Telescope with a triangular topology exhibits a greater reach than its 'L'-shaped counterpart with 10 km or 15 km arm lengths. However, the 'L'-shaped configuration with a 20 km arm length demonstrates a slightly better reach compared to the triangular configuration.
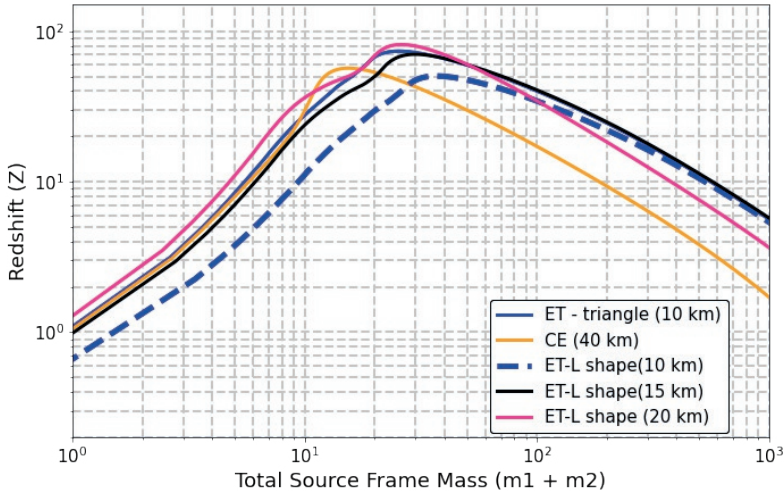
Figure 6.4: Maximum attainable redshift for the compact binary sources versus it's total mass (in the source frame) with the third-generation gravitational wave detectors: the Einstein Telescope and the Cosmic Explorer. The binary systems considered here are of equal mass and non-spinning. The sensitivity curves for the Cosmic Explorer and the Einstein Telescope with different arm lengths are shown in figure 6.1. The blue solid and dashed curves represent the maximum redshift attainable by the ET with triangular and 'L' configurations, respectively. The orange curve corresponds to the Cosmic Explorer. The black and red curves indicate the ET with an 'L' configuration and arm lengths of 15 km and 20 km, respectively. Higher reach values indicate greater sensitivity of the detectors.

6.4 Network of detectors

In this section, we focus on the network of detectors used in our analysis, specifically the third-generation gravitational wave ground-based detectors, namely the Einstein Telescope and Cosmic Explorer. The Einstein Telescope employs a xylophone configuration, which consists of two interferometers per detector optimized for different frequency ranges: low frequencies (LF) and high frequencies (HF). For our analysis, we utilize the design sensitivity curve (ET-D) specifically optimized for both high and low frequencies. We aim to compare two different topologies of the

Einstein Telescope: the 'Triangular' configuration and the 'L' shaped configuration. In the 'Triangular' configuration, we assume an interferometer arm length of 10 km. For the 'L' configuration, we consider various arm lengths, including 10 km, 15 km, and even 20 km. Based on these configurations, we examine two distinct types of networks, as illustrated in figure 6.5. For each network, we have evaluated the performance using two types of sources. The first type is modeled sources, where we can accurately model the waveform based on the known source parameters. The second type is unmodeled sources, where we lack detailed knowledge of the waveform.
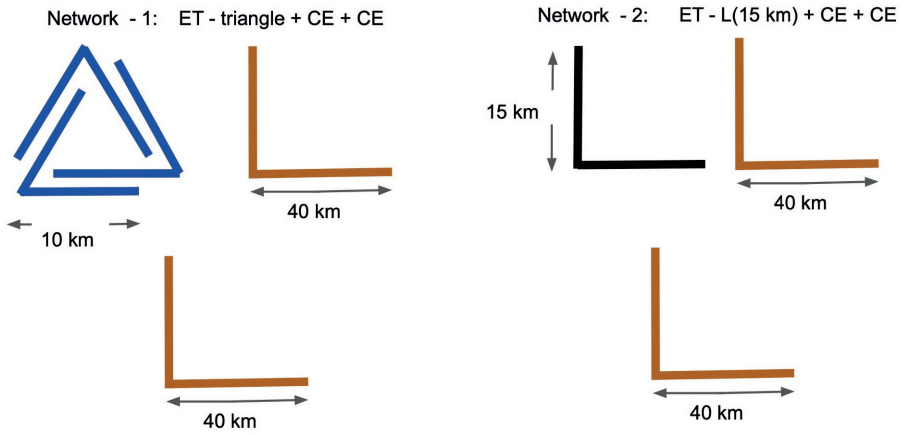
Figure 6.5: Different network configurations considered in our analysis. (a) Network 1: Einstein Telescope in a 'Triangular' configuration with two Cosmic Explorers. (b) Network 2: Einstein Telescope in an 'L' shaped configuration with a 15 km arm length, accompanied by two Cosmic Explorers. (c) Network 3: Einstein Telescope in an 'L' shaped configuration with a 20 km arm length, along with two Cosmic Explorers.

6

6.4.1 Network-1

Our network configuration for Network-1 includes the Einstein Telescope in a triangular configuration and two Cosmic Explorers. The Einstein Telescope is assumed to be located at the same position as Virgo, while the Cosmic Explorers are positioned at LIGO Hanford and LIGO Livingston. The design sensitivity curves for the Einstein Telescope and Cosmic Explorer can be seen in figure 6.1.

6.4.2 Network-2

In Network-2, we assume the network with the Einstein Telescope as a single 'L' shaped detector and two Cosmic Explorers. The arm lengths of the Einstein Telescope are considered to be $10 \, \text{km}$, $15 \, \text{km}$, and $20 \, \text{km}$, respectively. The location of the detectors remains the same as mentioned earlier.

As mentioned earlier, we calculate the sky localization accuracy for both modeled and unmodeled sources in these configurations. Additionally, we have also computed the sky localisation accuracy results for the network consisting of one Einstein Telescope (triangle) and one Cosmic Explorer. However, we have not considered the network configuration with one Einstein Telescope (L-shaped) and one Cosmic Explorer, as the sky localization for GW sources using only two detectors is limited. With only two detectors, the sky localization of a gravitational wave source is constrained to a ring on the sky, based on the time difference in arrival of the GW signal at the detector sites. Adding a third detector introduces another time delay information, which narrows down the possible sky locations to a smaller region. However, it is important to note that the amplitude of the signal also depends on the directional sensitivity of the detectors, which can provide additional information about the source location. Despite these constraints and partial information, the sky localization achieved using two detectors is not sufficient for conducting multi-messenger astronomy, which requires more precise and accurate localization of the GW source. For comprehensive multi-messenger studies, a network of detectors with improved sensitivity and more detectors in different locations is necessary to achieve better sky localization and enable coordinated observations with other astronomical instruments.

6.5 Mathematical formulation

Let's consider the data from a gravitational wave detector, denoted as $d(t)$, which consists of both the gravitational wave signal $h(t)$ and the noise $n(t)$. Assuming that the gravitational wave signal is a linear combination of the plus and cross polarizations, we can express it as:

$$d(t) = F_+ h_+(t) + F_\times h_\times(t) + n(t), \tag{6.1}$$

where F_+ and $F_\times$ are the antenna pattern factors of the detector for the plus and cross polarizations, respectively. For a network of N_d detectors, the data received by the I-th detector, denoted as $d_I(t + \tau_d)$, is given by:

$$d_I(t + \tau_d) = F_+^I h_+(t) + F_\times^I h_\times(t) + n_I(t + \tau_d),\qquad(6.2)$$

where τ_d is the time delay between the signal arrival times on the detectors, which depends on the separation between them. The antenna pattern factors for the I-th detector are denoted as F_+^I and $F_\times^I$.

The time delay τ_d is determined by the direction to the gravitational wave source $(\hat{n})$ and the separation between the detectors $(\vec{r})$, given by $\tau_d = \frac{\hat{n} \cdot \vec{r}}{c}$, where c is the speed of light. Here, e_+ and $e_\times$ represent the polarization basis vectors, which describe the two orthogonal polarizations of the gravitational wave. The detector tensor D is defined as:

$$D = \frac{\vec{u} \otimes \vec{u} - \vec{v} \otimes \vec{v}}{2}.\qquad(6.3)$$

where $\vec{u}$ and $\vec{v}$ are unit vectors along the arms of the interferometer. The detector tensor captures the directional sensitivity of the detector to the two polarizations of the gravitational wave.

In the frequency domain, the detector data can be expressed as:

$$d_I(\omega) = \int_0^T d_I(t) e^{i\omega t} dt,\qquad(6.4)$$

where $d_I(t)$ is the detector data in the time domain and ω is the angular frequency. T represents the total time duration over which the detector data $d_I(t)$ is being observed. The whitened data set, denoted as $\hat{d}_I(\omega)$, is obtained by dividing the detector data by the square root of the one-sided noise power spectral density $S_I(\omega)$ of the I-th detector:

$$\hat{d}_I(\omega) = \frac{d_I(\omega)}{\sqrt{S_I(\omega)}}.\qquad(6.5)$$

If we assume that the signal duration is short compared to the circular motion of the detector due to the Earth's rotation, then the antenna pattern does not change significantly. Now, for N_d number of detectors, we can express the network of detector data as:

$$\begin{pmatrix} \hat{d}_1(\omega) \\ \hat{d}_2(\omega) \\ ... \\ \hat{d}_{N_d}(\omega) \end{pmatrix} = \hat{A} h(\omega) e^{-i(t_0 + \tau_d)},\qquad(6.6)$$

where $\hat{A}$ is an $N_d \times 2$ matrix that represents the antenna pattern factors weighted by the noise spectral density of the detectors, $h(\omega)$ is the gravitational wave signal in the frequency domain and t_0 is a reference time. $\hat{d}_1(\omega), \hat{d}_2(\omega), ..., \hat{d}_{N_d}(\omega)$ denote the detector data in the frequency domain for each of the N_d detectors. The matrix A can be expressed as:

$$\hat{A} = \begin{pmatrix} F_+^1/\sqrt{S_1(\omega)} & F_\times^1/\sqrt{S_1(\omega)} \\ F_+^2/\sqrt{S_2(\omega)} & F_\times^2/\sqrt{S_2(\omega)} \\ ..... & ..... \\ F_+^{N_d}/\sqrt{S_{N_d}(\omega)} & F_\times^{N_d}/\sqrt{S_{N_d}(\omega)} \end{pmatrix} \tag{6.7}$$

where $F_+^I/\sqrt{SI(\omega)}$ and $F_\times^I/\sqrt{S_I(\omega)}$ are the antenna pattern factors divided by the square root of the noise power spectral density for the I-th detector.

The gravitational wave signal vector, denoted as h, is given by:

$$\vec{h} = \begin{pmatrix} h_+ \\ h_\times \end{pmatrix}. \tag{6.8}$$

The matrix $\hat{A}$ depends on the source position and its polarization angle, and since we divide the antenna pattern factor by the detector noise spectral density, $\hat{A}$ is also a function of ω, the angular frequency.

6.6   Fisher Information Matrix

The Fisher information matrix provides a method-independent lower bound for the uncertainty of estimated parameters and quantifies the performance of an estimator. It establishes a relationship between this lower bound and the variance of the estimator. Essentially, the Fisher information matrix serves as a measure of how well our estimator can capture the underlying parameters of interest.

The Cramer Rao bound is a fundamental result in statistical estimation theory. It states that for an unbiased estimator, the covariance matrix denoted as $C(\theta)$ must satisfy the inequality $C(\theta) \leq \Gamma(\theta)$. Here, Θ represents the set of parameters to be estimated, such as θ_1, θ_2, and so on. $\Gamma(\theta)$ represents the Fisher information matrix which quantifies the amount of information available in the data for estimating the parameters. Let's consider a scenario where we are estimating multiple parameters $\theta = \theta_1, \theta_2, \ldots, \theta_n$ from a given dataset. The covariance matrix

$C(\theta)$ is an $n \times n$ symmetric matrix that characterizes the variances and covariances between these estimated parameters. The element in the ith row and jth column of the covariance matrix represents the covariance between the estimated values of θ_i and θ_j. The diagonal elements of the covariance matrix, i.e., C_{ii}, represent the variances of the estimated parameters. They provide information about the spread or dispersion of each individual parameter estimate. A larger variance indicates higher uncertainty or greater variability in the estimated value of the parameter. The off-diagonal elements of the covariance matrix, i.e., C_{ij} where $i \neq j$, represent the covariances between pairs of parameters. These elements indicate the extent to which the estimated values of two parameters vary together. A positive covariance suggests that the parameters tend to increase or decrease together, while a negative covariance indicates an inverse relationship between the parameters. For every pair of corresponding elements in the covariance matrix and the Fisher information matrix, the element in the covariance matrix is either smaller or equal to the element in the Fisher information matrix. More specifically, if we consider the element in the ith row and jth column of the covariance matrix $C(\theta)$, denoted as C_{ij}, and the corresponding element of the Fisher information matrix $\Gamma(\theta)$, denoted as Γ_{ij}, the inequality states that $C_{ij} \leq \Gamma_{ij}$. It implies that the covariance matrix, representing the uncertainty and variability of parameter estimates, cannot exceed the information content provided by the Fisher information matrix.

In scenarios with high signal-to-noise ratio (SNR) and under the assumption of Gaussian noise, an interesting relationship emerges. The covariance matrix that characterizes the statistical error of the estimated parameters can be approximated as the inverse of the Fisher information matrix, $(\Gamma^{-1})_{ij}$. This approximation suggests that in high SNR conditions with Gaussian noise, the precision of parameter estimation is inversely related to the Fisher information matrix.

For Gaussian noise, the optimal signal-to-noise ratio (SNR) can be defined as the inner product between the whitened data. Mathematically, this can be expressed as:

$$\rho_I^2 = \langle \hat{d}_I | \hat{d}_I \rangle \tag{6.9}$$

Here, $\hat{d}_I$ represents the whitened data, which is the observed data after being preprocessed to remove the frequency-dependent noise properties.

The Fisher information matrix for a parameter θ can be defined as:

$$\Gamma_{ij} = \langle \frac{\partial \hat{d}}{\partial \theta_i} | \frac{\partial \hat{d}}{\partial \theta_j} \rangle \tag{6.10}$$

This matrix quantifies the information content of the observed data regarding the parameter of interest. It involves taking the inner product between the partial derivatives of the observed data with respect to the parameters θ_i and θ_j.

To calculate the angular resolution for a network of detectors, we can estimate the Fisher information matrix for the corresponding parameters. If (θ, ϕ) represents the actual source direction, we can calculate the error solid angle which gives us the range within which the estimated source direction could deviate from the true direction helps us to understand how good we are at pointing to the direction of the source. The error solid angle (measured in steradian) can be expressed as:

$$\Delta\Omega = 2\pi\sqrt{\Delta\theta^2\,\Delta\phi^2 - \langle\Delta\theta\Delta\phi\rangle^2} = 2\pi\sqrt{det\left(\Gamma^{-1}\right)} \tag{6.11}$$

Here, $\Delta\theta$ and $\Delta\phi$ represent the errors in estimating the angular components of the source direction. The term $\langle\Delta\theta\Delta\phi\rangle$ denotes the covariance between these errors. The error solid angle, $\Delta\Omega$, provides a measure of the uncertainty in determining the source direction. It is related to the inverse of the covariance matrix, which is equivalent to the Fisher information matrix Γ. In summary, the error solid angle, determined by the Fisher information matrix and covariance between angular errors, provides valuable information about the angular resolution of a network of detectors in estimating the source direction. It quantifies the uncertainty in determining the source direction and serves as an indicator of the precision of the estimation procedure.

6.7 Sky localisation accuracy

6.7.1 Unmodelled Sources

When a gravitational wave is detected, each detector receives a slightly different version of the signal due to its location and orientation. By combining the data from multiple detectors, it is possible to extract information about the source direction of the gravitational wave. To achieve sky localization, the idea is to construct a null stream that captures the common features shared by the detectors' data but eliminates

any contribution from the gravitational wave signal itself. This null stream is designed in such a way that it becomes truly null when the source direction is correctly determined. The null space projection technique is particularly useful for short-duration signals, as it does not depend on Earth's rotation during the time span of the signal. It allows us to extract the directional information of the gravitational wave source from the network of detectors, even when the exact waveform of the signal is unknown. The work by Gürsel and Tinto (1989) [110] has demonstrated the sky localization technique using the null stream approach, which we discussed earlier. This technique is further discussed in the next chapter.

In this context, the Fisher matrix for the sky localization problem can be expressed as:

$$\Gamma_{jk} = \langle (\partial_{n_j}\phi)d | (I - P)\,(\partial_{n_k}\phi)d \rangle \tag{6.12}$$

Detailed derivation can be found in [221]. Here, I is the identity matrix and P is a $N_d \times N_d$ matrix, functioning as the projection operator into the whitened signal space. It can be expressed as:

$$P = A(A^T A)^{-1} A^T \tag{6.13}$$

In this equation, A represents a matrix related to the detector network configuration. The matrix $(I - P)$ projects the data into the null space. The projected data contains only noise when projected along the actual position of the source and the signal will cancel out. This is because the null stream construction ensures that the signal component is eliminated, leaving only the noise contribution.

The sky localization error, denoted as $\Delta\Omega$, can be computed using the following equation:

$$\Delta\Omega = 2\pi \left(det\,\Gamma\right)^{-\frac{1}{2}} \tag{6.14}$$

In this equation, $det\,\Gamma$ represents the determinant of the Fisher matrix Γ, which provides the precision of the sky localization. The expression for $det(\Gamma)$ is given by:

$$det(\Gamma) = \frac{1}{8c^4} \sum_{J,K,L,M} \Delta_{JK}\,\Delta_{LM} |(\vec{r}_{JK} \times \vec{r}_{ML}) \cdot \hat{n}|^2 \tag{6.15}$$

Here, the indices J, K, L, and M range from 1 to N_d, representing the detectors in the network. The term Δ_{JK} can be interpreted as the

projection of the whitened data correlation between the J-th and K-th detectors while being projected into null space. Mathematically, it can be expressed as:

$$\Delta_{JK} = (\delta_{JK} - P_{JK}) \left(2 \int_{-\infty}^{\infty} \hat{d}_J^* \, \hat{d}_K \, \omega^2 \frac{d\omega}{2\pi} \right) \tag{6.16}$$

The term $(\vec{r}_{JK} \times \vec{r}_{ML}) \cdot \hat{n}$ represents the area resulting from the projections of detectors J, K, L, and M onto the plane that is perpendicular to the direction of gravitational wave propagation($\hat{n}$). This indicates that if the direction of propagation of the gravitational wave signal lies in the plane of the detector, the resulting localization accuracy achieved by the network will be lowered. By evaluating $\det \Gamma$ using the given expression and plugging it into the equation for $\Delta\Omega$, we can calculate the sky localization error. This error represents the uncertainty in determining the source location in terms of solid angle, providing insights into the precision of the sky localization method based on the null stream approach.

6.7.2 Modelled Sources

Now let us explore the best-case scenario where we have a known waveform for the gravitational wave signal, but the arrival time of the signal remains unknown. In this scenario, we can make use of the known waveform to optimize the sky localization process and achieve higher precision.

By having access to the waveform, we can analytically calculate the determinant of the Fisher information matrix, denoted as $\det \Gamma$, which can be expresssed as:

$$\det \Gamma = \frac{1}{8c^4} \sum \frac{\xi_J \, \xi_K \, \xi_L \, \xi_M \, |(\vec{r}_{JK} \times \vec{r}_{LM}) . \hat{n}|^2}{(\sum_{I=1}^{N_d} \xi_I)^2} \tag{6.17}$$

ξ_I represents the noise-weighted energy flux received by the detector I. The term ξ_I can be calculated as:

$$\xi_I = 2 \int_{-\infty}^{\infty} \frac{d\omega}{2\pi} \omega^2 \, |\hat{d}_I|^2 \tag{6.18}$$

This formulation allows us to compute the angular resolution of modelled sources for a network of detectors. In the case of a network with

two detectors, only one-dimensional angular resolution is possible. The uncertainty in 1D angular resolution can be determined from the trace of the Fisher information matrix:

$$\Delta\Theta = \frac{2c}{\sqrt{\xi_1 + \xi_2}\, D_\perp} \sqrt{\frac{1}{\xi_1\, \xi_2/(\xi_1 + \xi_2)^2}} \tag{6.19}$$

Here, $D_\perp$ represents the projection of the distance between the two detectors onto the plane perpendicular to the direction of propagation.

By employing the equations mentioned above, we can evaluate the angular resolution of modelled sources within a network of detectors. The angular resolution provides information about the uncertainty in determining the source direction and contributes to the understanding of the performance and capabilities of the detector network.

6.8 Results

In this section, we present the computed sky localization accuracy for both modeled and unmodeled gravitational wave sources for the network discussed in 6.4. We assess the angular resolution for all possible sky locations, considering the same gravitational wave source.

Figure 6.6 illustrates the sky localization accuracy for the detector network consisting of the Einstein Telescope with a triangular configuration and the Cosmic Explorer. This analysis explores scenarios where the gravitational wave source can either be modeled or unmodeled. On the left side, we have the modeled case, where the waveform of the gravitational wave source is known. The color bar represents the sky localization accuracy, labeled as $\Delta\Omega$. Each point on the graph corresponds to a specific direction in the sky. The value associated with each point indicates the error in estimating the source's location when it originates from that particular direction. The differences between the modeled and unmodeled scenarios highlight the importance of waveform knowledge in achieving higher directional precision. In the modeled case, when we know the exact waveform of the gravitational wave signal, we can make more precise predictions about its behavior and, consequently, its source location in the sky. In contrast, without a waveform model, our ability to accurately determine the source direction becomes less certain, resulting in a potentially larger localization error.
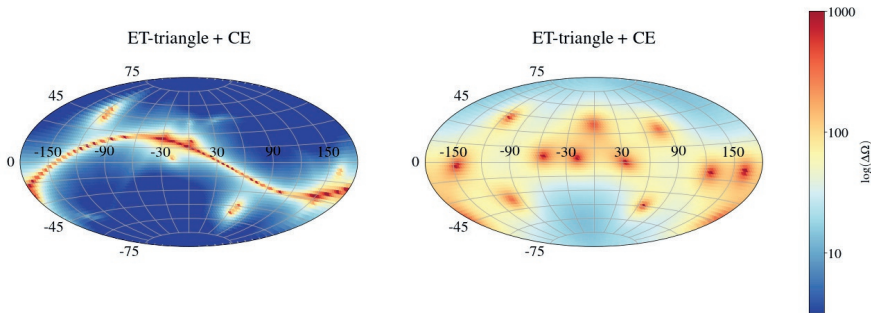
Figure 6.6: Directional precision for modeled and unmodeled gravitational wave signals in the detector network consisting of the Einstein Telescope with a proposed triangular configuration and the Cosmic Explorer. The plot shows the sky localization error for the modeled case (left) and the unmodeled case (right), indicating the accuracy of determining the source direction. The color bar represents the sky localization accuracy ($\Delta\Omega$), with lower values indicating higher precision. We have considered that the locations of the ET and CE correspond to the positions of Virgo and LIGO Hanford, respectively.

We have computed the sky localization accuracy for various networks comprising different configurations of the Einstein Telescope and two Cosmic Explorers, as discussed in Section 6.4. In figure 6.7, we present the results for the sky localization accuracy specifically considering an unmodeled gravitational wave source. The figure shows graphical representations of the directions from which the gravitational wave signal can propagate, with a color bar indicating the level of error in estimating the position of the gravitational wave source. Upon analyzing the results, it is evident that the overall angular resolution of the ET with a triangular configuration outperforms the ET with an 'L'-shaped detector configuration of varying arm lengths.

To provide a quantitative demonstration, we present the cumulative fraction of sources in figure 6.8. The X-axis represents the uncertainty in sky localization ($\Delta\Omega$), while the Y-axis represents the fraction of the sky area with an error in localization less than or equal to $\Delta\Omega$.

For reference, let's consider the value of 20 deg^2 along the X-axis. For the ET with a triangular configuration, approximately 70% of the
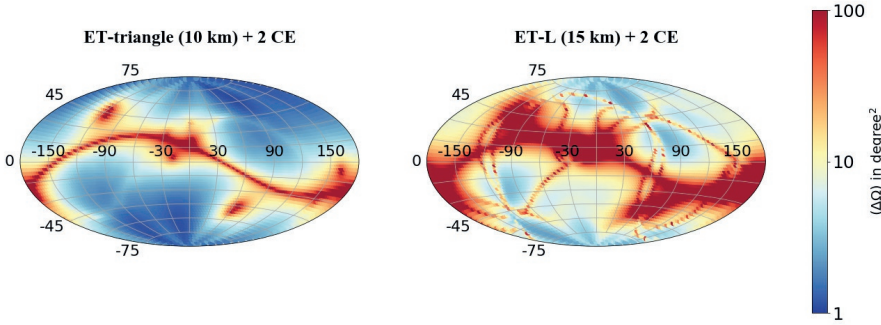
Figure 6.7: This plot depicts the directional precision of the detector network for unmodeled gravitational wave signals. On the left side, the plot illustrates the sky localization error for the ET with a triangular configuration (arm's length $10\,\mathrm{km}$) and two Cosmic Explorers ($40\,\mathrm{km}$ each) located at the Hanford and Livingston sites. On the right side, the plot displays the localization accuracy for an unmodeled source using the same network but with an ET configured as an 'L' shape and an arm length of $15\,\mathrm{km}$. The color bar represents the sky localization accuracy ($\Delta\Omega$), where each point in the plot indicates the error in the sky localization of the gravitational wave source arriving from the corresponding direction.
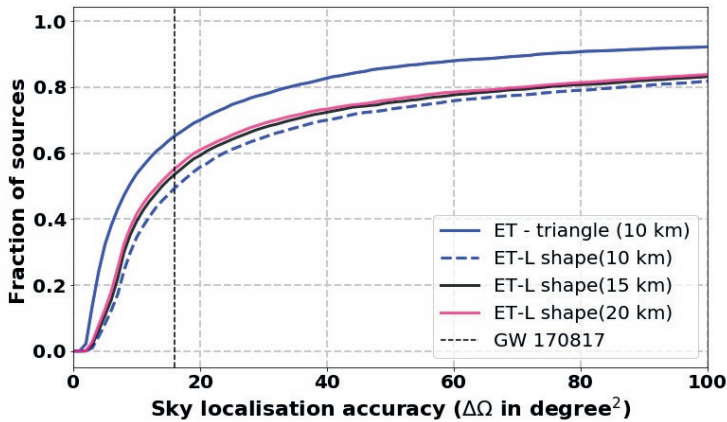
Figure 6.8: This plot illustrates the fraction of the sky area that exhibits specific sky localization errors along the x-axis. The black and pink trace lines represent the cumulative distribution of sky localization errors for the network consisting of the Einstein Telescope with an 'L'-shaped configuration, with arm lengths of 15 km and 20 km respectively, along with two Cosmic Explorer-like detectors. Additionally, the blue solid and dashed lines depict the cumulative distribution for the ET with a triangular configuration (10 km arm length) and the ET with an 'L'-shaped configuration (10 km arm length), both in combination with two Cosmic Explorer-like detectors. The black dashed line serves as a reference, representing the sky localization accuracy associated with GW170817 [16].

sky area exhibits a better accuracy in directional uncertainty, with errors below 20 deg^2. On the other hand, for the ET with an 'L'-shaped configuration (20 km arm length), this percentage decreases to 60%. It's worth noting that the directional precision of the ET with an 'L'-shaped configuration improves with longer arm lengths due to the increased sensitivity. However, the improvement is not as significant because we have considered the ET in the network alongside two CE-like detectors. These findings highlight the advantages of the ET with a triangular configuration in achieving better angular resolution compared to the ET with an 'L'-shaped configuration. The presence of additional detectors in the network, similar to the CE, contributes to the improved localization performance.

The directional precision results for modeled sources are depicted in figure 6.9. The sky localization error, as represented by the color bar in the plot, provides a quantitative measure of the uncertainty in determining the source direction. Lower values on the color bar indicate higher precision in localizing the source. It is evident from the plot that the network with the ET triangular configuration achieves higher accuracy compared to the ET-'L' configuration with 15 km arm lengths.

To provide a quantitative analysis, we present the cumulative distribution plot in figure 6.10, which is similar in format to figure 6.8. The X-axis in this plot represents the uncertainty in sky localization for the modeled source. Once again, we observe that the accuracy is better for the network with the ET triangular configuration when compared to the 'L' configuration.

6
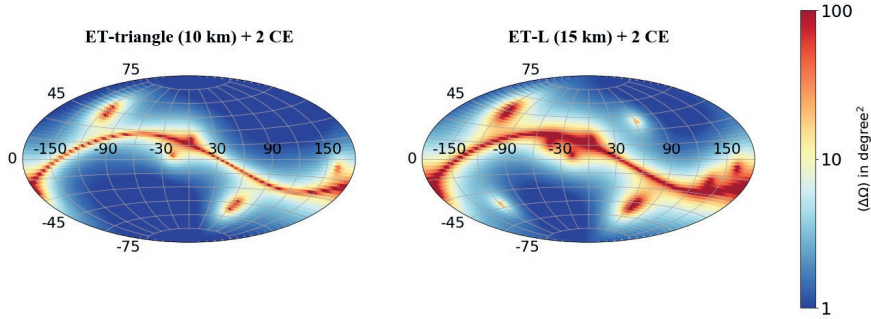
Figure 6.9: This plot illustrates the directional precision of the network of detectors for modeled gravitational wave signal. The left panel shows the sky localization error for the Einstein Telescope with a triangular configuration (10 km arm length) and two Cosmic Explorers (40 km arm length) positioned at the Hanford and Livingstone sites. The right panel displays the sky localization error for the ET-'L' configuration with a 15 km arm length. The color bar represents the value of sky localization accuracy ($\Delta\Omega$), where lower values indicate higher precision in localizing the gravitational wave source. Each point in the plot corresponds to the error in the sky localization when the gravitational wave signal arrives from a specific direction. Overall, the plot demonstrates that the triangular configuration of the ET yields better sky localization accuracy within the considered network.

6.9 Discussion

In this chapter, I have shown the angular resolution for both modeled and unmodeled gravitational wave sources, considering different configurations of the Einstein Telescope along with two Cosmic Explorer detectors. My findings demonstrate that, within the network involving two CE detectors, the ET-triangular configuration offers superior angular resolution compared to ET-'L' shaped detector with a 15 km arm length. This trend is consistent for both modeled and unmodeled sources.

One advantage of the ET-triangular configuration is its intrinsic null stream, which carries information about the detector noise. This enables the estimation of the noise power spectral density and facilitates the distinction between genuine gravitational wave signals and glitches. The null stream contains no signal, making it a valuable tool in the analysis.
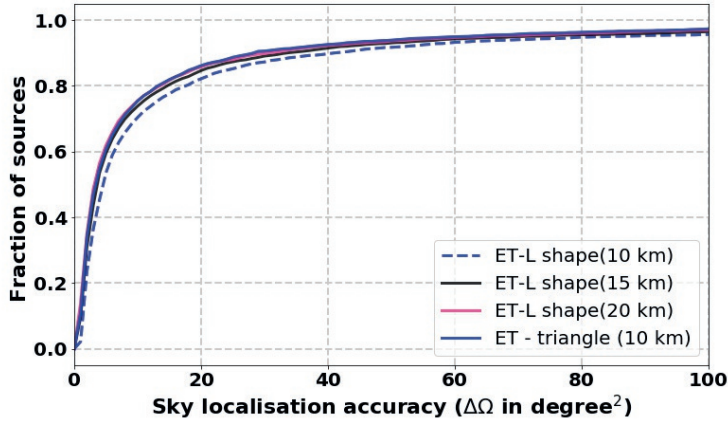
Figure 6.10: This plot displays the cumulative distribution of sky local-ization errors for different configurations of the Einstein Telescope when localizing modeled gravitational wave signals. The X-axis represents the uncertainty in sky localization, similar to figure 6.8. The black and pink trace lines depict a network configuration featuring the ET-'L' with arm lengths of 15 km and 20 km respectively, along with two Cosmic Explorer-like detectors. The blue solid and dashed lines illustrate cumu-lative distributions for the ET triangular configuration and the ET-'L' configuration (both with a 10 km arm length) within the network of two CE detectors. The plot demonstrates that, in the case of modeled sources, the ET-triangle exhibits slightly superior sky coverage compared to the 'L' shape within the network comprising two CE detectors.

This calculations focused on short-duration signals and I did not account for the effect of Earth's rotation. However, for longer duration gravitational wave waveforms originating from low-mass binary systems, it is important to numerically compute the Fisher information matrix, incorporating the variations in antenna patterns due to Earth's rotation.

Several studies have contributed to the understanding of parameter estimation and performance evaluation for future detector networks. In [106], Grimm et al. investigated parameter estimation combining cur-rent (LIGO/Virgo) and future detectors using the Fisher matrix ap-proach, incorporating information from present and future detectors such as ET and LISA. In another study [114], Hall et al. considered numerous possible third-generation detector networks, including Voy-

ager, Einstein Telescope, and Cosmic Explorer detectors, and evaluated their performance based on metrics such as sky localization area, signal-to-noise ratio, and uncertainty in distance and inclination angle. These analyses aid in decision-making for future detector designs, aligning with scientific goals, and expanding our ability to explore the mysteries of the universe.

Overall, this study highlights the importance of network configuration in achieving optimal angular resolution for gravitational wave source localization. By refining our understanding of parameter estimation and performance metrics, we can make informed decisions regarding the design and implementation of future-generation detectors, maximizing their scientific potential and unraveling the secrets of the universe.

Chapter 7

Optimizing gravitational wave source sky localization and calibration error using the null stream of the Einstein Telescope

7.1 Introduction

In contrast to the currently operating detectors that use L-shaped interferometers with orthogonal arms, the Einstein Telescope is proposed as a a triangular geometry consisting of six colocated interferometers forming three xylophone detectors, with the arms forming a 60-degree angle [176]. This unique triangular configuration of ET offers several advantages. One notable advantage is the construction of a sky location-independent null stream for detecting gravitational waves.

According to the theory of general relativity, gravitational waves are tensor waves comprising two independent polarisations known as "plus" and "cross". In the context of a network of gravitational wave detectors, when there are more than two independent and non-aligned interferometers, the network becomes over-defined. This means that the network provides more data streams than the independent polarisations of gravitational waves. By combining the outputs of the interferometers in a special way in such a network, it is possible to generate a composite res-

7

ult that does not contain any gravitational wave signal. This composite result is known as a "null stream".

A significant contribution to the understanding and application of null streams in gravitational wave detection was made by Gürsel and Tinto in 1989 [110]. Their work demonstrated that in a general network of gravitational wave detectors, the combination of network outputs that forms the null stream yields a signal contribution of zero only for the precise sky location of the gravitational wave source. This implies that the null stream is location-dependent, and its characteristics can be used to reconstruct both the direction of the source and the time series of gravitational wave strain by minimizing the residual signal present in the null stream.

Expanding on this concept, Wen and Schutz (2005) [222] further developed the utilization of null streams within a redundant network of detectors. They refined the approach by using null streams to test the consistency of a candidate gravitational wave signal and to determine its origin, whether astrophysical or stemming from detector noise. Since the null stream does not contain any gravitational wave signal, the absence of unusual excitation within the null stream serves as an indicator that the event under consideration could indeed be a genuine gravitational wave signal. By analyzing the null stream in a model-independent manner, they established a framework to discriminate between genuine gravitational wave signals and coincidental non-Gaussian noise. The work by Zhu et al. (2015) further emphasized the significance of null streams as a tool for discrimination [230].

The work of Ajith et al. (2006), as described in [29], introduced a statistical approach known as the null stream veto to differentiate genuine gravitational wave triggers from transient noise events. They employed excess power statistics to analyze the null stream, allowing for the identification of significant deviations caused by gravitational waves. This technique provides a means to validate GW signals by examining the absence of excess power in the null stream. The authors also addressed practical challenges associated with implementing the null stream veto. Calibration uncertainties and correlated noise components can introduce complications in the analysis. To overcome these issues, Ajit et al. presented a new formalism that accounts for calibration uncertainties and addresses the impact of correlated noise components. This improved approach enhances the reliability and effectiveness of the null stream veto in distinguishing true GW events from transient noise.

Building upon this work, Chatterjee et al. (2006) further developed the null stream veto technique in [76]. They conducted a more robust analysis that incorporates the effects of calibration uncertainties and transient noise glitches. By considering these factors, their approach offers increased sensitivity and accuracy in identifying genuine GW signals. This advancement addresses practical concerns and improves the applicability of the null stream veto method in real-world gravitational wave detection scenarios.

In the context of the Einstein Telescope, Regimbau et al. [182] demonstrated the application of ET's intrinsic null stream in the first ET mock data challenge analysis. They utilized the ET mock data challenge to simulate gravitational wave signals and corresponding noise in order to assess the performance of ET's null stream in estimating the stochastic background of BBH and BNS. By analyzing the null stream data and employing appropriate statistical techniques, they were able to extract information about the populations of these compact binary systems. In [195], Schutz and Satyaprakash proposed a technique known as self-calibration of the detectors, which utilizes the null stream for modeling calibration errors using detected gravitational wave signals.

In their study discussed in [225], Wong et al. demonstrated a decomposition of the observational space of the Einstein Telescope into two subspaces: the null space and the signal space. The null space refers to the span of the set of independent null streams, which is a combination of detector outputs that cancel out any gravitational wave signal. The signal space is the span of the two gravitational wave signal polarisations of interest. They discussed that the result of Bayesian parameter estimation remains unaffected when considering only the signal space. Analytically proving this result, they showed that discarding the null space and focusing solely on the signal space does not introduce any biases or alter the estimation process. By doing so, one can reduce the memory cost and computational power required for the analysis, as the data from the null stream, which does not contain gravitational wave signals, can be omitted.

Goncharov and Harms, in [104], discuss various approaches developed for utilizing the null stream of the Einstein Telescope. They highlight the versatility of the null stream and its potential applications in gravitational wave analysis. One significant finding presented in their work is that the null stream can be utilized to provide unbiased estimations of the power spectral density (PSD) of each detector within ET. The

7

power spectral density characterizes the distribution of signal power across different frequencies. Accurate estimation of the PSD is crucial for understanding the noise properties of the detectors and distinguishing gravitational wave signals from instrumental artifacts.

In this chapter, I focus on the application of the null stream for source localization of gravitational wave sources using the network of third-generation detectors, specifically the Einstein Telescope and Cosmic Explorer. The proposed topology of the Einstein Telescope, which consists of three xylophone detectors arranged in a unilateral triangle, offers a unique advantage in terms of source localization. The null stream in this configuration does not depend on the sky location of the GW source or any other source parameters, resulting in reduced computational costs [182]. The null stream in this setup primarily contains pure noise from the three interferometers, assuming calibration uncertainties are ignored [195]. By optimally subtracting this pure noise from the data stream output of the entire network, one can reduce one data stream to estimate the sky localization parameters of the source. However, we haven't observed any change or improvement in the sky localisation accuracy. This approach allows us to exploit the benefits of the unique null stream characteristic of the Einstein Telescope configuration.

It is also important to consider potential calibration errors when modeling the strain of the detectors. In such cases, the null stream may contain residual signals due to imperfect cancellation of the gravitational wave signal. Therefore, the null stream can be a valuable tool for probing and refining the calibration error modeling of the detectors. In this context, I discuss the concept of self-calibration, which involves improving the calibration of the detectors based on the detection of astronomical signals. By utilizing the null stream and the detected signals, the self-calibration process enables a more accurate estimation of calibration errors, leading to enhanced precision in gravitational wave measurements.

This chapter is structured as follows. Section 7.2 provides a discussion on the mathematical formulation of the inverse problem of reconstructing GW signals from the data of the network of detectors, laying the foundation for the subsequent analyses. Section 7.3 focuses on the utilization of the Einstein Telescope's intrinsic null stream for noise subtraction during an unmodeled search for the sky location of a gravitational wave source. This involves minimizing the residual in the null stream for the network consisting of ET and Cosmic Explorer (CE). Sec-

tions 7.4 and 7.5 delve into the topic of calibration errors in modeling the strain data obtained from the photodetector of the GW interferometer. The effect of calibration errors on the null stream of ET is discussed. In Section 7.6, the focus remains on the null stream of ET, specifically addressing the impact of calibration errors on its characteristics. Section 7.7 introduces the matched filtering technique as a means to probe the residual signal present in the null stream. Section 7.9 presents the results obtained from finding the optimal filter and discusses the implications and outcomes of the analyses conducted. Finally, in Section 7.10, the chapter concludes with a summary of the key findings and their significance in the context of source localization using the null stream, as well as suggestions for future research directions.

7.2 Exploiting the null stream for sky localization in GW signal reconstruction

In this section, the goal is to develop the mathematical formulation of the sky location-dependent nullstream, incorporating the intrinsic nullstream of the Einstein Telescope. Following up on section 6.5 of chapter 6, one can express equation (6.2) in matrix form as follows:

$$\vec{d}(t + \tau_{d_I}) = \mathbb{F} \cdot \vec{h}(t) + \vec{n}(t + \tau_{d_I}) \tag{7.1}$$

where $\mathbb{F}$ is a $N_d \times 2$ matrix comprised of antenna pattern factors of the individual detectors of the network.

$$\mathbb{F} = \begin{pmatrix} F_+^1 & F_\times^1 \\ F_+^2 & F_\times^2 \\ ..... & ..... \\ F_+^{N_d} & F_\times^{N_d} \end{pmatrix} \tag{7.2}$$

$\vec{h} = \begin{pmatrix} h_+ \\ h_\times \end{pmatrix}$ is the vector of GW polarisation components, and $\vec{n}(t + \tau_{d_I})$ is the vector of pure noise contributions from each of the detectors of the network. The inverse problem of reconstruction of GW signals from the data $\vec{d}(t + \tau_{d_I})$ of the network of N_d GW detectors [179] can be formulated as follows: one needs to find the gravitational-wave amplitudes $\vec{h}(t) = h_+(t), h_\times(t)$ and the source location in the sky i.e declination(θ_s) and right ascension(ϕ_s) by solving the following (overdetermined) system of linear equations

$$\mathbb{F}(\theta_s, \phi_s) \cdot \vec{h}(t) = \vec{d}(t + \tau_{d_I}) \tag{7.3}$$

where $\vec{d}(t+\tau_{d_I})$ is contaminated by the noise of the corresponding detectors. In general, the problem is ill-posed since the matrix F is not square and thus not invertible. In order to solve for $\vec{h}(t)$ one could seek for the functions $\vec{h}(t)$ that minimize the so-called residual function $R(\theta, \phi)$ can be expressed as

$$R(\theta, \phi) = \left\| (\vec{d}(t + \tau_{d_I}) - \mathbb{F}(\theta, \phi) \cdot \vec{h}(t)) \right\|^2 \tag{7.4}$$

This function is not only dependent on and minimal for a true GW signal waveform $\vec{h}$ but also carries the dependence on the sky location of the source through $\mathbb{F}(\theta, \phi)$ and thus can be used to find the true location of the source, (ϕ_s, θ_s). From the mathematics perspective, minimizing the residual is equivalent to the projection of detectors' data on the null space of the GW signal in the N_d-dimensional space of the network data outputs.

As shown by Sutton *et al.*[204] the above formulation of the inverse problem for a gravitational wave signal is particularly useful for detecting burst sources. Using the above formalism one can construct a source location-dependent null stream from the combination of the detector data, which turns to null (zero signal) once one gets the propagation direction of the GW source right without even having to detect the GW signal waveform. For N_d detectors, there are, in general, $(N_d - 2)$ source location-dependent null streams assuming the two independent polarisations of GW strain. E.g. in the case of three non-aligned detectors, there should be one source location-dependent null stream, which can be written as [220]

$$\mathcal{N}(\theta, \phi) = A_{23}\, d_1(t) + A_{31}\, d_2(t + \tau_{12}) + A_{12}\, d_3(t + \tau_{13}). \tag{7.5}$$

Here, τ_{12} and τ_{13} are the time delays between detectors 1 and 2 and detector 1 and 3, respectively. The coefficients A_{ij} are defined as:

$$A_{ij} = F_i^+ F_j^\times - F_i^\times F_j^+. \tag{7.6}$$

The coefficients A_{ij} depend on the sky position i.e.(θ, ϕ). One can also construct a null stream by performing the singular value decomposition of $\mathbb{F}$ and recombine the detector data so that this becomes null for the

actual source location [222]. Hence, $\mathbb{F} = \mathbb{U}\mathbb{S}\mathbb{V}^+$, where:

$$\mathbb{S} = \begin{pmatrix} s_1 & 0 \\ 0 & s_2 \\ 0 & 0 \\ ..... & ..... \\ 0 & 0 \end{pmatrix} \tag{7.7}$$

Here, s_1 and s_2 are two singular values with $s_1 \geq s_2$. Matrices $\mathbb{U}$ and $\mathbb{V}$ are unitary with dimensions $N_d \times N_d$ and 2×2, respectively. The new data streams can be written as

$$\mathbb{U}^T \cdot \vec{d} = \mathbb{S}\mathbb{V}^T \cdot \vec{d}. \tag{7.8}$$

Hence, we see that the first two rows of the $\mathbb{U}^T \cdot \vec{d}$ simply project the data into the signal space (corresponding to two non-zero singular values), and the remaining rows represent the null space $N(\Omega)$. Hence we can write,

$$N(\Omega) = \begin{pmatrix} (\mathbb{U}^T d)_3 \\ (\mathbb{U}^T d)_4 \\ .... \\ (\mathbb{U}^T d)_{N_d} \end{pmatrix} = \mathbb{U}_{null} \cdot \vec{d} \tag{7.9}$$

7.3 Optimisation of the 3G network null stream using Einstein Telescope's intrinsic null stream

The triangular geometrical configuration of the Einstein Telescope offers a unique advantage in the form of a null stream, which contains combined noise information from three detectors. This null stream is an inherent property of the ET's triangular shape and is independent of the source location. Let's consider the data stream from the output of the three detectors in the ET network:

$$\begin{aligned} d_1^{ET} &= h_1^{ET} + n_1^{ET} \\ d_2^{ET} &= h_2^{ET} + n_2^{ET} \\ d_3^{ET} &= h_3^{ET} + n_3^{ET} \end{aligned} \tag{7.10}$$

Here, h_I^{ET} represents the gravitational wave signals and n_I^{ET} represents the noise of each corresponding detector in the ET network. The

triangular geometry of the ET implies that the sum of the gravitational wave signals from the three detectors is zero:

$$h_1^{ET} + h_2^{ET} + h_3^{ET} = 0 \tag{7.11}$$

As a result, when we add up all the data streams from the ET network, the signal content in the sum cancels out, leaving only the sum of the three noise terms:

$$\mathcal{N}^{ET} = n_1^{ET} + n_2^{ET} + n_3^{ET} \tag{7.12}$$

As $\mathcal{N}^{ET}$ doesn't contain any signal, we can rewrite the source location dependent null stream $N_\alpha(\theta, \phi)$ from equation 7.9, after optimally subtracting $\mathcal{N}^{ET}$.

$$N_\alpha'(\theta, \phi) = N_\alpha(\theta, \phi) - C_\alpha \mathcal{N}^{ET} \tag{7.13}$$

To determine the coefficients C_α, we employ a strategy of minimizing the variance of the noise for the estimator. Under the assumption of a zero-mean noise with known variances σ_i^2, we define the modified null stream $N_\alpha'(\theta, \phi)$ as the original null stream $N_\alpha(\theta, \phi)$ minus the weighted sum of the detector outputs i.e. d_1^{ET}, d_2^{ET}, and d_3^{ET}, where the weights are represented by the coefficients C_α. This is expressed mathematically as:

$$N_\alpha'(\theta, \phi) = N_\alpha(\theta, \phi) - C_\alpha \left(d_1^{ET} + d_2^{ET} + d_3^{ET} \right) \tag{7.14}$$

Here, α ranges from 3 to $(N_d - 2)$, as $\alpha = 1$ and $\alpha = 2$ correspond to the signal space. The variance of the data time series $x(t)$ over a total duration T is defined as $\sigma^2 = \frac{1}{T} \int_0^T x(t)^2 \, dt$.

For example, we consider a network consisting of one ET with a triangular configuration ($10\,\text{km}$ arms) and one CE with $40\,\text{km}$ arms. It's important to note that this configuration is presented as an illustrative case, and the analysis can be generalized for a network comprising an ET-triangle and any number of CE-like detectors. The expression for $N_\alpha(\theta, \phi)$ involves the linear combination of the detector outputs d_1^{ET}, d_2^{ET}, d_3^{ET}, and d_4^{CE}, weighted by the coefficients U_α^1, U_α^2, U_α^3, and U_α^4, respectively. It can be written as:

$$N_\alpha(\theta, \phi) = U_\alpha^1 d_1^{ET} + U_\alpha^2 d_2^{ET} + U_\alpha^3 d_3^{ET} + U_\alpha^4 d_4^{CE} \tag{7.15}$$

The variance of the modified null stream N_α' is determined by the sum of squared differences between the weights U_α^1, U_α^2, U_α^3, and C_α, each

multiplied by the corresponding noise variances σ_1^2, σ_2^2, and σ_3^2 (where σ_1, σ_2, and σ_3 represent the variances of the noise terms from the three detectors of the Einstein Telescope, respectively), along with the noise variance σ_4^2 itself.

$$\sigma_{N'_\alpha}^2 = (U_\alpha^1 - C_\alpha)^2 \, \sigma_1^2 + (U_\alpha^2 - C_\alpha)^2 \, \sigma_2^2 + (U_\alpha^3 - C_\alpha)^2 \, \sigma_3^2 + \sigma_4^2 \quad (7.16)$$

The coefficients C_α can be determined by minimizing $\sigma_{N'_\alpha}^2$. Specifically, C_α is computed as a weighted sum of the products between the weights $U_{\alpha i}$ and the corresponding noise variances σ_i^2, divided by the sum of the noise variances σ_i^2:

$$C_\alpha = \frac{U_\alpha^1 \, \sigma_1^2 + U_\alpha^2 \, \sigma_2^2 + U_\alpha^3 \, \sigma_3^2}{\sigma_1^2 + \sigma_2^2 + \sigma_3^2} \quad (7.17)$$

In our analysis, we have assumed no correlations between the noise of the individual detectors. However, in practice, due to shared seismic environments, it is reasonable to expect some degree of correlation among interferometers located in the same tunnels. To account for these correlations, we introduce a covariance matrix $\Sigma_{jk} = \langle n_j | n_k \rangle$ [187].

The optimized null combination of the data in the general case can be expressed as:

$$N' = \mathbb{U}'_{null} \cdot \vec{d}, \quad (7.18)$$

where:

$$\vec{d} = \begin{pmatrix} d_1^{ET} \\ d_2^{ET} \\ d_3^{ET} \\ d_4 \\ .... \end{pmatrix} \quad (7.19)$$

and

$$\mathbb{U}'_{null} = \mathbb{U}_{null} - Cq. \quad (7.20)$$

Here, $\mathbb{U}_{null} \subset \mathbb{U}^T = (u_{ij}^T)$, $i = 3, 4 ... N_d$ and $\mathbb{U}$ can be found from the singular value decomposition (SVD) of F i.e. $\mathbb{F} = \mathbb{U}\mathbb{S}\mathbb{V}^+$, where U and V are unitary matrices, and S is a diagonal matrix containing the singular

7

values [219, 218].

Optimized coefficient matrix C can be expressed as:

$$C^T = \begin{pmatrix} C_1 & C_2 & C_3 & C_4 & .. & C_{N_d-2} \end{pmatrix}_{1 \times (N_d-2)}$$

and

$$q = \begin{pmatrix} 1 & 1 & 1 & 0 & .. & 0 \end{pmatrix}_{1 \times N_d}.$$

One can express the variance of N' as:

$$\langle (N')^2 \rangle = (\mathbb{U}')^T \Sigma \, \mathbb{U}' = (\mathbb{U} - Cq)^T \Sigma \, (\mathbb{U} - Cq), \tag{7.21}$$

where Σ is the covariance matrix which will be diagonal for the assumption that there are no correlations between the noise of the three nested ET detectors. In case of the presence of correlations the covariance matrix will not be diagonal and it will have off-diagonal components consisting of the cross-covariance of noise.

The values of the coefficients can be fixed from the optimization problem of the noise covariance matrix. This results in:

$$q \, \Sigma \, (\mathbb{U} - Cq) = 0 \tag{7.22}$$

which leads to:

$$C = \frac{q^T \, \Sigma \, \mathbb{U}}{q^T \, \Sigma \, q}. \tag{7.23}$$

Hence, after subtracting the intrinsic null stream of the ET, we observe the optimization of the null operator. In this specific example, considering one ET and one CE-like detector, we have a total of four detectors in the network. Therefore, we initially expect to have two signal-dependent null streams that can be utilized for detecting sky localization. However, this optimization does not alter the results, as demonstrated in figure 7.1. Figure 7.1 depicts the results before and after the subtraction of the null stream, showing no differences in the probability distribution. This is because the subtraction of the intrinsic null stream does not alter the signal-to-noise ratio. Due to the triangular configuration of the ET, it possesses one signal-independent null stream as an inherent property. Consequently, in principle, we should have one signal-dependent null stream available for further analysis. To refine the null combination, we performed optimization by removing the intrinsic null stream from the operator U, resulting in a single null stream. Our findings are consistent

with the paper by Wong et al. [225], which illustrates that the data stream from the Einstein Telescope can be effectively decomposed into signal and null spaces, resulting in two distinct data streams instead of three, which are crucial for parameter estimation. This reduction of the data stream from the ET may lead to computational advantages in the context of parameter estimation.
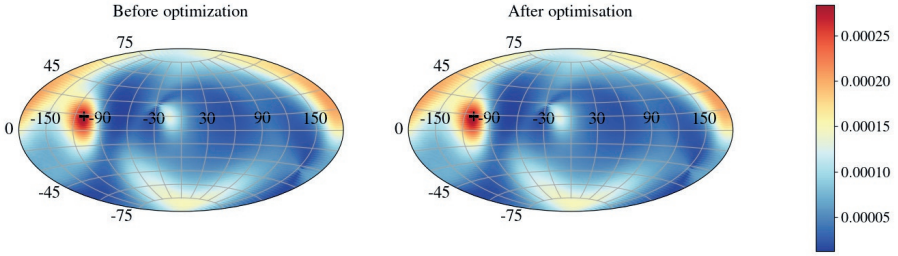
Figure 7.1: Probability distribution for the sky localization of the gravitational wave source. The source is injected from the direction indicated by the '+' sign. The color bar shows the most probable region indicating the direction of the gravitational wave signal arrival. We observe that the probability distribution remains unchanged even after subtracting the intrinsic null stream of the Einstein Telescope. This lack of change is expected since the subtraction does not alter the statistical properties of the analysis.

7.4 Calibration of gravitational waves detectors

In the context of gravitational wave detectors, calibration is a crucial process that comprises two steps. The initial step focuses on establishing a relation between the quantity of interest, such as gravitational wave strain, and a measurement standard. This is achieved by measuring the differential arm length displacement (DARM) of the interferometer when a gravitational wave passes through the detector. The DARM displacement is proportional to the gravitational wave strain, and the relation is given by:

$$\Delta L = \Delta L_X - \Delta L_Y = h\,L \tag{7.24}$$

where ΔL is the difference in X-arm displacement (ΔL_X) and Y-arm displacement (ΔL_Y), and L is the average length of the arms. This length

fluctuation within the gravitational wave detector is translated into a corresponding light fluctuation at the output of the interferometer. At the output port, a photo-detector records the photon fluctuation, which is a representation of the differential arm length variation. The second step of calibration involves converting the output signals from the photodetector into units of meters of differential arm length variation. This conversion allows for the analysis of the calibrated signals to detect gravitational waves and extract astrophysical information from the sources. The calibration process is essential to accurately interpret the data obtained from gravitational wave detectors.

The GW detector possesses a very high level of sensitivity to effectively detect GW signals. This demands a greater level of precision in calibration, which in turn makes the calibration process exceptionally challenging and complex. However, the accurate calibration of the detector response can be challenging due to the tiny changes in the arm length caused by gravitational waves. Currently, gravitational wave detectors use photon calibrators, which artificially move the mirrors with fiducial displacements that are proportional to the power of the laser photons incident on the mirrors. The mirror movements must be modeled with high precision, considering the extremely small displacements involved. Ongoing advancements in modeling techniques have resulted in photon calibrators being capable of characterizing the detector's response with an accuracy of better than 0.5%.

The arm of the interferometric gravitational wave detector consists of mirrors or test masses that are suspended from multi-stage vibration isolation systems. The displacement of these mirrors due to gravitational waves causes a phase shift in the laser light circulating within the detector. This phase shift is then amplified by a series of optical resonators. To ensure the resonance condition of the optical cavities in the interferometric gravitational wave detector, the freedom of the differential arm length is controlled through a feedback system. The feedback control system comprises of actuators that transform the digital control signals from the digital filters. These actuators work to dampen the motion of the test masses by generating physical forces upon them. This process contributes to stabilizing and controlling the movement of the test masses within the system. Figure 7.2 provides a block diagram representation of the interferometer and the differential arm (DARM) feedback control system. The block diagram highlights the key components and processes involved in the detector's operation. The output of
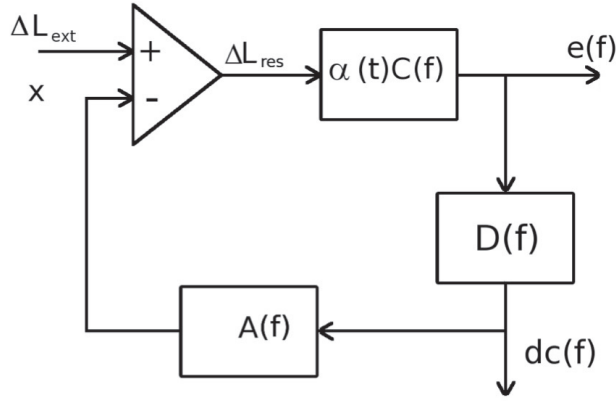
Figure 7.2: A schematic representation of interferometric gravitational wave detector and feedback control loop to suppress the displacements. Figure taken from [216]

.

the detector is regulated by the feedback loop, which adjusts the control signal to maintain the desired level of displacement and optimize the detector's performance.

To convert the error signal into meaningful strain data in a gravitational wave detector, it is crucial to have a comprehensive understanding of the transfer function of all components within the detector's response function. The strain of the detector, denoted as $\Delta L_{ext}(f)$, is directly related to the DARM (differential arm length) error signal $d_{err}(f)$ and can be expressed as:

$$\Delta L_{ext}(f) = R(f, t)\, d_{err}(f), \tag{7.25}$$

where the response function $R(f, t)$ represents the frequency-dependent characteristic of the entire interferometer. It describes how the detector responds to gravitational waves at different frequencies. The response function incorporates both time-independent factors related to the model parameters of the optical components, as well as potential time-dependent variations in the behavior of the instrument itself.

The residual DARM displacement $\Delta L_{res}(f)$, which represents the remaining motion after considering the error signal, can be estimated using the sensing function $C(f)$. The sensing function relates the digital error signal $d_{err}(f)$ to the residual displacement. In other words,

it quantifies the sensitivity of the detector to changes in the DARM displacement. The sensing function $C(f)$ can be defined as:

$$C(f) = \frac{d_{\mathrm{err}}(f)}{\Delta L_{res}(f)}. \tag{7.26}$$

It is important to note that the sensing function is a complex-valued function that depends on the frequency f and also has a time-dependent component that accounts for any gradual drift or variation in the detector's behavior over time. In addition to the sensing function, the actuation function and the digital filters are crucial components of the calibration process in gravitational wave detectors. The actuation function, denoted as $A(f)$, describes the relationship between the control signal $\Delta L_{ctrl}(f)$ and the resulting displacement $d_{ctrl}(f)$. It can be written as:

$$A(f) = \frac{\Delta L_{ctrl}(f)}{d_{ctrl}(f)}. \tag{7.27}$$

The control signal is generated by the digital filters $D(f)$, which converts the error signal $d_{err}(f)$ into the control signal $\Delta L_{ctrl}(f)$. The digital filters play a critical role in shaping and modifying the error signal to generate the appropriate control signal for the actuator. By combining the error signal $d_{err}(f)$, the control signal $\Delta L_{ctrl}(f)$, and the residual displacement $\Delta L_{res}(f)$, we can express the relationship as:

$$\Delta L_{res}(f) = \Delta L_{ext}(f) - \Delta L_{ctrl}(f), \tag{7.28}$$

which represents the residual displacement obtained by subtracting the control displacement from the external displacement. Similarly, by rearranging the equation, we have:

$$\Delta L_{ext}(f) = \Delta L_{res}(f) + \Delta L_{ctrl}(f). \tag{7.29}$$

The equations also highlight the role of the sensing function ($C(f)$), the actuation function ($A(f)$), and the digital filters ($D(f)$) in the calibration process. By combining these terms, the equations can be further simplified as:

$$\Delta L_{ext}(f) = \frac{1}{C(f)} d_{err}(f) + A(f) D(f) d_{err}(f). \tag{7.30}$$

Hence, we can express the external displacement $\Delta L_{ext}(f)$ as the product of the response function $R(f)$ and the error signal $d_{err}(f)$, where $R(f) = \frac{1+G(f)}{C(f)}$. The term $G = C\,D\,A$ represents the DARM open loop gain, which combines the contributions from the sensing function, digital filters, and actuation function. Any errors in the modeling of the response function can lead to inaccuracies in the reconstruction of strain data [216]. Therefore, accurate modeling of the response function is crucial and depends on the proper modeling of the sensing and actuation functions [203, 68].

The sensing function, which represents the transfer function between the DARM error signal and the residual motion, is a complex-valued function of frequency that slowly varies with time. A commonly used model to approximate the sensing function is the single pole approximation, as shown in [68]. This approximation can be expressed as:

$$C^{model}(f,t) = \frac{K_C(t)\,H_C}{1 + if/f_{CC}} C_R(f)\, e^{-2\pi i\,f\tau_c} \frac{f^2}{f^2 + f_s^2 - if\,f_s\,Q_s^{-1}}, \quad (7.31)$$

where, $K_C(t)$ represents the time-dependent scale factor that accounts for variations in the interferometer response over time. H_C is the optical gain, which scales the sensing function and converts the counts into the error signal per unit DARM displacement. f_{CC} is the coupled cavity pole frequency, which defines the interferometer's bandwidth. τ_c is the sensing delay, representing the time it takes for the light to travel between the arms of the interferometer. $C_R(f)$ represents the response of the digital acquisition system, which is considered to have negligible inaccuracies. f_s is the optical-spring pole frequency, which models the detuning between the arm cavities and the signal recycling cavity and Q_s is the optical-spring quality factor, which characterizes the damping in the system. By using this single pole approximation, we can obtain an approximate model for the sensing function that captures the frequency-dependent behavior of the interferometer's response to the DARM error signal.

The actuation function can be modeled as (taken from [68]):

$$\begin{aligned} A^{model}(f,t) =&[k_T(t)F_T(f)H_TA_T(f) + k_{PU}(t)(F_P(f)H_PA_P(f) \\ &+ F_U(f)H_UA_U(f)]e^{-2\pi if\tau_A} \end{aligned} \quad (7.32)$$

Hence, the model considers different stages of the detector, namely the upper-intermediate (U), penultimate (P), and test mass (T) stages.

159

For each stage, the actuation function $A_i(f)$ is defined, representing the response of the actuator at that stage to the control signal. Additionally, there are digital distribution filters $D_i(f)$ associated with each stage, which govern the transformation of the control signal into the appropriate form for actuation. The scale factors H_i account for the scaling of the actuation response. The actuation function for each stage is combined in the overall actuation function $A^{model}(f, t)$, which takes into account the contributions from each stage. The model also includes time-dependent scale factors $K_i(t)$, which capture any variations in the actuation response over time. The overall actuation function is further modified by an overall digital delay τ_A. In practice, the actuation functions for each stage are measured independently and incorporated into the model. The modeling of the actuation function is considered to have negligible inaccuracy due to the inclusion of the measured responses. However, errors in the model can arise from inaccuracies in the scale factors and computational time delays.

7.5   Calibration error

Calibration error in gravitational wave detectors is an important factor that needs to be considered in order to accurately interpret the data and extract astrophysical information. The calibration model, which relates the detector output signals to physical quantities such as the gravitational wave strain, is subject to systematic errors and uncertainties [203].

To estimate the calibration error, a calibration error budget is typically constructed. This involves generating multiple realizations of the overall response function by incorporating the distribution of estimated differential arm length (DARM) parameters. The DARM parameters characterize the behavior of the interferometer and its response to gravitational waves. In practice, the sensing and actuation functions are measured using a photon calibrator. This involves applying swept sine transfer functions in the DARM control loop, where the detector is excited at different frequencies within its detection bandwidth. The cross-correlation between the actuator excitation and the detector response during the excitation provides the transfer function. The actuation strength $[K_i A_i(f)]$ for the i-th suspension stage is determined by comparing the interferometer's response $d_{\text{err}}(f)$ to excitations from both the suspension stage's actuator $(\text{exci}(f))$ and the photon calibrator

$(x_{\mathrm{PC}}(f))$. Mathematically, this relationship is expressed as:

$$[K_i A_i(f)]_{\mathrm{meas}} = \frac{x_T^{\mathrm{PC}}(f)}{d_{\mathrm{err}}(f)} \times \frac{d_{\mathrm{err}}(f)}{\mathrm{exci}(f)} \qquad (7.33)$$

The determination of the sensing function $C^{\mathrm{meas}}(f)$ involves compensating the interferometer response for the displacement caused by the photon calibrator $(d_{\mathrm{err}}(f)/x_{\mathrm{PC}}(f))$ and taking into account the suppression effect attributed to the differential arm length control, denoted as $[1 + G(f)]$. Mathematically, this relationship can be expressed as:

$$C^{\mathrm{meas}}(f) = (1 + G(f)) \times \frac{d_{\mathrm{err}}(f)}{x_{\mathrm{PC}}(f)} \qquad (7.34)$$

By performing these measurements at multiple frequencies, a comprehensive characterization of the sensing and actuation functions can be obtained. The calibration error budget is then determined by analyzing the statistical properties of the measured transfer functions and comparing them to the expected values from the calibration model. The discrepancies between the measured and expected transfer functions provide insights into the calibration error and its impact on the accuracy of the calibration model.

To generate the distribution of the model parameters of sensing function $(\Lambda_c = [H_C, f_{CC}, f_s, Q_s, \kappa_c(t)])$ and actuation function $(\Lambda_A = [H_U, H_P, H_T, A_U,$
$A_P, A_T])$, observed data are fitted with Markov Chain Monte Carlo (MCMC) algorithms. The MCMC algorithm explores the parameter space by generating a sequence of samples that approximate the posterior distribution of the model parameters. The posterior distribution is obtained by combining the likelihood function, which represents the probability of the observed data given the model parameters, and the prior distribution, which represents our prior knowledge or assumptions about the model parameters. In the calibration process, the likelihood function is formulated as the joint probability of the measured data given the model parameters. The goal is to find the set of model parameters that maximizes this likelihood, thereby providing the best fit to the observed data. The prior distributions of the model parameters are assumed to be flat, meaning that there are no specific biases or preferences for certain values of the parameters. This assumption allows for a more objective and unbiased estimation of the model parameters. By running the MCMC algorithm, a large number of samples from the posterior distribution are obtained. These samples represent different combinations

of the model parameters that are consistent with the observed data. From this sample distribution, various statistical quantities and uncertainties can be computed to characterize the calibration error and the overall uncertainty of the calibration model. The model parameters that correspond to the maximum value of the posterior distribution are considered as the best-fit model parameters for the observed data. These parameters provide the most likely values that explain the observed data within the framework of the calibration model.

To quantify the frequency-dependent error in the calibration uncertainty, measurements taken during an observation period are divided by the best-fit model function obtained from the MCMC analysis. The resulting residuals represent the deviations from the model and contain information about the systematic errors in the calibration. By analyzing all the residuals obtained over a science run period, a distribution of the systematic error function can be generated using Gaussian process regression. This method allows for the estimation of the systematic errors at arbitrary frequencies and provides an uncertainty budget for the calibration.

The total calibration uncertainty is influenced by various components of the response function. These components can be categorized into three parts:

1. DARM Model Parameters: The model parameters for the sensing and actuation functions are drawn from the sample points of the posterior distribution obtained from the MCMC analysis. These parameters capture the inherent uncertainties in the calibration model.

2. Unknown Systematic Errors: There may be unknown systematic errors in constructing the functional forms of the sensing and actuation functions using Gaussian process regression. These errors are represented by terms such as $\delta C^{GP}(f)$, $\delta A_U^{GP}(f)$, $\delta A_P^{GP}(f)$, and $\delta A_T^{GP}(f)$, where GP stands for Gaussian process regression. These terms account for the uncertainties in modeling the functional dependencies of the sensing and actuation functions.

3. Time-dependent Parameter Errors: The calibration also depends on time-dependent parameters such as $\kappa_T(t)$, $\kappa_{PU}(t)$, $\kappa_c(t)$, and $f_{CC}(t)$. These parameters are monitored by injecting calibration lines with a high signal-to-noise ratio. The statistical uncertainty of these time-dependent parameters is determined by analyzing the coherence of the injected calibration lines.

In the next section, we will explore the impact of the calibration error

on the null stream. The null stream refers to the data stream where no gravitational wave signals are expected. We will discuss strategies and techniques employed to mitigate the effects of calibration errors in the null stream and enhance the accuracy of gravitational wave detections.

7.6 Impact of calibration errors on the signal independent null stream of the Einstein Telescope

In previous sections, I explored the significance of the null stream in localizing gravitational wave sources by utilizing the detector's data projected into the null space of the detector network (as discussed in Section 7.3). I have also discussed the calibration process, which is crucial for accurately converting the optomechanical response and controlling the mirror position. Achieving precise calibration is essential for extracting accurate information from gravitational wave signals.

Currently, LIGO estimates a frequency-dependent systematic error of approximately 2 percent, which has proven adequate for the signal-to-noise ratio of the detected signals thus far. However, with the advent of third-generation detectors, which will exhibit sensitivities at least ten times better than current detectors and detect events with significantly higher SNR, there is a need for calibration accuracy at the sub-percent level. In this section, we will explore the impact of calibration errors on the signal-independent null stream of the Einstein Telescope. Understanding and mitigating calibration errors become even more critical as the precision and sensitivity of gravitational wave detectors continue to improve.

For the proposed design of the Einstein Telescope, the null stream is a straightforward algebraic summation of the data output from the interferometer, without any time delay due to the colocated nature of ET's detectors. Let's denote the calibrated data stream of each detector of ET as:

$$\tilde{d}_i(f) = \tilde{R}_i(f)d_i\text{err}(f) \tag{7.35}$$

Here, $i = 1, 2, 3$ denotes the three nested detectors of the Einstein Telescope. The calibration function, denoted as $R(\lambda_c, \lambda_A, f)$, combines the model parameters of sensing and actuation. In this discussion, we will consider the systematic error in the model parameters as the primary source of calibration error. Future work will involve incorporating the

unknown systematic errors in the calibration model from Gaussian process regression. The error signal $(d_i \text{err}(f))$ comprises both the gravitational wave signal and noise. Consequently, the signal-independent null stream of the Einstein Telescope, which is the numerical sum of the data from the three detectors, can be expressed as:

$$\Sigma_{i=1}^{3} d_i(f) = \Sigma_{i=1}^{3} \delta \tilde{R}_i(f) h_i(f) + \Sigma_{i=1}^{3} n_i(f) \tag{7.36}$$

Here, $\delta \tilde{R}$ represents the fractional calibration error. Ideally, the first term $\delta \tilde{R}_i(f) h_i(f)$ should be zero if our measurements are free from calibration errors. However, in reality, the impact of calibration errors persists in the null stream as a residual signal. To extract this information, one can perform matched filtering, which will yield the signal-to-noise ratio, as discussed in Section 7.7. The presence of calibration errors in the null stream highlights the importance of accurate calibration for reliable gravitational wave analysis and localization.

7.7 Matched filtering: Estimating calibration error and maximizing signal-to-noise ratios

Matched filtering is a powerful technique used to identify the presence of an underlying signal in noisy data by comparing it to a known template waveform. In the context of gravitational wave analysis, matched filtering plays a crucial role in detecting and characterizing gravitational wave signals. The basic idea behind matched filtering is to compute the phase-coherent correlation between the output of the interferometer and the template waveform, taking into account the expected power spectral density of the data.

The output of the matched filtering process is the signal-to-noise ratio, which quantifies the strength of the detected signal relative to the background noise. Maximizing the SNR allows us to select the optimal filter or template waveform that closely matches the expected gravitational wave signal. The matched filtering search can be computationally demanding, especially when covering a large parameter space and using a large number of template waveforms. The design of a template bank, which covers the parameter space with appropriate spacing, is essential to ensure that the detectability of signals is not compromised by the mismatch between the template waveform and the data.

As discussed in Section 7.6, our focus is on capturing residual signals present in the null stream caused by calibration errors in the detector

data. Therefore, referring to equation 7.36, we can express the null stream of the triangular Einstein telescope as follows:

$$\mathcal{N}(f) = N_n^{123} + \varepsilon^{123}(f) \tag{7.37}$$

In this equation, $\varepsilon^{123}(f)$ represents the calibration error signal, given by the summation over $i = 1$ to 3 of $\delta\tilde{R}_i(\vec{\lambda}_c, \vec{\lambda}_A, f)h_i(f)$. The notation and the basis of the mathematical formulation have been adapted from [195].

To simplify our analysis, we assume the response function $\tilde{R}(f)$ does not vary with time. This means we ignore the time dependency of the parameters and any unknown systemic errors that may be present. This means we consider the calibration error to be dependent on model parameters P_i, i.e.,

$$P_i \; \epsilon \; (\vec{\lambda}_c, \vec{\lambda}_A) \tag{7.38}$$

To perform matched filtering, we start by constructing a filter denoted as $E^{123}(f)$. This filter depends on the model parameters of the calibration function, namely $\vec{\lambda}_c^m$ and $\vec{\lambda}_A^m$, as well as the gravitational waveform template, represented as $\tilde{h}^T$.

The cross-correlation between the filter template and the residual signal in the null stream can be written as:

$$\langle\varepsilon^{123}(f)|E^{123}(f)\rangle = \int_{-\infty}^{\infty} \frac{\sum_{i=1}^{3} \delta\tilde{R}_i(\vec{\lambda}_c, \vec{\lambda}_A, f)\,\delta\tilde{R}_i(\vec{\lambda}_c^m, \vec{\lambda}_A^m, f)\,(\tilde{h}_i')^T\tilde{h}_i}{S_{Null}(f)}df. \tag{7.39}$$

In this equation, $S_{Null}(f)$ represents the power spectral density of the null stream. If we detect the event with a high signal-to-noise ratio, we are able to accurately model the gravitational waveform. In that case, the equation can be simplified as follows:

$$\langle\varepsilon^{123}(f)|E^{123}(f)\rangle = \int_{-\infty}^{\infty} \frac{\Sigma_{i=1}^{3}\delta\tilde{R}_i^*(\vec{\lambda}_c, \vec{\lambda}_A, f)\,\delta\tilde{R}_i(\vec{\lambda}_c^m, \vec{\lambda}_A^m, f)\,|\tilde{h}_i(f)|^2}{S_{Null}(f)}df. \tag{7.40}$$

To quantitatively measure the strength of the calibration error signal relative to the filter's energy and overall noise level, we define the signal

7

to noise ratio as follows:

$$\rho = \frac{\langle \varepsilon^{123}(f) | E^{123}(f) \rangle}{\sqrt{\langle E^{123}(f) | E^{123}(f) \rangle}}. \tag{7.41}$$

To perform calibration error-matched filtering, we can construct a filter template using the model parameters of the calibration function, assuming we have knowledge of the gravitational wave waveforms and other relevant geometric parameters. Additionally, the knowledge of gravitational waveforms and geometric parameters allows us to account for their influence in the filtering process.

In order to make sure that we consider all possible calibration errors, it is necessary to cover the entire parameter space associated with the calibration inaccuracy. To achieve this, we can generate a template bank that consists of a collection of filters, each corresponding to a different point in the parameter space. For each filter in the template bank, we can compute the signal-to-noise ratio using matched filtering. The SNR serves as a quantitative measure of how effectively the filter aligns with the calibration error signal that exists within the null stream. By evaluating the SNR for each filter, we can determine the maximum SNR attained. The filter associated with this maximum SNR represents the optimal choice for the filter template that aligns most effectively with the specific calibration error present in the data.

The calibration error signal has a weak amplitude, typically at the sub-percent level of inaccuracy. Let's consider we have detected a gravitational signal with an optimal SNR of 20. Now, let's assume a calibration error with a magnitude of 2%. This means that the calibration process introduces an inaccuracy of 2% of the signal amplitude. If we apply this calibration error to the detected gravitational signal, the signal to noise strength in the null stream would be reduced to 0.4, which is 2% of the original signal strength. As a result, the weak amplitude of the calibration error signal, in this case 0.4, can be easily masked by the noise in the null stream. This makes it challenging to detect and accurately estimate the calibration error using a single event or measurement. Hence to characterise the calibration error signal, we can combine the signal-to-noise ratio from multiple events within the same observation period. This is based on the expectation that systematic calibration errors tend to remain relatively stable over weeks, months, or approximately during one observation run. Systematic calibration errors arise from the factors that affect the measurement process, such as instrumental characteristics, environmental conditions, or calibration procedures. These

errors are not random but rather exhibit a certain level of persistence over time. In the next section, we will discuss how combining the SNRs from multiple events enable us to estimate the calibrated error signal, find the optimal filter by maximizing the SNR, and effectively model the calibration error.

7.8 Cumulative SNR for null-stream residuals due to calibration error in triangular Einstein Telescope

In the previous section, I have discussed the statistics of matched filtering to determine the SNR for the calibration error signal in the intrinsic null stream of the triangular configuration of Einstein Telescope. Since the amplitude of the residual signal is much weaker compared to the actual gravitational wave signal, which is expected given the calibration errors are at a few percent level, detecting and distinguishing the calibration error signal poses a significant challenge. To gather meaningful information about the calibration error signal, one effective approach is to accumulate the SNR from all the events detected during a observing run. This can be done by considering a set of non-overlapping signals obtained by collecting data from different time periods. The number of events required to achieve a certain SNR for the calibration error signal depends on the SNR of the incident (ρ) and the sub-percent level calibration error (δ).

The SNR of the calibration error signal grows as the square root of the number of events, represented by $\sqrt{N}$. For each event, the matched filtering SNR for the calibration error signal is $\rho\delta$. By accumulating the SNR over N events, the cumulative SNR becomes $\sqrt{N}\rho\delta$. This cumulative SNR reflects the accumulated statistical evidence and increased sensitivity to the calibration error signal as more events are considered. Consequently, the number of events needed to obtain a desired SNR (denoted as S) for the calibration error signal can be estimated using the formula $(\frac{S}{\rho\delta})^2$.

7.9 Results

In this section, I will present the results of modeling of the calibration error signal using the cumulative signal-to-noise ratio. In this analysis, I only assume the modeling error associated with the calibration function parameters. Also in this analysis, I do not make any assumptions about

systematic errors in the calibration function, and do not consider errors related to the time variation of these parameters. I consider the presence of an error in the calibration function, specifically associated with certain parameters, such as for instance the cavity pole frequency (f_{CC}). For simplicity and computational cost, I assume that all other parameters remain consistent with their true values. In the Einstein Telescope, we have three interferometers, each of which exhibits an error in its calibration function related to the cavity pole frequency. My objective is to minimize the error by utilizing the intrinsic null stream of the Einstein Telescope. In Figure 7.3, I present the error in the response function of one of the interferometers in the Einstein Telescope. This error arises due to a mismatch in the cavity pole frequency compared to its true value. The black curve in the plot represents the modeled value of the cavity pole frequency, which slightly deviates from its actual true value. My objective is to converge toward the true value of the cavity pole frequency by estimating the signal-to-noise ratio of the residual present in the null stream. This analysis will help us correct the mismatch and bring the modeled cavity pole frequency in alignment with its actual, accurate value. In this example, I have considered a true value of the pole frequency set at 330 Hz, while the modelled pole frequency is at 352 Hz. The black trace illustrates the deviation in the response function resulting from this discrepancy in pole frequencies. To address this difference and refine the calibration function, I have selected a range of cavity pole frequency values close to the modeled 352 Hz. These selected values can be regarded as the parameters for the calibration function template bank. By analyzing the response at these values of cavity pole frequencies, I try to improve the accuracy of our calibration and align it with the true pole frequency of 330 Hz. The gray-shaded curves in figure 7.3 represent the relative calibration error for different values of the pole frequency (f_{CC}) within the range of 332 to 372. From the plot, it is evident that for some of the gray curves, the error is reduced as we approach the actual value of the parameter.

This process is repeated for three interferometers. In each interferometer, I have chosen ten different values for the cavity pole frequency, slightly varying its modelled value. When one combines these parameters, one effectively constructs a three-dimensional grid of data points. Each point within this 3D grid represents a unique combination of cavity pole frequencies for each of the three interferometers. Since I have chosen ten different values for the cavity pole frequency for each in-
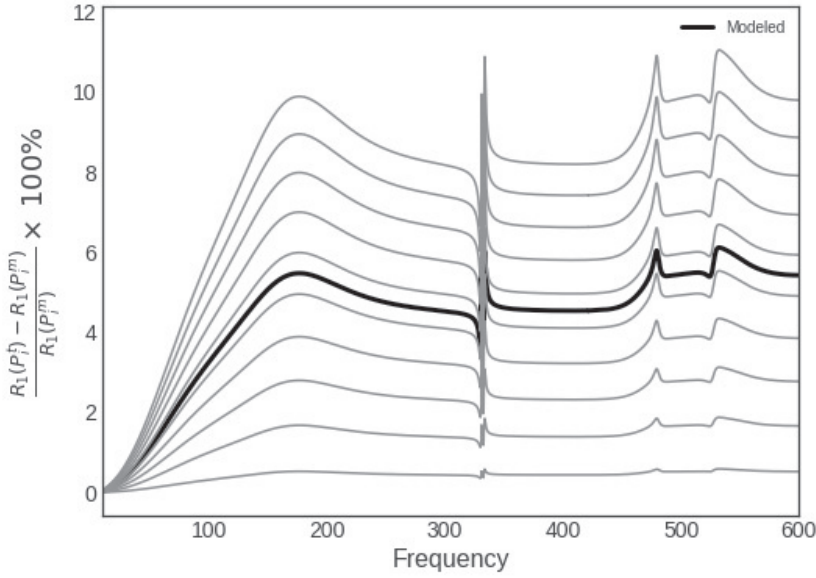
Figure 7.3: Amplitude of the relative calibration error as a function of frequency is illustrated. The black curve shows the error associated with the modeled calibration parameter, assuming a cavity pole frequency (f_{CC}) of 352 Hz, while the actual value is 330 Hz. To enhance calibration accuracy, we vary the modeled parameter, considering a range of possible f_{CC} values, such as 332, 336, 340, and up to 372 Hz as parameters for the templates of calibration error. The grey curves represent the relative calibration error for the selected templates. The grey curve with the smallest relative calibration error corresponds to $f_{CC} = 332\,\mathrm{Hz}$, and the highest one corresponds to $f_{CC} = 372\,\mathrm{Hz}$.

terferometer, this results in a total of 1000 different points within this three-dimensional grid. Each point represents a specific configuration of cavity pole frequencies across the three interferometers, allowing us to thoroughly explore and analyse this parameter space. The next step is to inject a signal into the noisy data recorded by each of the three interferometers. Ideally, when we combine or sum the data from these three interferometers, the signal should cancel. As a result of the calibration error, the signal within the zero stream will not be completely zero. This calibration error introduces residual signals into the null stream.
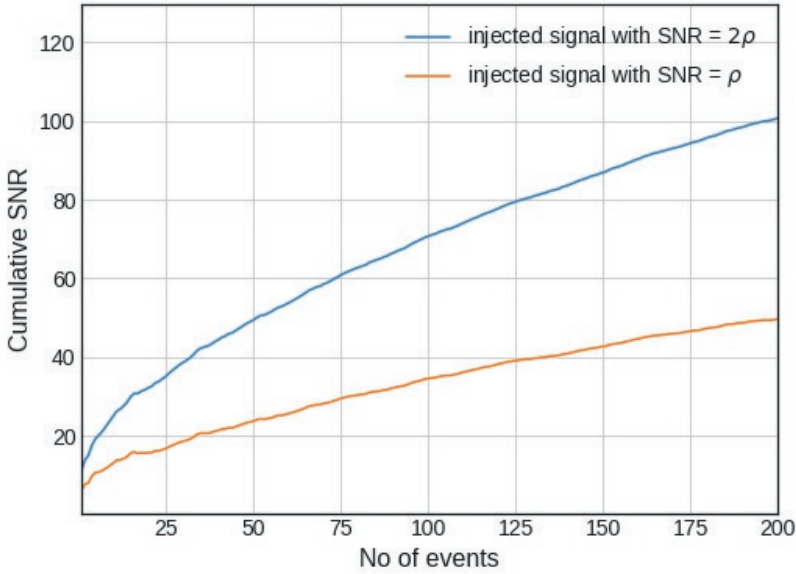
Figure 7.4: Cumulative signal-to-noise ratio of the calibration error signal within the null stream as a function of the number of events. In the graph, you can see two curves: orange and blue. These curves represent the accumulated SNR obtained from the null stream when the injected signal in the detector data has two different SNRs—one with a lower SNR of $\rho = 100$ and the other with a higher SNR of $\rho = 200$

The signal-to-noise ratio of the residual signal within the null stream is significantly reduced due to a calibration error of a few percent. This low signal-to-noise ratio makes it unreliable to detect the residual signal using data from a single event. This is why we need to estimate the cumulative signal-to-noise ratio by analyzing data from many events that will be detected by the Einstein Telescope over a time span of several weeks to months. By aggregating data from multiple events, we can improve the signal-to-noise ratio and increase our chances of detecting the residual signal. In figure 7.4, I illustrate the cumulative signal-to-noise ratio as a function of the number of events. To simplify the demonstration, I have assumed the same event with different noise realizations and plotted the accumulated SNR. For a more general scenario, this can be extended to consider the distribution of sources that could be detected

by the Einstein Telescope. The blue and orange curves in the plot represent the cumulative signal-to-noise ratio of the residual signal within the null stream for injected sources with higher (2ρ) and lower SNRs (ρ), respectively.

I previously introduced 1000 different templates, each representing a specific set of cavity pole frequencies for the three interferometers within ET. My goal is to identify the template that optimally enhances the cumulative signal-to-noise ratio from this collection of templates. This process helps us determine the most accurate calibration and cavity pole frequency values for the interferometers. I have estimated f_{CC} and depicted the error or deviation of the estimated f_{CC} concerning its true value. Figure 7.5 shows histograms representing the distribution of relative deviations in the cavity pole frequency obtained from the template maximizing the cumulative signal-to-noise ratio after a certain number of events. On the X-axis of these histograms, I plot the differences between the best-fit cavity pole frequency and its true value and then divide this difference by the actual value to compute the percentage relative deviation. The Y-axis of these histograms represents the number of occurrences or counts within specific deviation ranges in the data. This figure shows how well the best-fit cavity pole frequencies determined by the template, match with the true values. It offers a visual representation of the deviations associated with a specific number of events. In the top left, top right, and bottom left plots, we can observe the distributions for the deviation of f_{CC} in the three xylophone interferometers of ET. The dotted reference line represents the initial error in the calibration process, which I aim to refine based on the cumulative signal-to-noise ratio. The concentration of counts around zero deviation indicates that the best-fit templates and their corresponding values of f_{CC} closely match the actual values. Furthermore, as the number of events increases, the cumulative signal-to-noise ratio enhances, improving the accuracy of these estimations. In the bottom right plot, I display a histogram that illustrates the distribution of Δf_{CC} after 100 events, with two different injected SNR, denoted as ρ and 2ρ, as shown in figure 7.4. As expected, when the SNR of the detected signal is high, the histogram shows a higher count for zero deviation compared to a lower SNR. This implies that a signal detected with a higher SNR provides a more reliable and precise determination of the parameter.

7.10   Summary and outlook

In this chapter, I have explored the advantages of utilizing the intrinsic null stream of the Einstein Telescope for both sky localization and modeling calibration errors. I have observed that subtracting the ET's intrinsic null stream within the detector network containing ET employs one less data stream to estimate the sky localization parameters. This result is consistent with the findings of the paper by Wong et al. They have projected the three data streams of the ET into signal space and null space. They have shown that, for parameter estimation, we need to analyze two data streams in the signal space instead of three from each of the detectors of ET. Furthermore, I have discussed the concept of the self-calibration method, inspired by Schutz et al.'s work [195], which uses ET's intrinsic null stream to address calibration uncertainties. I have demonstrated using mock data how the calibration error parameter can be effectively modeled based on the accumulated signal-to-noise ratio of the residual signal found in the null stream. To manage computational costs, I have specifically considered one of the parameters associated with calibration error, assuming that the other parameters are accurately modeled. It is worth noting that this estimation process can be made more rigorous by including other parameters of the calibration error modeling. This estimation can be further refined by considering a population distribution of sources based on the sensitivity of the Einstein Telescope.
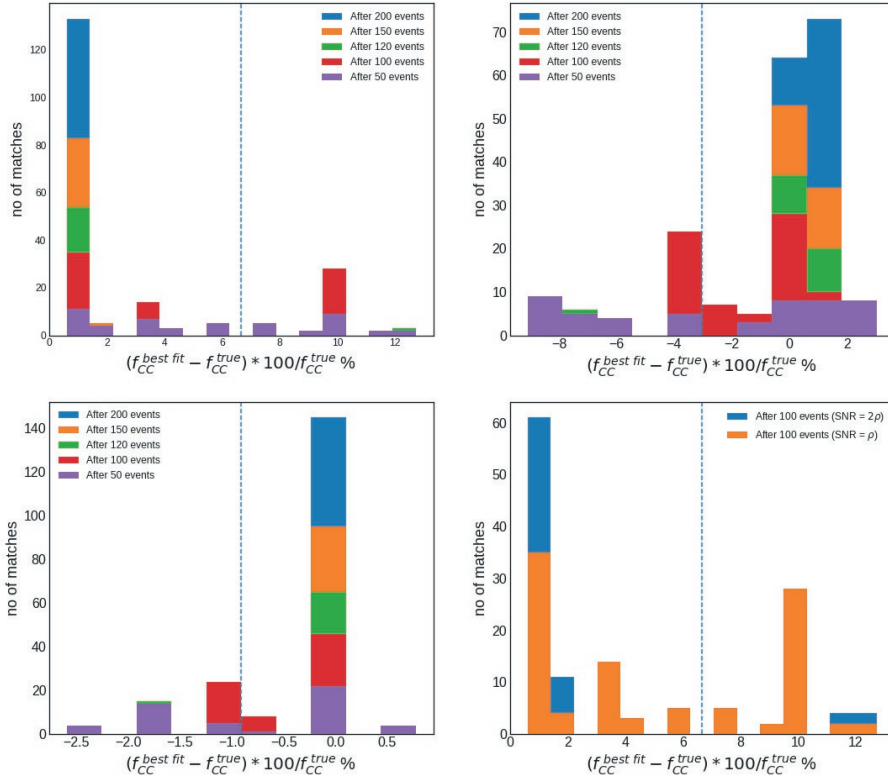
Figure 7.5: The histogram shows the relative deviation between the estimated value of f_{CC} obtained from the best-fit template and its true value. The Y-axis represents the frequency or count of occurrences where the estimated value of f_{CC} matches the relative deviation indicated on the X-axis. The best-fit template is determined by maximizing the accumulated signal-to-noise ratio of the calibration error signal, which is present as a residual in the null stream. Different colors in the histogram correspond to distributions resulting from the accumulation of SNR based on different numbers of events. The histograms for the three interferometers of the ET detectors (ET1, ET2, ET3) show peaks around zero deviation, indicating accurate parameter estimation with a significantly high detection rate; furthermore, the lower right plot shows that the probability of accurately measuring the calibration parameter is higher when the signals are detected with higher SNR.

Bibliography

[1] An upper limit on the stochastic gravitational-wave background of cosmological origin. *Nature*, 460(7258):990–994, 2009.

[2] Kagra: 2.5 generation interferometric gravitational wave detector. *Nature Astronomy*, 3(1):35–40, 2019.

[3] J Aasi, J Abadie, BP Abbott, R Abbott, TD Abbott, M Abernathy, T Accadia, F Acernese, C Adams, T Adams, et al. Prospects for observing and localizing gravitational-wave transients with advanced ligo and advanced virgo. *Living Reviews in Relativity*, 19, 2016.

[4] Benjamin P Abbott, Richard Abbott, TD Abbott, MR Abernathy, Fausto Acernese, Kendall Ackley, Carl Adams, Thomas Adams, Paolo Addesso, RX Adhikari, et al. Observation of gravitational waves from a binary black hole merger. *Physical review letters*, 116(6):061102, 2016.

[5] Benjamin P Abbott, Rich Abbott, TD Abbott, Fausto Acernese, Kendall Ackley, Carl Adams, Thomas Adams, Paolo Addesso, RX Adhikari, Vaishali B Adya, et al. Gw170817: observation of gravitational waves from a binary neutron star inspiral. *Physical review letters*, 119(16):161101, 2017.

[6] Benjamin P Abbott, Rich Abbott, Thomas D Abbott, Fausto Acernese, Kendall Ackley, Carl Adams, Thomas Adams, Paolo Addesso, Rana X Adhikari, Vaishali B Adya, et al. First low-frequency einstein@ home all-sky search for continuous gravitational waves in advanced ligo data. *Physical Review D*, 96(12): 122004, 2017.

[7] Benjamin P Abbott, Richard Abbott, TD Abbott, F Acernese, K Ackley, C Adams, T Adams, P Addesso, Rana X Adhikari, Vaishali B Adya, et al. Gw170814: a three-detector observation of gravitational waves from a binary black hole coalescence. *Physical review letters*, 119(14):141101, 2017.

[8] Benjamin P Abbott, Richard Abbott, Thomas D Abbott, MR Abernathy, K Ackley, C Adams, P Addesso, Rana X Adhikari, VB Adya, C Affeldt, et al. Exploring the sensitivity of next generation gravitational wave detectors. *Classical and Quantum Gravity*, 34(4):044001, 2017.

[9] Benjamin P Abbott, Robert Abbott, TD Abbott, Fausto Acernese, K Ackley, C Adams, T Adams, P Addesso, Rana X Adhikari, VB Adya, et al. On the progenitor of binary neutron star merger gw170817. *The Astrophysical Journal Letters*, 850(2):L40, 2017.

[10] Benjamin P Abbott, Rich Abbott, Thomas D Abbott, Fausto Acernese, Kendall Ackley, Carl Adams, Thomas Adams, Paolo Addesso, Rana X Adhikari, Vaishali B Adya, et al. Gw170817: implications for the stochastic gravitational-wave background from compact binary coalescences. *Physical review letters*, 120(9): 091101, 2018.

[11] Benjamin P Abbott, Richard Abbott, TD Abbott, S Abraham, F Acernese, K Ackley, C Adams, RX Adhikari, VB Adya, C Affeldt, et al. All-sky search for continuous gravitational waves from isolated neutron stars using advanced ligo o2 data. *Physical Review D*, 100(2):024004, 2019.

[12] Benjamin P Abbott, R Abbott, TD Abbott, S Abraham, F Acernese, K Ackley, C Adams, VB Adya, C Affeldt, M Agathos, et al. Prospects for observing and localizing gravitational-wave transients with advanced ligo, advanced virgo and kagra. *Living reviews in relativity*, 23(1):1–69, 2020.

[13] BP Abbott, R Abbott, TD Abbott, F Acernese, K Ackley, C Adams, and T Adams. Scientific collaboration, and virgo collaboration. 2017 gw170817: observation of gravitational waves from a binary neutron star inspiral. *PhRvL*, 119:161101, 2017.

[14] BP Abbott, SV Angelova, R Birney, and NA Lockerbie. Macfoy, s. and reid, s. and tokmakov, kv, ligo scientific collaboration, virgo

collaboration (2018) gw170817: Measurements of neutron star radii and equation of state. physical review letters, 121. issn 0031-9007, http://dx. doi. org/10.1103/physrevlett. 121.161101. *PHYSICAL REVIEW LETTERS Phys Rev Lett*, 121:161101, 2018.

[15] BP Abbott, R Abbott, TD Abbott, S Abraham, Fausto Acernese, K Ackley, A Adams, C Adams, RX Adhikari, VB Adya, et al. Search for intermediate mass black hole binaries in the first and second observing runs of the advanced ligo and virgo network. *Physical Review D*, 100(6):064064, 2019.

[16] BP Abbott, R Abbott, TD Abbott, F Acernese, K Ackley, C Adams, T Adams, P Addesso, RX Adhikari, VB Adya, et al. Properties of the binary neutron star merger gw170817. *Physical Review X*, 9(1):011001, 2019.

[17] BP Abbott, Richard Abbott, TDea Abbott, S Abraham, F Acernese, K Ackley, C Adams, RX Adhikari, VB Adya, Christoph Affeldt, et al. Gwtc-1: a gravitational-wave transient catalog of compact binary mergers observed by ligo and virgo during the first and second observing runs. *Physical Review X*, 9(3):031040, 2019.

[18] BP Abbott, R Abbott, TD Abbott, S Abraham, F Acernese, K Ackley, C Adams, RX Adhikari, VB Adya, Christoph Affeldt, et al. Gw190425: Observation of a compact binary coalescence with total mass 3.4 m. *The Astrophysical journal letters*, 892(1): L3, 2020.

[19] R Abbott, R Adhikari, G Allen, D Baglino, C Campbell, D Coyne, E Daw, D DeBra, J Faludi, P Fritschel, et al. Seismic isolation enhancements for initial and advanced ligo. *Classical and Quantum Gravity*, 21(5):S915, 2004.

[20] R Abbott, TD Abbott, S Abraham, F Acernese, K Ackley, A Adams, C Adams, RX Adhikari, VB Adya, Christoph Affeldt, et al. Observation of gravitational waves from two neutron star–black hole coalescences. *The Astrophysical journal letters*, 915(1): L5, 2021.

[21] R Abbott, TD Abbott, F Acernese, K Ackley, C Adams, N Adhikari, RX Adhikari, VB Adya, C Affeldt, D Agarwal, et al. Gwtc-

3: compact binary coalescences observed by ligo and virgo during the second part of the third observing run. *arXiv preprint arXiv:2111.03606*, 2021.

[22] Rich Abbott, TD Abbott, S Abraham, F Acernese, K Ackley, A Adams, C Adams, RX Adhikari, VB Adya, Christoph Affeldt, et al. Population properties of compact objects from the second ligo–virgo gravitational-wave transient catalog. *The Astrophysical journal letters*, 913(1):L7, 2021.

[23] Rich Abbott, Thomas D Abbott, Sheelu Abraham, Fausto Acernese, Kendall Ackley, Carl Adams, Rana X Adhikari, Vaishali B Adya, Christoph Affeldt, Michalis Agathos, et al. Open data from the first and second observing runs of advanced ligo and advanced virgo. *SoftwareX*, 13:100658, 2021.

[24] Richard Abbott, TD Abbott, S Abraham, F Acernese, K Ackley, C Adams, RX Adhikari, VB Adya, Christoph Affeldt, M Agathos, et al. Gw190521: a binary black hole merger with a total mass of 150 m. *Physical review letters*, 125(10):101102, 2020.

[25] Matt Abernathy, F Acernese, P Ajith, B Allen, P Amaro Seoane, N Andersson, S Aoudia, P Astone, B Krishnan, L Barack, et al. Einstein gravitational wave telescope conceptual design study. 2011.

[26] T Accadia, F Acernese, F Antonucci, P Astone, G Ballardin, F Barone, M Barsuglia, Th S Bauer, MG Beker, A Belletoile, et al. The seismic superattenuators of the virgo gravitational waves interferometer. *Journal of low frequency noise, vibration and active control*, 30(1):63–79, 2011.

[27] T Adams, D Buskulic, V Germain, GM Guidi, F Marion, Matteo Montani, B Mours, Francesco Piergiovanni, and Gang Wang. Low-latency analysis pipeline for compact binary coalescences in the advanced gravitational wave detector era. *Classical and Quantum Gravity*, 33(17):175012, 2016.

[28] Juri Agresti, Giuseppe Castaldi, Riccardo DeSalvo, Vincenzo Galdi, Vincenzo Pierro, and Innocenzo M Pinto. Optimized multilayer dielectric mirror coatings for gravitational wave interferometers. In *Advances in Thin-Film Coatings for Optical Applications III*, volume 6286, pages 62–71. SPIE, 2006.

[29] Parameswaran Ajith, Martin Hewitson, and Ik Siong Heng. Null-stream veto for two co-located detectors: implementation issues. *Classical and Quantum Gravity*, 23(19):S741, 2006.

[30] Keiiti Aki and Paul G Richards. *Quantitative seismology.* 2002.

[31] Bruce Allen. Stochastic gravity-wave background in inflationary-universe models. *Physical Review D*, 37(8):2078, 1988.

[32] A Allocca, Andrea Berbellini, Lapo Boschi, Enrico Calloni, Giovanni Luca Cardello, Alessandro Cardini, Massimo Carpinelli, Andrea Contu, L D'Onofrio, Domenico D'Urso, et al. Seismic glitchness at sos enattos site: impact on intermediate black hole binaries detection efficiency. *The European Physical Journal Plus*, 136(5): 1–12, 2021.

[33] Pau Amaro-Seoane and Lucia Santamaria. Detection of imbhs with ground-based gravitational wave observatories: a biography of a binary of black holes, from birth to death. *The Astrophysical Journal*, 722(2):1197, 2010.

[34] Pau Amaro-Seoane, Nils Andersson, K Arun, Sukanta Bose, Leone Bosi, James Clark, Thomas Dent, Jonathan Gair, Kostas Glampedakis, Mark Hannam, et al. Einstein telescope design study: vision document. *Codified Document ET-030-09*, 2009.

[35] Pau Amaro-Seoane, Sofiane Aoudia, Stanislav Babak, Pierre Binetruy, Emanuele Berti, Alejandro Bohe, Chiara Caprini, Monica Colpi, Neil J Cornish, Karsten Danzmann, et al. Low-frequency gravitational-wave science with elisa/ngo. *Classical and Quantum Gravity*, 29(12):124016, 2012.

[36] I Andreoni, K Ackley, J Cooke, A Acharyya, JR Allison, GE Anderson, MCB Ashley, D Baade, M Bailes, K Bannister, et al. Follow up of gw170817 and its electromagnetic counterpart by australian-led observing programmes. *Publications of the Astronomical Society of Australia*, 34, 2017.

[37] John Antoniadis, Thomas M Tauris, Feryal Ozel, Ewan Barr, David J Champion, and Paulo CC Freire. The millisecond pulsar mass distribution: Evidence for bimodality and constraints on the maximum neutron star mass. *arXiv preprint arXiv:1605.01665*, 2016.

179

[38] Vikas Aragam, Sonia Paban, and Robert Rosati. Primordial stochastic gravitational wave backgrounds from a sharp feature in three-field inflation. *arXiv preprint arXiv:2304.00065*, 2023.

[39] Yoichi Aso, Yuta Michimura, Kentaro Somiya, Masaki Ando, Osamu Miyakawa, Takanori Sekiguchi, Daisuke Tatsumi, Hiroaki Yamamoto, Kagra Collaboration, et al. Interferometer design of the kagra gravitational wave detector. *Physical Review D*, 88(4): 043007, 2013.

[40] Stanislav Babak, Jonathan Gair, Alberto Sesana, Enrico Barausse, Carlos F Sopuerta, Christopher PL Berry, Emanuele Berti, Pau Amaro-Seoane, Antoine Petiteau, and Antoine Klein. Science with the space-based interferometer lisa. v. extreme mass-ratio inspirals. *Physical Review D*, 95(10):103012, 2017.

[41] F Badaracco and J Harms. Optimization of seismometer arrays for the cancellation of newtonian noise from seismic body waves. *Classical and Quantum Gravity*, 36(14):145006, 2019.

[42] F Badaracco, J Harms, A Bertolini, T Bulik, I Fiori, B Idzkowski, A Kutynia, K Nikliborc, F Paoletti, A Paoli, et al. Machine learning for gravitational-wave detection: surrogate wiener filtering for the prediction and optimized cancellation of newtonian noise at virgo. *Classical and Quantum Gravity*, 37(19):195016, 2020.

[43] Maria Bader, Soumen Koley, Jo van den Brand, Xander Campman, Henk Jan Bulten, Frank Linde, and Bjorn Vink. Newtonian-noise characterization at terziet in limburg—the euregio meuse–rhine candidate site for einstein telescope. *Classical and Quantum Gravity*, 39(2):025009, 2022.

[44] M Bailes, BK Berger, PR Brady, M Branchesi, K Danzmann, M Evans, K Holley-Bockelmann, BR Iyer, T Kajita, S Katsanevas, et al. Gravitational-wave physics and astronomy in the 2020s and 2030s. *Nature Reviews Physics*, 3(5):344–366, 2021.

[45] Z Barkat, G Rakavy, and N Sack. Dynamics of supernova explosion resulting from pair formation. *Physical Review Letters*, 18(10):379, 1967.

[46] L Barsotti, P Fritschel, M Evans, and S Gras. Ligo document t1800044-v5. Technical report, Tech. rep, 2018.

[47] Simone S Bavera, Gabriele Franciolini, Giulia Cusin, Antonio Riotto, Michael Zevin, and Tassos Fragos. Stochastic gravitational-wave background as a tool for investigating multi-channel astrophysical and primordial black-hole mergers. *Astronomy & Astrophysics*, 660:A26, 2022.

[48] Matteo Beccaria, M Bernardini, S Braccini, C Bradaschia, A Bozzi, C Casciano, G Cella, A Ciampa, E Cuoco, G Curci, et al. Relevance of newtonian seismic noise for the virgo interferometer sensitivity. *Classical and Quantum Gravity*, 15(11):3339, 1998.

[49] Mark G Beker. *Low-frequency sensitivity of next generation gravitational wave detectors*. PhD thesis, Vrije University Amsterdam, 2013.

[50] MG Beker, JFJ Van Den Brand, and DS Rabeling. Subterranean ground motion studies for the einstein telescope. *Classical and Quantum Gravity*, 32(2):025002, 2014.

[51] K Belczynski, Alexander Heger, W Gladysz, Ashley J Ruiter, S Woosley, G Wiktorowicz, H-Y Chen, Tomasz Bulik, Richard O'Shaughnessy, Daniel E Holz, et al. The effect of pair-instability mass loss on black-hole mergers. *Astronomy & Astrophysics*, 594: A97, 2016.

[52] Krzysztof Belczynski, Vassiliki Kalogera, and Tomasz Bulik. A comprehensive study of binary compact objects as gravitational wave sources: evolutionary channels, rates, and physical properties. *The Astrophysical Journal*, 572(1):407, 2002.

[53] Enis Belgacem, Yves Dirian, Stefano Foffa, and Michele Maggiore. Gravitational-wave luminosity distance in modified gravity theories. *Physical review D*, 97(10):104066, 2018.

[54] Ari Ben-Menahem and Sarva Jit Singh. *Seismic waves and sources*. Springer Science & Business Media, 2012.

[55] Emanuele Berti, Enrico Barausse, Vitor Cardoso, Leonardo Gualtieri, Paolo Pani, Ulrich Sperhake, Leo C Stein, Norbert Wex, Kent Yagi, Tessa Baker, et al. Testing general relativity with present and future astrophysical observations. *Classical and Quantum Gravity*, 32(24):243001, 2015.

[56] Eric D Black and Ryan N Gutenkunst. An introduction to signal extraction in interferometric gravitational wave detectors. *American Journal of Physics*, 71(4):365–378, 2003.

[57] Luc Blanchet, Thibault Damour, and Gerhard Schäefer. Post-newtonian hydrodynamics and post-newtonian gravitational wave generation for numerical relativity. *Monthly Notices of the Royal Astronomical Society*, 242(3):289–305, 1990.

[58] Hermann Bondi, M Gr J Van der Burg, and AWK Metzner. Gravitational waves in general relativity, vii. waves from axi-symmetric isolated system. *Proceedings of the Royal Society of London. Series A. Mathematical and Physical Sciences*, 269(1336):21–52, 1962.

[59] Ssohrab Borhanian and BS Sathyaprakash. Listening to the universe with next generation ground-based gravitational-wave detectors. *arXiv preprint arXiv:2202.11048*, 2022.

[60] Peter Bormann and Erhard Wielandt. Seismic signals and noise. In *New manual of seismological observatory practice 2 (NMSOP2)*, pages 1–62. Deutsches GeoForschungsZentrum GFZ, 2013.

[61] Markus Böttcher and Charles D Dermer. High-energy gamma rays from ultra-high-energy cosmic-ray protons in gamma-ray bursts. *The Astrophysical Journal*, 499(2):L131, 1998.

[62] Marica Branchesi. Multi-messenger astronomy: gravitational waves, neutrinos, photons, and cosmic rays. In *Journal of Physics: conference series*, volume 718, page 022004. IOP Publishing, 2016.

[63] Marica Branchesi, Michele Maggiore, David Alonso, Charles Badger, Biswajit Banerjee, Freija Beirnaert, Enis Belgacem, Swetha Bhagwat, Guillaume Boileau, Ssohrab Borhanian, et al. Science with the einstein telescope: a comparison of different designs. *Journal of Cosmology and Astroparticle Physics*, 2023 (07):068, 2023.

[64] Davide Brundu, Mariano Cadoni, Mauro Oi, Piero Olla, and Andrea Pierfrancesco Sanna. Atmospheric newtonian noise modeling for third-generation gravitational wave detectors. *arXiv preprint arXiv:2206.02610*, 2022.

[65] Adam Burrows. Colloquium: Perspectives on core-collapse supernova theory. *Reviews of Modern Physics*, 85(1):245, 2013.

[66] Arnaud Burtin, Niels Hovius, and Jens M Turowski. Seismic monitoring of torrential and fluvial processes. *Earth Surface Dynamics*, 4(2):285–307, 2016.

[67] Juan Calderón Bustillo, Sascha Husa, Alicia M Sintes, and Michael Pürrer. Impact of gravitational radiation higher order modes on single aligned-spin gravitational wave searches for binary black holes. *Physical Review D*, 93(8):084019, 2016.

[68] Craig Cahillane, Joe Betzwieser, Duncan A Brown, Evan Goetz, Evan D Hall, Kiwamu Izumi, Shivaraj Kandhasamy, Sudarshan Karki, Jeff S Kissel, Greg Mendell, et al. Calibration uncertainty for advanced ligo's first and second observing runs. *Physical Review D*, 96(10):102001, 2017.

[69] Enrico Calloni, Archimedes Collaboration, and Virgo Collaboration. High-bandwidth beam balance for vacuum-weight experiment and newtonian noise subtraction. *The European Physical Journal Plus*, 136(3):335, Mar 2021. ISSN 2190-5444. doi: 10.1140/epjp/s13360-021-01214-4. URL `https://doi.org/10.1140/epjp/s13360-021-01214-4`.

[70] Chiara Caprini and Nicola Tamanini. Constraining early and interacting dark energy with gravitational wave standard sirens: the potential of the elisa mission. *Journal of Cosmology and Astroparticle Physics*, 2016(10):006, 2016.

[71] J Carriere, CJ Horowitz, and J Piekarewicz. Low-mass neutron stars and the equation of state of dense matter. *The Astrophysical Journal*, 593(1):463, 2003.

[72] Jerry A Carter, Noel Barstow, Paul W Pomeroy, Eric P Chael, and Patrick J Leahy. High-frequency seismic noise as a function of depth. *Bulletin of the Seismological Society of America*, 81(4): 1101–1114, 1991.

[73] Jorge L Cervantes-Cota, Salvador Galindo-Uribarri, and George F Smoot. A brief history of gravitational waves. *Universe*, 2(3):22, 2016.

[74] Walid Chaibi, Remi Geiger, Benjamin Canuel, Andrea Bertoldi, Arnaud Landragin, and Philippe Bouyer. Low frequency gravitational wave detection with ground-based atom interferometer arrays. *Physical Review D*, 93(2):021101, 2016.

[75] Man Leong Chan, Ik Siong Heng, and Chris Messenger. Detection and classification of supernova gravitational wave signals: A deep learning approach. *Physical Review D*, 102(4):043022, 2020.

[76] Shourov Chatterji, Albert Lazzarini, Leo Stein, Patrick J Sutton, Antony Searle, and Massimo Tinto. Coherent network analysis technique for discriminating gravitational-wave bursts from instrumental noise. *Physical Review D*, 74(8):082005, 2006.

[77] Katerina Chatziioannou and Will M Farr. Inferring the maximum and minimum mass of merging neutron stars with gravitational waves. *Physical Review D*, 102(6):064063, 2020.

[78] Nelson Christensen. Stochastic gravitational wave backgrounds. *Reports on Progress in Physics*, 82(1):016903, 2018.

[79] LIGO Scientific Collaboration, Virgo Collaboration, et al. Low-latency gravitational-wave alerts for multimessenger astronomy during the second advanced ligo and virgo observing run. *The Astrophysical Journal*, 875(2):161, 2019.

[80] Michael Coughlin, Jan Harms, Nelson Christensen, Vladimir Dergachev, Riccardo DeSalvo, Shivaraj Kandhasamy, and Vuk Mandic. Wiener filtering with a seismic underground array at the sanford underground research facility. *Classical and Quantum Gravity*, 31(21):215003, 2014.

[81] Michael Coughlin, Nikhil Mukund, Jan Harms, Jenne Driggers, Rana Adhikari, and Sanjit Mitra. Towards a first design of a newtonian-noise cancellation system for advanced ligo. *Classical and Quantum Gravity*, 33(24):244001, 2016.

[82] Michael Coughlin, Jan Harms, DC Bowden, Patrick Meyers, Victor C Tsai, Vuk Mandic, Gary Pavlis, and Tanner Prestegard. Coherence-based approaches for estimating the composition of the seismic wavefield. *Journal of Geophysical Research: Solid Earth*, 124(3):2941–2956, 2019.

[83] Michael W Coughlin, Jan Harms, J Driggers, DJ McManus, Nikhil Mukund, MP Ross, BJJ Slagmolen, and K Venkateswara. Implications of dedicated seismometer measurements on newtonian-noise cancellation for advanced ligo. *Physical review letters*, 121(22): 221104, 2018.

[84] Curt Cutler and David Ian Jones. Gravitational wave damping of neutron star wobble. *Physical Review D*, 63(2):024002, 2000.

[85] Thibault Damour, Piotr Jaranowski, and Gerhard Schäfer. Conservative dynamics of two-body systems at the fourth post-newtonian approximation of general relativity. *Physical Review D*, 93(8):084014, 2016.

[86] Stefan L Danilishin and Farid Ya Khalili. Quantum measurement theory in gravitational-wave detectors. *Living Reviews in Relativity*, 15(1):1–147, 2012.

[87] Shinji Miyoki David Shoemaker, Alessio Rocchi. Compact object masses, 3 2023. URL `https://dcc.ligo.org/LIGO-G2002127-v12/public`.

[88] DB DeBra. Vibration isolation of precision machine tools and instruments. *CIRP annals*, 41(2):711–718, 1992.

[89] F Douchin and P Haensel. A unified equation of state of dense matter and neutron star structure. *Astronomy & Astrophysics*, 380(1):151–167, 2001.

[90] Jennifer C Driggers, Jan Harms, and Rana X Adhikari. Subtraction of newtonian noise using optimized sensor arrays. *Physical Review D*, 86(10):102001, 2012.

[91] Jennifer C Driggers, S Vitale, AP Lundgren, Matthew Evans, Keita Kawabe, SE Dwyer, K Izumi, RMS Schofield, A Effler, D Sigg, et al. Improving astrophysical parameter estimation via offline noise subtraction for advanced ligo. *Physical Review D*, 99 (4):042001, 2019.

[92] Sheila Dwyer, Daniel Sigg, Stefan W Ballmer, Lisa Barsotti, Nergis Mavalvala, and Matthew Evans. Gravitational wave detector with cosmological reach. *Physical Review D*, 91(8):082001, 2015.

[93] Richard Easther, John T Giblin Jr, and Eugene A Lim. Gravitational wave production at the end of inflation. *Physical Review Letters*, 99(22):221301, 2007.

[94] Motohiro Enoki, Kaiki T Inoue, Masahiro Nagashima, and Naoshi Sugiyama. Gravitational waves from supermassive black hole coalescence in a hierarchical galaxy formation model. *The Astrophysical Journal*, 615(1):19, 2004.

[95] ET Science Team. Einstein gravitational wave Telescope conceptual design study. *available from European Gravitational Observatory, document number ET-0106C-10*, 2011.

[96] Benjamin Farr, Vicky Kalogera, and Erik Luijten. Efficient estimation of highly structured posteriors of gravitational-wave signals with markov-chain monte carlo. *arXiv preprint arXiv:1309.7709*, 2013.

[97] Marco Ferraris, Mauro Francaviglia, and Cesare Reina. Variational formulation of general relativity from 1915 to 1925 "palatini's method" discovered by einstein in 1925. *General relativity and gravitation*, 14(3):243–254, 1982.

[98] I Fiori, L Holloway, and F Paoletti. Studies of the $1-4\,\mathrm{Hz}$ seism. *Virgo TDS*, 2003. URL `https://tds.virgo-gw.eu/?content=3&r=1463`.

[99] Janyce Franc, Nazario Morgado, Raffaele Flaminio, Ronny Nawrodt, Iain Martin, Liam Cunningham, Alan Cumming, Sheila Rowan, and James Hough. Mirror thermal noise in laser interferometer gravitational wave detectors operating at room and cryogenic temperature. *arXiv preprint arXiv:0912.0107*, 2009.

[100] Aaron Geller Frank Elavsky. Compact object masses, 2023. URL `https://www.ligo.org/science/Publication-O3bCatalog/`.

[101] Yoshinori Fujii, Thomas Adams, Frédérique Marion, and Raffaele Flaminio. Fast localization of coalescing binaries with a heterogeneous network of advanced gravitational wave detectors. *Astroparticle Physics*, 113:1–5, 2019.

[102] Masahiko Fuyuki and Yoshiro Matsumoto. Finite difference analysis of rayleigh wave scattering at a trench. *Bulletin of the Seismological Society of America*, 70(6):2051–2069, 1980.

[103] Chad R Galley and Manuel Tiglio. Radiation reaction and gravitational waves in the effective field theory approach. *Physical Review D*, 79(12):124027, 2009.

[104] Boris Goncharov, Alexander H Nitz, and Jan Harms. Utilizing the null stream of the einstein telescope. *Physical Review D*, 105(12): 122007, 2022.

[105] Interferometer Gravitational-Wave. Ligo detects gravitational waves. *Physics Today*, 2016.

[106] Stefan Grimm and Jan Harms. Multiband gravitational-wave parameter estimation: A study of future detectors. *Physical Review D*, 102(2):022007, 2020.

[107] Hartmut Grote, Andreas Freise, Michaela Malec, Gerhard Heinzel, Benno Willke, Harald Lück, Kenneth A Strain, Jim Hough, and Karsten Danzmann. Dual recycling for geo 600. *Classical and Quantum Gravity*, 21(5):S473, 2004.

[108] Hartmut Grote, LIGO Scientific Collaboration, et al. The geo 600 status. *Classical and Quantum Gravity*, 27(8):084003, 2010.

[109] L Gualtieri, R Ciolfi, and V Ferrari. Structure, deformations and gravitational wave emission of magnetars. *Classical and Quantum Gravity*, 28(11):114014, 2011.

[110] Yekta Gürsel and Massimo Tinto. Near optimal solution to the inverse problem for gravitational-wave bursts. *Physical Review D*, 40(12):3884, 1989.

[111] Martin G Haehnelt. Low-frequency gravitational waves from supermassive black holes. *Monthly Notices of the Royal Astronomical Society*, 269(1):199–208, 1994.

[112] Alex Hall, Andrew D Gow, and Christian T Byrnes. Bayesian analysis of ligo-virgo mergers: Primordial versus astrophysical black hole populations. *Physical Review D*, 102(12):123524, 2020.

[113] Evan D Hall. Cosmic explorer: A next-generation ground-based gravitational-wave observatory. *Galaxies*, 10(4):90, 2022.

[114] Evan D Hall and Matthew Evans. Metrics for next-generation gravitational-wave detectors. *Classical and Quantum Gravity*, 36 (22):225002, 2019.

[115] J Harms, F Acernese, F Barone, I Bartos, M Beker, J F J van den Brand, N Christensen, M Coughlin, R DeSalvo, S Dorsher, J Heise, S Kandhasamy, V Mandic, S Márka, G Mueller, L Naticchioni, T O'Keefe, D S Rabeling, A Sajeva, T Trancynger, and V Wand. Characterization of the seismic environment at the Sanford Underground Laboratory, South Dakota. *Classical and Quantum Gravity*, 27(22):225011, 2010. URL `http://stacks.iop.org/0264-9381/27/i=22/a=225011`.

[116] J. Harms, E. L. Bonilla, M. W. Coughlin, J. Driggers, S. E. Dwyer, D. J. McManus, M. P. Ross, B. J. J. Slagmolen, and K. Venkateswara. Observation of a potential future sensitivity limitation from ground motion at LIGO Hanford. *Phys. Rev. D*, 101: 102002, May 2020. doi: 10.1103/PhysRevD.101.102002. URL `https://link.aps.org/doi/10.1103/PhysRevD.101.102002`.

[117] Jan Harms. Terrestrial gravity fluctuations. *Living reviews in relativity*, 18:1–150, 2015.

[118] Jan Harms. Terrestrial gravity fluctuations. *Living Reviews in Relativity*, 22(1):6, Oct 2019. ISSN 1433-8351. doi: 10.1007/s41114-019-0022-2. URL `https://doi.org/10.1007/s41114-019-0022-2`.

[119] Jan Harms and Stefan Hild. Passive Newtonian noise suppression for gravitational-wave observatories based on shaping of the local topography. *Classical and Quantum Gravity*, 31(18):185011, 2014. URL `http://stacks.iop.org/0264-9381/31/i=18/a=185011`.

[120] Jan Harms and Ho Jung Paik. Newtonian-noise cancellation in full-tensor gravitational-wave detectors. *Physical Review D*, 92 (2):022001, 2015.

[121] Jan Harms and Krishna Venkateswara. Newtonian-noise cancellation in large-scale interferometric GW detectors using seismic tiltmeters. *Classical and Quantum Gravity*, 33(23):234001, oct 2016. doi: 10.1088/0264-9381/33/23/234001. URL `https://doi.org/10.1088%2F0264-9381%2F33%2F23%2F234001`.

[122] Jan Harms, Yanbei Chen, Simon Chelkowski, Alexander Franzen, Henning Vahlbruch, Karsten Danzmann, and Roman Schnabel. Squeezed-input, optical-spring, signal-recycled gravitational-wave detectors. *Physical Review D*, 68(4):042001, 2003.

[123] Jan Harms, Riccardo DeSalvo, Steven Dorsher, and Vuk Mandic. Simulation of underground gravity gradients from stochastic seismic fields. *Phys. Rev. D*, 80:122001, Dec 2009. doi: 10.1103/PhysRevD.80.122001. URL `http://link.aps.org/doi/10.1103/PhysRevD.80.122001`.

[124] Jan Harms, Riccardo DeSalvo, Steven Dorsher, and Vuk Mandic. Gravity-gradient subtraction in 3rd generation underground gravitational-wave detectors in homogeneous media. *arXiv preprint arXiv:0910.2774*, 2009.

[125] Jan Harms, Edgard Bonilla, Michael W. Coughlin, Jennifer C. Driggers, Sheila E. Dwyer, David J. McManus, Michael Ross, Bram J. J. Slagmolen, and Krishna Venkateswara. Observation of a potential future sensitivity limitation from ground motion at ligo hanford. *Physical Review D*, 2020.

[126] Jan Harms, Filippo Ambrosino, Lorella Angelini, Valentina Braito, Marica Branchesi, Enzo Brocato, Enrico Cappellaro, Eugenio Coccia, Michael Coughlin, Roberto Della Ceca, et al. Lunar gravitational-wave antenna. *The Astrophysical Journal*, 910(1):1, 2021.

[127] Jan Harms, Luca Naticchioni, Enrico Calloni, Rosario De Rosa, Fulvio Ricci, and Domenico D'Urso. A lower limit for newtonian-noise models of the einstein telescope. *The European Physical Journal Plus*, 137(6):1–16, 2022.

[128] Waled Hassan and Peter B Nagy. Simplified expressions for the displacements and stresses produced by the rayleigh wave. *The Journal of the Acoustical Society of America*, 104(5):3107–3110, 1998.

[129] Alexander Heger and Stanford E Woosley. The nucleosynthetic signature of population iii. *The Astrophysical Journal*, 567(1):532, 2002.

[130] S Hild, M Abernathy, F Acernese, P Amaro-Seoane, N Andersson, K Arun, F Barone, B Barr, M Barsuglia, M Beker, et al. Sensitivity studies for third-generation gravitational wave observatories. *Classical and Quantum gravity*, 28(9):094013, 2011.

[131] Stefan Hild, Simon Chelkowski, and Andreas Freise. Pushing towards the et sensitivity using'conventional'technology. *arXiv preprint arXiv:0810.0604*, 2008.

[132] Ting Hong, Huan Yang, Eric K Gustafson, Rana X Adhikari, and Yanbei Chen. Brownian thermal noise in multilayer coated mirrors. *Physical Review D*, 87(8):082001, 2013.

[133] Jim Hough and Sheila Rowan. The search for gravitational waves. *Physics world*, 18(1):37, 2005.

[134] Wensheng Hua. *Low frequency vibration isolation and alignment system for advanced LIGO.* stanford university, 2005.

[135] Scott A. Hughes and Kip S. Thorne. Seismic gravity-gradient noise in interferometric gravitational-wave detectors. *Phys. Rev. D*, 58:122002, Nov 1998. doi: 10.1103/PhysRevD.58.122002. URL http://link.aps.org/doi/10.1103/PhysRevD.58.122002.

[136] Scott A Hughes and Kip S Thorne. Seismic gravity-gradient noise in interferometric gravitational-wave detectors. *Physical Review D*, 58(12):122002, 1998.

[137] RA Hulse and JH Taylor. A deep sample of new pulsars and their spatial extent in the galaxy. *The Astrophysical Journal*, 201:L55–L59, 1975.

[138] Russell A Hulse and Joseph H Taylor. Discovery of a pulsar in a binary system. *The Astrophysical Journal*, 195:L51–L53, 1975.

[139] Russell Alan Hulse and JH Taylor. A high-sensitivity pulsar survey. *The Astrophysical Journal*, 191:L59, 1974.

[140] Karan Jani and Abraham Loeb. Gravitational-wave lunar observatory for cosmology. *Journal of Cosmology and Astroparticle Physics*, 2021(06):044, 2021.

[141] H-Th Janka, K Langanke, Andreas Marek, G Martínez-Pinedo, and B Müller. Theory of core-collapse supernovae. *Physics Reports*, 442(1-6):38–74, 2007.

[142] Alexander C Jenkins, O'Shaughnessy Richard, Mairi Sakellariadou, and Daniel Wysocki. Anisotropies in the astrophysical gravitational-wave background: The impact of black hole distributions. *Physical review letters*, 122(11):111101, 2019.

[143] Hajime Kawahara, Takami Kuroda, Tomoya Takiwaki, Kazuhiro Hayama, and Kei Kotake. A linear and quadratic time–frequency analysis of gravitational waves from core-collapse supernovae. *The Astrophysical Journal*, 867(2):126, 2018.

[144] S Klimenko, G Vedovato, M Drago, F Salemi, V Tiwari, GA Prodi, C Lazzaro, K Ackley, S Tiwari, CF Da Silva, et al. Method for detection and reconstruction of gravitational wave transients with networks of advanced detectors. *Physical Review D*, 93(4):042004, 2016.

[145] S Koley, H J Bulten, J van den Brand, M Bader, X Campman, and M Beker. S-wave velocity model estimation using ambient seismic noise at virgo, italy seg technical program expanded. *Society of Exploration Geophysicists*, 2017. URL `10.1190/segam2017-17681951.1`.

[146] Soumen Koley, Henk Jan Bulten, Jo van den Brand, Maria Bader, Xander Campman, and Mark Beker. *S-wave Velocity Model Estimation using Ambient Seismic Noise at Virgo, Italy*, pages 2946–2950. SEG LIBRARY, 2017. doi: 10.1190/segam2017-17681951.1. URL `https://library.seg.org/doi/abs/10.1190/segam2017-17681951.1`.

[147] IS Kondrashov, DA Simakov, F Ya Khalili, and SL Danilishin. Optimizing the regimes of the advanced ligo gravitational wave detector for multiple source types. *Physical Review D*, 78(6):062004, 2008.

[148] Kei Kotake, Katsuhiko Sato, and Keitaro Takahashi. Explosion mechanism, neutrino burst and gravitational wave in core-collapse supernovae. *Reports on Progress in Physics*, 69(4):971, 2006.

[149] H. Krim and M. Viberg. Two decades of array signal processing research: the parametric approach. *Signal Processing Magazine, IEEE*, 13(4):67–94, Jul 1996. ISSN 1053-5888. doi: 10.1109/79. 526899.

[150] Sachiko Kuroyanagi, Takeshi Chiba, and Tomo Takahashi. Probing the universe through the stochastic gravitational wave background. *Journal of Cosmology and Astroparticle Physics*, 2018 (11):038, 2018.

[151] Koutarou Kyutoku, Masaru Shibata, and Keisuke Taniguchi. Gravitational waves from nonspinning black hole-neutron star binaries: dependence on equations of state. *Physical Review D*, 82(4): 044049, 2010.

[152] Eric Lerner. *The Big Bang never happened: a startling refutation of the dominant theory of the origin of the universe*. Vintage, 2010.

[153] Yuk Tung Liu and Kip S Thorne. Thermoelastic noise and homogeneous thermal noise in finite sized gravitational-wave test masses. *Physical Review D*, 62(12):122002, 2000.

[154] Melissa López, Marco Drago, Irene Di Palma, Fulvio Ricci, and Pablo Cerdá-Durán. Deep learning algorithms for gravitational waves core-collapse supernova detection. In *2021 International Conference on Content-Based Multimedia Indexing (CBMI)*, pages 1–6. IEEE, 2021.

[155] G Losurdo, G Calamai, E Cuoco, L Fabbroni, G Guidi, M Mazzoni, R Stanga, F Vetrano, L Holloway, D Passuello, et al. Inertial control of the mirror suspensions of the virgo interferometer for gravitational wave detection. *Review of Scientific Instruments*, 72(9):3653–3661, 2001.

[156] AK Mal and L Knopoff. Transmission of rayleigh waves past a step change in elevation. *Bulletin of the seismological society of America*, 55(2):319–334, 1965.

[157] Ilya Mandel and Richard O'Shaughnessy. Compact binary coalescences in the band of ground-based gravitational-wave detectors. *Classical and Quantum Gravity*, 27(11):114007, 2010.

[158] F Marin, L Conti, and M De Rosa. A folded fabry–perot cavity for optical sensing in gravitational wave detectors. *Physics Letters A*, 309(1-2):15–23, 2003.

[159] Chris Messenger and Jocelyn Read. Measuring a cosmological distance-redshift relationship using only gravitational wave observations of binary neutron star coalescences. *Physical review letters*, 108(9):091101, 2012.

[160] Cameron Mills and Stephen Fairhurst. Measuring gravitational-wave higher-order multipoles. *Physical Review D*, 103(2):024042, 2021.

[161] Suvodip Mukherjee and Joseph Silk. Can we distinguish astrophysical from primordial black holes via the stochastic gravitational wave background? *Monthly Notices of the Royal Astronomical Society*, 506(3):3977–3985, 2021.

[162] L Naticchioni, M Perciballi, F Ricci, E Coccia, V Malvezzi, F Acernese, F Barone, G Giordano, R Romano, M Punturo, et al. Microseismic studies of an underground site for a new interferometric gravitational wave detector. *Classical and Quantum Gravity*, 31(10):105016, 2014.

[163] Lara Nava. High-energy emission from gamma-ray bursts. *International Journal of Modern Physics D*, 27(13):1842003, 2018.

[164] John Norton. How einstein found his field equations: 1912-1915. *Historical studies in the physical sciences*, 14(2):253–316, 1984.

[165] Laura K Nuttall and Patrick J Sutton. Identifying the host galaxy of gravitational wave signals. *Physical Review D*, 82(10):102002, 2010.

[166] E Oelker, L Barsotti, S Dwyer, D Sigg, and N Mavalvala. Squeezed light for advanced gravitational wave detectors and beyond. *Optics express*, 22(17):21106–21121, 2014.

[167] Christian D Ott. The gravitational-wave signature of core-collapse supernovae. *Classical and Quantum Gravity*, 26(6):063001, 2009.

[168] Christian D Ott, Adam Burrows, Luc Dessart, and Eli Livne. A new mechanism for gravitational-wave emission in core-collapse supernovae. *Physical Review Letters*, 96(20):201102, 2006.

[169] Chris Pankow, Eve A Chase, Scott Coughlin, Michael Zevin, and Vassiliki Kalogera. Improvements in gravitational-wave sky localization with expanded networks of interferometers. *The Astrophysical Journal Letters*, 854(2):L25, 2018.

[170] Keenan Pepper. Newtonian noise simulation and suppression for gravitational-wave interferometers. *Pasadena, CA: LIGO*, 2007.

[171] Philip Carl Peters. Gravitational radiation and the motion of two point masses. *Physical Review*, 136(4B):B1224, 1964.

[172] Matthew Pitkin, Stuart Reid, Sheila Rowan, and Jim Hough. Gravitational wave detection by interferometry (ground and space). *Living Reviews in Relativity*, 14(1):1–75, 2011.

[173] Reinhard Prix. Search for continuous gravitational waves: Metric of the multidetector f-statistic. *Physical Review D*, 75(2):023004, 2007.

[174] M Punturo, M Abernathy, F Acernese, B Allen, Nils Andersson, K Arun, F Barone, B Barr, M Barsuglia, M Beker, et al. The einstein telescope: a third-generation gravitational wave observatory. *Classical and Quantum Gravity*, 27(19):194002, 2010.

[175] Michele Punturo and Kentaro Somiya. Underground gravitational wave observatories: Kagra and et. *International Journal of Modern Physics D*, 22(05):1330010, 2013.

[176] Michele Punturo, M Abernathy, F Acernese, B Allen, N Andersson, K Arun, F Barone, B Barr, M Barsuglia, M Beker, et al. The third generation of gravitational wave observatories and their science reach. *Classical and Quantum Gravity*, 27(8):084007, 2010.

[177] David Radice, Albino Perego, Francesco Zappa, and Sebastiano Bernuzzi. Gw170817: joint constraint on the neutron star equation of state from multimessenger observations. *The Astrophysical Journal Letters*, 852(2):L29, 2018.

[178] M Rakhmanov, RL Savage Jr, DH Reitze, and DB Tanner. Dynamic resonance of light in fabry–perot cavities. *Physics Letters A*, 305(5):239–244, 2002.

[179] Malik Rakhmanov. Rank deficiency and tikhonov regularization in the inverse problem for gravitational-wave bursts. *Classical and Quantum Gravity*, 23(19):S673, 2006.

[180] Tania Regimbau. The astrophysical gravitational wave stochastic background. *Research in Astronomy and Astrophysics*, 11(4):369, 2011.

[181] Tania Regimbau. The quest for the astrophysical gravitational-wave background with terrestrial detectors. *Symmetry*, 14(2):270, 2022.

[182] Tania Regimbau, Thomas Dent, Walter Del Pozzo, Stefanos Giampanis, Tjonnie GF Li, Craig Robinson, Chris Van Den Broeck, Duncan Meacher, Carl Rodriguez, Bangalore S Sathyaprakash, et al. Mock data challenge for the einstein gravitational-wave telescope. *Physical Review D*, 86(12):122001, 2012.

[183] David Reitze, Rana X Adhikari, Stefan Ballmer, Barry Barish, Lisa Barsotti, GariLynn Billingsley, Duncan A Brown, Yanbei Chen, Dennis Coyne, Robert Eisenstein, et al. Cosmic explorer: the us contribution to gravitational-wave astronomy beyond ligo. *arXiv preprint arXiv:1907.04833*, 2019.

[184] Clifford E Rhoades Jr and Remo Ruffini. Maximum mass of a neutron star. *Physical Review Letters*, 32(6):324, 1974.

[185] Keith Riles. Recent searches for continuous gravitational waves. *Modern Physics Letters A*, 32(39):1730035, 2017.

[186] Jameson Graef Rollins, Evan Hall, Christopher Wipf, and Lee McCuller. pygwinc: Gravitational wave interferometer noise calculator. *Astrophysics Source Code Library*, pages ascl–2007, 2020.

[187] Joseph D Romano and Neil J Cornish. Detection methods for stochastic gravitational-wave backgrounds: a unified treatment. *Living reviews in relativity*, 20(1):2, 2017.

[188] Surabhi Sachdev, Tania Regimbau, and BS Sathyaprakash. Subtracting compact binary foreground sources to reveal primordial gravitational-wave backgrounds. *Physical Review D*, 102(2):024051, 2020.

[189] Mohammadtaher Safarzadeh, Sylvia Biscoveanu, and Abraham Loeb. Constraining the delay time distribution of compact binary objects from the stochastic gravitational-wave background searches. *The Astrophysical Journal*, 901(2):137, 2020.

[190] Jeremy Sakstein, Djuna Croon, Samuel D McDermott, Maria C Straight, and Eric J Baxter. Beyond the standard model explanations of gw190521. *Physical Review Letters*, 125(26):261105, 2020.

[191] M Saleem, Javed Rana, V Gayathri, Aditya Vijaykumar, Srashti Goyal, Surabhi Sachdev, Jishnu Suresh, S Sudhagar, Arunava Mukherjee, Gurudatt Gaur, et al. The science case for ligo-india. *Classical and Quantum Gravity*, 39(2):025004, 2021.

[192] Bangalore Suryanarayana Sathyaprakash and Bernard F Schutz. Physics, astrophysics and cosmology with gravitational waves. *Living reviews in relativity*, 12(1):1–141, 2009.

[193] Peter R Saulson. Terrestrial gravitational noise on a gravitational wave antenna. *Physical Review D*, 30(4):732, 1984.

[194] Bernard F Schutz. Networks of gravitational wave detectors and three figures of merit. *Classical and Quantum Gravity*, 28(12): 125023, 2011.

[195] Bernard F Schutz and BS Sathyaprakash. Self-calibration of networks of gravitational wave detectors. *arXiv preprint arXiv:2009.10212*, 2020.

[196] DA Shaddock. Space-based gravitational wave detection with lisa. *Classical and Quantum Gravity*, 25(11):114012, 2008.

[197] Masaru Shibata. Constraining nuclear equations of state using gravitational waves from hypermassive neutron stars. *Physical review letters*, 94(20):201101, 2005.

[198] Leo P Singer and Larry R Price. Rapid bayesian position reconstruction for gravitational-wave transients. *Physical Review D*, 93 (2):024013, 2016.

[199] Ayatri Singha, Stefan Hild, and Jan Harms. Newtonian-noise reassessment for the virgo gravitational-wave observatory including local recess structures. *Classical and Quantum Gravity*, 37(10): 105007, 2020.

[200] Ayatri Singha, Stefan Hild, Jan Harms, Maria C Tringali, Irene Fiori, Federico Paoletti, Tomasz Bulik, Bartosz Idzkowski, Alessandro Bertolini, Enrico Calloni, et al. Characterization of the seismic field at virgo and improved estimates of newtonian-noise suppression by recesses. *Classical and Quantum Gravity*, 38(24): 245007, 2021.

[201] Marcelle Soares-Santos, DE Holz, J Annis, R Chornock, K Herner, Eric Berger, D Brout, H-Y Chen, R Kessler, M Sako, et al. The electromagnetic counterpart of the binary neutron star merger ligo/virgo gw170817. i. discovery of the optical counterpart using the dark energy camera. *The Astrophysical Journal Letters*, 848(2):L16, 2017.

[202] Mario Spera and Michela Mapelli. Very massive stars, pair-instability supernovae and intermediate-mass black holes with the sevn code. *Monthly Notices of the Royal Astronomical Society*, 470 (4):4739–4749, 2017.

[203] Ling Sun, Evan Goetz, Jeffrey S Kissel, Joseph Betzwieser, Sudarshan Karki, Aaron Viets, Madeline Wade, Dripta Bhattacharjee, Vladimir Bossilkov, Pep B Covas, et al. Characterization of systematic error in advanced ligo calibration. *Classical and Quantum Gravity*, 37(22):225008, 2020.

[204] Patrick J Sutton, Gareth Jones, Shourov Chatterji, Peter Kalmus, Isabel Leonor, Stephen Poprocki, Jameson Rollins, Antony Searle, Leo Stein, Massimo Tinto, et al. X-pipeline: an analysis package for autonomous gravitational-wave burst searches. *New Journal of Physics*, 12(5):053034, 2010.

[205] Marek J Szczepańczyk, Javier M Antelis, Michael Benjamin, Marco Cavaglia, Dorota Gondek-Rosińska, Travis Hansen, Sergey Klimenko, Manuel D Morales, Claudia Moreno, Soma Mukherjee, et al. Detecting and reconstructing gravitational waves from the next galactic core-collapse supernova in the advanced detector era. *Physical Review D*, 104(10):102002, 2021.

[206] Nial R Tanvir, AJ Levan, C González-Fernández, O Korobkin, Ilya Mandel, Stephan Rosswog, Jens Hjorth, Paolo D'Avanzo, AS Fruchter, CL Fryer, et al. The emergence of a lanthanide-rich

kilonova following the merger of two neutron stars. *The Astrophysical Journal Letters*, 848(2):L27, 2017.

[207] Maria Concetta Tringali, Tomasz Bulik, Jan Harms, Irene Fiori, Frederico Paoletti, Neha Singh, Bartosz Idzkowski, Adam Kutynia, Krzysztof Nikliborc, Maciej Suchiński, Alessandro Bertolini, and Soumen Koley. Seismic array measurements at Virgo's West End Building for the configuration of a Newtonian-noise cancellation system. *Classical and Quantum Gravity*, 2019. URL `http://iopscience.iop.org/10.1088/1361-6382/ab5c43`.

[208] Elenora Troja, LUIGI Piro, H Van Eerten, RT Wollaeger, M Im, OD Fox, NR Butler, SB Cenko, T Sakamoto, CL Fryer, et al. The x-ray counterpart to the gravitational-wave event gw170817. *Nature*, 551(7678):71–74, 2017.

[209] CS Unnikrishnan. Indigo and ligo-india: Scope and plans for gravitational wave research and precision metrology in india. *International Journal of Modern Physics D*, 22(01):1341010, 2013.

[210] Yousuke Utsumi, Masaomi Tanaka, Nozomu Tominaga, Michitoshi Yoshida, Sudhanshu Barway, Takahiro Nagayama, Tetsuya Zenko, Kentaro Aoki, Takuya Fujiyoshi, Hisanori Furusawa, et al. J-gem observations of an electromagnetic counterpart to the neutron star merger gw170817. *Publications of the Astronomical Society of Japan*, 69(6):101, 2017.

[211] Henning Vahlbruch, Simon Chelkowski, Boris Hage, Alexander Franzen, Karsten Danzmann, and Roman Schnabel. Demonstration of a squeezed-light-enhanced power-and signal-recycled michelson interferometer. *Physical review letters*, 95(21):211102, 2005.

[212] Stefano Valenti, J David, Sheng Yang, Enrico Cappellaro, Leonardo Tartaglia, Alessandra Corsi, Saurabh W Jha, Daniel E Reichart, Joshua Haislip, and Vladimir Kouprianov. The discovery of the electromagnetic counterpart of gw170817: kilonova at 2017gfo/dlt17ck. *The Astrophysical Journal Letters*, 848(2):L24, 2017.

[213] Michele Vallisneri. Prospects for gravitational-wave observations of neutron-star tidal disruption in neutron-star–black-hole binaries. *Physical Review Letters*, 84(16):3519, 2000.

[214] Jan Van Eijk. On the design of plate-spring mechanisms. 1985.

[215] Salvatore Vitale. Multiband gravitational-wave astronomy: parameter estimation and tests of general relativity with space-and ground-based detectors. *Physical Review Letters*, 117(5):051102, 2016.

[216] Salvatore Vitale, Walter Del Pozzo, Tjonnie GF Li, Chris Van Den Broeck, Ilya Mandel, Ben Aylott, and John Veitch. Effect of calibration errors on bayesian parameter estimation for gravitational wave signals from inspiral binary systems in the advanced detectors era. *Physical Review D*, 85(6):064034, 2012.

[217] Stefano Vitale. Space-borne gravitational wave observatories. *General Relativity and Gravitation*, 46:1–19, 2014.

[218] Michael E Wall, Andreas Rechtsteiner, and Luis M Rocha. Singular value decomposition and principal component analysis. In *A practical approach to microarray data analysis*, pages 91–109. Springer, 2003.

[219] Linqing Wen. Data analysis of gravitational waves using a network of detectors. *International Journal of Modern Physics D*, 17(07): 1095–1104, 2008.

[220] Linqing Wen and Yanbei Chen. Geometrical expression for the angular resolution of a network of gravitational-wave detectors. *Phys. Rev. D*, 81:082001, Apr 2010. doi: 10.1103/PhysRevD.81. 082001. URL https://link.aps.org/doi/10.1103/PhysRevD. 81.082001.

[221] Linqing Wen and Yanbei Chen. Geometrical expression for the angular resolution of a network of gravitational-wave detectors. *Physical Review D*, 81(8):082001, 2010.

[222] Linqing Wen and Bernard F Schutz. Coherent network detection of gravitational waves: the redundancy veto. *Classical and Quantum Gravity*, 22(18):S1321–S1335, sep 2005. doi: 10.1088/0264-9381/ 22/18/s46. URL https://doi.org/10.1088/0264-9381/22/18/ s46.

[223] Benno Willke, Peter Aufmuth, Carsten Aulbert, Stanislav Babak, Ramachandran Balasubramanian, BW Barr, S Berukoff, Sukanta

Bose, G Cagnoli, Morag M Casey, et al. The geo 600 gravitational wave detector. *Classical and Quantum Gravity*, 19(7):1377, 2002.

[224] Stacy Wise, G Mueller, D Reitze, DB Tanner, and BF Whiting. Linewidth-broadened fabry–perot cavities within future gravitational wave detectors. *Classical and Quantum Gravity*, 21(5): S1031, 2004.

[225] Isaac CF Wong and Tjonnie GF Li. Signal space in the triangular network of the einstein telescope. *Physical Review D*, 105(8): 084002, 2022.

[226] Stanford Earl Woosley, S Blinnikov, and Alexander Heger. Pulsational pair instability as an explanation for the most luminous supernovae. *Nature*, 450(7168):390–392, 2007.

[227] Kent Yagi and Leo C Stein. Black hole based tests of general relativity. *Classical and Quantum Gravity*, 33(5):054001, 2016.

[228] Mare Yamamoto and Haruo Sato. Multiple scattering and mode conversion revealed by an active seismic experiment at asama volcano, japan. *Journal of Geophysical Research: Solid Earth*, 115 (B7), 2010.

[229] Xuan-Neng Zhang, Ling-Feng Wang, Jing-Fei Zhang, and Xin Zhang. Improving cosmological parameter estimation with the future gravitational-wave standard siren observation from the einstein telescope. *Physical Review D*, 99(6):063510, 2019.

[230] X-J Zhu, Linqing Wen, George Hobbs, Yilin Zhang, Yan Wang, Dustin R Madison, Richard N Manchester, Matthew Kerr, Pablo A Rosado, and J-B Wang. Detection and localization of single-source gravitational waves with pulsar timing arrays. *Monthly Notices of the Royal Astronomical Society*, 449(2):1650–1663, 2015.

[231] Michael E Zucker and Stanley E Whitcomb. Measurement of optical path fluctuations due to residual gas in the ligo 40 meter interferometer. In *Proceedings of the Seventh Marcel Grossman Meeting on recent developments in theoretical and experimental general relativity, gravitation, and relativistic field theories*, pages 1434–1436, 1996.

Summary

Gravitational waves are extremely small ripples in the stationary curvature of space-time in the Universe, produced by the motion and collisions of astrophysical objects of extreme mass and density, such as neutron stars and black holes. They were predicted by Albert Einstein in 1916 and detected by LIGO 100 years later. Detecting gravitational waves is an extremely challenging task because of their tiny amplitude, which requires exceptional precision from the measuring instrument.

Laser interferometer gravitational wave detectors split a laser beam into two arms with mirrors at the ends. When a gravitational wave passes through, it changes the lengths of the arms, causing a phase difference in the recombined laser beams. Detection challenges arise from various sources of noise, including seismic, thermal, quantum, Newtonian, detector noise and instrumental artifacts that can mimic a GW signal.

In the first half of the dissertation, I discussed Newtonian noise mitigation techniques for gravitational wave detectors, focusing on a comprehensive analysis of Newtonian noise in the Virgo detector. Newtonian noise, also known as gravitational gradient noise, manifests as the fluctuations of local gravitational fields, which originate from the density variations in the surroundings of the test masses caused by seismic, atmospheric, or anthropogenic factors. These density variations exert excess gravity force on the test mass in the gravitational wave detector, thereby mimicking GW signals at low frequencies.

While it is not possible to shield the detector directly from NN, there are conventional strategies for noise reduction. One such approach is to select for detector construction seismically quiet sites with minimal natural and man-made seismic disturbances. Going underground, as planned for the Einstein telescope, reduces seismic noise. Current detectors use NN subtraction with seismic sensors close to the test masses to estimate and cancel NN. This is challenging due to the complexity of

real seismic fields. It is favorable to choose flat surfaces to avoid scattering. Proper seismometer placement is critical due to limited coverage. Another possible method involves modifying the infrastructure, such as creating depressions around test masses. These recessed structures raise the test mass above the ground, reducing the NN. Virgo used such structures for operational reasons, raising questions about their effectiveness in reducing NN. I detailed the dimensions of recesses under Virgo's input and end test mirrors in central and end buildings in chapter 3, section 3.3

Figure 3.9 (bottom) illustrates the reduction factors of NN attributable to the VIRGO recess. I have calculated a nearly 2-fold reduction in Newtonian noise (NN) within the 12 to 15 Hz range. Reduction of Rayleigh-wave Newtonian noise by a factor of 2 or more is significant, especially considering that achieving a similar reduction through Newtonian noise cancellation typically requires the use of large arrays and complex techniques.

In chapter 4, I conducted spectral analyses, both spatially and temporally, and characterized the seismic field using data from the indoor and outdoor seismic arrays in the North End Building of the Virgo detector. Figure 4.3 provides an example of a spatial spectrum obtained from seismic arrays at a frequency of 10 Hz, where we observe multiple modes simultaneously present within the spectrum. I have considered the dominant seismic sources for different frequencies and estimated their corresponding velocities and propagation directions, as shown in figure 4.10. Through the array analysis, It is observed a lower speed of Rayleigh waves at Virgo, suggesting that NN suppression may be more pronounced than previously estimated when assuming a constant Rayleigh wave speed of 250 m/s.

Incorporating seismic dispersion into the estimation of Newtonian noise reduction has resulted in a more substantial reduction compared to previous estimates, as shown in figure 4.16. We observed a reduction in Newtonian noise by a factor of up to 10, attributed to the lower seismic velocity. According to these findings, the Newtonian noise cancellation system may only require minor additional noise reduction efforts, as seismic NN is already anticipated to be below the sensitivity targets for most frequencies. The verification of these findings will contribute to the optimization and fine-tuning of the Virgo detector's performance in preparation for the upcoming observation runs.

In chapters 5, 6, 7, I studied different topologies of Einstein Tele-

scope within the networks of third-generation gravitational wave detectors and their influences on the data analysis of gravitational wave signals. The response of a gravitational wave detector network to a GW signal depends on several critical factors, including the positions, orientations, and geometrical topologies of individual detectors. The antenna response function characterizes how a detector's orientation and geometry influence its ability to detect gravitational waves originating from various directions and polarizations. In figure 5.5, as presented in chapter 5, we observe that the antenna response function for a triangular detector, like the proposed Einstein Telescope (ET), offers several advantages. Specifically, ET's response is 50% higher compared to a single L-shaped detector, which lacks null directions.

Another important metric for evaluating detector performance is the horizon distance, which is the maximum distance at which a gravitational wave source directly above the detector can be detected, assuming optimal polarisation. Figure 5.9 shows the detectable redshift range for sources of different masses, illustrating the capabilities of both the Einstein Telescope and the Cosmic Explorer. Gravitational wave sources are diverse and distributed across the sky, so an evaluation of the detectors' capabilities requires consideration of their coverage of the entire sky. I have assumed that the sources are uniformly distributed across all sky locations, with random polarisations and tilt angles, and have shown that the redshift achieved for 50%, 90% of the best sources provides a realistic assessment of detector performance.

In chapter 6, I have examined the sky localization capabilities of third-generation gravitational wave detector networks such as the Einstein Telescope and Cosmic Explorer. This investigation includes a comparison between the 'L' shape and the proposed triangular topology of the Einstein Telescope.

I analyze two configurations: the 'Triangular' setup with a 10 km arm length and the 'L' configuration with arm lengths of 10 km, 15 km, and 20 km. I evaluate the performance of these networks using two types of sources: modeled sources and unmodeled sources. Then I utilize the Fisher information matrix to estimate the uncertainty associated with the sky localization of gravitational wave sources.

In figures 6.7 and 6.9, I compare the directional precision for an unmodeled gravitational wave source between the Einstein Telescope with a proposed triangular configuration and a single 'L' shaped detector in the network with two Cosmic Explorers, which provides insights into

the accuracy of sky localization. The findings consistently show that, for both modeled and unmodeled gravitational wave sources in a network with two Cosmic Explorer detectors, the Einstein Telescope configured in a triangular shape outperforms the 'L' shaped detector with a 15 km or 10 km arm length in terms of angular resolution.

In chapter 7, I explored the application of the Einstein Telescope's intrinsic null stream, focusing on its usefulness for the source localization. This null stream combines signals from the telescope's three xylophone interferometers, and it is unaffected by the source's location. My goal was to subtract the null stream noise from the estimator to improve the accuracy of the sky localization estimates. However, it is found that there would be no improvement in the accuracy of sky localization, and it would reduce a data stream from the estimator. This result is consistent with the findings of Wong et al. [225]

I have utilized the ET's null stream to enhance the calibration of the detector's data, employing the self-calibration method as described by Schutz et al [195]. This approach involves modeling the calibration error by analyzing the residual signal found in the null stream. Given that the calibration error in modeling the detector data is at a sub-percent level, the residual signal strength within the null stream is exceedingly faint and difficult to detect individually. Therefore, instead of focusing on a single event, I analyzed a group of events and computed the cumulative signal-to-noise ratio for the residual signal within the null stream. By maximizing this accumulated SNR, I have demonstrated how one can achieve calibration parameter estimates with an accuracy of less than 2% error after analyzing 100 events. While I have considered only one parameter of the calibration function for each side of the ET, in principle, it can be generalized to include more calibration parameters.

Samenvatting

Gravitatiegolven zijn extreem kleine rimpelingen in de stationaire kromming van de ruimtetijd in het heelal, geproduceerd door de beweging en botsingen van astrofysische objecten met extreme massa en dichtheid, zoals neutronensterren en zwarte gaten. Ze werden in 1916 voorspeld door Albert Einstein en 100 jaar later gedetecteerd door LIGO. Het detecteren van zwaartekrachtgolven is een extreem uitdagende taak vanwege hun kleine amplitude, die een uitzonderlijke precisie van het meetinstrument vereist.

Laser-interferometer-detectoren voor gravitatiegolven splitsen een laserstraal in twee armen met spiegels aan de uiteinden. Wanneer een gravitatiegolf passeert, verandert de lengte van de armen, wat een faseverschil veroorzaakt in de gerecombineerde laserstralen. Uitdagingen met betrekking tot detectie komen voort uit verschillende bronnen van ruis, waaronder seismische, thermische, kwantum-, Newtoniaans, detectorruis en instrumentele artefacten die een GW-signaal kunnen nabootsen.

In de eerste helft van dit proefschrift heb ik technieken besproken om Newtoniaans ruis voor gravitatiegolfdetectoren te beperken, waarbij ik me heb gericht op een uitgebreide analyse van Newtoniaans ruis in de Virgo-detector. Newtoniaans ruis (NR), ook bekend als gravitationele gradiëntruis, manifesteert zich als de fluctuaties van lokale zwaartekrachtvelden, die voortkomen uit de dichtheidsvariaties in de omgeving van de testmassa's veroorzaakt door seismische, atmosferische of antropogene factoren. Deze dichtheidsvariaties oefenen een overmatige zwaartekracht uit op de testmassa in de zwaartekrachtgolfdetector, waardoor GW-signalen bij lage frequenties worden nagebootst.

Hoewel het niet mogelijk is om de detector direct af te schermen van NR, zijn er conventionele strategieën voor ruisreductie. Eén zo'n aanpak is om voor de bouw van de detector seismisch rustige locaties te kiezen met minimale natuurlijke en door de mens veroorzaakte seismische verstoringen. Ondergronds gaan, zoals gepland voor de Einstein-

telescoop, vermindert seismische ruis. De huidige detectoren gebruiken NR-subtractie met seismische sensoren dicht bij de testmassa's om NR te schatten en te annuleren. Dit is een uitdaging vanwege de complexiteit van echte seismische velden. Het is gunstig om vlakke oppervlakken te kiezen om verstrooiing te voorkomen. Een juiste plaatsing van de seismometer is cruciaal vanwege de beperkte dekking. Een andere mogelijke methode bestaat uit het aanpassen van de infrastructuur, zoals het creëren van depressies rond testmassa's. Deze verzonken structuren tillen de testmassa boven de grond, waardoor het NR wordt verminderd. Virgo gebruikte dergelijke structuren wegens operationele redenen, wat vragen oproept over hun effectiviteit bij het verminderen van NR. Ik heb de afmetingen van uithollingen onder Virgo's ingangs- en eindtestspiegels in centrale en eindgebouwen gedetailleerd beschreven in hoofdstuk 3, sectie 3.3.

Figuur 3.9 (onder) illustreert de reductiefactoren van NR die kunnen worden toegeschreven aan de VIRGO-uitsparing. Ik heb een bijna 2-voudige reductie berekend van Newtoniaanse ruis binnen het bereik van 12 tot 15 Hz. Het verminderen van Newtoniaanse ruis veroorzaakt door Rayleigh-golven met een factor 2 of meer is aanzienlijk, vooral gezien het feit dat het bereiken van een vergelijkbare vermindering door Newtoniaanse ruisonderdrukking meestal het gebruik van grote arrays en complexe technieken vereist.

In hoofdstuk 4 voerde ik spectrale analyses uit, zowel spatiaal als temporaal, en karakteriseerde ik het seismische veld met behulp van data van de seismische arrays binnen en buiten het noordelijke eindgebouw van de Virgo detector. Figuur 4.3 geeft een voorbeeld van een spatiaal spectrum verkregen uit seismische arrays bij een frequentie van 10 Hz, waar we meerdere modi zien die tegelijkertijd aanwezig zijn in het spectrum. Ik heb de dominante seismische bronnen voor verschillende frequenties in rekening genomen en schatte hun overeenkomstige snelheden en voortplantingsrichtingen, zoals weergegeven in figuur 4.10. Door middel van de array-analyse is er een lagere snelheid van Rayleigh-golven waargenomen bij Virgo, wat suggereert dat NR-onderdrukking meer uitgesproken kan zijn dan eerder werd geschat bij de aanname van een constante Rayleigh-golfsnelheid van 250 m/s.

Het opnemen van seismische dispersie in de schatting van de reductie van Newtoniaans ruis heeft geresulteerd in een meer substantiële reductie vergeleken met eerdere schattingen, zoals te zien is in figuur 4.16. We hebben tot een factor 10 aan reductie van Newtoniaans ruis waargen-

omen, die wordt toegeschreven aan de lagere seismische snelheid. Volgens deze bevindingen vereist het Newtoniaanse ruisonderdrukkingssysteem mogelijk slechts kleine extra inspanningen om het ruis te onderdrukken, aangezien het seismische NR naar verwachting voor de meeste frequenties al onder de gevoeligheidsdoelen ligt. De verificatie van deze bevindingen zal bijdragen aan de optimalisatie en fijne afstemming van de prestaties van de Virgo-detector ter voorbereiding op de komende observatiereeks.

In de hoofdstukken 5, 6, 7, bestudeerde ik verschillende topologieën van de Einstein Telescoop binnen de netwerken van gravitatiegolfdetectoren van de derde generatie en hun invloeden op de data-analyse van gravitatiegolfsignalen. De responsiviteit van een netwerk van gravitatiegolfdetectoren op een GW-signaal hangt af van verschillende kritische factoren, waaronder de posities, oriëntaties en geometrische topologieën van individuele detectoren. De antenna response function karakteriseert hoe de oriëntatie en geometrie van een detector zijn vermogen beïnvloedt om gravitatiegolven afkomstig uit verschillende richtingen en polarisaties te detecteren. In figuur 5.5, zoals gepresenteerd in hoofdstuk 5, zien we dat de antenna response function voor een driehoekige detector, zoals de voorgestelde Einstein Telescoop (ET), verschillende voordelen biedt. In het bijzonder is de responsiviteit van ET 50% hoger vergeleken met een enkele L-vormige detector, die geen nulrichtingen heeft.

Een andere belangrijke metriek voor het evalueren van de prestaties van de detector is de horizonafstand, de maximale afstand waarop een gravitatiegolfbron direct boven de detector kan worden gedetecteerd, uitgaande van optimale polarisatie. Figuur 5.9 toont het detecteerbare roodverschuivingsbereik voor bronnen van verschillende massa's, ter illustratie van de mogelijkheden van zowel de Einstein Telescoop als de Cosmic Explorer. Gravitatiegolfbronnen zijn divers en verspreid over de hemel, dus een evaluatie van de capaciteiten van de detectoren vereist een beschouwing van hun dekking van de volledige hemel. Ik heb aangenomen dat de bronnen uniform verdeeld zijn over alle hemellocaties, met willekeurige polarisaties en kantelhoeken, en heb aangetoond dat de roodverschuiving die bereikt is voor 50%, 90% van de beste bronnen een realistische beoordeling van de detectorprestaties aangeeft.

In hoofdstuk 6 heb ik het lokalisatievermogen aan de hemel onderzocht voor netwerken voor gravitatiegolfdetectoren van de derde generatie, zoals de Einstein Telescoop en de Cosmic Explorer. Dit onderzoek

omvat een vergelijking tussen de 'L'-vorm en de voorgestelde driehoekige topologie van de Einstein Telescoop.

Ik analyseer twee configuraties: de 'driehoekige' opstelling met een armlengte van 10 km en de 'L'-configuratie met armlengtes van 10 km, 15 km en 20 km. Ik evalueer de prestaties van deze netwerken met behulp van twee typen bronnen: gemodelleerde bronnen en niet-gemodelleerde bronnen. Daarna gebruik ik de Fisher-informatiematrix om de onzekerheid te schatten die samenhangt met de lokalisatie van gravitatiegolfbronnen aan de hemel.

In figuren 6.7 en 6.9, vergelijk ik de directionele precisie voor een niet-gemodelleerde gravitatiegolfbron tussen de Einstein Telescoop met een voorgestelde driehoekige configuratie en een enkele 'L' vormige detector in het netwerk met twee Cosmic Explorers, wat inzicht geeft in de nauwkeurigheid van het lokaliseren aan de hemel. De bevindingen tonen consistent dat, voor zowel gemodelleerde als niet-gemodelleerde gravitatiegolfbronnen in een netwerk met twee Cosmic Explorer detectoren, de Einstein Telescoop geconfigureerd in een driehoekige vorm beter presteert dan de 'L' vormige detector met een armlengte van 15 km of 10 km in termen van hoekresolutie.

In hoofdstuk 7 onderzocht ik de toepassing van de intrinsieke nulstroom van de Einstein-telescoop, waarbij we ons concentreerden op het nut ervan voor bronlokalisatie. Deze nulstroom combineert signalen van de drie xylofooninterferometers van de telescoop en wordt niet beïnvloed door de locatie van de bron. Mijn doel was om de ruis van de nulstroom van de schatter af te trekken om de nauwkeurigheid voor hemellokalisatie te verbeteren. Het bleek echter dat de nauwkeurigheid van de hemellokalisatie niet zou verbeteren en het zou een datastroom van de schatter verminderen. Dit resultaat komt overeen met de bevindingen van Wong et al. [225]

Ik heb de nulstroom van ET gebruikt om de kalibratie van de data van de detector te verbeteren met behulp van de zelfkalibratiemethode zoals beschreven door Schutz et al [195]. Bij deze aanpak wordt de kalibratiefout gemodelleerd door het restsignaal in de nulstroom te analyseren. Aangezien de kalibratiefout bij het modelleren van de detectorgegevens op een niveau van minder dan één procent ligt, is de sterkte van het restsignaal in de nulstroom buitengewoon zwak en moeilijk afzonderlijk te detecteren. Daarom heb ik, in plaats van me op één enkel event te richten, een groep events geanalyseerd en de cumulatieve signalto-noise ratio (SNR) voor het restsignaal in de nulstroom berekend.

Door deze geaccumuleerde SNR te maximaliseren, heb ik aangetoond dat schattingen van de kalibratieparameter met een nauwkeurigheid van minder dan 2% bereikt kunnen worden na het analyseren van 100 events. Hoewel we slechts één parameter van de kalibratiefunctie voor elke kant van ET hebben overwogen, kan deze in principe worden veralgemeend om meer kalibratieparameters op te nemen.

Impact Paragraph

Gravitational waves are produced by the accelerated motion of massive objects, changing the curvature of space and time. In binary systems, where neutron stars or black holes orbit each other, their interaction modifies the curvature of space-time and emits energy in the form of gravitational waves. Detecting gravitational waves is extremely challenging because of their weak interaction with matter. Measuring the minuscule strain caused by gravitational waves using gravitational wave detectors poses significant challenges, as various sources of noise mask the signal, requiring advanced mitigation techniques for effective suppression.

In the first part of the dissertation I look at a specific source of noise known as seismic Newtonian noise. This type of noise arises from local density variations due to seismic wave propagation and introduces additional gravitational pull on the test masses, causing them to move. Newtonian noise can potentially limit the sensitivity of advanced detectors in the low frequency range up to 15 Hz. In particular, it is a significant source of noise for third-generation detectors, which aim to achieve improved low-frequency sensitivity. Low-frequency sensitivity is essential for better observations of our target astronomical sources, such as pulsars and massive black hole mergers, etc. Therefore, it is imperative to explore methods to mitigate the Newtonian noise. I have shown that this noise can be reduced for surface detectors by creating cavities around the test masses. This technique has significant implications for the design of future surface detectors so that Newtonian noise can be minimized.

For site-specific noise mitigation, it is important to understand the primary sources of seismic noise. I have therefore carried out detailed seismic analyses to characterize the spatial and temporal characteristics of the seismic field. This technique provides valuable insights into seismology and geoscience. Understanding the sources, velocities and

211

propagation directions of seismic waves has applications in earthquake studies and environmental monitoring. The propagation of seismic waves is influenced by the subsurface geology. By studying these waves, researchers can obtain information about the composition and structure of the Earth's subsurface. I have used comprehensive seismic field information, including details of the subsurface structure, to calculate the reduction in Newtonian noise for the Virgo gravitational wave detector.

As mentioned above, third generation detectors such as the Einstein Telescope and Cosmic Explorer are expected to have improved sensitivity compared to detectors currently in operation. For the Einstein telescope, two topology options are being considered by the collaboration: the L-shape and the triangular topology. Understanding which topology of the Einstein telescope will lead to better scientific results is crucial for determining the final configuration. Therefore, the decision on the topology has to be made soon. In the second part of my dissertation, I analyze how the two different topologies of the Einstein telescope (L versus triangle) affect the accuracy of sky localisation within networks of third-generation gravitational wave detectors. The L-shaped topology of the Einstein telescope considered here consists of two co-located detectors with an aperture angle of 90°, one of which is oriented at an angle of 45°relative to the other. The proposed triangular setup consists of three detectors arranged in an equilateral triangle with a 60°aperture angle. In particular, improved gravitational wave detectors have the potential to have a more significant scientific impact.

The triangular configuration has an additional advantage in that it contains a redundant number of detectors that can produce a null stream. In the general case, the null stream can be constructed by combining data from the network of detectors while canceling out the underlying gravitational wave signal. Canceling out the signal requires prior knowledge of the source location. However, the null stream for the Einstein telescope, with its triangularly arranged detectors, does not depend on the source location. This feature distinguishes the triangular configuration from others and makes it unique in its ability to generate a source location independent null stream. In the dissertation, I have demonstrated the usefulness of this null stream using rigorous analysis and specialized techniques for source localisation and detector calibration. To measure the gravitational wave signal accurately, we need to understand the response of the gravitational wave detector as precisely as possible. This requires knowing the parameters of the gravitational

wave detector with high precision. The process of determining these parameters is known as calibration. The technique I have developed using the null stream has the potential to have a significant impact on improving the calibration of all three detectors of the Einstein telescope. The null-stream methods can be applied to any instrument that has a redundant number of outputs compared to the number of parameters being evaluated.

Acknowledgment

I began my PhD journey at the University of Glasgow, where I spent one-year conducting research. Subsequently, I transitioned to Maastricht University, where I continued my studies and research for the following three years. As I sit down to write these words of gratitude, my mind is flooded with memories that go back to the very beginning of this remarkable journey. I remember the day when I was a physics master's student working on a project in gravitational wave data analysis. I emailed Prof Stefan Hild and received a reply. Our conversations and the research projects we discussed left a deep impression on me. Prof. Hild, your expertise in the field and the dedication of the group were truly inspiring. I remember applying for funding to do my PhD at the University of Glasgow. Despite of our best efforts, my application was initially rejected due to a missing form. Despite the setback, you never lost faith in me. With your support and guidance, I eventually secured the prestigious Ron Rever Scholarship for my PhD in Glasgow. I'll never forget the day you told me the news; it felt like a dream come true. It was also my first international tour. I am incredibly grateful for your unwavering support and guidance throughout my PhD journey. Your comments and feedback have been invaluable in pushing my research forward. You have shown me not only how to navigate research directions within projects, but also how to cultivate independence as a researcher. Our discussions have been instrumental in shaping the direction of this dissertation and I am sincerely grateful for your mentorship. You have always helped me with all my problems.

In Glasgow, I have been envisioned by my second supervisor Prof. Ken Strain. I remember discussing with you about the project I was working on. You gave me your advice, and your thoughts on my quests. I remember you asked me, where I want to see myself in the next five years, and this question, still embedded in my mind, helps me to direct myself in many aspects of my life.

After moving to Maastricht University in my second year of PhD, I had the opportunity to speak with Prof. Stefan Danilishin and I feel fortunate to have worked under his supervision. Prof. Danilishin, you have played a crucial role in guiding my doctoral research and in shaping my dissertation. I am deeply grateful to you for your unwavering support and guidance throughout this journey. Your friendly attitude has made it easier for me to understand concepts and direct my research. During the challenging times of COVID-19 restrictions, working from home without much interaction posed significant difficulties, but our long discussions over Zoom were invaluable in keeping my research progress steady even in the midst of the pandemic. Thank you for being a source of guidance and inspiration throughout this journey.

I would like to express my sincere gratitude to all the members of my reading committee for your diligent efforts and valuable insights into my work. Your constructive feedback and thoughtful suggestions have been instrumental in refining and strengthening my dissertation. I greatly appreciate your time and expertise and am truly grateful for your unwavering support throughout the review process.

One of the best parts of this journey for me is the opportunity to interact with other researchers, PhDs, PostDocs, and professors. Collaborating within the broader academic community has been invaluable. I had the opportunity to work with Prof. Jan Harms on Newtonian noise. Prof. Harms, I want to express my sincere gratitude for your guidance. The concepts and techniques I learned from our collaboration have been essential to me, shaping the project I am currently working in. Your prompt responses to the emails were always appreciated, and it was truly a pleasure to work with you and benefit from your guidance. I would also like to extend my thanks to Dr. Francesca Badaracco. Francesca, your assistance in understanding Newtonian noise cancellation has been invaluable. Additionally, I am grateful to the entire Virgo Newtonian Noise group, from whom I have gathered information over time. It has been a wonderful experience to collaborate with such a talented group of individuals.

I also had the privilege of being part of the science team at the Einstein Telescope, where we had stimulating discussions on various fascinating topics. The brainstorming sessions within the team helped me to explore fundamental concepts and perspectives in my research journey.

I would like to express my sincere thanks to the GWFP (Gravitational Wave Fundamental Physics) team at the University. It has been

a pleasure to work with you all. Our coffee conversations around the kitchen table were really enjoyable and time seemed to fly by with you. Being away from my family, thousands of kilometers away, and not being able to visit them often has not been easy. However, your company has allowed me to work with a clear mind and stay motivated. It's always enlightening to learn about the projects others are working on, to understand their challenges, and to engage in discussions about my work. I would like to thank Tim Hiert for your invaluable help and support. Tim, you have efficiently assisted with the problems that have arisen and ensured that they have been resolved smoothly. I would like to thank Zeb Van Ranst. Zeb, you helped to translate the Dutch summary of this dissertation. You didn't even mind when I asked you again for some corrections. I am delighted to have good friends like Diksha, Luise, and Viola. Thank you all for your unwavering support throughout this journey.

I would like to express my sincere gratitude to my parents, both my mum and dad, as well as my grandma, for your support throughout my academic journey. Your consistent provision of not only emotional support but also encouragement and understanding has been invaluable to me. Your belief that you have in me has served as a constant source of motivation, inspiring me to overcome challenges and to strive for excellence in all of my endeavors. I'd like to express my deepest gratitude to Dr. Pushan R. Dasgupta and Manisha Dasgupta for loving, supporting and guiding me in many aspects of my life. Your constant encouragement has been a source of strength for me, especially during my challenging times. Thank you for always being by my side, for motivating me and for your invaluable presence in my life.

I am grateful for the opportunity to express my appreciation to my two close friends, Harshita and Dipika. Our discussions have spanned numerous intriguing topics, encompassing life, society, academic and non-academic matters. Despite our occasional debates, I've come to realize that your insights often hold, even if it takes me some time to grasp them fully. Your role as a friend and advisor has been invaluable to me, and I am truly thankful for your friendship and support.

I acknowledge the support and resources provided by Maastricht University, Nikhef and the University of Glasgow. The support I received from Maastricht University has been remarkable. Despite transitioning from Glasgow, the move has been seamless, and I am grateful to Maastricht University for facilitating the process. The facilities and

Basic scientific research leads us to understand the world around us and provides critical knowledge to address real-world challenges. As an author fortunate enough to be immersed in the fascinating field of gravitational wave astronomy, I am deeply grateful for the opportunity to contribute to this exciting field. Having had the privilege of working on the LIGO, Virgo, and ET collaborations, I have explored the possibilities and potential of this pioneering field.

Thank you all for being part of this academic journey.
Ayatri Singha

Curriculum vitae

Born in 1993 in West Bengal, India, Ayatri Singha started her academic journey with a passion for physics. She completed her Bachelor's degree in Physics from Durgapur Government College, affiliated to Burdwan University. Taking the next step in her academic pursuit, Ayatri moved to Gujarat, India, where she successfully completed her Master of Science with a major in Physics from the Indian Institute of Technology (IIT), Gandhinagar. During her master's program, she was actively involved in various projects related to gravitational wave data analysis.

Ayatri received the Gold Medal from IIT Gandhinagar in recognition of her achievement in securing the highest grade in the Master of Science in Physics program. She also received the Best Researcher Award from IIT Gandhinagar. This award was given to her across all disciplines in the Master of Science program. In 2018, Ayatri Singha was awarded the prestigious Prof. Ron Driver Scholarship, which enabled her to pursue her Ph.D. at the University of Glasgow, UK. During this time, she successfully completed a comprehensive one-year Ph.D. training program under the supervision of Prof. Stefan Hild. After her time at the University of Glasgow, Ayatri Singha moved to Maastricht University to continue her Ph.D. research under the supervision of Prof. Stefan Hild and Prof. Stefan Danilishin. Over the course of four years, she enrolled in her doctoral research in the field of gravitational of astronomy.

Ayatri has presented her research at several LIGO-VIRGO collaboration meetings, VIRGO Weeks, demonstrating her active participation in collaborative efforts. She has published two papers in peer-reviewed journals. She has attended courses at the University of Glasgow and two topical lectures by Nikhef in Amsterdam. She attended a gravitational summer school where her work won the best poster award. Ayatri has played an active role in various tutorials within the science program of Maastricht University and the University of Glasgow. She has also given workshops on gravitational wave data analysis.